

Optimization of NH_3 -MBE grown *p*-doped (Al)GaN layers and their implementation in long wavelength laser diodes and tunnel junctions

THÈSE N° 6747 (2015)

PRÉSENTÉE LE 30 OCTOBRE 2015

À LA FACULTÉ DES SCIENCES DE BASE

LABORATOIRE EN SEMICONDUCTEURS AVANCÉS POUR LA PHOTONIQUE ET L'ÉLECTRONIQUE

PROGRAMME DOCTORAL EN PHOTONIQUE

ÉCOLE POLYTECHNIQUE FÉDÉRALE DE LAUSANNE

POUR L'OBTENTION DU GRADE DE DOCTEUR ÈS SCIENCES

PAR

Marco MALINVERNI

acceptée sur proposition du jury:

Prof. J.-E. Moser, président du jury
Prof. N. Grandjean, Dr J.-F. Carlin, directeurs de thèse
Prof. P. Perlin, rapporteur
Prof. M. Kneissl, rapporteur
Prof. M. Illegems, rapporteur



ÉCOLE POLYTECHNIQUE
FÉDÉRALE DE LAUSANNE

Suisse
2015

Experience is not what happens to you;
it's what you do with what happens to you.

— Aldous Huxley

To my family and friends...

Acknowledgements

Many people contributed to this Ph.D and deserve special thanks. Above all, I would like to thank my supervisor Professor Nicolas Grandjean for allowing me to live this beautiful experience. He guided and supported me throughout the last 4 years, being a constant source of motivation. His commitment and dedication into research are fascinating. His teachings, beyond pure academic knowledge and for which I am extremely grateful, will surely help me in my future career. I also would like to thank Dr. Jean-François Carlin, my thesis co-director, who has been a source of inspiration during these years for the growth of III-nitrides.

Thanks also to Prof. Jacques-Edouard Moser, Prof. Emer. Marc Illegems, Prof. Michael Kneissl, and Prof. Piotr Perlin for accepting being part of the jury, carefully reading the thesis manuscript, and having created a cordial and inspiring environment during the private defense.

Dr. Amélie Dussaigne deserves a special thanks. She introduced me to molecular beam epitaxy (MBE) and stimulated my interest in this growth technology and III-nitrides. On the other hand, all the work performed would have not be possible without Denis Martin, who allowed me to access a perfectly working MBE system, constantly improving. I want to warmly thank him for the support he gave me during these years in EPFL.

I had the chance to work with extremely competent people without whom most of the results would have not been obtained: first of all I want to thank Dr. Antonino Castiglia for sharing his deep knowledge on *p*-type doping and on the electrical characterization of devices and Dr. Marco Rossetti, for being always available for discussion and help. In the same way I thank Dr. Eric Feltin and Dr. Julien Dorsaz for their effort put in the development of green laser diodes. I am grateful to Dr. Jean-Michel Lamy for all the support he gave me in the device processing and for the deposition of the dielectric mirrors. I also have to acknowledge Dr. Jerome Napierala for his contribution at the beginning of the CTI project.

I would like to express my gratitude to the MBE team. Thanks to Etienne Giraud and Nils Kaufmann for all the nice Monday morning discussions and for keeping a relaxed working atmosphere. Special thanks to Dr. Lorenzo Lugani and Dr. Marlene Glauser, two great colleagues and friends, for having shared the same office and for all the nice experiences we had together. I am thankful to Dr. Raphaël Butté for all the patience he had in correcting the thesis and the papers, for his support, and for all the discussions we had together. A big thank to all my LASPE colleagues: Jacques, Gatien, Georg, Marcel, Guillaume, Luca, Lise, Yoshi, Munise, Alexei, and Pascal.

Acknowledgements

I wish to thank as well Mohammed Adam and Christophe Le Gros for all the fruitful discussions and for making my stay in Lausanne unforgettable.

I finally thank my marvelous family who allowed me to benefit from countless experiences and Fabri, who is everyday on my side full of enthusiasm and hunger for discovery.

Lausanne, June 2015

M. M.

Abstract

Over the last two decades III-nitride optoelectronic devices have experienced an impressive evolution in terms of performance. However, their potential is far from being fully exploited. Although they offer bandgaps from the deep UV to the infrared spectral range, lasing is currently restricted to the 336–536 nm wavelength region. Several challenges still need to be overcome. For example, the thermal stability of the InGaN active region becomes an issue in long-wavelength ($\lambda > 500$ nm) laser diodes: high indium content ($x_{In} > 25\%$) quantum wells (QWs) have been shown to markedly degrade when kept above 900 °C. For this reason, the growth temperature of the subsequent *p*-type waveguide and cladding layers must be sufficiently low to avoid QW degradation, which is accompanied by a reduction in the internal quantum efficiency. Thanks to the high vacuum environment, molecular beam epitaxy (MBE) allows growing these layers at a much lower temperature compared to metalorganic vapor phase epitaxy (MOVPE), and could be used to reduce the thermal budget on the active region, further extending the wavelength range. Thus the aim of this thesis is the realization of long-wavelength laser diodes by combining high efficiency active regions grown by MOVPE with *p*-doped layers grown by ammonia- (NH_3 -) MBE.

Hence, the *p*-type doping by NH_3 -MBE is first scrupulously studied and optimized on 500 nm thick (Al)GaN layers. In order to comprehensively address the physical processes governing the doping efficiency, the role of the growth temperature, the V-III ratio, and the growth rate is investigated. In addition, the Mg cell configuration resulting in the best doping profile control and reproducibility is studied as well. Electrochemical capacitance-voltage profiling is extensively used to study the compensation mechanisms. The optimization leads to the achievement of layers exhibiting low dopant compensation (below 5%) up to high doping levels ($[\text{Mg}] = 7 \times 10^{19} \text{ cm}^{-3}$) and resistivity values as low as $0.4 \Omega \text{ cm}$.

These layers are then implemented on top of active regions grown by MOVPE and lasing is obtained for the first time in hybrid structures exhibiting state-of-the-art electrical characteristics. The threshold voltage is as low as 4.3 V in an index guided structure with $800 \times 2 \mu\text{m}^2$ ridge dimension designed for violet emission ($\lambda = 400$ nm). These excellent current-voltage characteristics are achieved owing to the doping profile control in the cladding and contact layers which is confirmed by the low contact resistance value of $5 \times 10^{-4} \Omega \text{ cm}^2$. Lasing is also demonstrated beyond 500 nm, keeping state-of-the-art electrical characteristics, despite the reduced doping in the cladding layer. These devices also exhibit values for internal optical

Abstract

losses as low as 6 cm^{-1} .

Given the high net acceptor concentrations mastered in this work, the growth of tunnel junctions is also attempted. Low specific resistance values are demonstrated in NH_3 -MBE grown GaN tunnel homojunctions. The absence of hydrogen passivation and the reduced memory effects of MBE are considered to be crucial for the realization of these devices together with the stability of the doping at reduced growth temperatures. $n^+ - p^+ - n$ structures featuring a tunnel junction in series with a $p - n$ junction are then used to spread the current across light-emitting diodes. A device architecture featuring a buried tunnel junction to be used for current injection in micro-LEDs or vertical cavity surface emitting lasers is also demonstrated and excellent current confinement properties are obtained.

These results highlight the potential of the p -type doping by NH_3 -MBE and open new prospects in terms of design architecture and growth procedures.

Keywords: NH_3 -MBE, gallium nitride, aluminium gallium nitride, III-nitrides, p -type doping, laser diodes, dopant compensation, hydrogen passivation, tunnel junctions, current spreading, current confinement, buried tunnel junctions.

Riassunto

Nel corso degli ultimi due decenni, le prestazioni dei dispositivi optoelettronici a base di nitrucci hanno subito un'evoluzione impressionante. Tuttavia, il loro potenziale non viene completamente sfruttato. Pur offrendo bande proibite che vanno dal profondo ultravioletto (UV) fino all'infrarosso (IR), l'emissione di luce laser è attualmente limitata alle lunghezze d'onda comprese tra 336 e 536 nm. Questo perché molti problemi devono ancora essere risolti. Ad esempio, la stabilità termica della regione attiva formata da InGaN costituisce un problema per i diodi laser che emettono ad alte lunghezze d'onda ($\lambda > 500$ nm) : quando i pozzi quantici ad alto contenuto di indio ($x_{In} > 25$ %) vengono mantenuti al di sopra di 900°C , la loro qualità cristallina si degrada. Per questa ragione la temperatura di crescita degli strati di tipo *p*, quali la guida d'onda e gli strati di cladding, deve essere sufficientemente bassa per evitare il degrado dei pozzi quantici che provoca una riduzione dell'efficienza quantica interna. L'epitassia da fasci molecolari (MBE), grazie al suo ambiente ad alto vuoto, permette la crescita di questi strati epitassiali ad una temperatura molto più bassa rispetto a quella utilizzata in epitassia metallorganica in fase vapore (MOVPE), e può essere utilizzata per ridurre il bilancio termico della regione attiva. Questo processo potrebbe quindi di estendere ulteriormente la gamma di lunghezze d'onda dei diodi laser a base di nitrucci. Quindi, l'obiettivo di questa tesi è la realizzazione di diodi laser che operano ad alta lunghezza d'onda combinando regioni attive ad alta efficienza cresciute per MOVPE con strati di tipo *p* cresciuti per NH_3 -MBE.

Con questo scopo la crescita di strati epitassiali di (Al)GaN di tipo *p* tramite NH_3 -MBE è stata scrupolosamente studiata e successivamente ottimizzata. Il ruolo della temperatura di crescita, del rapporto V-III e della velocità di crescita sull'efficienza di drogaggio è stato analizzato col fine di comprendere i processi fisici che la governano. Inoltre è stata esaminata la configurazione della cellula di Mg che consente il migliore controllo del profilo e la migliore riproducibilità di drogaggio. I profili degli accettori ottenuti tramite la misura elettrochimica delle caratteristiche capacità-tensione sono stati ampiamente utilizzati per studiare i meccanismi di compensazione. L'ottimizzazione ha permesso la crescita di strati epitassiali che presentano una bassa compensazione (sotto al 5 %) ad elevati livelli di drogaggio ($[\text{Mg}] = 7 \times 10^{19} \text{ cm}^{-3}$) e una bassa resistività ($0.4 \Omega \text{ cm}$).

Questi strati sono stati fabbricati su regioni attive cresciute per MOVPE e per la prima volta si è riuscita ad ottenere l'emissione di luce laser in strutture ibride. Queste strutture hanno caratteristiche elettriche che corrispondono allo stato dell'arte d'oggi. Si è raggiunta

una bassa tensione di soglia di 4.3 V in una struttura a guida a contrasto di indice di dimensioni $800 \times 2 \mu\text{m}^2$ progettata per l'emissione nel viola ($\lambda = 400 \text{ nm}$). Le eccellenti caratteristiche corrente-tensione sono state ottenute grazie al controllo del profilo di drogaggio negli strati di cladding e di contatto. Il basso valore di resistenza di contatto di $5 \times 10^{-4} \Omega \text{ cm}^2$ ne è un'ulteriore conferma. In aggiunta è stata dimostrata l'emissione di luce laser al di là dei 500 nm mantenendo caratteristiche elettriche allo stato dell'arte, nonostante la ridotta concentrazione di drogaggio nel cladding. Le perdite ottiche interne di questi dispositivi sono state ridotte fino a un valore di 6 cm^{-1} .

La crescita di giunzioni tunnel è stata anch'essa investigata, date le alte concentrazioni di accettori netti raggiunte durante questa tesi. Sono stati ottenuti bassi valori di resistenza specifica in omogiunzioni tunnel a base di GaN grazie all'utilizzo dell' NH_3 -MBE. L'assenza della passivazione dell'idrogeno e i ridotti effetti di memoria in MBE, insieme alla stabilità del drogaggio a temperature di crescita ridotte, sono cruciali per la realizzazione di questi dispositivi. In seguito sono state realizzate strutture $n^+ - p^+ - n$ dotate di una giunzione tunnel posta in serie a una giunzione $p - n$ per diffondere la corrente in diodi elettroluminescenti. Inoltre, eccellenti proprietà elettriche di confinamento sono state ottenute utilizzando un'architettura di dispositivo che comprende una giunzione tunnel sepolta. Questa architettura è molto promettente per l'iniezione di corrente in micro-LED o nei laser a cavità verticale ed emissione superficiale (VCSELs).

I risultati ottenuti dimostrano il potenziale del drogaggio di tipo p tramite NH_3 -MBE e aprono nuovi orizzonti in termini di architetture di dispositivi innovative e procedure di crescita.

Parole chiave: NH_3 -MBE, nitruro di gallio, nitruro di alluminio-gallio, drogaggio di tipo p , diodi laser, compensazione del drogaggio, passivazione dell'idrogeno, giunzioni tunnel, confinamento della corrente, giunzioni tunnel sepolte.

Contents

Acknowledgements	v
Abstract (English/Italiano)	vii
List of Acronyms	xv
Introduction	1
1 Properties of III-nitrides and experimental techniques	5
1.1 Crystalline structure	5
1.2 Polarization effects in III-nitrides	7
1.2.1 Spontaneous and piezoelectric polarization	7
1.2.2 Quantum confined Stark effect	9
1.3 Band gap	10
1.4 Electrical properties	11
1.4.1 <i>p-n</i> junction	11
1.4.2 Metal-semiconductor contacts	15
1.5 Experimental techniques	17
1.5.1 Growth and substrates	17
1.5.2 Metal organic vapor phase epitaxy	18
1.5.3 Molecular beam epitaxy	18
1.5.4 Electrochemical capacitance-voltage profiling	21
1.5.5 Transmission-line measurement	23
1.5.6 Variable stripe length method	25
2 Magnesium p-type doping of (Al)GaN using MBE	27
2.1 Introduction	27
2.1.1 Magnesium and other impurities	28
2.2 Dopant compensation	30
2.2.1 Polarity inversion and pyramidal inversion domains	31
2.2.2 Native point defects	33
2.2.3 Mg clustering	35
2.2.4 Hydrogen	36
2.3 Alternatives to bulk doping	37

2.3.1	Delta doping	37
2.3.2	Polarization engineered doping, 2D and 3D cases	37
2.3.3	Codoping	38
2.4	Experimental	39
2.4.1	Mg solid source effusion cell	39
2.4.2	Growth temperature window	42
2.4.3	V/III ratio optimization	45
2.4.4	Morphological features	47
2.4.5	Acceptor compensation versus [Mg]	50
2.4.6	Hydrogen incorporation in MBE	55
2.4.7	Thermal stability of p -type layers	57
2.4.8	Mg doping of AlGaIn alloys	61
2.5	Modeling of the compensation	63
2.5.1	Net acceptors as a function of [Mg]	63
2.5.2	Temporal/depth dependence	64
2.6	Summary	67
3	Devices I: Hybrid laser diodes	69
3.1	Lasing in semiconductor LDs	69
3.2	Green laser diodes: a challenging spectral region	74
3.2.1	Thermal budget reduction	74
3.2.2	Optical confinement	76
3.3	Growth approach	76
3.4	Transfer method	77
3.5	Electrical characteristics of p - n junctions	78
3.6	Index-guided LDs at EPFL	81
3.7	First generation violet LDs	82
3.8	Interface contamination	83
3.9	Second generation violet LDs	84
3.10	Optical pumping	86
3.11	Long wavelength hybrid laser diodes	90
3.12	Summary	96
4	Devices II: Tunnel junctions	97
4.1	Theory	97
4.2	III-nitride based TJs	99
4.3	Interest in III-nitride tunnel junctions	101
4.4	Technical challenges for achieving efficient TJs	102
4.5	n^+ -type doping of GaN in NH_3 -MBE	103
4.6	n - p - n structures featuring TJs	105
4.6.1	Hybrid LEDs with TJs	105
4.6.2	TJs on FS-GaN substrates	107
4.6.3	Hybrid TJs	109

4.6.4 Buried tunnel junctions	110
4.7 Towards LDs featuring BTJs	113
4.8 Summary	116
A Appendix	123
A.1 Resistivity vs net acceptor concentration	123
A.2 MOVPE net acceptor profiles	124
Bibliography	141
Curriculum Vitae	143

List of Acronyms

AFM	Atomic force microscopy
APT	Atom probe tomography
BTJ	Buried tunnel junction
CDF	Cumulative distribution function
ECV	Electrochemical capacitance-voltage
EBL	Electron blocking layer
HEMT	High electron mobility transistors
HVPE	Hydride vapor phase epitaxy
IDB	Inversion domain boundary
IQE	Internal quantum efficiency
LEEBI	Low energy electron beam irradiation
LED	Light emitting diode
LD	Laser diode
MOVPE	Metalorganic vapor phase epitaxy
NH₃-MBE	Ammonia molecular beam epitaxy
PAMBE	Plasma assisted molecular beam epitaxy
PhC	Photonic crystal
PID	Pyramidal inversion domain
RTA	Rapid thermal annealing
SC	Self-compensation
sccm	Standard cubic centimeters per minute
SIMS	Secondary ion mass spectrometry
TCO	Transparent conductive oxide
TEM	Transmission electron microscopy
TLM	Transmission-line measurement
TJ	Tunnel Junction
VCSEL	Vertical cavity surface emitting laser
VSL	Variable stripe length
XRD	X-ray diffraction

Introduction

Thanks to their unique structural and optical properties, III-nitride semiconductors are at the heart of the recent solid-state lighting revolution. The investigation of III-nitride semiconductors can be considered to have started at the end of the 60s in the central research laboratories of the Radio Corporation of America (RCA) in Princeton, NJ. With the ambitious idea of making flat colour display, the demonstration of the first epitaxial growth of gallium nitride (GaN) on sapphire was demonstrated [1]. However, the remarkable challenges associated with *p*-type doping for this material system prevented researchers to realize efficient light-emitting diodes (LEDs). It was only in 1989 that Hiroshi Amano, under the supervision of Isamu Akasaki, developed the low-energy electron beam irradiation technique, allowing *p*-type conduction to be obtained [2]. Two years later, Shuji Nakamura from Nichia Corporation demonstrated that thermal annealing in a nitrogen atmosphere was sufficient to obtain *p*-type conductivity [3]. The discoveries of these three Japanese scientists triggered an incredible research and development effort around the world on III-nitrides and their work was rewarded with the Nobel Prize in Physics in 2014.

Already in 1993 Nichia demonstrated a candela class blue LED [4], followed by the realization of the first electrically injected blue laser diode (LD) in 1996 [5] which led to the development of the Blu-ray technology. Nowadays LED efficiencies up to 300 lm/W are obtained in research laboratories and values around 150-200 lm/W are achieved by the best commercially available devices. By means of alloying III-nitrides potentially offer a tunable bandgap spanning from the ultraviolet (UV) to the infrared (IR) spectral range. It is however in the violet-blue spectral region that the maximum efficiencies are obtained.

When moving toward shorter wavelengths, the large activation energy of the Mg acceptors becomes an issue, which adds up to the crystal quality degradation for high Al compositions due to the lack of appropriate substrates. However, UV solid-state light sources could offer access to efficient water purification, disinfection, and medical diagnostic systems, which fuels their development. In this framework during the past few years the device performance evolution gained extra momentum [6] and 2 inch freestanding AlN substrates are becoming available.

On the other hand, the development of long wavelength devices ($\lambda > 500$ nm) is driven by compact RGB projection systems and communication over plastic optical fiber networks,

which feature an absorption minimum window around 550 nm. However, the efficiency of both III-nitride and AlGaInP based devices is strongly reduced in this spectral region, often referred to as green gap. Good laser performances have been demonstrated using II-VI materials [7], but their reliability is still preventing their commercial adoption. Thus, during a long time period, second harmonic generation was the only solution to produce a monochromatic compact light source in the green spectral range, benefiting from the maturity of the III-arsenides technology. However, the alignment optics together with the non-linear crystal make the devices much more expensive to manufacture and less compact than a direct LD based solution.

In the last five years remarkable progress has been made on long wavelength III-nitride based devices, partially fulfilling the green gap. Continuous-wave operation up to 537 nm [8], and output powers above 1 W [9] were demonstrated. This was obtained by improving the crystal quality of high In content quantum wells, at the heart of the device. Indium contents above 25% are required for lasing above 500 nm. The main challenges are the thermal stability of these layers, which degrade when kept at high temperature, the ternary alloy disorder also referred to as inhomogeneous broadening, and the reduction in the index contrast between the waveguide and the cladding layers, which results in lower modal gain values. All the above-mentioned issues have not prevented the commercialization of 515-520 nm LDs from leading companies such as Nichia and Osram.

While several problems have partially been solved, the potential of III-nitrides is far from being fully exploited. For example, their low p -type conductivity still limits the device performance in terms of I - V characteristics and wall plug efficiency values. Furthermore, efficient tunnel junctions are extremely difficult to obtain in this materials system and often necessitate the use of polarization engineered layers to assist the carrier tunneling [10, 11]. These polarization engineered layers however provide an additional absorption channel when included in opto-electronic devices such as vertical cavity surface emitting lasers (VCSELs), thereby limiting their performance.

In general p -type doping can still be considered as one of the major bottlenecks for III-nitride bipolar devices and the compensation mechanisms are far from being fully understood.

Objectives and outline

This PhD thesis was carried out in the framework of the CTI-KTI project “Nitride-based Green SLEDs” 10708.1 PFDP-NM in collaboration with two Swiss companies: Novagan and Exalos. The aim of the project was the realization of long wavelength III-nitride based laser diodes and superluminescent light-emitting diodes. To this aim, the growth by NH_3 -MBE of p -type material was investigated as a potential candidate to drastically reduce the thermal budget on high In content InGaN active regions, possibly preventing their degradation during the top cladding layer growth. This included the development of a hybrid growth process to combine the active region, bottom waveguides and cladding layers grown by MOVPE with the p -doped

layers grown by NH_3 -MBE.

Given the academic purpose of the PhD, the p -type doping characteristics were extensively studied to elucidate some debated aspects regarding the dopant compensation processes in p -type GaN. The doping potential of NH_3 -MBE was then exploited for the realization of tunnel junctions without employing polarization engineered layers, thus formed by a simple GaN highly doped homojunction.

The manuscript is divided in four chapters:

The basic materials properties of III-nitrides such as the crystal structure, the lattice and polarization mismatch between different alloys, and the bandgap, are presented in Chapter 1. The p - n junction characteristics are also discussed together with ohmic and Schottky metal-semiconductor contact configurations. An introduction of the principal growth techniques precedes the description of some measurement techniques employed during this work which concludes this first chapter.

In Chapter 2 the p -type doping by NH_3 -MBE is discussed in terms of morphological features, growth temperature window, and III-V ratio optimization. Electrochemical capacitance voltage profiling is thoroughly employed to investigate the dopant compensation mechanisms in these layers. The doping characteristics are compared to MOVPE grown samples before and after thermal annealing treatments and the differences are discussed. In addition the role of hydrogen during growth is studied. Finally, a model which includes a time dependent compensation process accounting for the experimental observations is presented. In this chapter the challenges linked to the use of solid Mg sources are treated as well.

The electrical characteristics of the so-formed epilayers are discussed in Chapter 3, where they are successfully implemented in hybrid devices. This chapter focuses on the realization of hybrid long wavelength laser diodes. The main limitations still affecting these devices serve as an introduction, together with the fundamental physics of lasing in semiconductor 2D heterostructures. The careful growth optimization leads to the demonstration of the first hybrid LD structures lasing beyond 500 nm. The optimization of the doping profile in the cladding layer is discussed in order to keep low internal losses and excellent electrical characteristics.

The last chapter deals with the realization of several tunnel junction structures enabling for current spreading and current confinement. The n -type doping characteristics of NH_3 -MBE grown GaN layers are studied prior to the description of the different device designs considered in this work. The properties of various n - p - n structures featuring a tunnel junction in series with a p - n one are also presented. A buried tunnel junction device is described and the realization of LDs featuring such structure is attempted.

Finally, the experimental results are summarized together with an outlook of the perspectives.

The work presented in Chapter 3 was partially published in two papers:

Introduction

M. Malinverni, J.-M. Lamy, D. Martin, E. Feltin, J. Dorsaz, A. Castiglia, M. Rossetti, M. Duelk, C. Vélez, and N. Grandjean, *Low temperature p-type doping of (Al)GaN layers using ammonia molecular beam epitaxy for InGaN laser diodes*, Appl. Phys. Lett. **105**, 241103 (2014).

M. Malinverni, J.-M. Lamy, D. Martin, L. Lahourcade, E. Feltin, J. Dorsaz, A. Castiglia, M. Rossetti, M. Duelk, C. Vélez, and N. Grandjean, *InGaN laser diodes emitting at 500 nm with p-layers grown by molecular beam epitaxy*, Appl. Phys. Express **8**, 022105 (2015).

The work presented in Chapter 4 is to be published in Applied Physics Letters:

M. Malinverni, D. Martin, and N. Grandjean, *InGaN based micro light emitting diode featuring buried GaN tunnel junction*.

Finally the growth optimization of *n*-type GaN doping by NH₃-MBE was published in the following paper:

L. Lugani, M. Malinverni, S. Tirelli, D. Marti, E. Giraud, J.-F. Carlin, C. R. Bolognesi, and N. Grandjean, *n^+ -GaN grown by ammonia molecular beam epitaxy: Application to regrown contacts*, Appl. Phys. Lett **105**, 202113 (2014).

1 Properties of III-nitrides and experimental techniques

This chapter deals with the unique structural, optical, and electrical characteristics of III-nitrides. In the first part, starting from the fundamental crystal properties of this semiconducting material family, the polarization effects and band gap properties are presented. The second part is an overview of the building blocks necessary for the device realization where the p - n junction characteristics are introduced together with some considerations on metal-semiconductor contacts in the context of III-nitrides. Finally, the different growth techniques for the growth of III-nitrides are discussed together with the introduction to some of the experimental techniques employed.

1.1 Crystalline structure

The crystalline structure of a material determines a wide range of its properties. Depending on the substrate orientation and growth conditions III-nitride compounds can crystallize in the tetrahedrally bonded wurtzite or zincblende structures [12]. While the wurtzite phase, which exhibits a hexagonal symmetry, is thermodynamically stable, the zincblende phase is metastable and is predicted to present an indirect band gap [13]. This situation is the opposite of other III-V compounds, such as GaSb, GaAs, and GaP, for which the zincblende phase is the stable one.

The wurtzite structure possesses a two-atom basis (Al/Ga/In and N in the case of III-nitrides) which form two interpenetrating hexagonal closed-packed sublattices each. The planes of the metal (cations) and nitrogen (anions) atoms are periodically intercalated along the stacking direction (c -axis) following an ABABAB... configuration. The separation between successive bilayers (AB) corresponds to the metal-nitrogen bond length and defines the internal parameter $u \cdot c$, where c is the lattice constant along the stacking direction. On the other hand, atoms within the basal plane are separated by the lattice constant a . In an ideal wurtzite structure, each atom is bonded to four atoms which are positioned at the corners of a tetrahedron, *i.e.* with bonding angles of 109.47° . As a consequence, the c , a , and u parameters

satisfy the following relations:

$$\frac{c}{a} = \sqrt{\frac{8}{3}} = 1.633 \quad \text{and} \quad u = \frac{3}{8} = 0.375. \quad (1.1)$$

However, the wurtzite structure lacks of inversion symmetry because of its atomic arrangement and non-unity atom basis. Because of the strong electronegativity difference between cations and anions, successive bilayer stacks are attracted to each other by an electrostatic force resulting in a deformation of the lattice with respect to the ideal case [14]. In fact, to minimize this energy, the separation between the two atomic planes forming the bilayer is reduced through the deformation of the bonding angles. For this reason, a deviation from the ideal relationships (1.1) between the three lattice parameters is always observed.

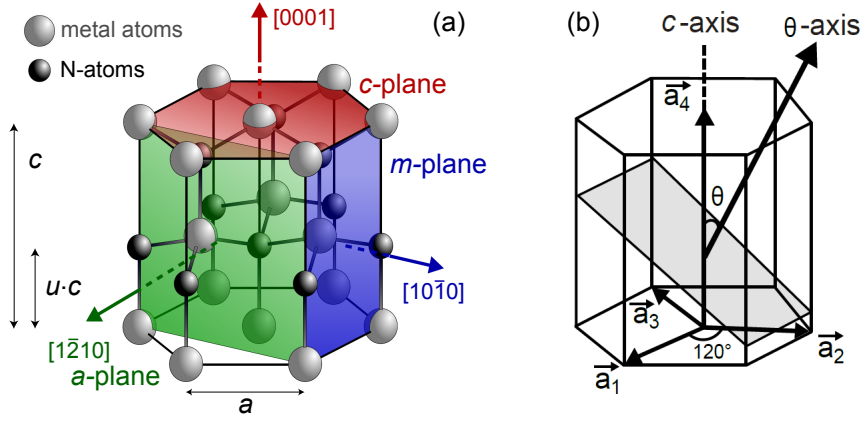


Figure 1.1: (a) Wurtzite unit cell of III-nitride compounds showing the arrangement of group-III metal atoms and nitrogen atoms. The polar plane (*c*-plane) and two non-polar planes (*a*- and *m*-) are outlined in red, green, and blue, respectively. (b) Four vector basis of the wurtzite lattice (\mathbf{a}_1 , \mathbf{a}_2 , \mathbf{a}_3 , \mathbf{a}_4). In grey an arbitrary semipolar plane is shown forming an angle θ with the *c*-axis.

While three orthogonal primitive vectors are sufficient to describe a three-dimensional lattice, it is common to use a four vector basis for the wurtzite lattice (\mathbf{a}_1 , \mathbf{a}_2 , \mathbf{a}_3 , \mathbf{a}_4). The latter, \mathbf{a}_4 , is collinear to the stacking direction *c* (high symmetry axis) and is orthogonal to the other three which lie in the same plane forming angles of 120° between each other. The use of this three in plane vector basis requires the condition $\mathbf{a}_3 = -\mathbf{a}_1 - \mathbf{a}_2$ to be satisfied. The corresponding four Miller indices *h, k, l, m* are then used to define crystallographic planes (*h, k, l, m*) and directions [*h, k, l, m*].

The lattice parameters *c* and *a* are strongly dependent on the atomic size of the cation and anion atoms and to a certain extent to their electronegativity difference. Al is the group-III element employed from the lowest period (3) in the periodic table. As a consequence the AlN lattice parameters are the lowest for III-nitrides binary compounds, followed by GaN, and InN, in increasing order as shown in Table 1.1 [15].

	AlN	GaN	InN
c (Å)	4.982	5.185	5.703
a (Å)	3.112	3.189	3.545

Table 1.1: Lattice parameters for III-nitrides binary compounds AlN, GaN, and InN at room temperature.

For ternary alloys the crystal structure does not change. Two metallic atoms coexist in the metal sublattice in a ratio given by the composition of the alloy. For example, the $\text{In}_{0.2}\text{Ga}_{0.8}\text{N}$ alloy will present 20% of the metal sites occupied by indium and 80% occupied by gallium. However, the lattice parameters are affected. It is found that a linear interpolation between the two binary compounds can be used (the so-called Vegard's law) to determine the a and c parameters (indicated by a general letter S) of the $A_xB_{1-x}\text{N}$ alloy:

$$S_{A_xB_{1-x}\text{N}} = x \cdot S_{\text{AN}} + (1 - x) \cdot S_{\text{BN}} , \quad (1.2)$$

where x is the alloy composition and A and B are the two metallic elements. A nonlinear term, $-bx(1-x)$, need to be added to equation (1.2) to reproduce the evolution of the u parameter, where b is generally referred to as the bowing parameter.

1.2 Polarization effects in III-nitrides

1.2.1 Spontaneous and piezoelectric polarization

We have previously emphasized the anisotropy, related to the wurtzite structure, of III-nitride crystals which are noncentrosymmetric. The lack of inversion symmetry results in the formation of electrostatic dipoles leading to the creation of a macroscopic spontaneous polarization vector (\mathbf{P}^{sp}) oriented along the c -axis. The significant difference in electronegativity between nitrogen and III-metallic atoms is responsible for the large values of spontaneous polarization in III-nitrides. Furthermore, \mathbf{P}^{sp} is linearly related to the internal parameter u and, in general, dependent on the relative separation between the anion and cation sublattices [16]. As a consequence similarly to the evolution of the internal parameter u as a function of the alloy composition (1.2), the spontaneous polarization can be expressed in the form:

$$\mathbf{P}_{A_xB_{1-x}\text{N}}^{sp} = x \cdot \mathbf{P}_{\text{AN}}^{sp} + (1 - x) \cdot \mathbf{P}_{\text{BN}}^{sp} - bx(1 - x) . \quad (1.3)$$

The spontaneous polarization for the binary compounds is : $\mathbf{P}_{\text{AlN}}^{sp} = -0.09 \text{ C/m}^2$, $\mathbf{P}_{\text{GaN}}^{sp} = -0.034 \text{ C/m}^2$, $\mathbf{P}_{\text{InN}}^{sp} = -0.042 \text{ C/m}^2$ [16]. Bowing parameters b of 0.037 C/m^2 , 0.021 C/m^2 , and 0.070 C/m^2 are proposed in Ref. [16] for InGaN, AlGaN, and AlInN ternary alloys, respectively.

For an epilayer at equilibrium the spontaneous polarization alone is sufficient to describe its polarization state. However, because of the device architecture complexity and the need for heterostructures, the epitaxial layers are generally grown pseudomorphically on substrates

and buffer layers having different lattice parameters and thermal expansion coefficients. The resulting crystal deformation affects the internal lattice parameters and eventually leads to a piezoelectric polarization component. The piezoelectric polarization is therefore closely related to the strain state of the epilayer, and its components are given by:

$$\mathbf{P}_i^{pz} = \sum_j e_{ij} \epsilon_j \quad \text{with } i = 1, 2, 3 \quad \text{and } l = 1, \dots, 6, \quad (1.4)$$

where e_{ij} are the piezoelectric constants [16], and ϵ_j is the strain tensor due to the mismatch in the lattice parameters expressed using Voigt notation.

The total polarization \mathbf{P} is then given by the sum $\mathbf{P}^{sp} + \mathbf{P}^{pz}$. A step-like discontinuity in \mathbf{P} , as it is the case at the quantum well (QW) interfaces, generates a polarization-induced sheet charge density σ_P given by Eq. 1.5. The total field inside a single QW with infinite barrier thickness and a superlattice (SL) structure can then be calculated using [17]:

$$\sigma_P = -\Delta \mathbf{P} \cdot \mathbf{n} \quad \mathbf{F}_{QW} = -\frac{\sigma_P}{\epsilon_w} \mathbf{n} \quad \mathbf{F}_{SL} = -\frac{\sigma_P}{\epsilon_w + \epsilon_b L_w / L_b} \mathbf{n}, \quad (1.5)$$

where \mathbf{n} is a vector perpendicular to the interface, ϵ_w and ϵ_b are the product of the relative permittivities for the QW and the barrier material with the vacuum permittivity (ϵ_0), and L_w and L_b are the QW and barrier thicknesses, respectively. For the case of a multiple quantum well (MQW) the built-in electric field magnitude will sit in between \mathbf{F}_{QW} and \mathbf{F}_{SL} depending on the number of QW periods. In general for III-nitrides, because of the strong spontaneous and piezoelectric polarization, the value of the built-in field can be as large as few MV/cm depending on the alloy composition of the well and barrier material [18–20]. This has strong implications on the recombination of carriers inside QWs which will be discussed in Section 1.2.2 and has been exploited for attempting the realization of devices with superior doping characteristics.

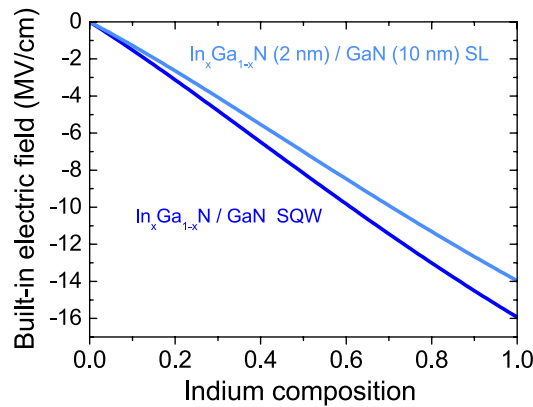


Figure 1.2: Built-in electric field in InGa_N/Ga_N QW heterostructures strained on Ga_N.

For the specific case of a Ga-polar InGa_N/Ga_N QW, the spontaneous polarization of the InGa_N layer points in the $[000\bar{1}]$ direction, while the piezoelectric polarization, because of

the compressive strain state of the well, is antiparallel and oriented in the [0001] direction [21]. The resulting polarization-induced sheet charge density is positive at the InGaN/GaN interface close to the surface, leading to the formation of a two-dimensional electron gas (2DEG) and opposite in sign at the other interface, possibly leading to the formation of a two-dimensional hole gas (2DHG) if holes are provided.

1.2.2 Quantum confined Stark effect

As we have seen in Sec. 1.2.1, the charges at the interfaces lead to a built-in electric field which is responsible for the quantum confined Stark effect (QCSE): the electric field results in the bending of the band structure which has profound implications on the optical properties and on the distribution of the carriers in III-nitride devices. This effect is always observed in III-nitride heterostructures grown along the c -axis as the polarization discontinuities cannot be suppressed. The fundamental transition energy in QW heterostructures is then given by [22]:

$$E_{e_1-hh_1} = E_{g,QW} + e_1 + hh_1 - E_B - eF_{QW}l_{QW}, \quad (1.6)$$

where $E_{g,QW}$ is the band gap of the strained well material, e_1 and hh_1 are the electron and hole confinement energy in the triangular potential, respectively, E_B is exciton binding energy (which generally can be neglected for optoelectronic devices), and l_{QW} is the QW thickness. The last term in equation (1.6) describes the QCSE. Its effect is the reduction of the transition energy which, for thick-enough QWs, can become even smaller than the band gap of the bulk material constituting the well. As a result the emission of a QW can be easily tuned by controlling its thickness.

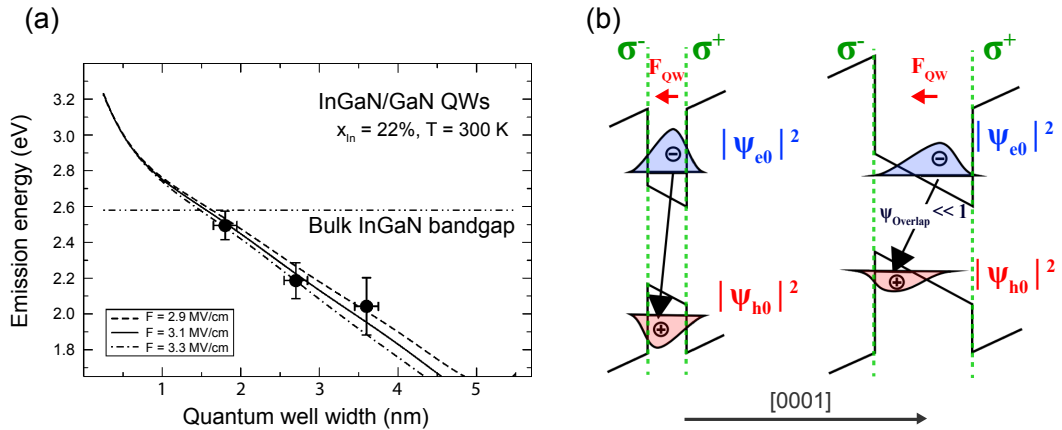


Figure 1.3: (a) Transition energy as a function of the well width for $In_{0.22}Ga_{0.78}N$ MQWs. (b) Schematic representation of the QCSE for the case of InGaN/GaN QWs of different thicknesses. Figures have been taken and adapted from Refs. [19] and [16], respectively.

However, the presence of opposite fixed charges at the interfaces of the heterostructure, and

the resulting band-bending which give rise to triangular-shaped QWs, lead to the spatial separation of the electron and hole wavefunctions as well (Fig. 1.3), the latter effect being proportional to the QCSE (*i.e.* to the product of the built-in field and the QW thickness). Moreover the electron and hole wavefunction overlap and oscillator strength are inversely proportional to the magnitude of the QCSE, ultimately giving rise to increasingly long radiative lifetimes (τ_{rad}) as the QW thickness increases. This impacts the QW internal efficiency (η_i) which is given by $\eta_i = \frac{\tau_{nrad}}{\tau_{nrad} + \tau_{rad}}$. It follows that controlling the emission wavelength by simply changing the QW thickness has a negative impact on the overall device performance and the tuning of the alloy composition is always preferred when possible.

One has also to mention the screening of the built-in field by either photogenerated, electrically injected, or extrinsic carriers in the quantum wells [23, 24]. The latter may be introduced by doping the QW and/or the barriers (preferred). Therefore the magnitude of F_{QW} can be reduced by doping. Furthermore, by increasing the optical or electrical pumping, the emission radiation blueshift because of the screening of the built-in field and consequent reduction of the QCSE. The dependence of the field screening to the free carriers concentrations is discussed in Ref. [25].

1.3 Band gap

GaN and related alloys are of major interest for the realization of optoelectronic devices thanks to their direct band gap. Theoretically, III-nitride based devices could span from the infrared (IR) to the ultraviolet (UV) spectral region covering a wide range of applications. Their direct band gap ranges from 0.7 eV for InN, to 3.507 eV for GaN, and 6.23 eV for AlN, when measured at cryogenic temperatures (2 K) [15]. Apart from $Al_{0.83}In_{0.17}N$ which is lattice-matched to GaN [26, 27], all ternary alloys have a lattice-mismatch with respect to GaN (as shown in Fig. 1.4(a)). This is often a limiting parameter in device design setting the uppermost constraint on the active region and cladding layer thicknesses for the case of laser diodes (LDs).

By means of alloying, the band gap of III-nitrides can be tuned as shown in Fig. 1.4(b) for ternary alloys. The evolution of the bandgap as a function of the alloy composition can be expressed in the form of a modified expression of Vegard's law including the non linear bandgap bowing parameter (in a similar fashion as for the u parameter, being strictly related to E_g). Values for the latter parameter of -0.70, -1.43, and -3.00 eV [28] for AlGaIn, InGaIn, and AlInN, respectively, have been used in Fig. 1.4(b).

A sketch of the band structure around the Γ point ($k = 0$) is reported in Fig 1.4(c). The wurtzite crystal structure of GaN has a high symmetry axis and is thus inherently anisotropic as previously discussed in Section. 1.1. The three-fold degeneracy of the valence band is split by the crystal field and the spin-orbit interaction giving rise to the A heavy hole, B light hole, and C split-off hole valence bands exhibiting Γ_9 , Γ_{7+} , and Γ_{7-} symmetry, respectively [29]. The crystal anisotropy is also responsible for the deviation from a pure parabolic dispersion as qualitatively represented in Fig. 1.4(c). It results that the optical properties of QWs grown on

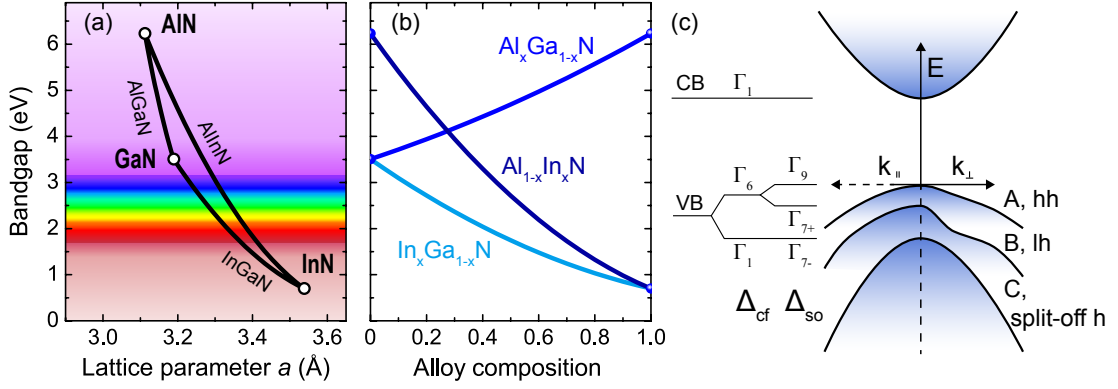


Figure 1.4: (a) Band gap of III-nitride alloys as a function of the in-plane lattice parameter a . (b) Evolution of the band gap as a function of the alloy composition for (Al,Ga,In)N ternary alloys. (c) Schematic representation of the GaN band structure around $k = 0$ illustrating the role of the crystal field (Δ_{cf}) and spin-orbit interaction (Δ_{so}) in the formation of the three distinct valence bands.

crystal planes differing from the c -plane are anisotropic as well. This has profound implications on the gain properties of LDs grown along these crystal orientations for which the optical gain strongly depends on the in-plane laser stripe direction [30].

1.4 Electrical properties

1.4.1 p - n junction

Nowadays p - n junctions are found in a vast variety of semiconductor devices. They are employed in electronic circuits for rectifying and switching applications. They are also at the heart of some of the most technologically relevant devices such as the metal-oxide-semiconductor field effect transistor (MOSFET), the bipolar junction transistor (BJT), and solar cells. Furthermore, they allow the realization of light emitting diodes (LEDs) and LDs, or more generally the realization of bipolar electrically driven photonic devices.

A p - n junction is formed when p - and n -type semiconducting materials are connected together. Hereafter we will consider the case of an abrupt p - n junction. Because of the large carrier concentration difference, carriers diffuse across the junction as described by Fick's law of diffusion: holes diffuse from the p -side to the n -side and the opposite is true for electrons. However, as the dopant impurity can not diffuse, the diffusion of the majority carriers leaves behind ionized impurities which are not compensated anymore by electrons and holes, for the case of donor and acceptor impurity atoms, respectively. As a result a negative space charge is created on the p -side of the junction and a positive space charge on the n -side. Consequently, an electric field (E) is formed, in the opposite direction to the diffusion current (J_{diff}) [31]. In other words this electric field generates a drift current (J_{drift}) oriented in the opposite direction of J_{diff} . The total current across the junction ($J_{p,n}$) is then given by the sum of

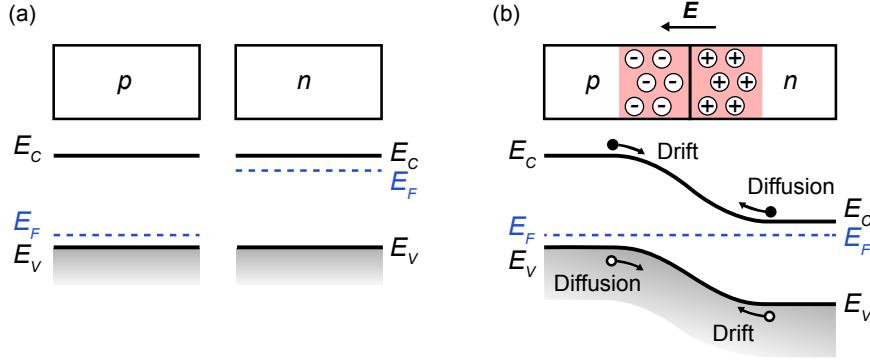


Figure 1.5: (a) Isolated p - and n -type semiconductors. E_C and E_V stand for conduction and valence band edge energy, respectively. (b) Energy band diagram of the p - n junction and schematic representation of the space charge region together with the electric field (E) formed.

$J_{diff} + J_{drift}$. At thermal equilibrium $J_p = J_n = 0$ and the Fermi level (E_F) is constant along the sample, as illustrated in Fig. 1.5b. The drift and diffusion currents counterbalance each other for each type of species (free carriers).

It follows that at thermal equilibrium a unique space charge distribution together with a well defined built-in potential exist (V_{bi}). The latter results from the difference in electrostatic potential between the n -type (ψ_n) and p -type (ψ_p) neutral regions which are given by [31]:

$$\psi_n = \frac{k_B T}{q} \ln \left(\frac{N_D}{n_i} \right), \quad \psi_p = \frac{k_B T}{q} \ln \left(\frac{N_A^-}{n_i} \right), \quad V_{bi} = \psi_n - \psi_p = \frac{k_B T}{q} \ln \left(\frac{N_A^- N_D}{n_i^2} \right), \quad (1.7)$$

where k_B is the Boltzmann constant, T is the temperature, N_D is the donor impurity concentration, N_A^- is the ionized acceptor impurity concentration, n_i is the intrinsic carrier concentration, and q is the elementary charge. Because of the large activation energy (E_A) of the magnesium (Mg) impurity, ionized acceptor impurities (N_A^-) must be considered to calculate the electrostatic potential in the neutral regions instead of the usual total acceptor impurity concentration (N_A). However, in the junction region the Fermi level is above the acceptor impurity level, thus the acceptors are fully ionized.

By solving Poisson equation with the appropriate boundary conditions (see Ref. [31]) the depletion region width (W), *i.e.* the width of the space charge region, can be calculated:

$$W = \sqrt{\frac{2\epsilon_0\epsilon_r}{q} \frac{N_A + N_D}{N_A N_D} (V_{bi} - V)}, \quad (1.8)$$

where V is the applied bias. From capacitance measurements it is confirmed that Mg acceptors are fully ionized in the depletion region, thus we can make use of N_A instead of N_A^- [32]. For a positive bias, when we apply a positive voltage $+V$ to the p -side with respect to the n -side, the space charge region width is reduced, which corresponds to a reduction by V of the

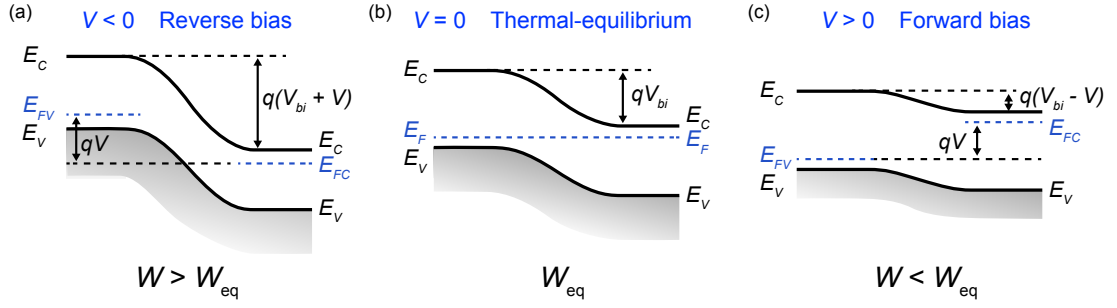


Figure 1.6: Energy band diagrams of a p - n junction under thermal equilibrium (b), and forward and reverse bias, (c) and (a), respectively. E_{FC} and E_{FV} are the quasi-Fermi levels positions for the conduction and the valence band, respectively. E_{FC} and E_{FV} are used to describe the carrier distributions when the junction is out of equilibrium.

total electrostatic potential becoming equal to $V_{bi} - V$ as shown in Fig. 1.6. On the other hand, under reverse bias conditions, the space charge region width is increased and the total electrostatic potential increases with respect to V_{bi} (Fig. 1.6(a)). In addition, the depletion region always spreads more on the less doped side of the junction when the N_D and N_A values are not the same.

The reduction in the total electrostatic potential under forward bias allows for more carriers to diffuse as the potential barrier decreases. By considering the diffusion equations of minority carriers outside the depletion region, one can derive the ideal diode equation [31]:

$$J = J_s \left[\exp\left(\frac{qV}{k_B T}\right) - 1 \right] \quad \text{where} \quad J_s \equiv \frac{qD_p p_n}{L_p} + \frac{qD_n n_p}{L_n}, \quad (1.9)$$

where J_s is the saturation current density, D_n and D_p are the diffusion coefficients for electrons and holes, respectively, n_p and p_n are the nonequilibrium electron and hole density in the n - and p - region, respectively, and L_n and L_p are the diffusion lengths for the two types of carriers. In a real p - n diode one needs to take into account the series resistance (R_s) and a parallel shunt resistance (R_p). The first arises from the non-negligible contact and sheet resistance of the doped layers, in the case of III-nitrides mostly related to the p -type doping. Its effect is shown in Fig. 1.7(a). The second is generally related to manufacturing imperfections and leakage currents occurring across the device (Fig. 1.7(b)). Eq. (1.9) becomes:

$$J = J_s \left[\exp\left(\frac{qV_d}{k_B T}\right) - 1 \right] - \frac{V_d}{R_p} \quad \text{where} \quad V_d = V - IR_s. \quad (1.10)$$

Finally, the current contribution of the recombination of carriers in the space charge region (Shockley–Read–Hall generation and recombination rate) and the diffusion due to recombinations taking place in the vicinity of the space charge region, needs to be included, as it usually dominates the current-voltage (I - V) characteristics for low forward biases (Fig.1.7(d)). Eq.

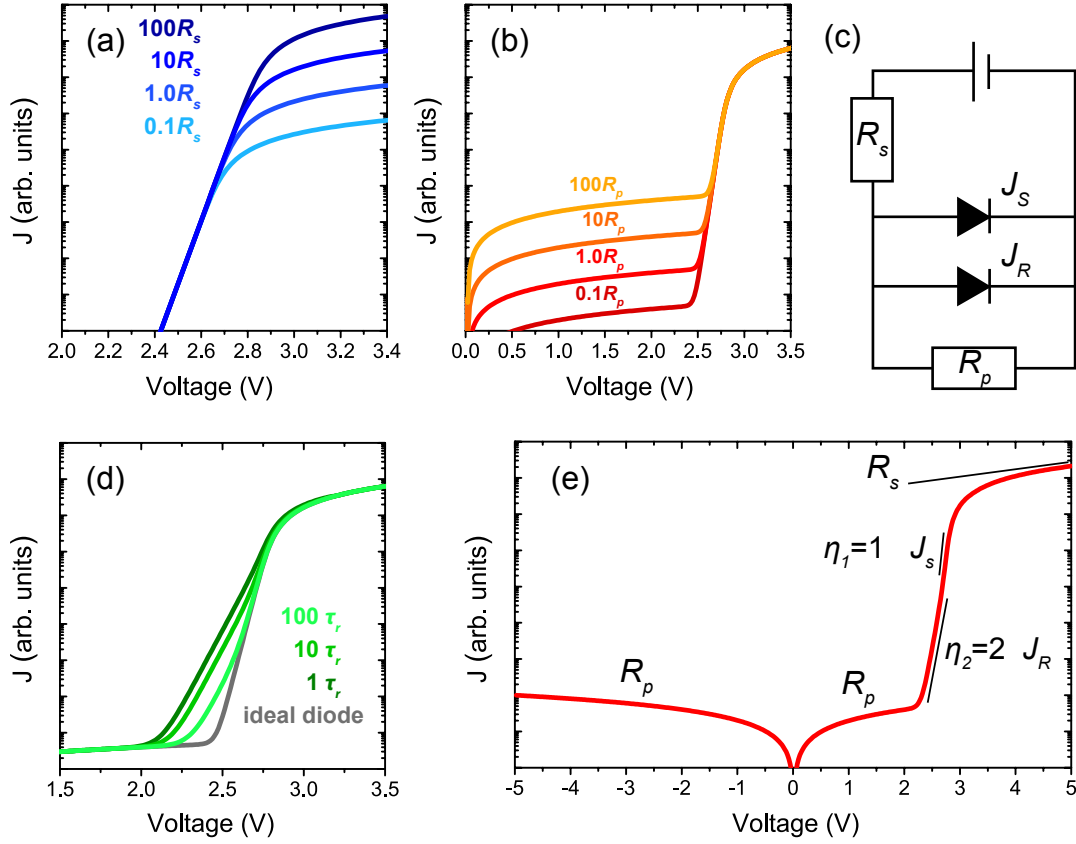


Figure 1.7: Influence of the series resistance R_s (a), the shunt resistance R_p (b), and the generation and recombination currents (d), on the diode characteristics. The equivalent circuit considered is shown in (c). All effects are summarized in (e).

(1.10) can then be written as:

$$J = J_s \left[\exp\left(\frac{qV_d}{\eta_1 k_B T}\right) - 1 \right] + J_R \left[\exp\left(\frac{qV_d}{\eta_2 k_B T}\right) - 1 \right] - \frac{V_d}{R_p}. \quad (1.11)$$

J_R is given by [33]:

$$J_R = \frac{qn_i W}{\tau_r}, \quad (1.12)$$

where τ_r is the effective recombination lifetime in the depletion region and $\eta_{1,2}$ are the ideality factors. For purely diffusive currents η is equal to 1, whereas when the recombination current dominates, $\eta=2$. Thus, $\eta_1 = 1$, and $\eta_2 = 2$. All the abovementioned effects are summarized in Fig. 1.7(e). However, for the case of GaN-based devices, ideality factors differing from 2 (typically considerably higher) are often observed for low forward voltages, which cannot be explained by the presence of leakage paths (shunt resistance R_p). This non ideality may originate from the higher dislocation density with respect to other semiconductors and from

non-abrupt doping interfaces [34]. Shah and coworkers [35] argued that the high ideality factors arise from the sum of the ones of the individual components forming the p - n structure, including the reverse biased Schottky metal contacts formed on p -type material and discussed in the next section.

Under reverse bias, the increase in the depletion region width combined with the increase in the electrostatic potential results in extremely low currents, mainly attributable to leakage. This will remain true until the reverse bias allows for either avalanche multiplication or interband tunnelling to occur, after which the junction breakdown, which allows a large amount of current to flow across it.

1.4.2 Metal-semiconductor contacts

To electrically inject devices, metal-semiconductor contact need to be formed. The contact properties are governed by the relation between the semiconductor and the metal work functions, ϕ_S and ϕ_M , respectively, and by the electron affinity (χ_S) of the semiconductor, *i.e.* the separation between the vacuum level (E_{VAC}) and the conduction band edge (E_C).

In the case of an n -contact, for $\phi_M > \phi_S$ (the opposite condition holds for a p -contact) an energy barrier ($q\phi_B$) is formed at the contact interface, limiting the injection of carriers as shown in Fig. 1.8. This barrier appears because of the migration of electrons from the semiconductor to the metal in order to establish equilibrium (for n -type material). The barrier height is then given by:

$$q\phi_B = q(\phi_M - \chi_S) \quad \text{for } n\text{-type} \quad \text{and} \quad q\phi_B = E_g - q(\phi_M - \chi_S) \quad \text{for } p\text{-type}. \quad (1.13)$$

When a barrier exists to the injection of carriers, a Schottky contact is formed as shown in Fig. 1.8. In this case, the semiconductor is depleted of majority carriers in the vicinity of the metal-semiconductor interface. The extension of the depletion region is then given by (\equiv one-sided abrupt junction):

$$W_n = \sqrt{\frac{2\epsilon_0\epsilon_r}{qN_D}(\phi_B - V)} \quad \text{for } n\text{-type} \quad \text{and} \quad W_p = \sqrt{\frac{2\epsilon_0\epsilon_r}{qN_A}(\phi_B - V)} \quad \text{for } p\text{-type}. \quad (1.14)$$

As expected, W decreases as the doping in the vicinity of the contact is increased. This type of contact (Schottky) arises when the work function of the metal is either too large or too small, for either n -type or p -type semiconductor, respectively.

In order to obtain an ohmic contact, the right metal must be chosen. The highest reported ϕ_M values for metals do not exceed 5.7 eV. However, the work function energy ($q\phi_S$) of p -type GaN has been reported to be as high as 5.9 ± 0.1 eV [36], with a slight dependence on the doping level. As a result, a fully ohmic contact cannot be realized on p -type GaN. As a consequence, the transport of carriers over the barrier results in large contact resistances (R_c).

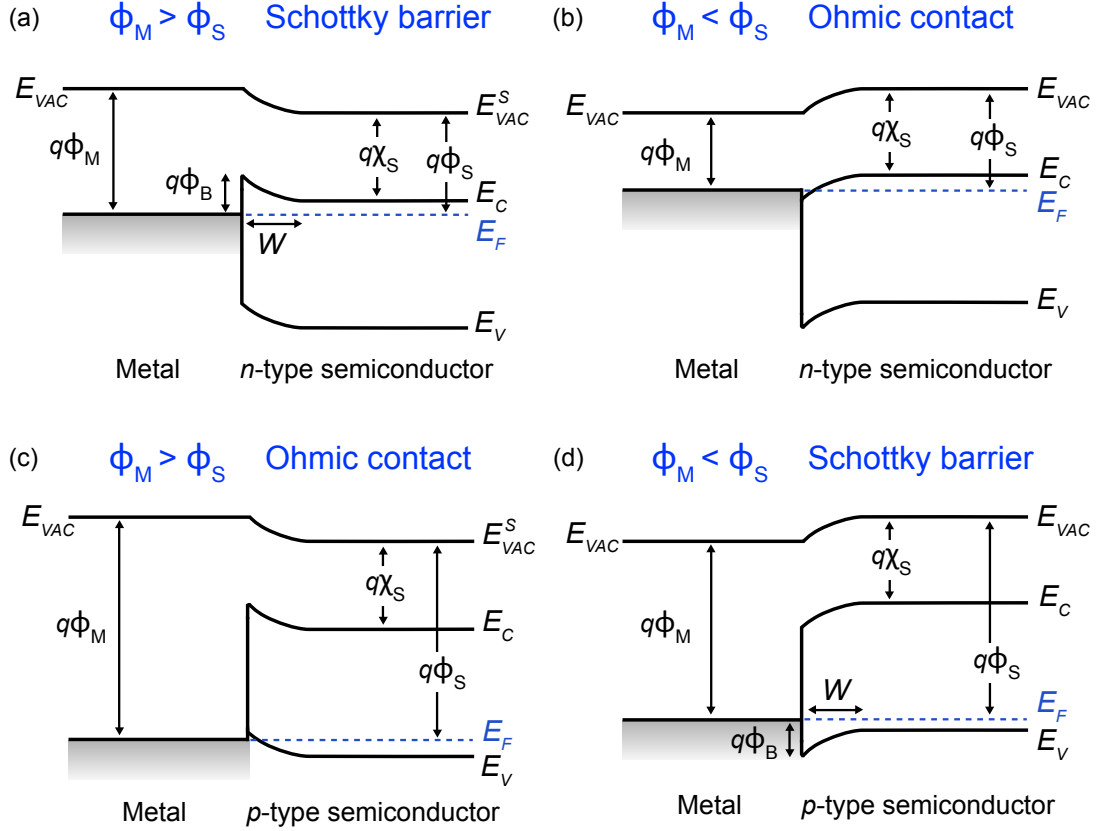


Figure 1.8: Band diagrams for metal-semiconductor contacts for the case of n -type semiconductors, (a) and (b), and p -type semiconductors, (c) and (d). The dependence to the relation between the metal and semiconductor work function is clearly shown for both types of contacts.

However, one can still achieve ohmic contact characteristics, despite the presence of the Schottky barrier, by exploiting the quantum mechanical tunneling of carriers through the barrier. As we have previously seen, the barrier width, which is determined by the width of the depletion region W , is inversely proportional to $\sqrt{N_D}$ (for n -type material). By increasing the doping in the proximity of the contact interface, it is possible to reduce W . Provided the barrier width, thus W , is thin enough, carriers can then tunnel across the barrier with a high probability. This results in a low R_c value despite the unfavorable band alignment. For this reason the contact layer, *i.e.* the last few tens of nanometers of semiconductor in contact with the metal, has often a higher doping level with respect to the rest of the device. The reduction in W as the doping level is increased is schematically represented in Fig. 1.9, showing as well the reduction in the separation of the conduction band edge to the Fermi level as the doping level is increased.

In conclusion, for the case of p -type GaN the doping of the contact layer is of primary importance to reduce as much as possible the value of R_c which strongly affects the I - V characteris-

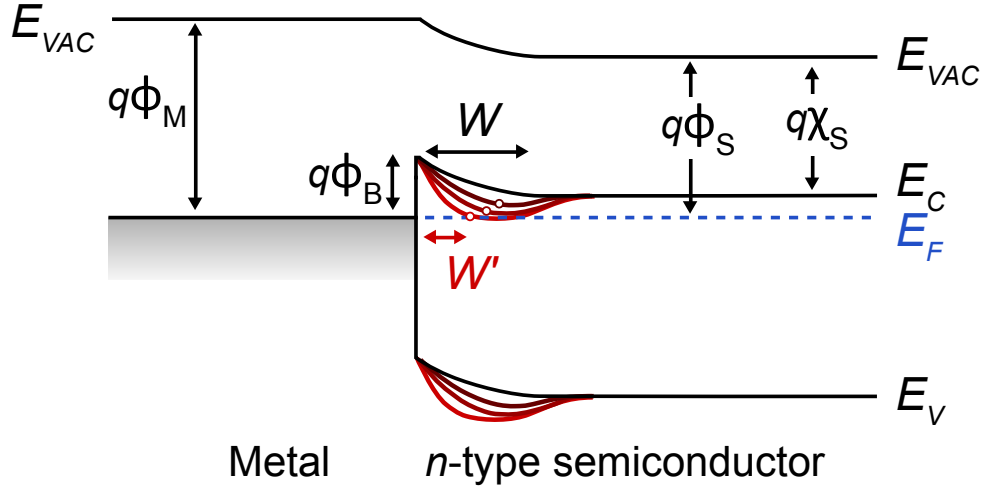


Figure 1.9: Band diagram for metal- *n*-type semiconductor Schottky contact. The evolution of the depletion width as the donor concentration in the cap layer is increased (from black to red) is schematically represented.

tics, especially at high currents.

1.5 Experimental techniques

1.5.1 Growth and substrates

GaN and related alloys can be grown by a variety of techniques. Metal organic vapor phase epitaxy (MOVPE) is by far the most used, and it is the growth technique of choice for the realization of optoelectronic devices such as LEDs and LDs which are nowadays the major commercial application of III-nitrides.

Hydride vapor phase epitaxy (HVPE) is extensively used for the fabrication of freestanding (FS) GaN substrates [37], thanks to its high growth rate, enabling the affordable realization of thick GaN epilayers. On the other hand, bulk GaN can be grown by ammonothermal growth [38, 39], which makes use of high pressures and high temperatures, up to 650–750 °C and 100–600 MPa, respectively. At the moment, however, this latter growth technique has still a limited market penetration. Regarding FS and bulk GaN substrates, they are used for the realization of LDs, vertical devices for high-power electronics [40], and LEDs. Since 2010, FS substrates up to 6-inch diameter are available [41] while ammonothermal GaN substrates are still limited to 2-inches.

Finally, molecular beam epitaxy (MBE) allows the growth of III-nitrides under ultra high vacuum, and it is well-known for its ability to achieve extremely sharp interfaces. It is mainly employed for research and still scarcely used in the industry.

The vast majority of the samples presented in this work was at least partly grown by MBE. In general, MOVPE GaN templates grown on sapphire substrates have been used to subsequently grow *p*-doped layers by MBE and study their characteristics. Furthermore, unless specified, GaN:Mg layers have been grown by MBE. Finally, both FS GaN and sapphire substrates have been employed, depending on the application.

1.5.2 Metal organic vapor phase epitaxy

MOVPE, member of metal organic chemical vapor deposition (MOCVD) family, is a growth technique that relies on the transportation of the precursors needed for the crystal growth to the wafer in the vapor phase. By using appropriate carrier gases, usually either N₂ or H₂, or a mixture of both, the chemicals are brought to the reactor. In such a way, ultrapure metalorganics used as the group-III element source are decomposed at the wafer surface, such as trimethylgallium (TMGa, Ga(CH₃)₃), triethylgallium (TEGa, Ga(C₂H₅)₃), trimethylaluminium (TMAI, Al(CH₃)₃), and trimethylindium (TMIn, In(CH₃)₃). On the other hand, the group-V source is ammonia (NH₃) which is thermally cracked on-surface. Eventually the reaction by-products are expelled from the growth surface and from the reactor. Dopants are also provided in the form of metalorganics. Bis(cyclopentadienyl)magnesium (Cp₂Mg) and silane (SiH₄) are commonly used for *p*- and *n*-type doping, respectively.

A large amount of ammonia is used during MOVPE growth, with V/III ratio typically ranging from a few hundreds when growing at 1050°C to several thousands when the growth temperature is reduced. This arises from the low cracking efficiency of ammonia. The pressure in the reactor is generally ranging between 2×10^3 Pa to atmospheric pressure and the typical growth temperature for GaN is around 1050°C.

Two MOVPE reactors have been used to grow the samples presented in this thesis which are an AIXTRON Close Coupled Showerhead vertical reactor which allows to grow up to three 2-inch wafers during the same run, and an AIXTRON 200 horizontal reactor allowing the growth of only one 2-inch wafer per run.

1.5.3 Molecular beam epitaxy

MBE was invented by J. R. Arthur and Alfred Y. Cho in the late 1960s at Bell Telephone Laboratories and further developed during the 1970s [42–45]. It is a physical epitaxial growth technique which is characterized by an ultra-high vacuum environment. This has two principal functions: first, to reduce the contamination from unwanted impurities, and secondly, to allow to work under the molecular beam regime. Under the latter, the mean free path of the atoms/molecules constituting the beam is much larger with respect to the cell to wafer distance. In such a way, the interaction between different species prior to their arrival on the growth surface is avoided.

In our case, the ultra-high vacuum is obtained via the combination of three pumping systems.

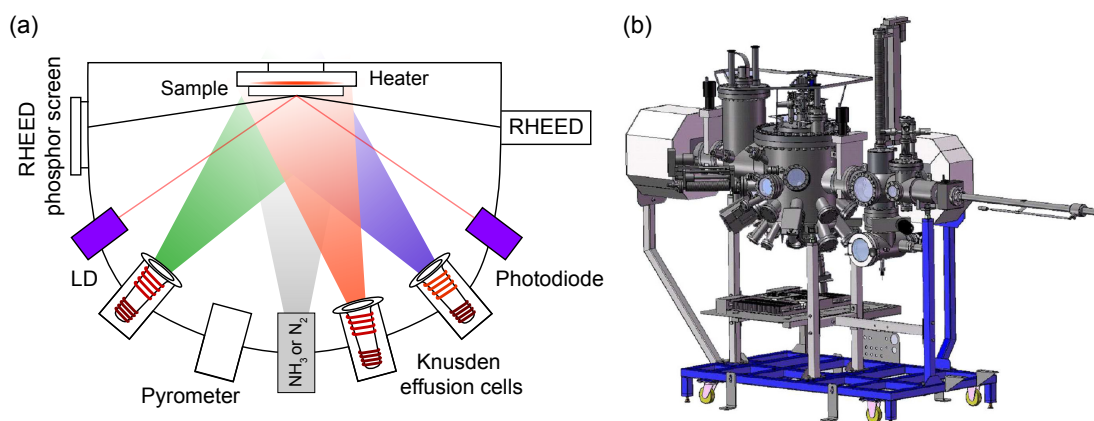


Figure 1.10: (a) Schematic representation of the MBE growth chamber. (b) Riber Compact 21 reactor configuration used during this thesis, image taken from [46].

A turbomolecular pump provides the highest pumping capacity of the system, assisted by a primary pump. In addition, ionic pumps are used. Finally, large-area liquid nitrogen (LN_2) cryopanel in the growth chamber trap the remaining impurities which condensate on their surface. This allows to obtain pressures in the reactor of 10^{-8} Pa enabling low unwanted contamination in the epilayers.

The group-III elements and dopants are heated in crucibles until evaporation/sublimation giving rise to a molecular beam directed toward the growth surface, in a typical Knusden cell configuration. The flux is controlled by the temperature of the effusion cell. A specific temperature range for evaporation exists for each element depending on its vapor pressure. Note that the majority of crucibles is made of pyrolytic boron nitride (pBN) because of its chemical inertness, low outgassing, and thermal stability.

The sample is heated by resistive heating of a molybdenum filament and the heat is transferred to the sample by irradiation-absorption. Thanks to the low pressure environment and the absence of metalorganic precursors, MBE allows using growth temperatures inferior to the MOVPE ones (typically 200°C less for GaN). Because of the absence of chemical reactions between the precursors, the ammonia, and the sample surface, in combination with the lower growth temperature which limits diffusion processes, sharper interfaces can be obtained by MBE with respect to MOVPE.

Concerning the group-V source, either ammonia (NH_3) or (N_2) can be used. In the case of ammonia-MBE (NH_3 -MBE), the NH_3 molecules are thermally cracked on the sample surface forming a variety of species such as NH_2 , NH , N , N_2 , and H_2 with proportions dependent on the growth temperature [47]. NH_3 -MBE growth is performed under nitrogen-rich conditions. On the other hand plasma-assisted MBE (PAMBE) uses N_2 , which is cracked by a radio-frequency plasma cell, as the nitrogen source, and a bilayer of metal on the growth surface is required to obtain smooth bi-dimensional GaN growth [48]. In our particular system a hydrogen line

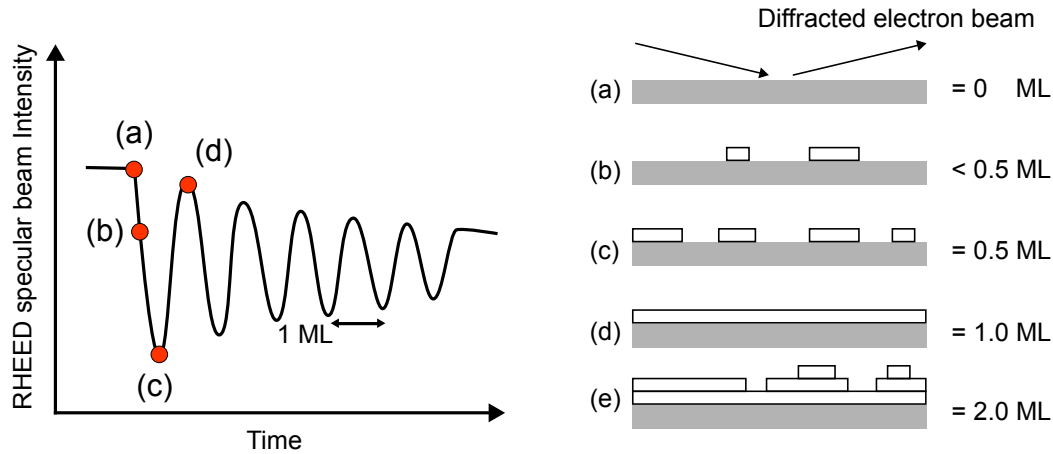


Figure 1.11: RHEED oscillations diagram. In (a) the growth is initiated. (e) The nucleation rate on top of the terraces prior to the completion of the underlying monolayer determines the damping of RHEED oscillations as the surface roughness is increased [49].

has been connected to the plasma cell in order to investigate the growth under an atomic hydrogen flow supplied to the growth surface. The hydrogen molecules in this case are cracked inside the plasma cell similarly to N_2 .

Several instruments can be used to monitor the growth. The growth temperature is measured by an optical pyrometer. Thanks to the high-vacuum environment, *in situ* monitoring techniques such as the reflection high energy electron diffraction (RHEED) can be implemented. A high energy electron beam originating from an electron gun is directed at grazing incidence ($1-5^\circ$) to the sample surface where diffraction occurs. The diffracted electrons then hit a phosphor screen allowing the observation of the diffraction pattern. Because of the grazing incidence angle, the electron beam penetration in the sample is very small, thus the diffraction is extremely sensitive to the surface state of the layer. From the diffraction pattern a large amount of information can be accessed: first of all, streaks indicate a smooth two-dimensional surface while a spotty pattern will indicate a rough 3D surface. Being a diffraction technique, the separation between the streaks is inversely proportional to the in-plane lattice parameter, which can therefore be monitored during growth. Furthermore, the intensity of the specular beam reflection allows to precisely determine the growth rate (as shown in Fig. 1.11) and the alloy composition by comparing the growth rate of different compounds (provided a sticking coefficient of 1).

The growth rate can also be measured by optical reflectivity. A laser diode is directed on the sample surface where it is partially reflected and detected by a photodiode. The sample acts as a Fabry-Perot interferometer, with reflections occurring at the semiconductor-air interface, and at the semiconductor-substrate interface. These two reflections interfere with each other having a phase difference (δ given by Eqn. (1.15)) due to the difference in optical path. For phase differences equal to 2π , constructive interference is obtained, and a maximum intensity

in the detected signal is measured. Given that the sample thickness (l) is the only variable, one period of oscillation is obtained when the thickness is increased by multiples of l_{period} (2π phase difference):

$$\delta = \left(\frac{2\pi}{\lambda}\right) 2nl \cos \theta . \quad \text{It follows:} \quad l_{period} = \frac{\lambda}{2n \cos \theta} , \quad (1.15)$$

where λ is the LD wavelength, n is the refractive index of the material under growth, and θ is the angle of incidence on the sample. In our system l_{period} is equal to 140 nm. The growth rate is then calculated by measuring the time interval for one period of oscillation.

Finally, the system is equipped with a quadrupole mass spectrometer (QMS), which is used to monitor the background impurity level, as well as the species which are desorbed from the sample or by hot MBE parts such as the heater. A flux gauge is regularly used to measure and calibrate the group-III and dopant flux.

1.5.4 Electrochemical capacitance-voltage profiling

This technique is based on the working principle of capacitance-voltage (C - V) measurements: when a metal-semiconductor Schottky contact is formed, the depletion region (W) only extends in the semiconductor side. By varying the applied voltage, W varies. In this region the ionized impurities are charged and behave like a capacitor. Thus varying the applied voltage changes the capacitance of the junction. The depletion width length change (dW) and the depletion width charge (dQ) induced by the applied voltage modulation dV are given by:

$$dW = d(\epsilon_r \epsilon_0 C^{-1}) = -\epsilon_r \epsilon_0 C^{-2} dC \quad \text{and} \quad dQ = qN(W)dW , \quad (1.16)$$

given that $C = \epsilon_r \epsilon_0 / W$, where $N(W)$ is the net dopant concentration in the region dW . By using the fact that $C = dQ/dV$, one can finally obtain:

$$dV = dQ/C = -qN(W)\epsilon_r \epsilon_0 C^{-2} dC/C \quad \text{and thus} \quad N(W) = \left(\frac{2}{q\epsilon_r \epsilon_0}\right) \left[\frac{1}{d(1/C^2)/dV} \right] . \quad (1.17)$$

Therefore by plotting $1/C^2$ versus V , $N(W)$ is obtained from the slope. Note that the capacitance and charge are defined per unit area in the above equations. In this configuration (metal-semiconductor contact) which corresponds to the classical C - V measurement by varying the applied voltage it is possible to obtain the doping profile. However, the depth range addressable is limited. To extend the depletion region, the voltage needs to be increased, eventually leading to electrical breakdown. Moreover the voltage range is further limited when the doping in the semiconductor is high, because the carriers can then easily tunnel in the contact. It is therefore impossible to obtain the dopant profile in highly doped samples with this experimental technique. In addition, the sample preparation may be time consuming as the electrode needs to be evaporated on the semiconductor and its size controlled, requiring a

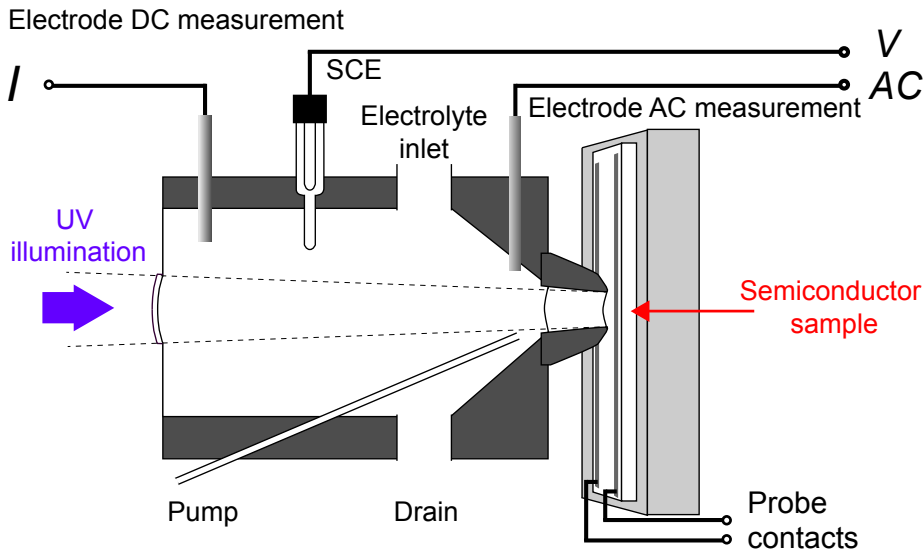


Figure 1.12: Schematic representation of the dage wafer profiler CVP 21 electrochemical C-V setup. The pump is used either to flush the surface with fresh electrolyte to remove the surface oxide, or to remove air bubbles from the surface.

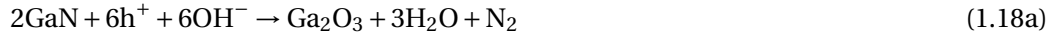
photolithographic step.

In order to circumvent these limitations, electrochemical capacitance voltage (ECV) was developed [50]. In 1974 Ambridge and Faktor proposed the use of an electrolyte to create a Schottky-like contact to the semiconductor and at the same time to etch it by electrochemical means. In such a way the sample can be repetitively measured and etched inside the same instrumental apparatus. By the use of Faraday's law of electrolysis it is possible to precisely control the amount of etched material, obtaining an accurate depth value when added to the depletion region width.

The semiconductor sample is brought in contact against a sealing ring, which applies a well-defined pressure. Behind the sealing ring lies the electrochemical cell which is filled with the electrolyte and features three electrodes. The etching and the measurement conditions are controlled by driving a DC signal between the sample and one electrode, while keeping a constant potential on the saturated calomel electrode reference (SCE) to maintain the required overpotential [51]. The differential capacitance measurement is performed by an AC signal measured by a Pt electrode positioned close to the sample surface, to limit the impedance of the electrolyte.

In order to etch the semiconductor, holes need to be created and brought to the sample surface. This is simply obtained by applying a forward voltage to the electrolyte-semiconductor Schottky contact for *p*-type material. On the other hand for *n*-type materials holes are generated by a high UV irradiation in order to insure the saturation of the negative charges surrounding dislocations and to achieve the formation of a homogeneous oxide layer on the surface [52].

This oxide forms and dissolves via the following reactions:



Thanks to the use of a diluted electrolyte (KOH 0.01 M, pH = 12) the reaction is controlled by the diffusion of OH^- ions to the sample surface. The consumption of these ions close to the sample surface stabilizes the oxide, and the pH in this region decreases. However, when a jet of fresh electrolyte is flushed toward the surface, the removal of the oxide is nearly instantaneous, and mirror-like surfaces can be obtained by the etching. More information can be found in Ref. [52].

Whereas the Mg dopant profile cannot be obtained by ECV, one can obtain the net acceptor ($N_A - N_D$) or net donor ($N_D - N_A$) profiles which govern the capacitance along the samples. However for the case of high $N_D - N_A$ values, the generation of holes under UV irradiation becomes extremely difficult and the etching of the sample cannot be obtained anymore.

1.5.5 Transmission-line measurement

It is often important to know the contact and sheet resistance of the epilayer under study. These quantities can be accurately measured by the means of the transmission-line measurement (TLM). The TLM structure consists of several identical stripe contacts separated by an increasing length l_i . When a voltage is applied between two neighboring contacts, the resistance $R = V/I$ will result from the sum of two components:

$$R = 2R_c + l_i \frac{R_s}{w}, \quad (1.19)$$

where R_s and R_c are the semiconductor sheet and contact resistance, respectively, and w the width of the metal contact. When R is plotted against the contact separation l_i , its values lie on a straight line characterized by a slope equal to $\frac{R_s}{w}$, and intercept equal to $2R_c$ as shown in Fig. 1.13. However, calculating the specific contact resistance from the value of R_c is not straightforward. If the metal was penetrating with abrupt walls on the entire thickness d of the semiconductor layer, then $\rho_c = R_c w d$. However the metal, in real contacts, does not penetrate into the semiconductor but just lies on its surface (slight penetration depth when the contact is annealed of the order of a few nanometers).

For the TLM type of contact, the equivalent circuit is represented in Fig. 1.14. The current is injected below the contact in an inhomogeneous way: the further one moves away from the contact edge sitting close to the separation l_i , the less current is injected as the total resistance increases due to the longer electrical path length. Therefore, the current tends to crowd at the edge of the contact. This system has been modeled by Berger [53, 54], and Murrmann and

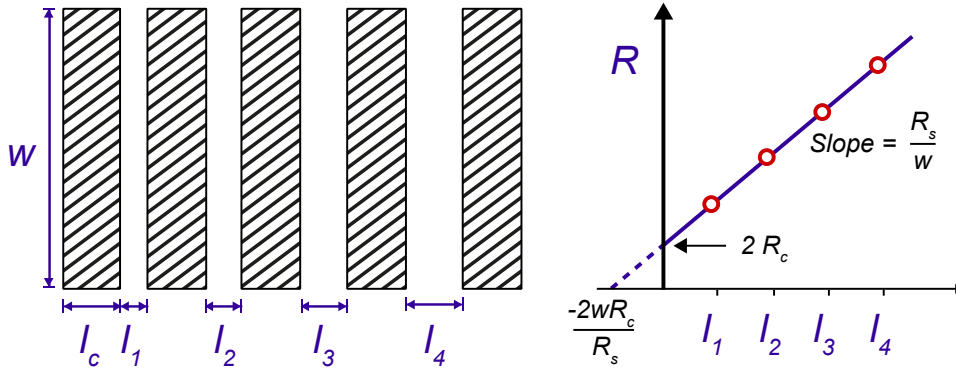


Figure 1.13: TLM structure with metal contacts of length l_c and width w lying on the semiconductor, separated by spacings l_1, l_2, l_3 , and l_4 .

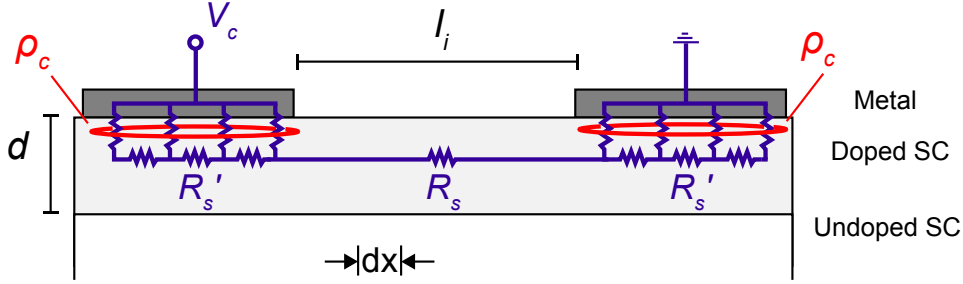


Figure 1.14: TLM equivalent circuit.

Widmann [55]. It can be described using the following differential equations:

$$dV(x) = -\frac{R_s'}{w} I(x) dx, \quad (1.20a)$$

$$dI(x) = \frac{w}{\rho_c} [V_c - V(x)] dx, \quad (1.20b)$$

where I is the current, V is the voltage, R_s' and R_s are the sheet resistances of the material below and between the contacts, respectively, ρ_c is the specific contact resistivity, and V_c is the bias applied between the contacts. The solution, obtained by using the appropriate boundary conditions (the derivation can be found in detail in Ref. [56]), yields:

$$R_c = \frac{\sqrt{R_s \rho_c}}{w} \coth(kl_c) \quad \text{and} \quad \rho_c \approx \frac{w^2 R_c^2}{R_s} \quad \text{for } kl_c > 2, \quad (1.21)$$

where $k^2 \equiv R_s/\rho_c$. If $kl_c > 2$, then $\coth(kl_c) \approx 1$. Indeed for long enough contacts, the last term in Eq. (1.21) is equal to 1. The effective contact length (l_T) over which the totality of the current flow is therefore $l_T = wR_c/R_s$, given that the effective contact area is equal to wl_T .

1.5.6 Variable stripe length method

LDs are based on the stimulated emission of photons inside the cavity. The ability to amplify the spontaneous emission, *i.e.* the gain of the amplifier, is a fundamental characteristic to investigate when developing and optimizing these devices. However, the edge emitting LD fabrication, because of a more complex geometry with respect to LEDs, requires multiple photolithographic and processing steps before the characterization of electrically injected devices becomes possible. This, especially in academic environments which lack of automated processing facilities, is a time consuming process which can easily require more than five working days. Moreover the gain measurement is often based on the Hakki-Paoli method which is also demanding in terms of instrumentation.

Consequently, techniques allowing for a fast characterization of the semiconductor optical gain are strongly appreciated. One of such techniques is the variable stripe length method (VSL) which enables gain measurements through the optical pumping of an unprocessed layer structure [57]. In this case, the only processing step needed is the cleavage of the laser bar to be investigated.

The principle is to simulate the ridge-like electrical injection by optical pumping. To this end, the pump laser beam is shaped in the form of a thin stripe by the use of either two cylindrical lenses or a beam expander combined with a cylindrical lens. Along the stripe length the beam needs to be made divergent (or expanded) in order to spread its Gaussian shape and obtain a homogeneous pump profile along such direction. On the other hand in order to form the stripe, the expanded laser beam is well focused by a cylindrical lens. The edge emission of the so-pumped laser bar is then collected and focused into an optical fiber which guides the signal to a spectrometer. When a stripe is homogeneously pumped, the spontaneous emission

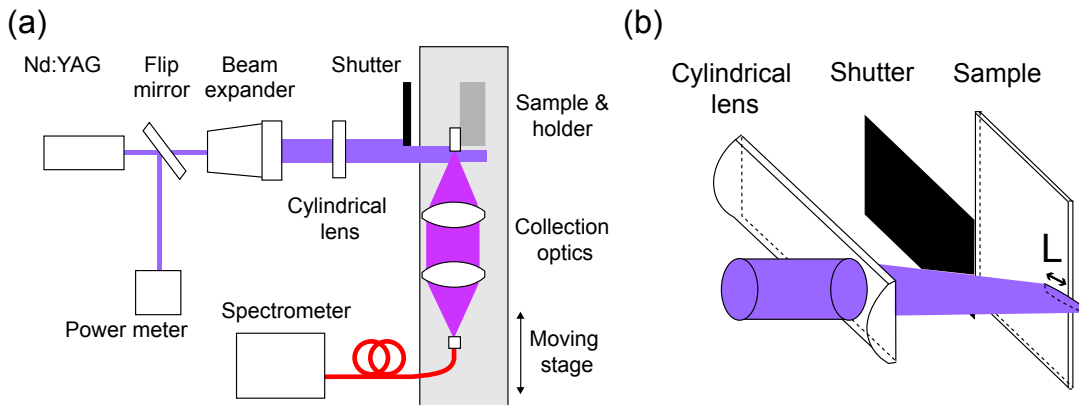


Figure 1.15: (a) Variable stripe length measurement setup. The sample and the collection optics lie on the same moving stage which is used to align the sample position with respect to the laser stripe maximum, without affecting the collection alignment. (b) Schematic representation of the pumping scheme and stripe length control.

is generated and amplified along the entire stripe. The edge emission intensity (at a given wavelength) as a function of the stripe length is given by:

$$I(l) = \frac{A_0}{g_{mod}} [e^{(g_{mod}l)} - 1] , \quad (1.22)$$

with the modal gain $g_{mod} = \Gamma g_m - \alpha$ where Γ is the optical confinement factor, g_m the material gain, and α is the propagation loss coefficient. l is the stripe length, and A_0 is a scaling factor dependent on the Einstein coefficient for spontaneous emission, pump intensity, and geometrical form factors [58]. The l - $2l$ method is based on the fact that $[I(2l)/I(l)] = \exp(g_{mod}l) + 1$. Hence, by comparing the edge emission from a double stripe length to the other one, g_{mod} can be calculated:

$$g_{mod} = \frac{1}{l} \ln \left[\frac{I(2l)}{I(l)} - 1 \right]. \quad (1.23)$$

During this PhD thesis stripe lengths of either 300-600 μm or 400-800 μm were employed and the measurements were performed under conditions such as the product $g_{mod}l$ would be lower than 4 to avoid gain saturation effects [59, 60]. Through Gaussian transport matrix calculations and beam profiling we estimated and measured the so-formed stripe to be 35 ± 10 μm wide. The third harmonic of a Q-switched Nd:YAG laser was used for the optical pumping ($\lambda = 355$ nm, pulse width 0.52 ns, pulse energy 2.45 μJ , repetition rate 8.1 kHz), with the shutter used to control the stripe length mounted on a translation stage controlled by a standard manual micrometer. By means of a beam expander the beam waist was expanded from 0.6 to 6 mm resulting in homogeneous pump intensity profiles along the whole maximum stripe length of 800 μm .

2 Magnesium *p*-type doping of (Al)GaN using MBE

In the framework of the CTI project "Nitride-based Green SLEDs" the *p*-type doping by NH₃-MBE was investigated. Besides its practical application concerning the thermal budget reduction on the active region for long wavelength LDs ($\lambda > 500$ nm) which will be discussed in Chapter 3, NH₃-MBE proved to be an interesting technique to investigate the peculiarities of magnesium doping in III-nitrides, with particular attention paid to GaN and AlGaN layers. When combined with the data acquired from MOVPE grown samples, MBE results shed some new light on the parameters influencing dopant compensation. This was supported by the possibility to perform annealings in a HVPE reactor under different atmospheres (either a NH₃ or N₂ one) and to investigate the net acceptor profile by electrochemical C-V.

In this chapter we discuss the advantages and limitations of NH₃-MBE to perform *p*-type doping. Particular attention is given to the growth temperature and pressure effect on the final characteristics. In addition the use of indium (In) as a surfactant is also presented. Finally, a model which reproduces the evolution of the net acceptor concentration as a function of time and Mg concentration ([Mg]) is proposed.

2.1 Introduction

The ability of achieving *p*-type doped III-nitride layers has revolutionized the whole field. From an isolated industrial interest in the late 1960s and the 1970s at Bell Labs and RCA laboratories [1, 29], during the 1990s III-nitride based devices have become increasingly popular, witnessing a remarkable evolution of their performance and of the available product portfolio. The work of Isamu Akasaki and Hiroshi Amano from Nagoya university on one side, and Shuji Nakamura at that time working for Nichia Chemical Industries Ltd. on the other side, led to the development of the Blu-ray technology and to the realization of high brightness blue LEDs, which was recently recognized with the Nobel prize in Physics 2014. While the prize was delivered for the achievement of energy efficient blue LEDs, the three Japanese scientists worked for many years on the *p*-type doping of GaN.

Until 1989, *p*-type conductivity could not be achieved. Many different dopant impurities were tested. However, apart from obtaining insulating material instead of the typical *n*-type conductivity exhibited by non-intentionally doped (nid) GaN layers, none seemed to work. In 1989, Amano and Akasaki published their work [2] on the low-energy electron beam irradiation technique (LEEBI). By irradiating the sample surface with an electron beam, they obtained *p*-type conductivity from a magnesium doped GaN epilayer, eventually leading to the first realization of a *p-n* GaN LED. In 1993 Nakamura demonstrated the activation of the Mg acceptor by thermal annealing [3] which is the preferred activation technique nowadays. Nakamura in fact suggested that during the LEEBI treatment the sample is locally heated, resulting in a thermal activation similar to the thermal annealing treatment.

Despite the successful realization of the aforementioned devices, the *p*-type doping compensation mechanisms in GaN are still under investigation and will be discussed hereafter. Furthermore, even though GaN-based devices exhibit incredible characteristics, high *p*-type resistivity still poses threats to the device performance, especially in the case of aluminium containing alloys.

2.1.1 Magnesium and other impurities

Several different impurities have been tested in order to obtain *p*-type conductivity. Many group-II atoms were eligible as potential dopants among which: beryllium (Be), magnesium (Mg), zinc (Zn), cadmium (Cd) and mercury (Hg) in increasing order of ionization energy [61, 62]. In addition, carbon (C) was found to be an amphoteric impurity both in GaN and AlN promising a great potential [63]. When occupying the gallium site, carbon acts as a shallow donor, while when sitting on a nitrogen site, it was predicted to act as a shallow acceptor.

Even though Be has potentially the lowest ionization energy with a value below 100 meV [61, 64], because of its low atomic size it can incorporate as an interstitial as well, acting in this configuration as a double donor [65]. Moreover, experimental observations indicated its low solubility in GaN [66].

In this context Mg was found as the best compromise in terms of activation energy (E_A) and solubility in the GaN crystal in the acceptor configuration. The only application of the other elements (mainly C and Zn) is the compensation of non-intentional *n*-type doping in electronic devices buffer layers to reduce leakage currents.

Indeed Mg doping produced the best results and rapidly became the preferred *p*-type impurity. Mg is located just below Be in the periodic table, with an atomic mass nearly three times larger than that of Be. Two electrons fill the outermost 3s orbital, making it suitable as acceptor when substituting Ga (Mg_{Ga}). Hereafter the exact value of the ionization energy of Mg is discussed. In fact, it is shown that the discrete energy level picture of the Mg acceptor in GaN is not in agreement with experimental data [67–69]. This explains the large variation in the published values.

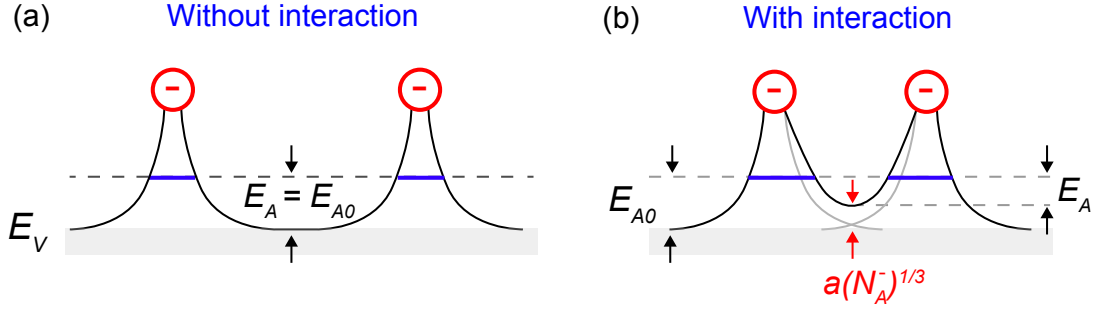


Figure 2.1: Influence of the overlap of the Coulomb potential on the apparent ionization energy E_A : (a) absence of overlap, impurities far away from each other, while in (b) the overlap and screening effects reduce the apparent activation energy.

In fact the apparent ionization energy (E_A , also referred to as activation energy) is dependent on the ionized acceptor impurity concentration (N_A^-) [70]. This arises from the overlap of the Coulomb potential of the dopants and from the screening of this potential by free carriers [68], as shown in Fig. 2.1. Indeed, E_A decreases as the ionized acceptor concentration increases. This effect was already discussed in 1949 for silicon doped with boron [71] giving rise to:

$$E_A = E_{A0} - a(N_A^-)^{1/3}, \quad (2.1)$$

where E_{A0} is the ionization/activation energy of an isolated impurity, and a is a constant. The

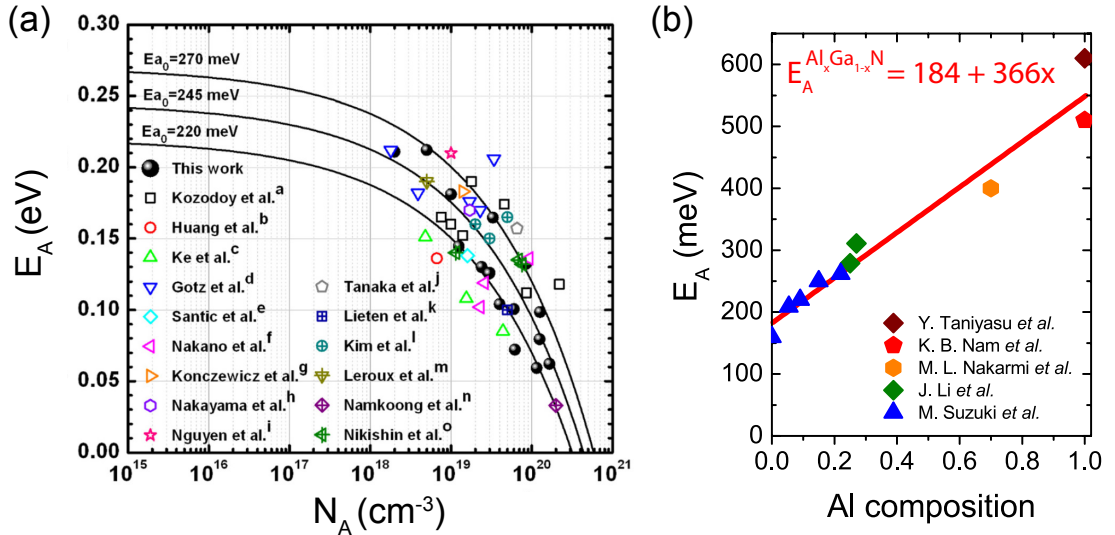


Figure 2.2: (a) Evolution of the apparent Mg ionization energy E_A as a function of N_A for GaN. Image taken from Ref. [69] where the references used can be found. (b) Evolution of E_A as a function of the Al composition for the $\text{Al}_x\text{Ga}_{1-x}\text{N}$ alloy. Starting from Y. Taniyasu the references used are Refs: [72–76]

a term was expressed by Götz *et al.* [68] as:

$$a = \Gamma(2/3) \left(\frac{4\pi}{3} \right)^{\frac{1}{3}} \frac{q^2}{4\pi\epsilon}, \quad (2.2)$$

where Γ is the gamma function, q the electronic charge and ϵ being the static dielectric constant of GaN equal to $9.5\epsilon_0$. By fitting E_A as a function of N_A [69] or N_A^- [68] the E_{A0} value was finally determined to be equal to 208 ± 4 meV and 245 ± 25 meV in those two papers, respectively.

Unfortunately the situation even worsens when dealing with the $\text{Al}_x\text{Ga}_{1-x}\text{N}$ alloys. E_A monotonically increases together with the Al composition up to a value as high as 610 meV, which was published for AlN [72], as shown in Fig. 2.2(b). The latter figure was created from a selection of published works. Using a linear interpolation, the evolution of E_A as a function of the Al composition exhibits a slope of 366 meV/Al%. However, the lack of extensive data does not allow to carefully determine E_{A0} for these alloys yet.

Given the high activation energies, low N_A^-/N_A ratios, hence low hole concentrations, are obtained at room temperature in (Al)GaN layers. This becomes an issue when combined to the high hole effective mass in wide band gap semiconductors. Reports suggested values around $m_h^* = 1.1 m_e$ for GaN [77] and $3.3 m_e$ in AlN [72]. The Drude model [78] relates the effective mass to the mobility by $\mu = q\tau/m^*$ where τ is the mean free time between collisions. The same model states that the conductivity (σ) of p -type material can be written as $\sigma_p = p_h \mu_h q$. In this case q is the hole charge, μ_h its mobility, and p_h the free hole density.

The combination of low carrier concentrations and mobility (around $10 \text{ cm}^2/\text{Vs}$) in GaN and related alloys give rise to a low p -type conductivity, *i.e.* a high resistivity ($\rho = 1/\sigma$). Furthermore, because of ionized impurity scattering, the mobility decreases as the carrier number increases. It is evident that the combination of all these effects poses a major threat to III-nitride based devices.

2.2 Dopant compensation

Because of the aforementioned limitations, high doping levels are often considered when attempting to achieve state-of-the-art current voltage (I - V) characteristics. For GaN:Mg doped in the 10^{18} - 10^{19} cm^{-3} range, the number of net-acceptors ($N_A - N_D$) and holes is seen to increase together with [Mg]. However, when the doping is further increased towards the 10^{20} cm^{-3} range, the acceptor and hole concentrations reach a maximum and then start to decrease in MOVPE grown samples. This phenomenon is the so-called dopant compensation. The degree of compensation corresponds to the deviation between the dopant concentration introduced in the lattice and the $N_A - N_D$ value measured. Compensation could arise from either an increase in the donor concentration or from the decrease in the acceptor concentration at high doping levels caused by the formation of electrically inactive clusters for example.

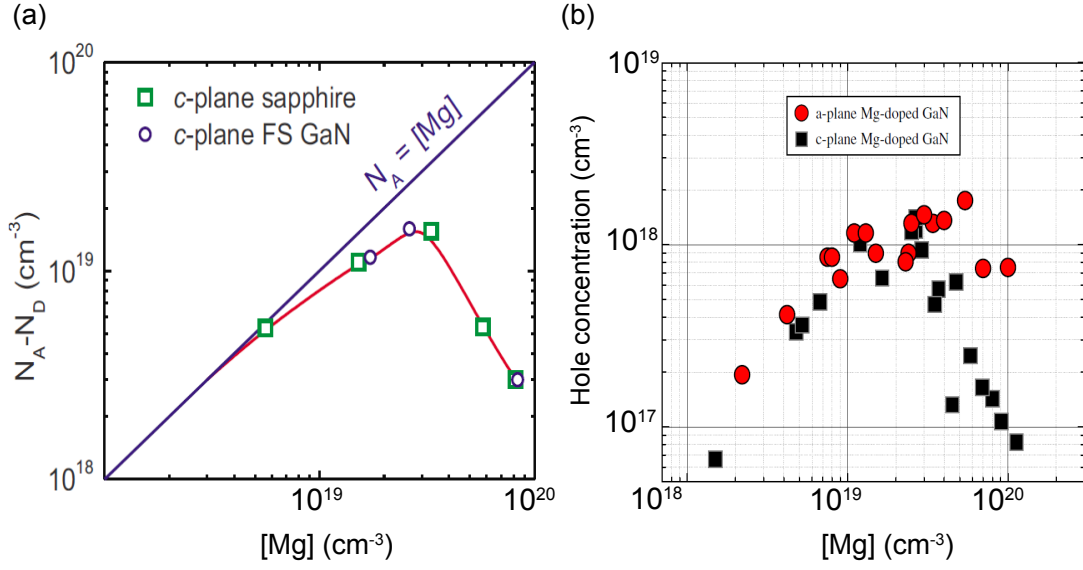


Figure 2.3: Evolution of (a) the net acceptor [80] and (b) hole [81] concentration as a function of the magnesium concentration for MOVPE grown samples.

In fact the compensation mechanisms are still debated and the main theories will be discussed in the following pages. Interestingly, several reports [79–84] showed that the maximum hole and net acceptor concentration measured on thick *c*-plane GaN samples are obtained for [Mg] in the vicinity of $3 \times 10^{19} \text{ cm}^{-3}$ when growth is performed by MOVPE, as shown in Fig. 2.3. For the case of MBE, data are more scattered, but the general trend is that the compensation effects arise for higher [Mg] allowing obtaining higher hole concentrations.

In this work the dopant compensation (C_{doping}) is defined as $\{[Mg] - (N_A - N_D)\} / [Mg]$. On the other hand the doping efficiency (η_{doping}) is given by $(N_A - N_D) / [Mg]$, thus the sum of the two is: $C_{doping} + \eta_{doping} = 1$.

2.2.1 Polarity inversion and pyramidal inversion domains

The upper limit for *p*-type doping still remains the solubility limit, *i.e.* when the formation of a second phase, Mg₃N₂ [85], is preferred to the Mg_{Ga} acceptor. In such arrangement the Mg atoms do not act as acceptors, leading to a deviation from a unity relationship between [Mg] and $N_A - N_D$.

When the solubility limit is overcome, polarity inversion is obtained. The control of the GaN polarity could be obtained by Mg exposure of the Ga-polar GaN surface in a MBE reactor [86–88]. Researchers showed that the formation of a new phase assigned to Mg₃N₂ (observed by means of RHEED), was responsible for the polarity inversion of the regrown GaN from Ga-polar to N-polar and vice versa. When the inversion was attempted during growth, its

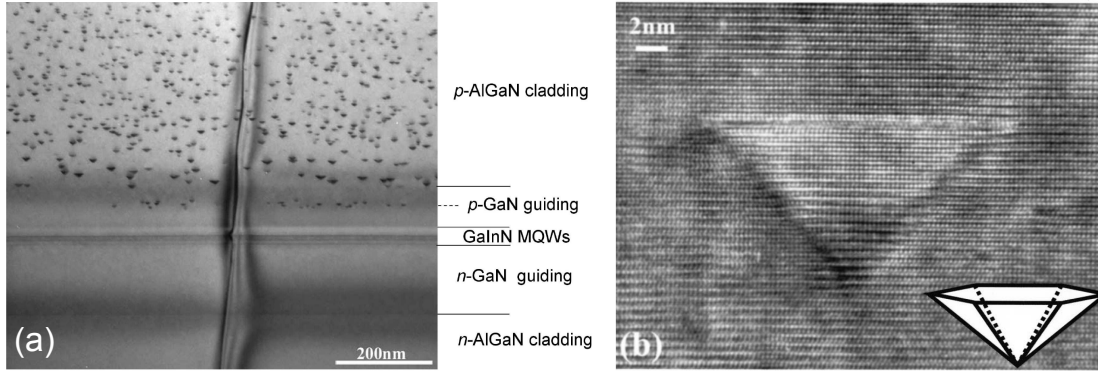


Figure 2.4: (a) Cross-sectional TEM image of an LD showing the presence of pyramidal inversion domains [89]. (b) High resolution TEM image along the $[11\bar{2}0]$ zone axis of a pyramidal inversion domain [91].

sharpness is proportional to the Mg flux supplied on the growth front. This was concluded from transmission electron microscopy (TEM) observation of the extension of the inversion domain boundary (IDB). Obviously, below a certain threshold of Mg flux no extended inversion could be observed.

However, for doping levels in the 10^{19} - 10^{20} cm^{-3} range, local inversions of the crystal polarity characterized by a pyramidal shape and consequently denoted pyramidal inversion domains (PID) are present in p -GaN layers grown by MOVPE, as shown in Fig. 2.4. In general they are considered to form for $[\text{Mg}]$ higher than $3\text{-}4 \times 10^{19} \text{ cm}^{-3}$ [89, 90]. Because of the slower growth rate of N-polar material, these defects can get buried in the epilayer given that the lateral growth rate is sufficiently high. This may not be the case during MBE growth where the PID can be at the origin of pits. Vennéguès and coworkers were among the first to extensively study PID by high resolution TEM [91, 92]. From their observation they proposed that the IDBs of the PIDs are likely composed of Mg_3N_2 . Furthermore they were able to show that PID always point towards the $[000\bar{1}]$ direction.

Two studies investigated the evolution of the PID size and density as a function of doping but found opposite results. Reference [89] observed the size of the PID to be inversely proportional to the $[\text{Mg}]$, while the density of these defects followed the doping evolution; in the second study [90] the size and density of the PIDs were both proportional to the doping in line with the results of Hansen *et al.* [93]. The dependence of the configuration of PIDs on the growth conditions (and possibly Mg segregation) may explain the discrepancy between the results.

However, despite the possible relation to dopant compensation, in a recent study the amount of Mg bound in PIDs was found to be around an order of magnitude below $[\text{Mg}]$ [94]. Furthermore, Kaufmann and coworkers determined the presence of a different phase with respect to Mg by means of X-ray diffraction (XRD) [79]. It could be assigned to Mg_3N_2 , with a volume fraction in the crystal below 1% and its effect on the compensation was assumed to be negligible. Note that no evolution along the growth direction of the PID density or size has been

reported to date.

PIDs can therefore be related to a certain extent to the dopant compensation, but are probably not the main driving force. Finally, *ab initio* calculations suggested the Mg_3N_2 ability to store hydrogen forming a strong bond stable under thermal annealing conditions [95].

2.2.2 Native point defects

Given the absence of extended defects in GaN:Mg layers, apart from the presence of PIDs, the decrease in acceptor/hole concentration at high doping levels may arise from intrinsic lattice defects generated when the doping is high, for a process often referred to as self-compensation (SC). This is supported by the lack of evidence of contamination by impurity donors accounting for compensation.

From first-principles calculations, carried out in the framework of density-functional theory using a supercell geometry, C.G. Van de Walle and J. Neugebauer have calculated the formation energies of several point defects and impurities in GaN (including Mg in various configurations) [96, 98]. It resulted that the nitrogen vacancy (V_N) is a donor which can occur in the form of V_N^+ or V_N^{3+} , *i.e.* either a single or triple donor, respectively. Its formation energy is high in *n*-type GaN, thus it is not present in large concentrations. However when the Fermi level is progressively decreased, thus the material becomes more and more *p*-type, the formation energy of the V_N^{3+} vacancy decreases, making it a good candidate for acceptor compensation. Furthermore they observed the incorporation of Mg as an acceptor under the form Mg_{Ga} and calculated a high formation energy for its interstitial state Mg_i , which is a donor and would thus compensate the acceptors [99].

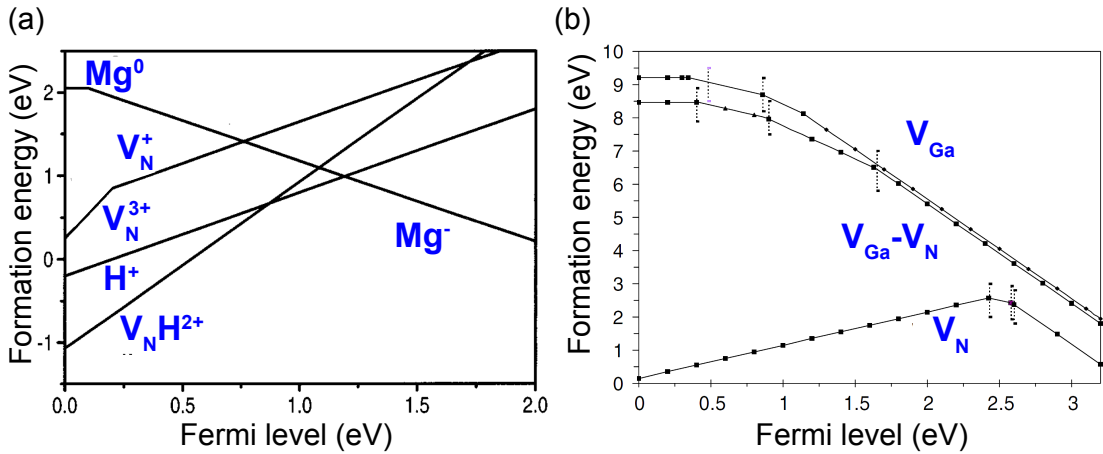


Figure 2.5: Formation energy as a function of the Fermi level for the nitrogen vacancy depending on its configuration as calculated in (a) Ref. [96] and (b) Ref. [97]. In (a) the formation energy of hydrogen and that of Mg are also plotted, while (b) shows the evolution of the gallium vacancy (V_{Ga}) as well as the mixed divacancy ($V_{\text{Ga}}-V_N$).

In a later study however, thanks to an improved computational methodology, Ganchenkova and Nieminen [97] derived low formation energies for the nitrogen vacancy in *n*-type material as well, which could explain the electrical conduction of n-d GaN. In addition only V_N^+ was found to be stable in *p*-type material implying the absence of the triply positively charged V_N^{3+} .

The formation energy (E_{For}) of the defect enables the calculation of the equilibrium density of compensating donors (N_D) at the growth temperature T [83]:

$$N_D = N_S \exp\left(\frac{-E_{For}}{k_B T}\right), \quad (2.3)$$

where N_S is the number of lattice sites per cubic centimeter for the substitutional defect. The dependence of E_{For} to the Fermi level E_F requires the determination of the latter during growth. This is given by Eq. (2.4) when residual donor impurities are neglected [79], and by Eq. (2.5) when the latter are included [83]:

$$E_F = k_B T \ln \left[\frac{N_V}{2N_A} \left(1 + \sqrt{1 + \alpha \frac{N_A}{N_V}} \right) \right], \quad (2.4)$$

$$E_F = -k_B T \ln \left[\frac{2\beta^{-1}(N_A - N_D)}{\beta^{-1}N_V\alpha_1 + N_D + \sqrt{(\beta^{-1}N_V + N_D\alpha_1)^2 + 4\beta^{-1}N_V(N_A - N_D)\alpha_1}} \right], \quad (2.5)$$

where β is the valence band degeneracy factor, N_V is the valence band density of states (temperature dependent), $\alpha = 4\beta \exp(E_A/k_B T)$, and $\alpha_1 = \alpha/4\beta$. In Eq. (2.5) solutions are found by iteration using Eq. (2.3) because of the dependence of E_F to N_D .

In the presence of compensating donor species, the hole concentration p is given by [70]:

$$p = \frac{-N_D + K}{2} + \sqrt{\left(\frac{N_D + K}{2}\right)^2 + K(N_A - N_D)}, \quad (2.6)$$

with $K = \beta^{-1}N_V \exp(-E_A/k_B T)$. The calculation of the compensating defects by neglecting their effect on the Fermi level (using Eq. (2.4)) led Kaufmann and coworkers [79] to suggest that the isolated nitrogen vacancy alone could not account for the experimentally observed compensation. On the other hand, when the formation of a nearest neighbor pair $Mg_{Ga}-V_N$ was considered, the evolution of the compensation could be reproduced. The full derivation of the model can be found in [79]. However, isolated V_N only have been used to explain this evolution in another report [83]. The low formation energy of the V_N -H complex was shown to translate into large concentrations during MOVPE growth. It was proposed that its dissociation during the thermal annealing process would leave V_N in the lattice acting as donors, thus compensating the acceptors, and eventually allowing the fitting of the experimental data.

While both models reproduce to a certain extent the observations, experiments which could strengthen the proposed hypothesis are strongly needed by the scientific community. Indeed

these defects are extremely difficult to study, partly because of their positive charge makes positron annihilation spectroscopy quite challenging [100].

2.2.3 Mg clustering

The net acceptor and hole concentration drop could originate from the clustering of Mg atoms which, may form microscopic Mg_3N_2 like complexes, preventing electrical activity. While similar to the formation of PID, it may not generate extended defects, thus making it difficult to be observed even by high resolution TEM.

Results from atom probe tomography (APT), which enables to identify the atomic elements and reconstruct their position in the crystal at the same time [101], suggest this possibility [102–104]. More precisely, the reports indicate that Mg atoms in GaN:Mg epilayers exhibited a non-random Mg atom arrangement for high doping levels. A deviation from a pure binomial distribution, as it would be expected during epitaxial growth, was indeed detected. By combining APT and TEM, Mg-rich regions were observed not to originate from PIDs and were also detected in samples free from PIDs. In Fig. 2.6(b) the appearance of such regions is shown for $[\text{Mg}] = 1 \times 10^{20} \text{ cm}^{-3}$. Moreover, Larson and coworkers performed APT on a commercial LED [105] and found Mg-Mg clustering features even in such high quality samples.

Finally, the preferential formation of Mg-rich regions in AlGaN was proposed in Ref. [106]. The Mg atom positions in homogeneously doped AlGaN/GaN superlattice were reconstructed. By combining results from secondary ion mass spectrometry (SIMS) and APT, both an increase in the Mg incorporation and an increased occurrence of Mg-rich regions in the AlGaN regions were observed.

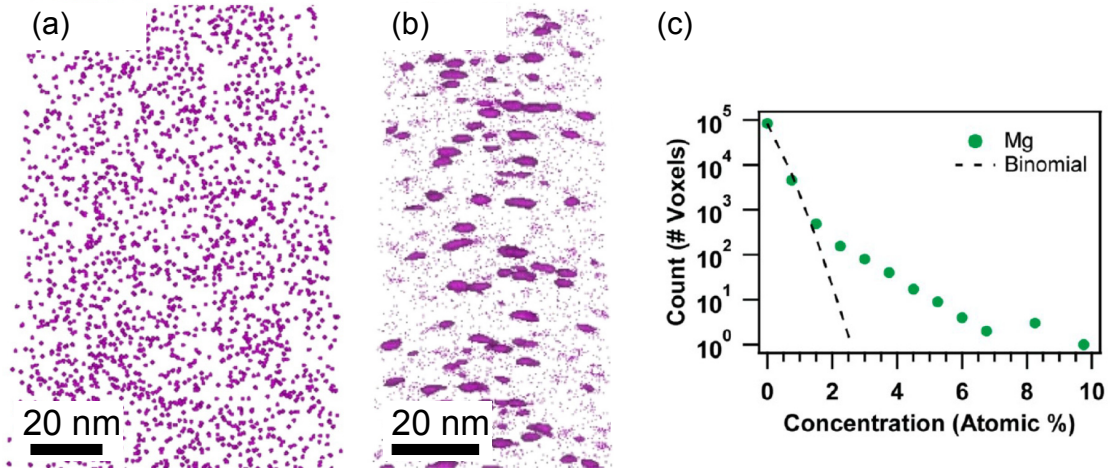


Figure 2.6: Atom probe map of Mg atoms in GaN samples doped with (a) $[\text{Mg}] = 5 \times 10^{19} \text{ cm}^{-3}$, and (b) $[\text{Mg}] = 1 \times 10^{20} \text{ cm}^{-3}$, showing the formation of Mg-rich regions for the higher doping, adapted from [103]. (c) Frequency distribution analysis indicating the deviation of the Mg distribution from a random distribution [102].

2.2.4 Hydrogen

Hydrogen plays a crucial role in the doping of III-nitrides. Nakamura [107], already in 1992, proposed that the achievement of *p*-type conductivity was strictly related to the removal of hydrogen [107] bonded with Mg forming Mg-H complex [108]. Because of the relatively low binding energy (0.7 eV [109]), H can be dissociated from the acceptor. This was made possible by the introduction of thermal annealing or LEEBI treatments. The former technique is preferred because of its simplicity, reliability, scaling-up, and no depth limitations.

However, hydrogen was proposed to be crucial during growth as well. In an MOVPE reactor, H arises from the decomposition of NH_3 during growth. Neugebauer and Van de Walle, by calculating its formation energy, found that in *p*-type material H is incorporated in the form of a positively charged interstitial, H^+ , which is a donor and therefore compensates the acceptors during growth. They concluded that hydrogen incorporates in large amounts during MOVPE growth to even match $[\text{Mg}]$ [85]. At elevated temperatures Mg_{Ga} and H^+ are dissociated, and Mg-H complexes only form during the cool down of the sample in the reactor. However, the presence of the positively charged H^+ during growth compensate the Mg acceptors. The Fermi level of the growing material is thus kept away from the valance band when hydrogen is present during growth, with two remarkable consequences: first, the incorporation of Mg_{Ga} is increased, and secondly, the formation energy of the nitrogen vacancy is increased, which translates into lower V_N concentrations in the epilayers. Therefore the presence of hydrogen is considered to reduce *p*-type compensation.

Nevertheless, despite the idea that $[\text{H}]$ always matches $[\text{Mg}]$ in MOVPE, above a certain level it might be difficult to further incorporate hydrogen. It was shown that $[\text{H}]$, in as-grown material prior to the thermal activation of the sample (defined as $[\text{H}]_0$), can saturate when the doping levels are in the 10^{19} cm^{-3} range [80]. The saturation level may be dependent on the growth conditions (carrier gases, growth temperature, and pressure). Together with the saturation of $[\text{H}]_0$, the onset of severe compensation was observed supporting the idea that $[\text{H}]$ plays a crucial role in the compensation process. Furthermore, there was an increase in $[\text{H}]$

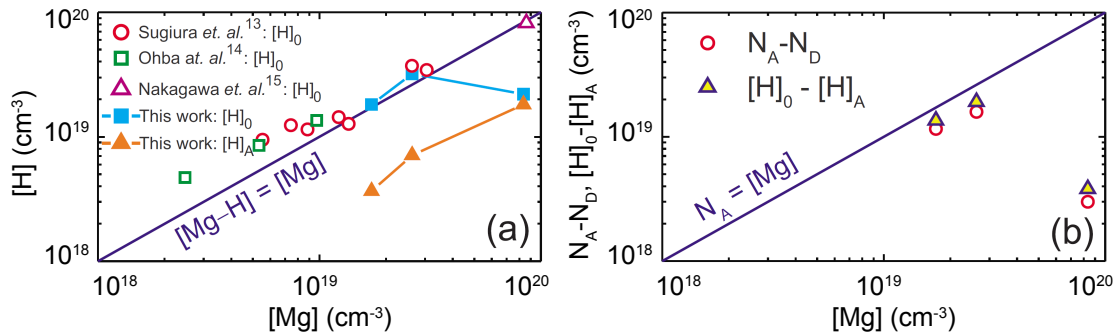


Figure 2.7: (a) Hydrogen concentration before ($[\text{H}]_0$) and after ($[\text{H}]_A$) the thermal annealing as a function of $[\text{Mg}]$. References can be found in Ref. [80]. (b) Comparison between $[\text{H}]_0 - [\text{H}]_A$ and $N_A - N_D$ as a function of $[\text{Mg}]$ [80].

remaining in the sample after the thermal activation treatment (defined as $[H]_A$), proportional to $[Mg]$. The difference $[H]_0 - [H]_A$ was also found to match the $N_A - N_D$ values. The results suggested that H can form two (or more) complexes in GaN:Mg. One is metastable and can be dissociated by the activation process while the other one (or more) is (are) stable and result(s) in compensation.

In case of MBE, as-grown *p*-type samples do not require any activation step (*i.e.* thermal annealing) [110]. This is obvious due to the absence of H in the reactor for PAMBE. This is less straightforward for NH_3 -MBE. However the electrical characteristics of as-grown films remain unchanged even after the thermal treatment (RTA), indicating the absence of dopant passivation [111]. In this chapter we will also discuss this point and its implications on the doping of III-nitrides with this growth technique.

2.3 Alternatives to bulk doping

Besides classical bulk doping, techniques enabling increased hole concentrations and/or mobilities have been proposed. For completeness of this work they are briefly presented hereafter, even though they have not been investigated or used during this PhD.

2.3.1 Delta doping

The delta doping technique consists in modulating the doping during growth in order to obtain periodic delta-function like doped regions surrounded by undoped material. By incorporating the impurities in the crystal in such a manner, it is believed that 3D equivalent dopant concentrations above the solubility limit can be obtained. This would be beneficial for lowering the apparent ionization energy (E_A) of Mg, as discussed in Sec. 2.1.1. In addition, the 2D atomic arrangement of the impurity atoms and their high concentration in the plane results in the bending of the valence band (in the case of acceptors) creating V-shaped QWs-like potential profiles. The quantization of the energy levels in this potential profile give rise to confined subbands. If the separation between the delta doped regions is small enough, the carriers can then tunnel across the so-formed subbands resulting in an enhancement of their mobility, thus of the layer conductivity [112].

2.3.2 Polarization engineered doping, 2D and 3D cases

When a periodic oscillation of the valence band is produced, the Fermi level can locally cross the band, even when the doping impurity has a large activation energy [113]. The valence band modulation can be obtained by using superlattices. In III-nitrides, high electric fields build-up due to the polarization mismatch of the layers forming the superlattice which bend the bands, giving rise to a periodic sawtooth potential energy centered around the Fermi level. The combined effects result in the ionization of the acceptors in the region where the

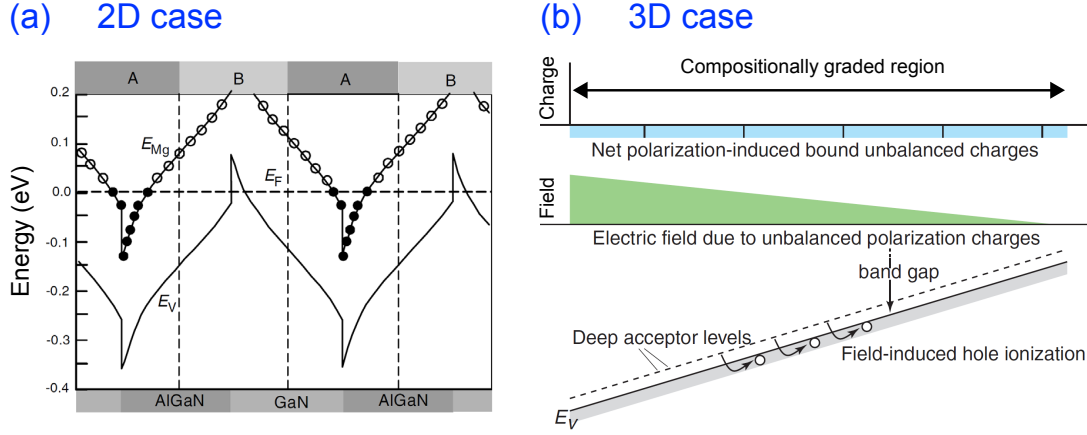


Figure 2.8: (a) Valence band diagram of a $\text{Al}_{0.2}\text{Ga}_{0.8}\text{N}/\text{GaN}$ superlattice (8 nm/ 8 nm) doped with Mg showing polarization induced band bending. Ref. [114] shows that doping region A while leaving region B undoped is preferable in terms of electrical performance. E_{Mg} is the Mg impurity band energy. (b) Schematic diagram of the polarization induced charge, field, and band bending resulting from a compositionally graded structure giving rise to 3D hole gases [116].

valence band is far below E_F as shown in Fig. 2.8(a) [114]. On the other hand, holes populate the region where the band edge is close to E_F . In this configuration the ionization of the acceptor is enhanced giving rise to high hole concentrations. However, the design must be carefully optimized to limit the negative effect of the potential barriers lowering the hole vertical mobility. For this reason, short period superlattices are generally adopted which allow for the tunneling of the carriers across the potential barriers. In the early stages, this configuration was adopted for the *p*-type cladding layers of commercial LDs [115].

It is also possible to exploit the polarization fields to create three-dimensional hole gases instead. If in place of an abrupt alloy transition the alloy is compositionally graded, the polarization discontinuity will extend along the growth direction and the induced polarization sheet charges will be homogeneously distributed in this region [116]. The polarization charge density then writes $\sigma_\pi(z) = -\nabla \mathbf{P}(z)$. Depending on the sign of the polarization charge either 3D electron (positive charge) or hole (negative charge) gases can be created using this approach. The ionization of the impurities is increased by electrostatic field ionization depicted in Fig. 2.8(b), giving rise to higher hole concentrations in *p*-type material. In the case of Ga-polar material, 3D hole gases can thus be formed by compositionally grading the composition from AlGa_N to GaN along the growth direction.

2.3.3 Codoping

Intentionally doping the semiconductor with both acceptor and donors simultaneously, referred as codoping, is an interesting approach to reduce the compensation and increase the

impurity ionization. In 1959, Reiss and coworkers discussed the interaction of defects in Si and developed the theory behind codoping [117]. The pairing of the two type of impurities increases their solubility in the crystal, which may be necessary to enhance the hole concentration in GaN:Mg. Furthermore, Katayama *et al.* from *ab initio* calculations proposed that an acceptor-donor-acceptor complex behaves as an acceptor having an $E_A = 0$ and that it can be created in GaN using Mg and H, or O [118]. A detailed review on the codoping of III-nitrides can be found in Ref. [119].

2.4 Experimental

On the basis of the observations published on *p*-type doping and dopant compensation, we discuss hereafter the growth characteristics and investigations performed during this PhD on (Al)GaN:Mg epilayers grown by NH_3 -MBE and compare the results to the characteristics of MOVPE grown samples realized in our laboratory. The MBE epilayers were grown on top of MOVPE GaN-on-sapphire templates from LUMILOG or directly made at EPFL. In order to limit the effects of surface contamination arising from air exposure, buffer layers thicker than 500 nm were deposited by MBE at 820°C under 100-150 sccm of NH_3 prior to the GaN:Mg layer growth.

At the beginning of this work the information about *p*-type doping by NH_3 -MBE were scarce, and the growth conditions nearly unknown, apart from the growth temperature. A decrease of the latter from 800°C to 740°C was found to strongly enhance the electrical properties [111] when using a solid Mg source. On the other hand when Cp_2Mg was used, $T_{\text{Growth}} = 950^\circ\text{C}$ was found to produce the best results [120], likely due to the need of removing C contamination. Many works focused instead on PAMBE due to its potential to obtain high doping levels [121–123]. This technique however, apart from the similar high vacuum environment, is governed by different growth kinetics and the results could not be transferred to the growth by NH_3 -MBE.

2.4.1 Mg solid source effusion cell

This configuration is often preferred in MBE technology: the relatively low growth temperatures prevent the chemical decomposition of the metalorganic molecules on the surface, and the chemical nature of the precursor may increase unwanted contamination in the reactor. Notice that researchers at Sharp Laboratories of Europe [120, 124] employed a precursor (Cp_2Mg) in the MBE reactor for the growth of GaN:Mg. This however required high growth temperatures, typically above 900°C.

Mg has a high vapor pressure with respect to Ga or Al. This translates into low evaporation temperatures which are below 300°C compared to the 900-1100°C range for the two group-III elements under standard MBE conditions. It is also characterized by a high chemical reactivity and, despite the high vacuum environment, the formation of condensates onto the Mg crucible

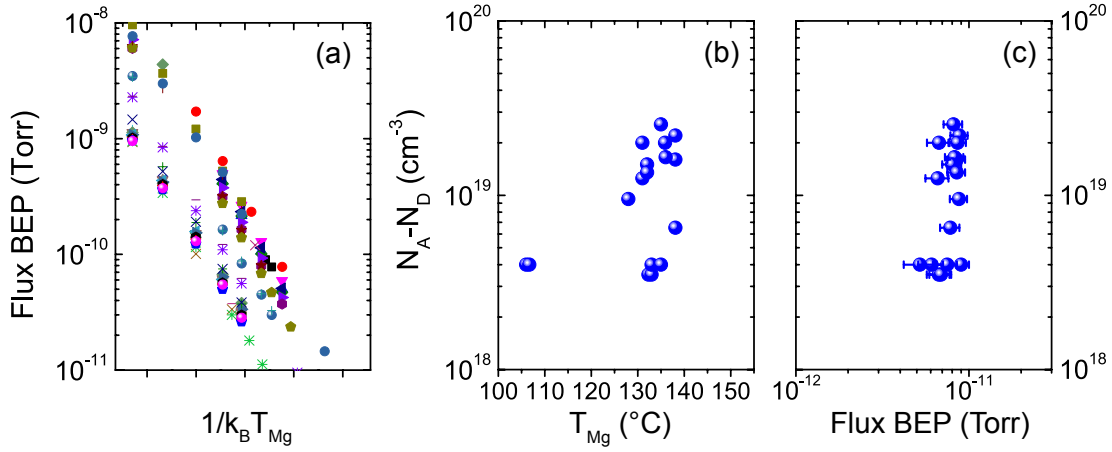


Figure 2.9: (a) Beam equivalent pressures (BEP) of the Mg flux measured overnight during a few months period outlining the Mg flux instability which spreads over one order of magnitude for a given temperature value. Figures (b) and (c) represent the $N_A - N_D$ value of the MBE grown samples as a function of the single-filament effusion cell temperature and doping flux, respectively.

may occur in the form of MgO or Mg₃N₃/Mg₃N₂. Especially, NH₃-MBE requires the weekly regeneration of the cryopanel, during which the Mg charge is exposed to high NH₃ pressures, which faster its contamination. This results in the uneven evaporation/sublimation of the surface and thus affects the dopant flux. The contaminated layer at the Mg source surface must therefore be evaporated or broken into small particles in order to recover the original flux as proposed in Ref. [125]. Consequently, special procedures must be implemented to outgas the cell. Nevertheless, it substantially compromises the growth reliability, which is needed for device fabrication.

This constitutes *per se* a limitation with respect to MOVPE, where a mass flow meter directly controls the dopant concentration. In this work, the MBE dopant flux has been measured during the night (before the heating of the group-III cells) in order to benefit from a low background pressure, in the 10^{-10} Torr range, to accurately measure dopant fluxes in the 10^{-12} - 10^{-8} Torr range (Fig. 2.9(a)). The outgassing procedure was always kept the same, with a slow temperature ramp up to 250°C and 1 hour of outgassing, followed by four flux measurements at lower temperatures performed after a long (> 30 min) cell stabilization step at the desired temperature. The fitting of the fluxes as a function of $1/k_B T$ was then used to determine the Mg cell temperature for the desired Mg flux. Despite the attention given to cell stability issues, when a single-filament effusion cell was employed for the doping, a reproducible relationship between dopant flux, cell temperature, and $N_A - N_D$ could not be obtained over the long term, as shown in Fig. 2.9(b) and (c).

On the other hand, by employing the right strategies it was still possible to obtain the desired doping level, but at the expenses of a time consuming process requiring a growth calibration and ECV measurement prior to the growth.

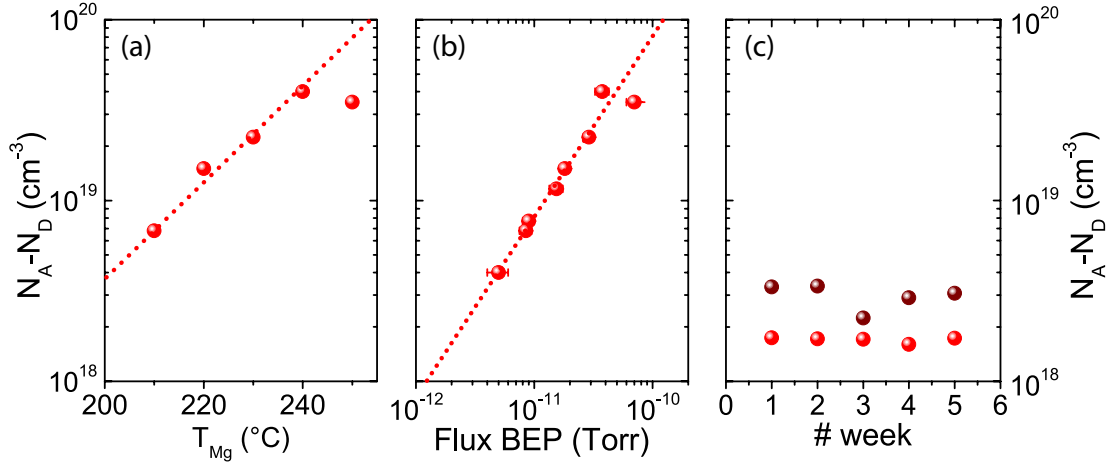


Figure 2.10: Evolution of $N_A - N_D$ as a function of (a) the Mg cell temperature and (b) Mg BEP when supplied from the valved cell. Note that the furthestmost point to the right of (a) and (b) does not follow the trend because of strong compensation. The dotted lines are guides to the eyes. Figure (c) depicts the doping levels as a function of the week during which the samples were produced, showing the reproducibility of the process. Two colors, brown and red, correspond to the valve openings of 15% and 10%, respectively.

In order to solve this problem, the MBE system has been equipped with a RIBER VCOR 110 valved effusion cell during this PhD. A remotely controlled conical valve is used either to seal the cell or to open it at different positions and the Mg flux can thus be modulated. The cell also features a cracker which can be brought up to high temperatures (above 600°C). It was kept at 400°C for all the samples described in this thesis. The net acceptor concentration plotted against either the Mg flux or the Mg cell temperature for the valved cell is shown in Figs. 2.10(a) and (b). In addition, keeping the experimental conditions exactly the same, we compared the doping evolution during one month for two valve positions, 10% and 15% (Fig. 2.10(c)). The net acceptor levels during the period of investigation remained nearly constant testifying the stability of the cell. It can be concluded that the valved cell allows the effective chemical protection of the Mg source during NH_3 regeneration and idle periods, simplifying handling procedure.

Also faster transient of the Mg flux through the mechanical opening of the valve can be achieved. This adds an additional degree of freedom in terms of flux control. While for standard effusion cells one can only vary the flux by changing the cell temperature, the valve opening control provides an additional and rapid way to tune the dopant flux. The relative flux of the cell as a function of the valve opening was characterized and showed a non-linear behavior. Figure 2.11(a) displays the relative flux, normalized with respect to the maximum flux, as a function of the valve opening.

Two samples were prepared for the characterization of the [Mg] transient produced by a rapid transition of the valve opening position from 10% to 15%. To this aim, two successive 300

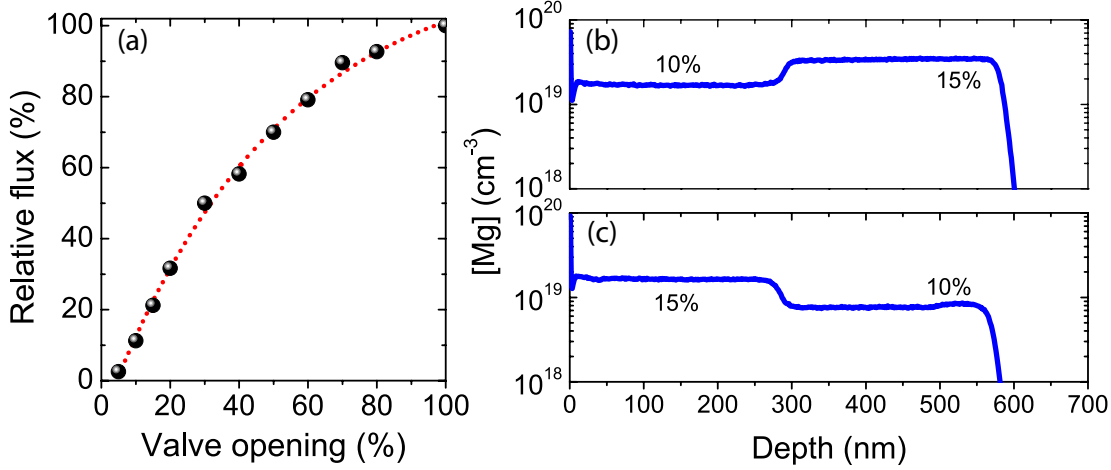


Figure 2.11: (a) Calibration of the flux dependence to valve opening. (b), (c) [Mg] SIMS doping profiles of two samples grown with two different valve openings of 15% and 10% used to investigate the magnesium rising (c) and decreasing (b) transients.

nm thick layers were grown under the two valve opening conditions and the [Mg] transient were determined by SIMS. In Figs. 2.11(b) and (c) the rise and decrease of the [Mg] doping is shown, with a slope below 20 nm/decade for both cases. The 5% change in the valve parameter induces a twofold increase/decrease in the magnesium concentration. From the similarity in the [Mg] change rate upon opening or closing the valve, we can conclude that with our MBE there are no significantly noticeable memory effects in our MBE system.

Remarkably flat doping profiles are also obtained for constant doping conditions, a further evidence of the cell stability. In conclusion in order to obtain stable and reproducible doping, special care must be given to the Mg cell. In our reactor, the use of a valved cell simplified the handling procedure and enabled us to meet the requirements for device fabrication, as discussed in Chapter 3. Interestingly, doping efficiencies significantly higher were obtained using the valve cell instead of the single filament one. This will be treated in Sec. 2.4.5.

2.4.2 Growth temperature window

Two works reported a drastic improvement of the *p*-type doping characteristics in NH₃-MBE when decreasing the growth temperature from 800 °C to 740–760°C [111, 126]. The hole concentration obtained for fixed Mg doping levels was shown to drastically increase while lowering the growth temperature. However, growth temperatures lower than 740°C were not investigated. With the objective of regrowing GaN:Mg on top of high indium content InGaN QWs, lowering further T_{Growth} was considered worth being investigated, even if for the regrowth on green LD structures, 740-760°C could already be sufficiently low. Furthermore, the trend showed in the above-mentioned papers suggests that the hole concentration could be further increased when employing growth temperatures below 740°C.

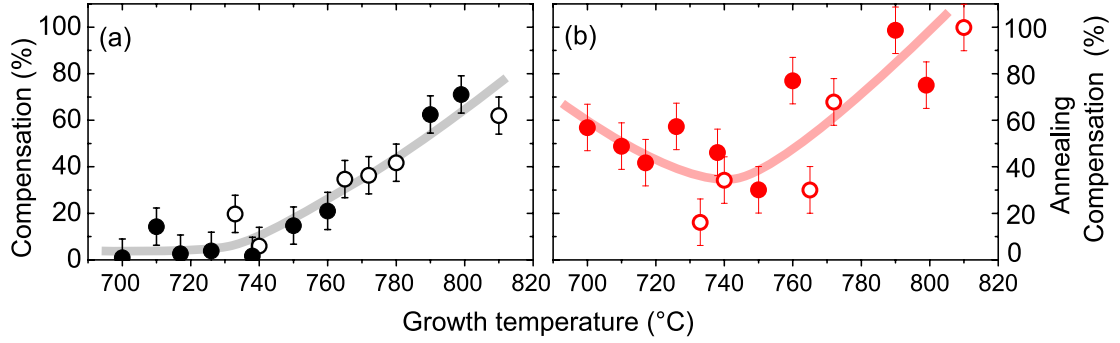


Figure 2.12: (a) Dopant compensation as a function of the growth temperature. (b) Compensation induced by the HVPE thermal treatment. Circles correspond to the layers grown using the surfactant effect of In.

The acceptor compensation (C_{doping}), as defined in Sec. 2.2, was investigated as a function of T_{Growth} by means of ECV profiling. The results are plotted in Fig. 2.12(a) : C_{doping} drastically decreases as the growth temperature is reduced to 740 °C. For lower temperatures however the acceptor compensation is clamped to a low level (less than 20%). These results are in agreement with the evolution shown by Hurni *et al.* in Ref. [126]; the decrease in acceptor compensation is accompanied by an increase in hole concentration. However when C_{doping} approaches values below 20% it remains clamped to a low level and higher hole concentrations are thus impossible. [Mg] was kept below $2 \times 10^{19} \text{ cm}^{-3}$ to avoid issues related to high doping effects. In this doping range a dependency of C_{doping} with [Mg] was not observed, but should not be discarded for higher doping concentrations. In other words, even if it is well known that C_{doping} is dependent on [Mg], the maximum in $N_A - N_D$ may appear at different doping levels depending on the growth temperature.

The samples were also annealed during one hour in a HVPE reactor under N_2 and NH_3 at 850°C to see if any changes were induced by this thermal treatment. After the annealing step, the activation by rapid thermal annealing (RTA) was necessary for the samples treated under NH_3 as acceptor passivation by H occurs. The ECV measurement did not show any remarkable difference whatever N_2 or NH_3 was employed. Figure 2.12(b) displays the results for N_2 , because of the completeness in measured data. After the HVPE thermal annealing the $N_A - N_D$ value for NH_3 -MBE grown samples always decreased, indicating the metastability of the Mg acceptor. In Fig. 2.12(b), the annealing compensation defined as $[(N_A - N_D)_1 - (N_A - N_D)_2] / (N_A - N_D)_1$ is plotted against the growth temperature, where $_1$ and $_2$ indicate the sample before and after the annealing step, respectively. The lowest decrease in net acceptor concentration appears in the vicinity of 740°C. For both higher and lower growth temperatures, the compensation induced by the annealing increases. The introduction of compensating defects during the HVPE step can be excluded (as discussed in Sec. 2.4.7) for the range of [Mg] employed. Indeed, the evolution observed in Fig. 2.12 must be related to intrinsic material properties varying as a function of T_{Growth} . The compensation could originate either from the creation of Mg-Mg clusters or from the creation of Mg- V_N complexes during the

annealing process. However the former hypothesis is unlikely since the compensation in this doping range is negligible during MOVPE growth at much higher temperatures, and therefore the clustering of Mg atoms as well. It could only be explained by a large density of point defects present in NH_3 -MBE layers, assuming a defect enhanced diffusion of Mg. The second possibility seems more likely, when the clustering of Mg with V_N is considered.

The decrease in the acceptor compensation in Fig. 2.12(a) can be explained as follows. Contrary to MOVPE where the incorporation of hydrogen during growth allows keeping the Fermi level of p -type layers away from the valence band and thus limits the nitrogen vacancy formation, the absence of hydrogen passivation in MBE makes the Fermi level closer to the valence band-edge during p -GaN growth. In this case, the formation energy of V_N is reduced and its creation rate is enhanced. The drastic reduction in the compensation observed between 810°C and 750°C can be explained by the combination of a lower vacancy creation rate and lower V_N /Mg mobility resulting in reduced Mg- V_N complexes.

Moreover, given the low growth temperature a large number of unclustered defects may still be present in as-grown samples. In the investigated low temperature region the origin of these defects can be related to growth kinetics which can induce defect densities exceeding equilibrium concentrations even in GaN [127]. These defects are "frozen" in their positions during the growth at 700°C and no longer can form complexes with Mg but are revealed after the annealing step at 850°C due to diffusion processes. In the high growth temperature region of Fig. 2.12, the combination of GaN low surface stability at low NH_3 pressures and the higher thermal energies can explain the higher defect density. Interestingly, the compensation is minimum at 740°C , which is thus the optimum temperature, *i. e.* a trade off between kinetics and thermodynamic compensation.

The effect was also observed in ECV profiles for layers grown at "high" temperatures. Figure 2.13(b) shows the net acceptor profile for a layer grown at two different temperatures, 800°C and 750°C . The high temperature growth induces a decreasing $N_A - N_D$ profile along the layer thickness indicating a time dependent compensation process during growth compatible with clustering. On the other hand the subsequent p -type layer grown at a reduced temperature of 750°C exhibits a flat net acceptor profile and no signs of potential clustering.

Furthermore, the Mg incorporation as a function of the temperature was characterized on a sample grown partially at 750°C and with a step temperature change to 720°C for the last 200 nm without performing a growth interruption (Fig. 2.13(a)). Refs. [111, 126] reported constant Mg incorporation as a function of growth temperature. For this structure as well [Mg] does not vary, but a peak of Mg is observed at the interface between the two regions. Changing the temperature may affect the steady state conditions at the surface, which could in turn introduce a transient on the Mg incorporation. Further investigation is clearly needed.

In summary, starting from standard growth conditions ($T_{\text{Growth}} = 800^\circ\text{C}$ and $V/\text{III} \approx 10$) we found that 740°C is the optimum growth temperature leading to low compensation and high thermal stability. In the following we will refine the growth conditions looking at carefully the

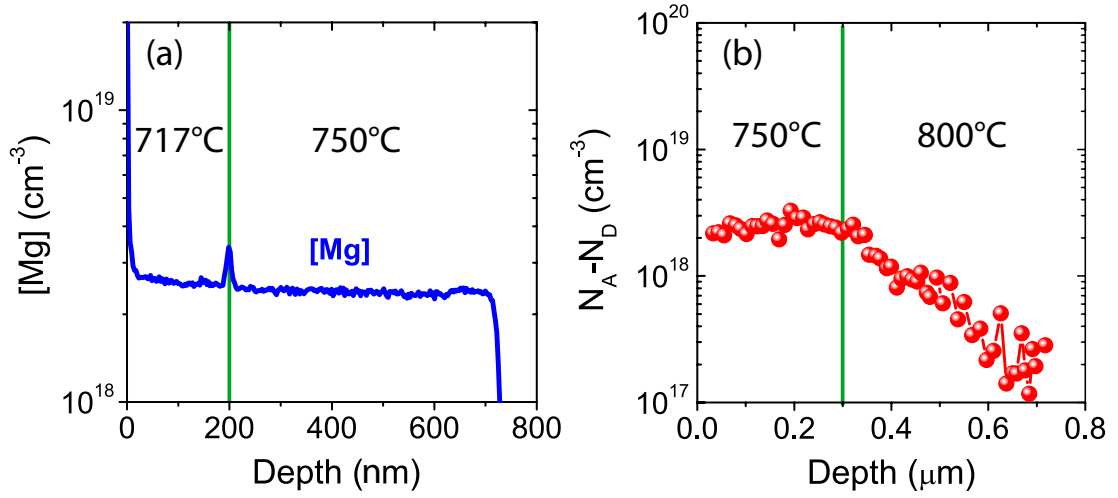


Figure 2.13: (a) SIMS profile showing the effect on the Mg incorporation of a sudden temperature change. (b) Temperature influence on the net acceptor profile.

impact of the V/III ratio.

2.4.3 V/III ratio optimization

Based on the optimization of the growth temperature, *p*-doped layers have been grown at 740-750°C at a growth rate in the 0.4-0.5 monolayer/s (ML/s) range (≈ 400 nm/h) in order to study the V/III ratio effect on the doping. This growth rate, which is lower than the reported one of 1 ML/s in Ref. [111], was set to avoid extensive stressing of the Ga cell. As we will discuss in the Sec. 2.4.4, a low growth rate also allows keeping the surface morphology smoother which may be important when forming the metal contact on to the *p*-surface.

One sample (sample A) was designed to study the V/III ratio effect on both the net acceptor concentration and Mg incorporation. To this aim, the ammonia flow was decreased along the growth direction from 100 sccm down to 25 sccm in three steps. The first part of the layer, deposited under the highest NH_3 flow, was set to a nominal thickness of 400 nm, 100 nm more than the other three regions, due to the potential doping delay at the start of the Mg incorporation. The so-formed structure was then measured by SIMS to inquire $[Mg]$ and $[H]$ levels and probed by ECV to access the $N_A - N_D$ level; the results are plotted in Fig. 2.14(a). The thickness of the doped region measured by SIMS is 100 nm (8%) thinner than the nominal thickness, suggesting either lower growth rate than the one considered or doping delay. A flat doping profile is obtained by supplying the Mg dopant impurity from a conventional single-filament effusion cell at a level of $8 \times 10^{18} \text{ cm}^{-3}$. No dependence with respect to the NH_3 flow is observed, which means that the incorporation of magnesium does not change upon variation of the V/III ratio at least in this flux range. Instead, the net acceptor profile was found to be affected by changing the V/III ratio. The highest $N_A - N_D$ values correspond to the lowest NH_3 fluxes, 25 and 50 sccm. On the other hand dopant compensation reaches nearly

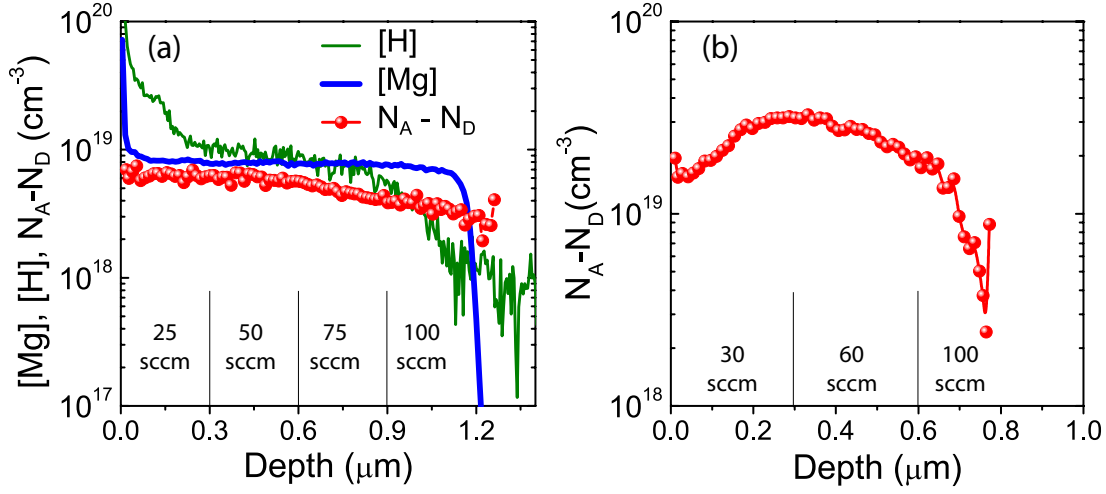


Figure 2.14: (a) SIMS and ECV data for sample A indicating the increase of compensation for higher V/III ratio when the doping is moderate. (b) $N_A - N_D$ profile for sample B.

50% for the layer section grown under 100 sccm, indicating a strong degradation.

The compensation mechanism responsible for this decrease is not well understood yet. Contamination from oxygen or carbon can be excluded: the two elements have been measured by SIMS and their concentration is seen to increase towards the surface, contrary to the compensation. Moreover the concentration of the two impurities does not match the decrease in $N_A - N_D$. Finally the hydrogen level is unexpectedly high. Its concentration matches [Mg] for NH_3 flows equal or smaller than 75 sccm. Note that the net acceptor profile is measured on the as-grown layer, without performing any activation treatment to remove H. The compensation observed in the layer cannot be understood as hydrogen passivation: first of all, the hydrogen level is much higher than the donors required for compensation along the whole sample. Secondly, in the mostly compensated region ($\text{NH}_3 = 100$ sccm), [H] decreases, a further indication that it is not the driving force for compensation. In addition, despite high [H] level, low compensation is obtained for low ammonia flows. It is therefore clear that hydrogen incorporation in the GaN lattice in NH_3 -MBE is different than in MOVPE.

Another sample (sample B) was grown with various ammonia flows similarly to the one reported above but with higher $[\text{Mg}] \approx 3 \times 10^{19} \text{ cm}^{-3}$. The flow was varied from 100 to 60 and 30 sccm forming three 300 nm thick regions. During growth, when the NH_3 flow was lowered down to 30 sccm, the RHEED pattern became spotty indicating 3D growth. Thus too low V/III ratios may be detrimental when [Mg] is high. Samples exhibiting 3D morphology are generally difficult to measure by ECV. The $N_A - N_D$ profile measured for this sample dropped after a thickness of 700 nm (depicted in Fig. 2.14(b)) showing that the depth evaluation by ECV may be incorrect if the surface is not of high quality. The net acceptor drop observed close to the surface corresponds to the region of the sample exhibiting 3D morphology. The incorporation of Mg and other impurities on the new growth front facets can strongly change and explain

the drop in $N_A - N_D$.

In conclusion we determined that the NH_3 flow of 50-60 sccm is a good compromise for keeping the compensation low and avoiding surface morphologies becoming 3D at high doping levels.

2.4.4 Morphological features

GaN has a high melting temperature ($\approx 2500^\circ\text{C}$) and extremely high nitrogen pressures in the tens of kbar range are required to stabilize its surface under thermodynamic equilibrium [128]. These prohibitive conditions make the Czochralski growth method nonviable. Growth is therefore performed away from equilibrium and stoichiometric conditions. This is especially true for MBE, where low temperatures and pressures are employed. In this context, the adatom kinetics on the surface determine the morphology. Hexagonal hillocks are reported in NH_3 -MBE [129] while growth under the step-flow growth mode is achieved under specific conditions by PAMBE [130]. The latter conditions require the formation of a bilayer of metallic Ga on the surface. If these requirements are not met, either droplets (Ga-rich) or rough pyramidal surfaces (N-rich) appear.

The hillock (or mound) formation in NH_3 -MBE has been ascribed to kinetic roughening [129] due to an Ehrlich-Schwöbel barrier (ESB) at the step-edges [131, 132]: the ESB limit the adatom mobility at the step-edges. Adatoms which cannot cross the ESB nucleate on top of the terraces, preventing step-flow growth and giving rise to mounds. Under the growth conditions typically employed in NH_3 -MBE (growth rate 0.5-1ML/s and 800°C) this effect is well-pronounced. The increase in growth temperature and/or decrease in growth rate enhance the adatom diffusion. This way one could overcome kinetic roughening and mound formation but these conditions are no longer appropriate for p -type doping.

On the other hand, the Ga bilayer used by PAMBE screens the ESB effect enabling smooth surface morphologies [133]. This is not possible when using ammonia as the nitrogen source. Here the growth is performed under nitrogen-rich conditions and the Ga accumulation on the surface is avoided.

The morphology of GaN:Mg as a function of the growth temperature was investigated. On top of a thick GaN buffer layer deposited at 820°C , 500 nm of p -type GaN were grown at different temperatures. Note that during the buffer deposition mounds are introduced so that the starting morphology at the beginning of GaN:Mg layers growth already exhibits these morphological features.

The roughening is inversely proportional to T_{Growth} as depicted in Fig. 2.15(f). In fact, even the RHEED pattern becomes spotty when the growth is performed at 660°C . For higher growth temperatures the RHEED pattern stays streaky but the rms roughness continues to evolve up to the point where the combination of high temperature and low growth rates enhance the diffusion length and lead to step meandering features (Fig. 2.15(e)). Indeed, while the samples

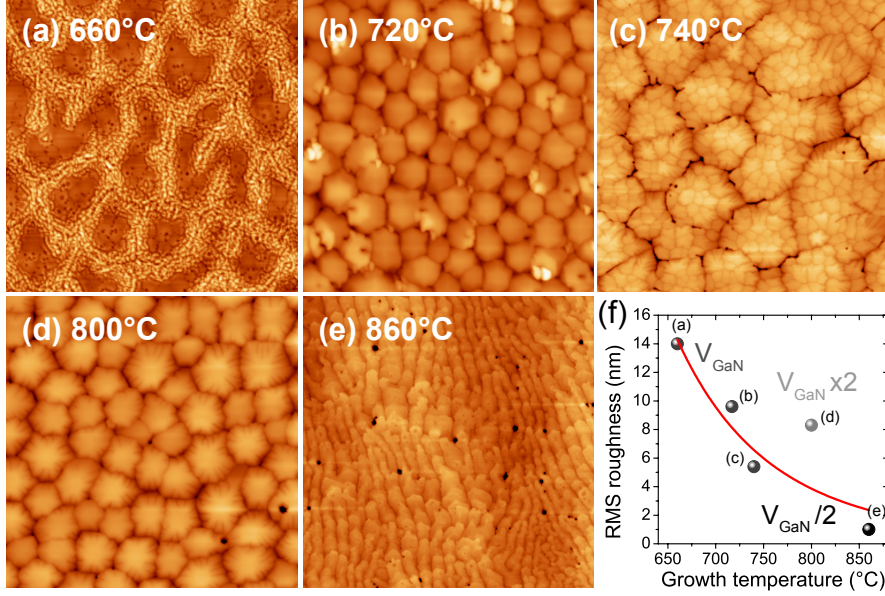


Figure 2.15: (a), (b), (c), and (d) $5 \times 5 \mu\text{m}^2$ AFM images of the GaN:Mg surface morphology for layers deposited between 660 and 860°C in increasing order. (e) Evolution of the rms roughness as a function of the growth temperature.

shown in Figs. 2.15(a), (b), and (c) are grown at the same growth rate (0.4 ML/s), (d) and (e) are obtained from layers grown with double or half growth rates with respect to (a), (b), and (c) as indicated in (f). From the rms roughness value for layers (c) and (d) of 5.5 nm and 8.5 nm, respectively, it is possible to conclude that despite the temperature difference between the two samples, the growth rate effect on the effective adatom diffusion lengths is stronger than the thermal energy increase, resulting in higher roughness values for sample (d) despite a growth temperature 60°C higher, as shown in Fig. 2.15(f).

Beside the valuable knowledge of the temperature and growth rate dependence, we are interested in characterizing the morphological features in the vicinity of $T_{\text{Growth}} = 740^\circ\text{C}$ identified as the optimum growth window for *p*-GaN. To this aim we varied [Mg] in otherwise identical samples and performed AFM measurements (Fig. 2.16). The lowest [Mg] employed is $5 \times 10^{19} \text{ cm}^{-3}$, which corresponds to the Mg level enabling the maximum net acceptor concentration when the single-filament effusion cell is used. When increasing [Mg] from $5 \times 10^{19} \text{ cm}^{-3}$, the compensation strongly increases in this experimental window and the effect on the morphology, if any, could be evidenced. Figure 2.16 clearly indicates the appearance of pits which grow in number and size with [Mg]. The origin of the pits might be related to PIDs that just form in the layer and which can not be efficiently buried because of low diffusion lengths combined to the ESB. On the other hand, the features observed can also originate from dislocations: the termination of the threading dislocations at the surface could become much more pronounced on the AFM images when the doping is increased. This could be a consequence of a stronger pinning of the surface due either to an increase of the tension line of the dislocation or to a

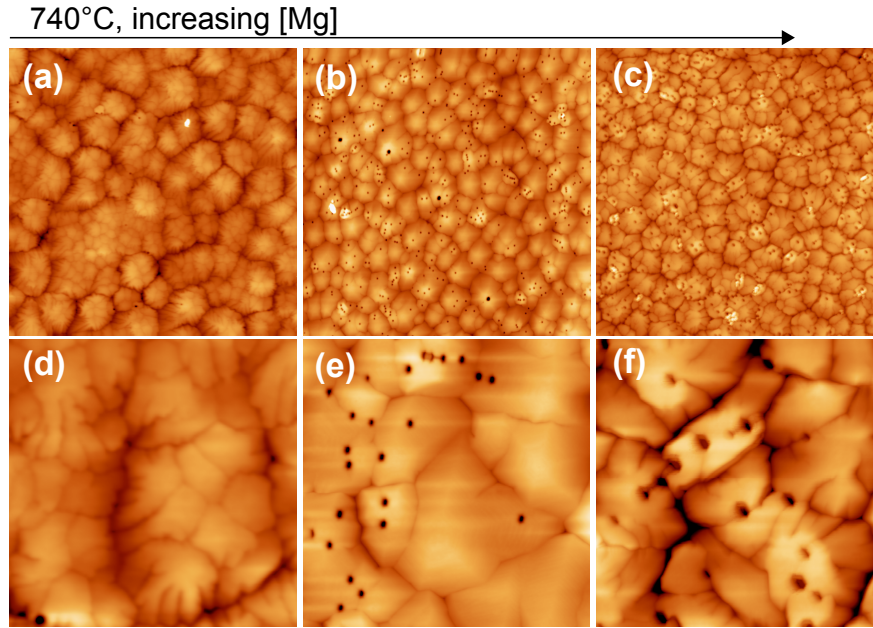


Figure 2.16: (a), (b), (c) $10 \times 10 \mu\text{m}^2$ AFM images and (c), (d), (e) corresponding $2 \times 2 \mu\text{m}^2$ ones of GaN:Mg grown by NH_3 -MBE with varying [Mg].

decrease of the surface free energy.

Given the interest in the low temperature conditions of NH_3 -MBE, at least 50°C lower than the standard growth window of $800\text{--}820^\circ\text{C}$, solutions to overcome the ESB effects have been investigated. In other words, solving the ESB issue could allow for the growth of p -doped layer at much lower temperatures and the p -doping growth window extended, which is always positive in terms of growth flexibility. One solution could be the growth rate reduction, but at the expenses of the compatibility of the process with industrial needs. Furthermore, it will be shown in this chapter that the compensation varies with time, suggesting that one needs to grow layers as fast as possible. Keeping these points in mind we investigated the use of indium as a surfactant in NH_3 -MBE. A surfactant in this case is a chemical species that can influence the growing surface properties without being incorporated in the epilayer [134, 135].

Indium requires low growth temperatures, below 680°C , to be incorporated in appreciable amounts in the MBE vacuum environment. At 740°C its incorporation is negligible but, if supplied to the growth front, indium can play a role similar to the bilayer of Ga in PAMBE acting as a surfactant. During this thesis, by providing indium to the growth front in a ratio of the Ga flux of 1:3, we were able to confirm this hypothesis. At 660°C , when indium is used as a surfactant, the surface exhibits reduced rms roughness values as shown in Figs. 2.17 (a) and (b). The comparison with Fig. 2.15 (a) is striking. However at this temperature slight In incorporation could take place. When looking at Figs. 2.17 (b) and (c), for which 740°C were used in combination with In, the small mounds found in Fig. 2.15 (c) disappear, with the remaining big mounds introduced during the growth of the buffer.

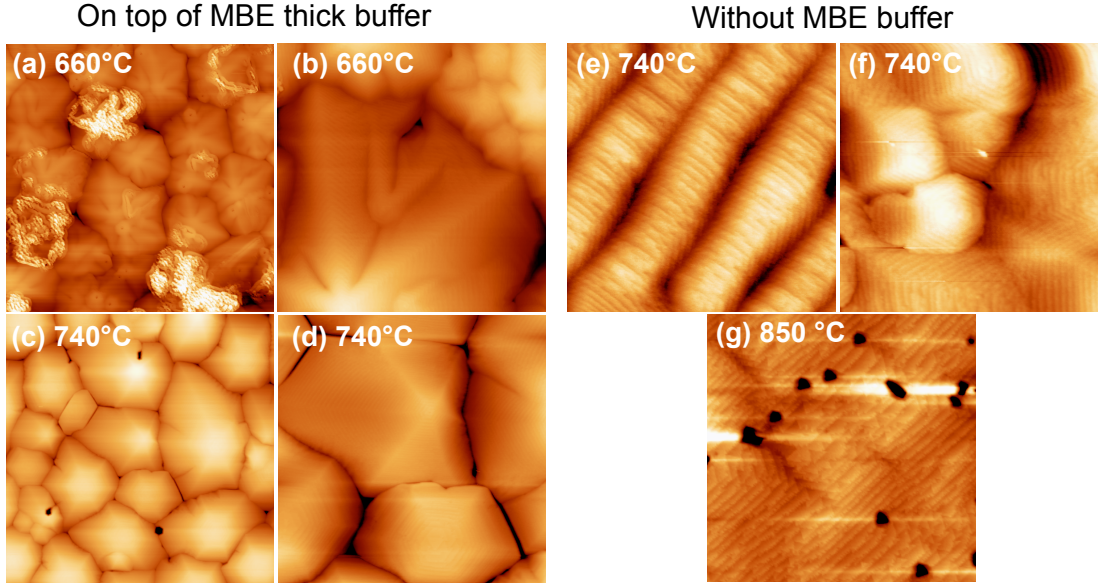


Figure 2.17: (a), (c) 5×5 and (b), (d), (e), (f), and (g), $2 \times 2 \mu\text{m}^2$ AFM images of GaN:Mg grown by NH_3 -MBE using the In surfactant effect. In samples (e), (f), and (g), the buffer layer was not used.

To confirm the role of In at the growth front, we show the surface morphologies of hybrid LDs grown using the surfactant effect of In (Figs. 2.17 (e) and (f)). In this case the MBE layer is grown directly on the MOVPE GaN surface grown in the step-flow regime. The surface morphology of these LDs exhibits step-meandering features indicating increased adatom diffusion lengths, despite the low temperature (740°C) of p -type cladding layers. Furthermore the AFM image of a layer grown at 850°C using In but without doping is also shown in Fig. 2.17(g) indicating again a smooth surface morphology. In conclusion indium can be used to reduce the ESB effect thus smoothing the surface morphology of NH_3 -MBE grown layers.

2.4.5 Acceptor compensation versus [Mg]

In this section we discuss the evolution of $N_A - N_D$ as a function of [Mg] and the effect of the doping on the $N_A - N_D$ profiles especially for high doping levels. Notice that we consider $N_A - N_D$ instead of the hole concentration because its determination from ECV measurements is much more reliable than Hall effect which can be affected by parasitical effects like geometrical factors, conduction in the buffer layer, and contact issues. Moreover, Hall effect measurements do not allow to access the valuable information given by the $N_A - N_D$ profiles.

The first set of epilayers was grown at 750°C under 60 sccm of NH_3 and with growth rate of 0.4-0.5 ML/s. In this case, magnesium was supplied by the single-filament cell. The corresponding evolution of $N_A - N_D$ and the doping efficiency (η_{doping}) as a function of [Mg] is shown in Fig. 2.18(a) and (b), respectively. The blue line indicates a 100% doping efficiency, which implies the absence of donors and a 1:1 relationship between acceptors and Mg atoms incorporated

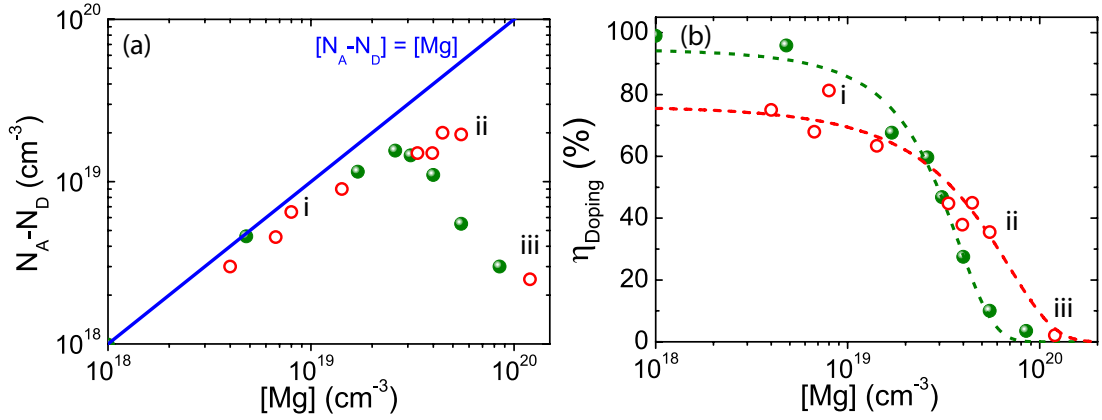


Figure 2.18: (a) $N_A - N_D$ as a function of $[Mg]$ for NH_3 -MBE (red circles) and MOVPE (green dots) grown layers. (b) η_{doping} as a function of $[Mg]$ following the same color scheme. The dashed lines have been constructed using the method discussed in Sec. 2.5.

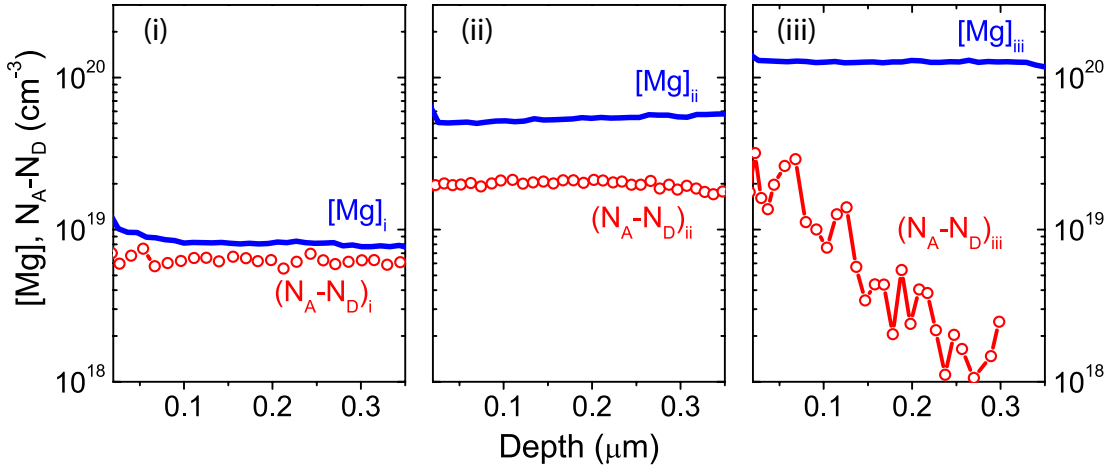


Figure 2.19: In (i), (ii), and (iii) the $[Mg]$ and $N_A - N_D$ are plotted for three layers doped with increasing $[Mg]$.

in the lattice. The results obtained for MOVPE samples are plotted in green for comparison. With NH_3 -MBE, $N_A - N_D$ values up to $2 \times 10^{19} \text{ cm}^{-3}$ are obtained for $[Mg]$ of $5\text{-}6 \times 10^{19} \text{ cm}^{-3}$. Both values are higher with respect to MOVPE. Above this level the net acceptor concentration levels do not saturate but decrease considerably for both growth techniques. When looking at the doping efficiency in Fig 2.18(b) for both growth techniques the net acceptor concentration maximum corresponds to moderate doping efficiencies around 45%. Indeed for high doping levels, at a given $[Mg]$, the η_{doping} value is higher for NH_3 -MBE samples. Finally, when the doping is further increased in the 10^{20} cm^{-3} range, the layers become strongly compensated exhibiting C_{doping} values above 90%.

As previously mentioned, the evolution of the net acceptor profiles as a function of $[Mg]$ shows some interesting features. In Fig. 2.19 the SIMS and ECV profiles are shown for three

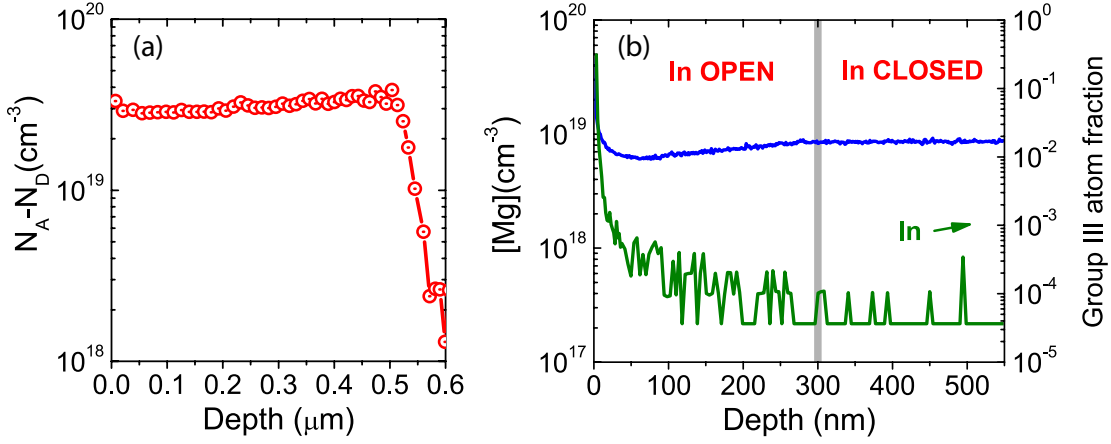


Figure 2.20: (a) Net acceptor profile for a highly doped sample grown while supplying In on the growth front. (b) SIMS profile of a different sample for [Mg] (blue), and In (green) showing the effect on the magnesium incorporation.

characteristic samples, indicated in Fig. 2.18 with the symbols i, ii, and iii. For the first two samples (i and ii), the SIMS and ECV profiles are flat, with the deviation between the two measurements given by the degree of compensation. However when the doping is high and $N_A - N_D$ drops, the ECV profile is not flat along the layer thickness but exhibits a decreasing $N_A - N_D$ value when moving away from the surface (Fig. 2.19(iii)). This behavior is not an artifact of the ECV measurement and can be easily corroborated to Hall effect or TLM results of highly doped samples (as discussed in Appendix A.1). To fully account for this effect on the doping of III-nitrides, thick samples were investigated with a thickness of 500 nm and 1 μm for MBE and MOVPE, respectively. Note that for the sake of comparison the $N_A - N_D$ value is taken at mid-layer thickness whatever the profile evolution. To understand the profile of Fig. 2.19(iii) we have to consider that larger depths correspond to longer high growth temperature exposure. On the other hand, close to the surface the epitaxial material witnesses a very short exposure to high temperatures. Thus, the time for compensation to occur is limited before freezing the process by cooling-down the layer to room temperature. This behavior can be ascribed to the clustering process of point defects with Mg atoms already proposed in Sec. 2.4.2. Here by increasing [Mg], the mean separation between dopant and point defects is reduced, up to the point where the two species are close enough to create clusters, provided that they are kept at high temperature for long enough time.

When indium was supplied at the growth front to benefit from its surfactant effect and for growth temperature of 740°C, more than 50% higher net acceptor concentrations, up to $3.2 \times 10^{19} \text{ cm}^{-3}$, could be obtained, as shown in Fig. 2.20(a). The effect of In on the Mg incorporation was studied by growing two successive 300 nm thick GaN:Mg layers under the same experimental conditions, except for the indium supply during the growth of the second part of the structure, as illustrated in Fig. 2.20(b). As soon as the In cell is opened, [Mg] starts to decrease indicating reduced Mg incorporation. An increase in the growth rate can

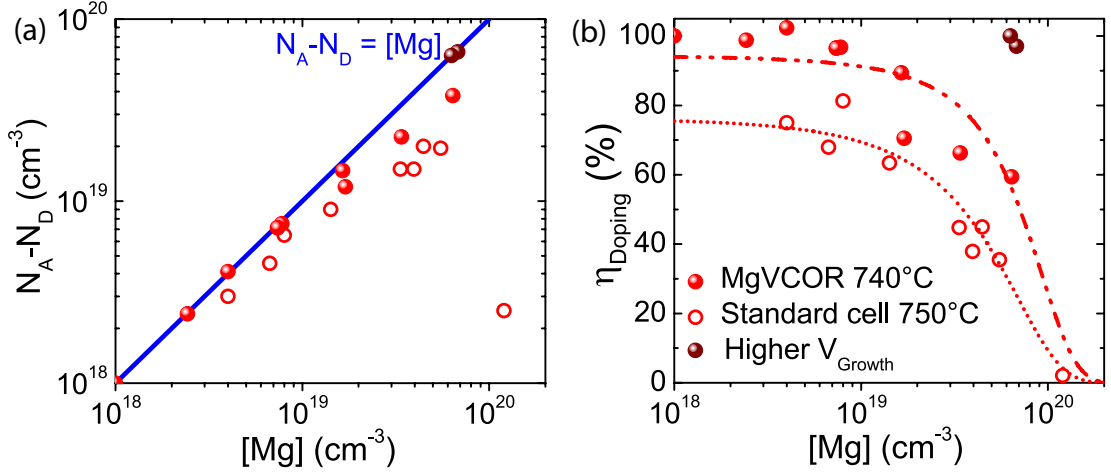


Figure 2.21: (a) $N_A - N_D$ as a function of $[Mg]$ for samples grown using the single-filament Mg source and $T_{Growth} = 750^\circ\text{C}$ (red circles), the valved-cell and $T_{Growth} = 740^\circ\text{C}$ (red dots), and the valved-cell, $T_{Growth} = 740^\circ\text{C}$ and higher growth rates (brown dots). (b) η_{doping} as a function of $[Mg]$ following the same color scheme. The dashed lines have been constructed using the method discussed in Sec. 2.5.

be discarded due to the sticking coefficient of 1 and to the extremely low In incorporation, as shown by SIMS measurements. The gradual reduction of the doping concentration could come from the surface accumulation of In during the first 100-200 nm, before reaching steady-state, reducing the dopant incorporation. No considerable differences were observed upon annealing when indium was used, as detailed in Fig. 2.12. At present, the effect of indium when supplied at the growth front is still not well understood. We speculate that it could prevent the incorporation of unwanted impurities and affect the surface properties because of its surfactant effect. Further studies are needed to elucidate these points and to study the influence of the indium flux on morphological and doping characteristics.

On the other hand, similar or even better results were obtained by employing the valved cell as the Mg source without using In. This configuration allowed to reach $N_A - N_D$ levels up to $3.8 \times 10^{19} \text{ cm}^{-3}$ while keeping the growth temperature, ammonia flow, and growth rate to 740°C , 60 sccm, and 0.4 ML/s, respectively. Apart from the increased purity of the Mg charge in this configuration, the valved cell is equipped with a cracker which was kept at 400°C during all experiments. This constitutes the major difference when comparing the growth conditions, as it could affect the Mg incorporation mechanism. The thermal cracker was shown in one report to increase Mg incorporation [136]. Further work is still needed to understand the influence of the cracker temperature on the incorporation mechanism. Decreasing $N_A - N_D$ profiles were also observed in this configuration for $[Mg]$ levels $\geq 6.4 \times 10^{19} \text{ cm}^{-3}$, corresponding to the uppermost red dot in Fig. 2.21(a). Below this concentration flat profiles are obtained. Furthermore, in the $10^{18} - 10^{19} \text{ cm}^{-3}$ doping range, low compensation values could be obtained as indicated by the red dots in Fig. 2.21. In Fig. 2.21(b) the improvement of the doping characteristics with respect to the results obtained using the single filament cell is evident.

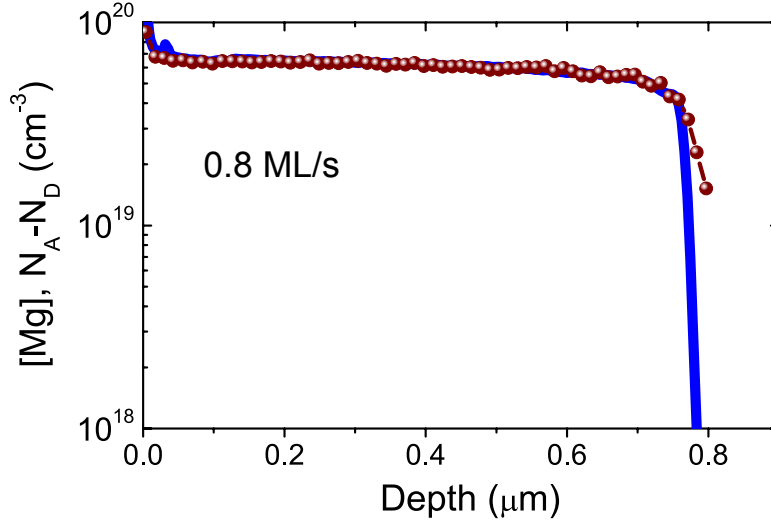


Figure 2.22: ECV and SIMS profiles for a sample grown at 0.8 ML/s exhibiting low compensation. The Mg profile is shown in blue.

Note that the layers grown using indium (not shown) give similar results.

Additional tuning of the growth conditions enabled the realization of highly doped layers ($[Mg] = 6-7 \times 10^{19} \text{ cm}^{-3}$) exhibiting extremely high doping efficiencies ($>90\%$). In fact, doubling the growth rate up to 0.8 ML/s, while keeping the V/III ratio and growth temperature unchanged, strongly reduced the compensation at this doping level, as shown by the two brown dots in Fig. 2.21. In this case, the net acceptor profile follows the $[Mg]$ profile as measured by SIMS despite the high doping level (Fig. 2.22). For this sample the growth time, V/III ratio, and growth temperature are the same when compared to the ones previously discussed. However, the NH_3 pressure is higher because of the increase in ammonia flow needed to keep the V/III ratio the same. This may stabilize the surface during MBE growth: Grandjean *et al.* [137] reported on the GaN evaporation in NH_3 -MBE showing that sufficiently large ammonia flows are needed to saturate the adsorption sites with nitrogen and block the nitrogen release from the surface leading to GaN decomposition. The V/III ratio was shown in Sec. 2.4.3 to strongly affect the compensation. Therefore when the growth rate is fixed, an optimum ammonia flow exists, and should not be increased. The price to pay under these conditions is the surface decomposition when the NH_3 pressure is not sufficient to block the nitrogen release from the surface. When the growth rate is increased, as it is the case here, to keep the same V/III ratio the NH_3 pressure needs to be increased. This has the beneficial effect of further stabilizing the surface, limiting the formation of defects, thus compensation. For this reason we believe that layers grown at increased growth rate exhibit reduced compensation, as the optimum V/III ratio is combined to higher surface stability.

In conclusion, the optimization of the growth parameters allowed to reach extremely high $N_A - N_D$ values, exhibiting low compensation and flat doping profiles. Four times higher net acceptor concentrations than the maximum values measured on bulk GaN:Mg layers

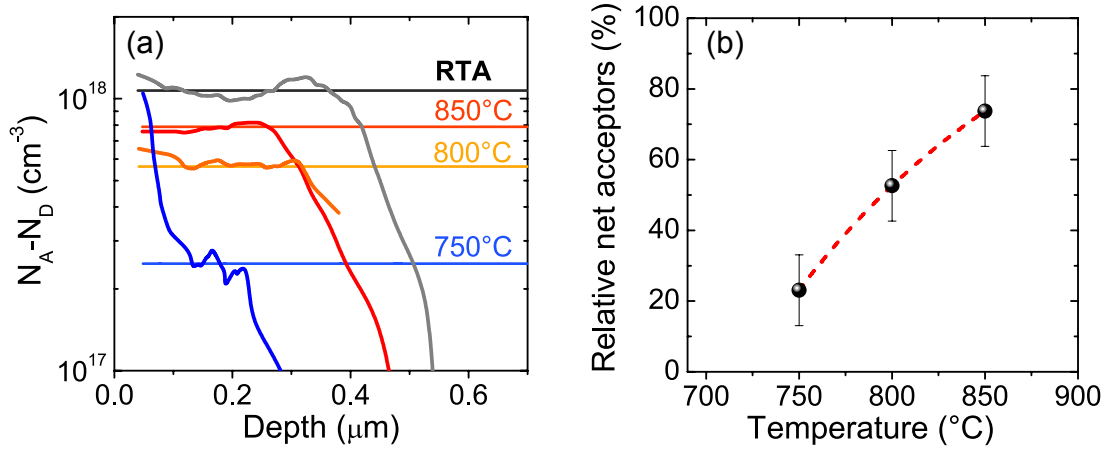


Figure 2.23: (a) ECV profiles for the four samples used to investigate the H incorporation in NH₃-MBE. (b) Relative net acceptor concentrations ($[N_A - N_D]_{\text{MBE}} / [N_A - N_D]_{\text{RTA}}$) for the three samples annealed in the MBE reactor under 100 sccm of NH₃ as a function of the process temperature.

grown by MOVPE have been demonstrated. Moreover the Mg charge purity, V/III ratio, and growth rate have all been shown to have a strong influence on the doping characteristics. However, the exact role of In on the doping is still unclear but it allows for smoothing the surface. The compensation processes observed in this section can be divided into two types. The first, which we will call "intrinsic compensation", is independent of the growth duration and give rise to flat $N_A - N_D$ profiles. This compensation is stable at the growth temperature (eg. Fig. 2.19(ii)). The second, which we will call "dynamical compensation", is dependent on the growth time and give rise to decreasing $N_A - N_D$ profiles (eg. Fig. 2.19(iii)). In this case this compensation increases with growth time indicating metastable *p*-type doping. Intrinsic compensation can be observed already for moderate doping levels while dynamical compensation is introduced at higher [Mg] adding up to the intrinsic compensation effects. The onset of the two processes and their strength strongly depends on the growth conditions.

2.4.6 Hydrogen incorporation in MBE

The role of hydrogen during MOVPE was briefly discussed in Sec. 2.2.4. The absence of acceptor passivation in NH₃-MBE was also mentioned. This must be related to the vacuum environment of MBE which prevents large amounts of this species to be incorporated. The question is whether hydrogen passivates the acceptors during growth and then its removal takes only place during the cool-down in the ultra-high vacuum environment when the ammonia supply is stopped at 600°C. Given that the presence of H in the lattice could keep the Fermi level high, thus limiting the formation of nitrogen vacancies and the acceptor compensation, understanding the MBE doping mechanisms is of prime importance.

To elucidate whether during the sample cool-down in the MBE reactor an activation process

takes place, four MOVPE grown p -doped samples were prepared from the same wafer, *i.e.* having the same $N_A - N_D$ value. One was activated using the standard RTA treatment. The others were introduced still fully passivated in the MBE chamber. While heating up the samples, 100 sccm of ammonia were introduced in the reactor when the temperature overcome 600°C to prevent surface decomposition. The three samples were heated up to 750, 800, and 850°C, respectively, and kept at the desired temperature during 30 min under NH_3 . During cooling-down, the supply of ammonia was stopped again at 600°C, and the samples were cooled down to RT under high vacuum. The three samples were then measured by ECV and compared to the sample activated by RTA as shown in Fig. 2.23. Interestingly, it was found that despite the presence of ammonia in the reactor, partial activation was observed on the three samples. This was seen to be proportional to the annealing temperature, with an activation up to 75% of the RTA value for the sample kept at 850°C. This value is only $\approx 20\%$ at 750°C. This temperature corresponds to the typical growth conditions of p -type layers in MBE. From the trend exhibited by the experimental points in Fig. 2.23(b), we can conclude that below 600°C under high vacuum a negligible amount of H is removed from the layer, at least smaller than 20%. The hypothesis that hydrogen passivation could be totally removed under high vacuum at temperatures lower 600°C is then incorrect. Therefore H passivation during MBE growth does not take place.

Besides the experimental evidence that H does not incorporate in large amounts as for MOVPE, SIMS measurements show that the Mg doping is accompanied by an [H] increase even with NH_3 -MBE, as shown in Fig. 2.24(b). One can notice that [H] is proportional to [Mg] Fig. 2.24(a). Also $[\text{H}]_A$ is lower in MBE samples compared to MOVPE ones (Fig. 2.7(a)). Moreover, the $[\text{H}]/[\text{Mg}]$ ratio (Fig. 2.25(b)) monotonically decreases as the doping concentration increases, with an opposite trend with respect to compensation. In addition, [H] cannot be considered a direct source of compensation as the $[\text{Mg}] - [N_A - N_D]$ value is strongly scattered around the [H]

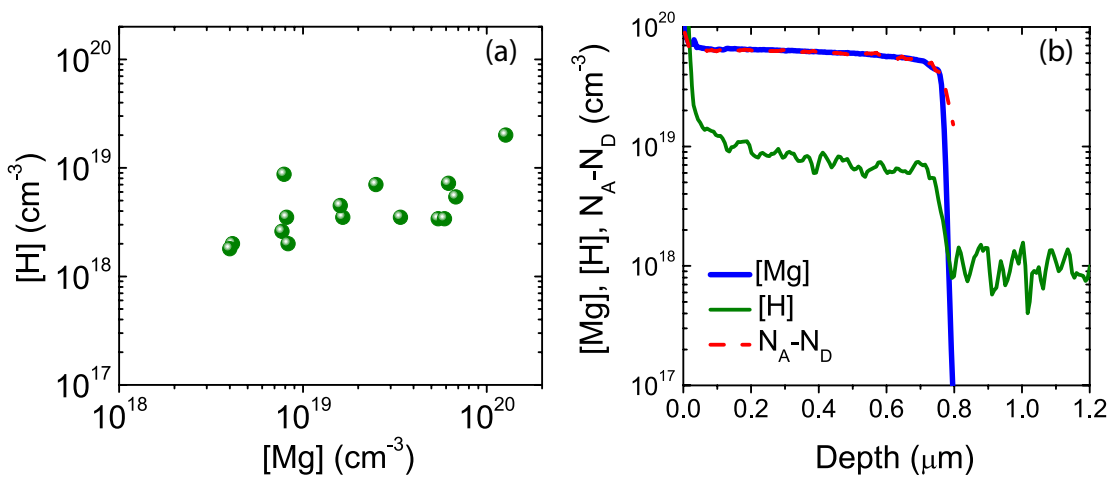


Figure 2.24: (a) [H] as a function of [Mg] for NH_3 -MBE p -doped layers, the red line is a guide to the eyes. (b) SIMS and ECV profile showing the increase in [H] following [Mg].

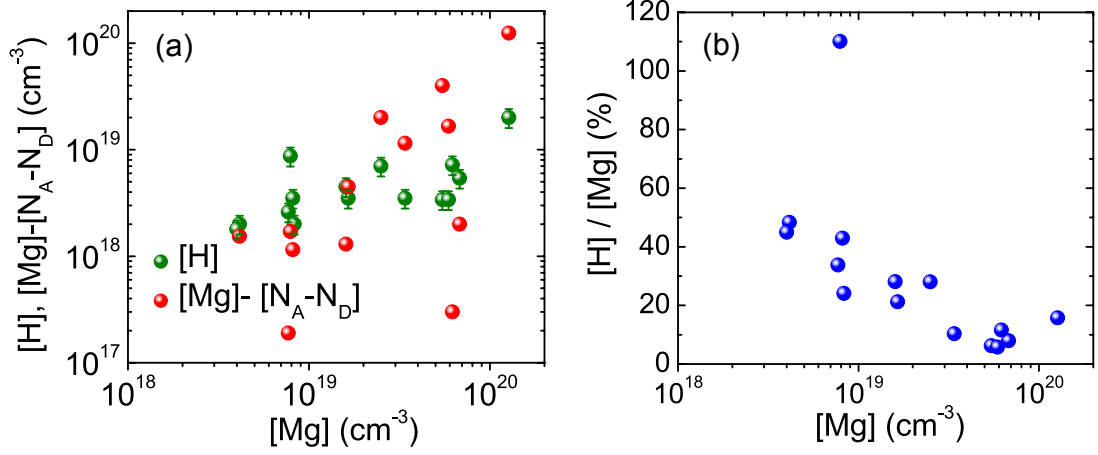


Figure 2.25: (a) [H] (green dots) and [Mg]-[N_A - N_D] (red dots) as a function of [Mg] for NH₃-MBE *p*-doped layers. (b) [H]/[Mg] as a function of [Mg] as measured by SIMS.

level as shown in Fig. 2.25(a). The formation of Mg-V_N-H and/or V_N-H complexes has been suggested [138, 139]. On the other hand, the hydrogen storage capability of Mg₃N₂ proposed in Ref. [95] could also be tentatively invoked.

In an attempt to passivate the acceptors during growth, thus to limit V_N formation, the MBE reactor was equipped with a hydrogen line connected to the plasma cell. In such a way a hydrogen plasma can be created and atomic hydrogen supplied to the growth front. First, N₂ plasma needs to be established in order to start the process. In a second step, hydrogen is progressively introduced in the cell and the nitrogen flow decreased. The first growth attempts under H plasma resulted in samples exhibiting a 3D morphology and high compensation both before and after RTA because of the limited purity of the hydrogen line. Recently a sample was grown showing promising results. The sample was grown at 720°C, under 100 sccm of NH₃, a growth rate of 0.4 ML/s, and a H₂/N₂ plasma mixture composed of 3.7 sccm of H₂ and 0.1 sccm of N₂. The as-grown sample already exhibited a high N_A - N_D value, as shown by the orange dots in Fig. 2.26. However, after RTA, an increase in the net acceptor concentration was observed up to 6 × 10¹⁹ cm⁻³, indicating H passivation in the as-grown layer. The difference between N_A - N_D before and after the activation step, denoted with the subscript 0 and A, respectively, corresponds to the [H] level in the layer measured before RTA (green line), a further indication of H passivation and its successful removal. In conclusion, thanks to the use of a hydrogen plasma combined to the pressure increase arising from the use of the plasma line, passivation of the Mg acceptors was obtained and hydrogen could then be removed by RTA.

2.4.7 Thermal stability of *p*-type layers

HVPE annealings were largely used during this thesis as discussed in Sec. 2.4.2, and 2.4.8. This technique was chosen as it allows several samples to undergo exactly the same treatment (in

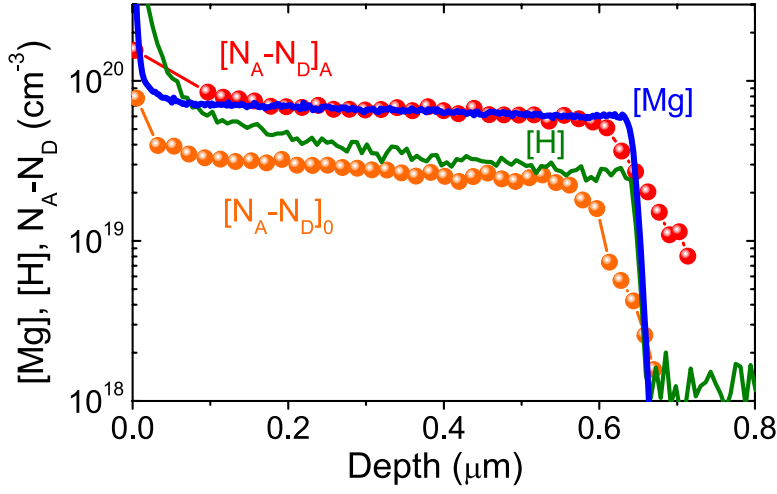


Figure 2.26: (a) ECV and SIMS profiles of [Mg] (blue line), [H] (green line), and $N_A - N_D$ before (orange dots) and after RTA (red dots) denoted with the subscript 0 and A, respectively.

the same run). Moreover both N_2 or NH_3 can be employed. When NH_3 is used the HVPE chamber pressure enable H passivation of the acceptors similarly to MOVPE. Therefore annealings on passivated material (using NH_3), or unpassivated one (using N_2), are possible. By comparing the results one has direct access to the role of H passivation on the compensation. Furthermore, the depth dependence of the compensation was already presented in Sec. 2.4.5, suggesting a time dependent process (dynamical compensation). By means of HVPE annealings the entire layer is exposed to the same treatment and the process duration can be easily varied. Finally, HVPE constitutes an additional tool to compare the doping properties of NH_3 -MBE and MOVPE grown p -doped epilayers.

The results reported hereafter have all been obtained on samples annealed at $850^\circ C$ (using N_2 or NH_3) during 1 hour. Both higher and lower annealing temperatures were also investigated but are not presented here as they do not add significant information to the presented results. Intuitively, when a degradation was induced by the HVPE treatment, the higher the annealing temperature, the stronger the effect, indicating a thermally activated process. In Figs. 2.27(a) and (b) the annealing effect is reported for two MBE samples grown at $740^\circ C$. As shown in Sec. 2.4.2, samples grown by NH_3 -MBE always exhibit compensation upon annealing. In Fig. 2.27(a), annealing under NH_3 seems to reduce this effect with respect to N_2 . However the experimental results are scattered from one sample to another and little compensation was also obtained when using N_2 , as shown in Fig. 2.27(b). In general, a change in the net acceptor level below 30% was hardly observed for annealed MBE samples. This is not the case when the samples are grown by MOVPE (Figs. 2.27(c), (d), and (e)). Note that after HVPE annealing the samples are always activated before the ECV measurement to remove H passivation. When the doping is moderate (below $2 \times 10^{19} \text{ cm}^{-3}$), the annealing step has no effect on the $N_A - N_D$ level, which remains unchanged regardless the presence of hydrogen passivation or not. This is a strong indication that the HVPE thermal treatment does not introduce any additional

defects in this doping range. Consequently, samples grown by MBE have some specifics that are revealed during the annealing step. Considering the large amount of work published on the role of point defects [79, 98, 140, 141], we suggest that MBE-grown samples are strongly affected by point defects which can create complexes, such as Mg-V_N , during the annealing treatment. During MBE growth, the reduced growth temperature does not allow a considerable amount of complexes to be formed, provided that the doping is not too high. The absence of annealing induced compensation in MOVPE grown samples can be understood by the growth conditions closer to thermodynamic equilibrium combined with hydrogen passivation during growth, which keeps the Fermi level high, thus limiting V_N formation.

Three remarks need to be made: first, the experimental results are also compatible with a defect enhanced Mg diffusion leading to Mg-Mg cluster formation. Secondly, because of the lack of compensation before HVPE annealing, the defects considered here are not charged, meaning that if the defects are V_N , they must possess an uncharged configuration in GaN. Third, the point defect enhancement of the Mg interstitial configuration is another possibility, where Mg acts as a donor. For the three aforementioned cases, point defects are required to explain the differences in the experimental observations between MBE and MOVPE grown samples. In the following paragraphs we will focus the discussion on V_N .

Interestingly for MOVPE grown samples, when the doping is increased above $2 \times 10^{19} \text{ cm}^{-3}$ and for which decreasing $N_A - N_D$ profiles are observed, additional compensation arises from the HVPE annealing step as shown in Figs. 2.27(f) and (g). Moreover, the compensation is much higher when the annealing is performed under N_2 . When N_2 is used, the Fermi level position depends on the $N_A - N_D$ value of the as-grown sample. For the two samples corresponding to Figs. 2.27(f) and (g), E_F is low enough to promote the V_N formation during the thermal treatment. The increasing $N_A - N_D$ value along the epilayer thickness after annealing (red dots), is opposite to the evolution in the as-grown sample (black line). Therefore, the higher the initial net acceptor concentration, the stronger the annealing induced compensation is, in agreement with the V_N formation energy dependence to E_F . Below $N_A - N_D \approx 1.5 \times 10^{19} \text{ cm}^{-3}$, this effect becomes less pronounced, in line with the results shown in Fig. 2.27(e). These considerations are in agreement with the reduced annealing induced compensation observed in (g) with respect to (f), because of the already lower as-grown $N_A - N_D$ value of the latter sample.

On the other hand, when ammonia is used, the acceptor passivation allows keeping the Fermi level high during the annealing, thus limiting V_N formation and compensation. However, we have already discussed that $[\text{H}]$ in the p -doped layers saturates for high doping levels (Sec. 2.2.4). The lack of complete passivation, especially for high $[\text{Mg}]$, leaves a portion of acceptors unpassivated. When this happens, the generation of V_N during the annealing increases. In Fig. 2.27(g) a decrease in $N_A - N_D$ is observed close to the surface after annealing. The high $N_A - N_D$ values close to the surface of the as-grown sample (black line) result in the dip observed on the ECV profile after the HVPE annealing step. This is similar to the result obtained using N_2 and indicates the incomplete passivation at these high doping levels. A small difference is

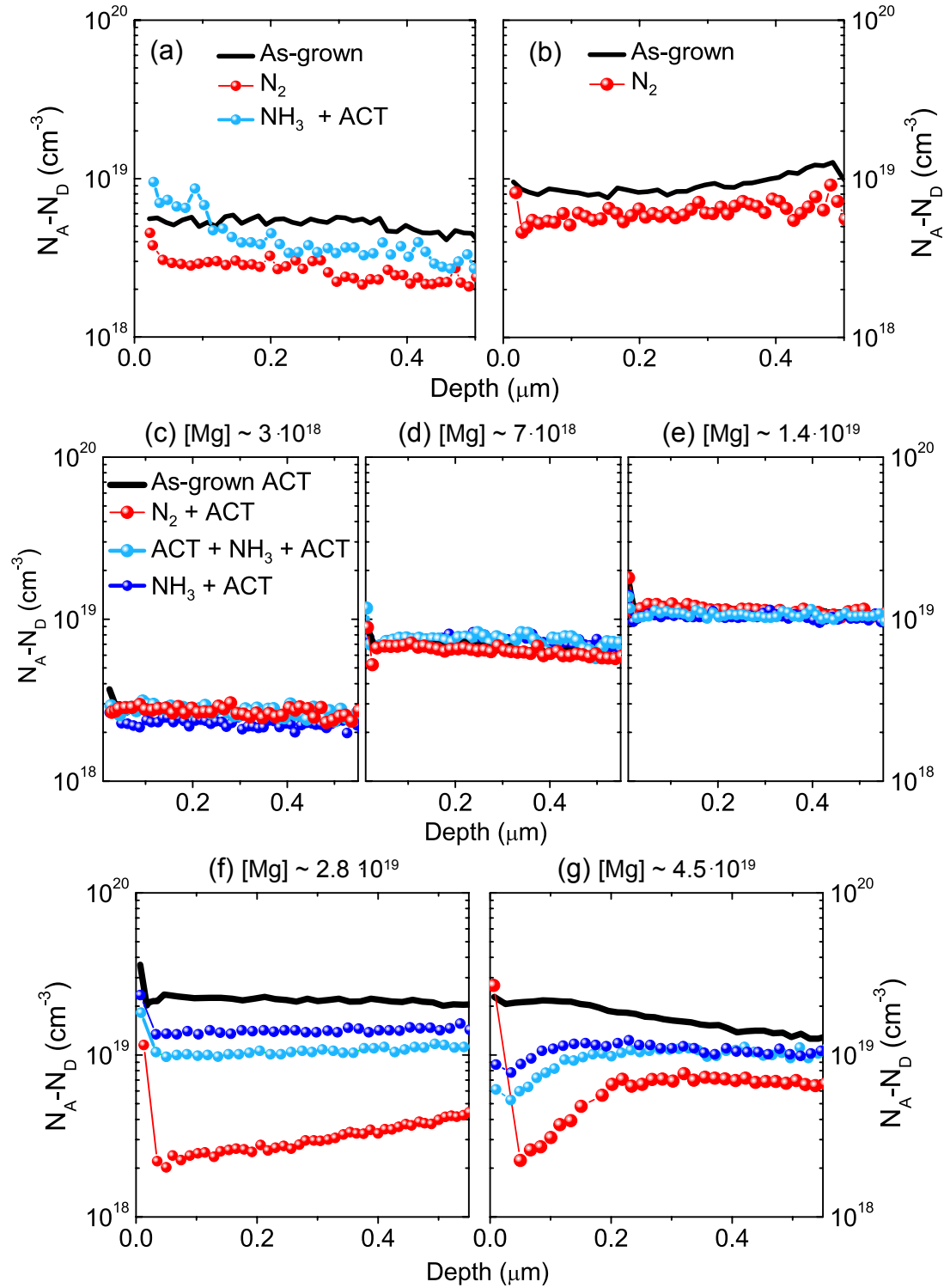


Figure 2.27: $N_A - N_D$ profiles for MBE grown samples (a) and (b), and MOVPE ones (c),(d),(e),(f), and (g), before and after an annealing step in HVPE performed at 850°C for 1 hour under N_2 or NH_3 atmosphere. The labels in (c) are valid for all MOVPE samples. ACT indicates sample activation by RTA.

observed in Figs. 2.27(f) and (g) between as-grown samples which have not been activated (dark blue dotted line), and samples activated prior to their introduction in the HVPE reactor (light blue dotted line). The activated samples, before being fully passivated again by NH_3 , exhibit much higher $N_A - N_D$ values leading to increased V_N formation during the short time period when passivation takes place, thus explaining the difference.

In addition it is interesting to notice that the decreasing $N_A - N_D$ profile of the as-grown sample becomes flat (Fig. 2.27(f)) after the HVPE treatment when using NH_3 . As we have previously discussed, the decrease of the $N_A - N_D$ profiles in as-grown samples results from the incomplete clustering of point defects (dynamical compensation). Close to the surface, the layer has not been kept long enough at high temperature to account for noticeable clustering. A homogenization of the clustering is thus observed along the epilayer thickness, giving rise to flat net acceptor profiles.

In conclusion [H] was shown to play a role on dopant compensation. For high [Mg], the annealing in H containing atmosphere (NH_3) induced reduced compensation compared to N_2 ones. However, because of limited H passivation for high [Mg] together with the incomplete clustering of point defects in these layers, the compensation process during the annealing could not be completely avoided. The annealing effect was also shown to be dependent on the $N_A - N_D$ profile, and not only on [Mg], supporting Fermi level arguments regarding p -type compensation processes. In fact, for $N_A - N_D < 1 \times 10^{19} \text{ cm}^{-3}$, no effect was observed upon annealing.

2.4.8 Mg doping of AlGaIn alloys

AlGaIn:Mg epilayers are fundamental building parts of LDs and UV LEDs. Both devices require increasing Al contents when moving to lower operation wavelengths. In addition, because of the reduction in refractive index contrast with respect to GaN for long wavelengths, green LDs may require cladding layers with increased Al compositions (with respect to 405 nm LDs) to efficiently confine the optical mode. However both the p -type doping and the achievement of low resistivity values for these alloys are challenging. The latter comes from the increasingly high ionization energy which increases together with the Al composition as shown in Fig. 2.2(b). Concerning the doping, precursors can cause parasitic reactions in the MOVPE reactor and, together with the increasingly dominant presence of nitrogen vacancies as Al increases [142], strongly affect the doping efficiency. Doping efficiencies of only 50% (referred to as electrical activity) were reported for MOVPE grown samples having 5 to 20% aluminium contents [76]. Unfortunately extensive C-V measurements have not been reported so far for these alloys and the drop in hole concentration has often been related only to an increase of the ionization energy.

In this context, p -type $\text{Al}_x\text{Ga}_{1-x}\text{N}$ layers with Al composition (x) up to 35% were grown to investigate the evolution of the dopant compensation as a function of x in NH_3 -MBE. The doping was kept below $2 \times 10^{19} \text{ cm}^{-3}$ to avoid initial compensation at high doping levels. The

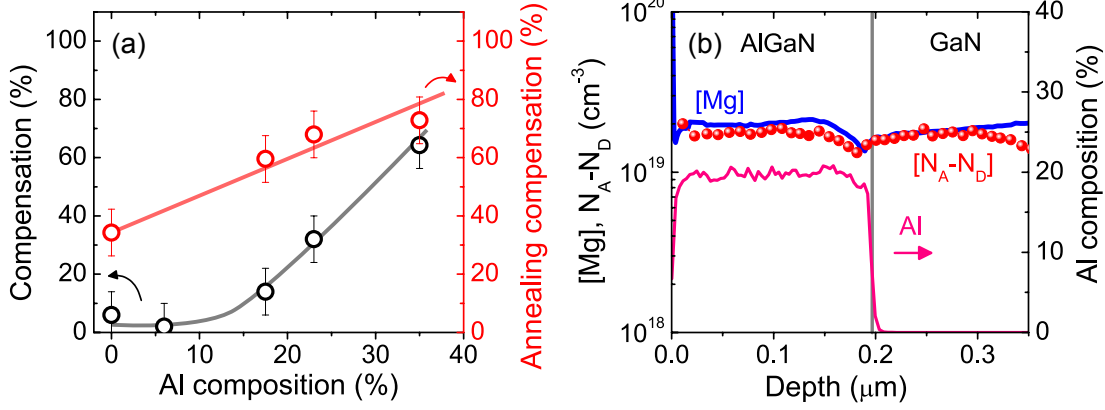


Figure 2.28: (a) Evolution of the acceptor compensation as a function of the Al composition for AlGa_{1-x}N layers grown using In as surfactant (black symbols). The compensation induced by the thermal annealing treatment is plotted as red symbols. Lines are guides to the eyes. (b) SIMS and ECV profiles of an Al_{0.18}Ga_{0.82}N sample showing low compensation despite the high Al composition. Note that the Al composition in (a) corresponds to the average value between SIMS and XRD measurements.

samples were grown at 740°C, at a growth rate of 0.4 ML/s, with 60 sccm of NH₃, and using In as a surfactant. The thickness of the AlGa_{1-x}N layers under investigation was chosen to avoid plastic relaxation. For this reason layers having $x > 20\%$ were sandwiched between GaN:Mg layers to avoid surface effects on the ECV and SIMS measurements given the reduced thickness. Two Ga cells were used to continuously grow GaN and Al_xGa_{1-x}N layers while keeping the growth rate unchanged, thus without performing growth interruptions to adjust the fluxes. The experimental data showed negligible C_{doping} values for compositions below 10% indicating close to 100% doping efficiency as shown by Fig. 2.28(a). For higher compositions, the compensation drastically increases reaching more than 60% for $x \approx 35\%$. The oxygen level was seen to increase in Al layers with respect to GaN, but without any clear relationship to the compensation nor Al composition.

The samples were also annealed during 1 hour under N₂ atmosphere at 850°C in the HVPE reactor. A compensation was observed, increasing with x (red circles in Fig. 2.28(a)). Therefore the doping stability of AlGa_{1-x}N alloys is inversely proportional to their Al composition. In the previous section we have seen that the thermal treatment does not introduce defects in GaN in this doping range. Provided that this holds for AlGa_{1-x}N alloys, the experimental results may indicate an increased concentration of point defects in as-grown samples as Al gets higher. In this case, for $x < 15\%$, the increased defect concentration may not be sufficient to provide noticeable clustering effects in as-grown samples. By further increasing x , the point defect concentration increase becomes evident even in as-grown samples, despite the low growth temperature.

In conclusion high quality *p*-doped AlGa_{1-x}N layers can be grown by MBE up to Al contents of 20%. Further tuning the experimental growth conditions may push the onset of strong

compensation to higher compositions.

2.5 Modeling of the compensation

We present in this section an empirical model which can be used to identify the best doping profile depending on the layer thickness and maximum [Mg] needed. This model clearly shows the actual limitations related to p -type doping and allows to anticipate the $N_A - N_D$ profile along epilayers with fixed [Mg]. During epitaxial growth, the dopant atoms supplied at the growth front are expected to incorporate stochastically on the gallium sites. When probing at the macroscopic level the dopant concentration (for example by SIMS) a constant concentration is always observed. However, at the microscopic level, the dopant atoms follow a random distribution centered around the macroscopic average value. It follows that microscopic Mg-rich regions can be formed even at moderate doping levels. Consequently, the Fermi level varies as well around the sample when microscopic regions are considered.

2.5.1 Net acceptors as a function of [Mg]

The model developed is based on a threshold Mg concentration above which all dopant atoms are fully compensated. The physical origin of this threshold separation is discussed at the end of this section. The dopant concentration is modeled having a normal distribution to take into account the stochastic Mg distribution, with a constant standard deviation independent on [Mg]. The standard deviation is considered to be constant for simplicity. By calculating the fraction of Mg atoms having a concentration below the threshold value for $1 \times 10^{18} \text{ cm}^{-3} < [\text{Mg}] < 2 \times 10^{20} \text{ cm}^{-3}$, the doping efficiency can be obtained as illustrated in Fig. 2.29. This can be performed by first calculating the cumulative distribution function (CDF or $\Phi(x)$), which can also be expressed in terms of the error function ($\text{erf}(x)$), for a standard normal distribution as:

$$\Phi(x) = \frac{1}{\sqrt{2\pi}} \int_{-\infty}^x e^{-t^2/2} dt \quad \text{and} \quad \Phi(x) = \frac{1}{2} \left[1 + \text{erf}\left(\frac{x}{\sqrt{2}}\right) \right]. \quad (2.7)$$

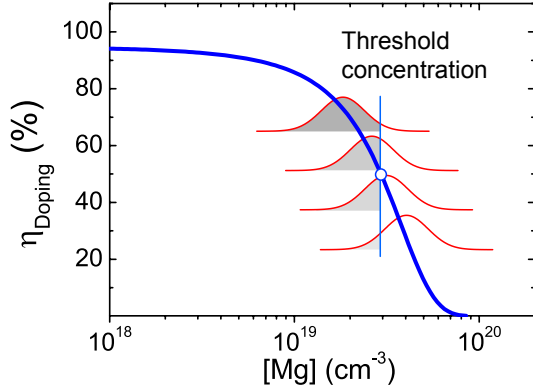
In the case of a general normal distribution with mean μ and standard deviation σ , the corresponding CDF is:

$$F(x) = \Phi\left(\frac{x-\mu}{\sigma}\right) = \frac{1}{2} \left[1 + \text{erf}\left(\frac{x-\mu}{\sigma\sqrt{2}}\right) \right]. \quad (2.8)$$

In fact the complement of the CDF, namely the Q -function, needs to be computed, indicating the fraction of atoms below the threshold concentration. It is given by:

$$Q(x) = 1 - F(x) = \frac{1}{2} - \frac{1}{2} \text{erf}\left(\frac{x-\mu}{\sigma\sqrt{2}}\right). \quad (2.9)$$

By fitting the experimental doping efficiencies expressed as a function of [Mg] (x value), μ



	$\mu (\times 10^{19} \text{ cm}^{-3})$	$\sigma (\times 10^{19} \text{ cm}^{-3})$
MOVPE	2.94	1.81
MBE S-Cell	3.50	4.93
MBE MgVCOR	7.08	4.49

Figure 2.29: Schematic representation of the modeling principle. The grey area indicates the fraction of dopants which are considered as acceptors.

Table 2.1: μ and σ values extracted from the fitting of the doping efficiency. S-Cell indicates the standard single filament effusion cell and MgVCOR the valved cell.

and σ can be found and are given in Table. 2.1. In our case μ corresponds to the threshold concentration while σ is the standard deviation of the Mg concentration distribution. The modeled doping efficiencies have already been shown in Figs. 2.19(b) and 2.21(b). Multiplying η_{doping} with $[\text{Mg}]$ gives the $N_A - N_D$ evolution as a function of $[\text{Mg}]$. In both cases, a good agreement is found between the modeled and experimental values as shown in Fig. 2.30.

Physically, the threshold concentration concept has different meanings depending on the compensation process considered, namely Mg-Mg cluster formation, Mg- V_N complex formation, or V_N assisted Mg interstitial formation. In the first case, its understanding is straightforward as it indicates the limit above which Mg atoms are sitting close enough in the lattice to form clusters by diffusion. In the second case, the threshold concentration can be related to a Fermi level, below which the probability of V_N formation and clustering with Mg is unity. The same treatment applies for Mg interstitial formation, where the V_N concentration leads to a unity probability of forming the interstitial configuration of Mg when $[\text{Mg}] > \mu$.

The μ values reported in Table. 2.1 are seen to vary depending on the growth technology and growth conditions. At this point this value is phenomenological because of the complex interplay between Mg and V_N .

2.5.2 Temporal/depth dependence

Note that the values plotted in Fig. 2.30 correspond to the half-thickness $N_A - N_D$ level due to the depth/time dependence of the acceptor compensation previously discussed. To account for the compensation occurring along the growth direction, the evolution of the threshold value μ can be considered as a function of growth time ($\mu(t)$). Indeed, for extremely short growth times, the compensation should be equal to the fraction of atoms above the solubility limit ($C_{solubility}$), thus $\mu(0) = C_{solubility}$, and possibly leading to PIDs. Given the above-mentioned

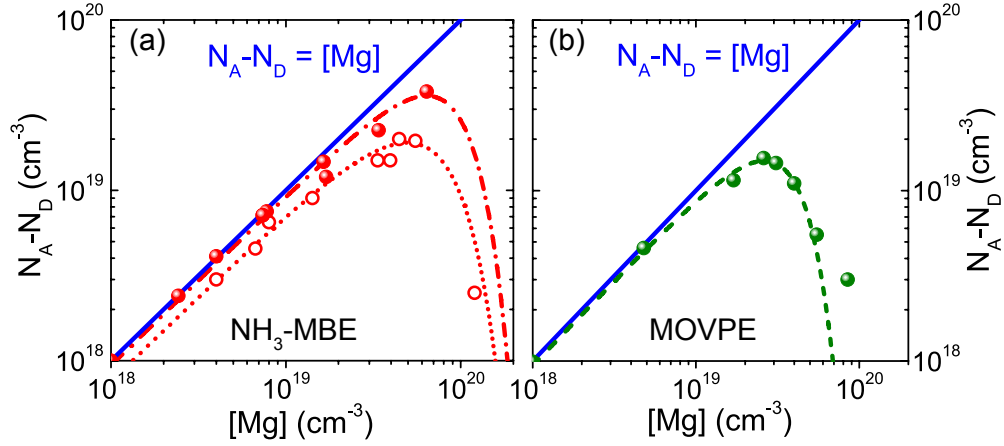


Figure 2.30: Net acceptor evolution as a function of $[Mg]$ for NH_3 -MBE (a), and MOVPE (b) grown samples. The dotted lines are obtained from the fitting of the doping efficiency values. In (a) the circles correspond to a growth temperature of $750^\circ C$ and standard cell doping, while the red dots indicate the samples grown at $740^\circ C$ using the valved cell.

clustering processes ($Mg-V_N$, $Mg-Mg$, or $Mg-V_N$ enhancing interstitial Mg formation), the average random walk of the species is considered and expressed for the 3D case as $\sqrt{6Dt}$. To calculate D , the μ values obtained from the Q -function fitting are used (Table. 2.1). First, from the threshold concentration values μ , the corresponding Wigner-Seitz radius (r_s) is calculated using:

$$r_s = \left(\frac{3}{4\pi\mu} \right)^{1/3} \quad \text{giving} \quad r_s^{MOVPE} = 2.01 \text{ nm}, \quad r_s^{S-Cell} = 1.90 \text{ nm}, \quad \text{and} \quad r_s^{VCOR} = 1.50 \text{ nm}. \quad (2.10)$$

This radius corresponds to the threshold separation between the species. Its time dependence is given by:

$$r_s(t) = \sqrt{6Dt} + r_{solubility} \quad \text{leading to} \quad D = \frac{(r_s - r_{solubility})^2}{6t_{\frac{1}{2}}}, \quad (2.11)$$

where $r_{solubility}$ is the radius associated with $C_{solubility}$ and $t_{\frac{1}{2}}$ is the half-thickness growth time which allows the calculation of D . Finally, a time dependent threshold concentration is obtained given by:

$$\mu(t) = \frac{3}{4\pi(\sqrt{6Dt} + r_{solubility})^3}, \quad (2.12)$$

Taking into account the solubility limit, or more generally a surface effect which may depend on the Mg accumulation, enables a much better fitting of the experimental values as shown in Fig. 2.31, for which a strong disagreement is found when $C_{solubility}$ is not considered.

This indicates that one simple compensation process does not fully account for the experi-

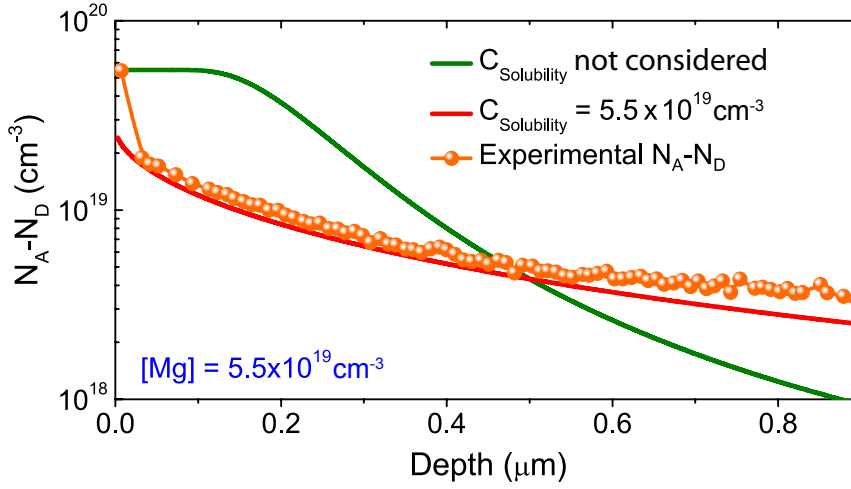


Figure 2.31: Modeled evolution of $N_A - N_D$ for an MOVPE grown sample as a function of the sample thickness taking into account $C_{solubility}$ values (red line) or not (green line).

mental observations but a combination of several processes is required. This can be related to the presence of both intrinsic and dynamical compensation in the layers. In this section the model is shown for MOVPE grown epilayers for which the literature is abundant. Close to the sample surface a deviation is observed between the modeled and experimental values. In this region the band bending can prevent the presence of a large number of positively charged defects (V_N) resulting in reduced clustering. The p -type doping in this region will be discussed for the realization of the device contact layers.

A contour plot was created using the MOVPE $N_A - N_D$ profiles to compare the model with the experimental results. The two plots are shown in Fig. 2.32. The agreement between the two is striking. Both show that above $[Mg] \approx 3 \times 10^{19} \text{ cm}^{-3}$, the net acceptor value decreases, especially for thick samples. Furthermore, the thinner the sample, the higher average $N_A - N_D$ value can be obtained for constant $[Mg]$. By increasing the growth rate the same effect should be obtained. The model, when including the time dependence, is only based on the fitting of the doping efficiency values and on the $C_{solubility}$ determination, no other fitting parameters are necessary. For the net acceptor maps shown in Fig. 2.32(a) and (c), $C_{solubility} = 5.5 \times 10^{19} \text{ cm}^{-3}$.

In conclusion an empirical model accounting for both $[Mg]$ and time/thickness dependence of the acceptor compensation was developed in agreement with the experimental data. A discrepancy is observed in the surface region suggesting different compensation kinetics. In addition, for high doping values, when the compensation is extremely high, a deviation is also observed (Fig. 2.30(b)) arising from the sensitivity to modeling errors at these high compensation levels.

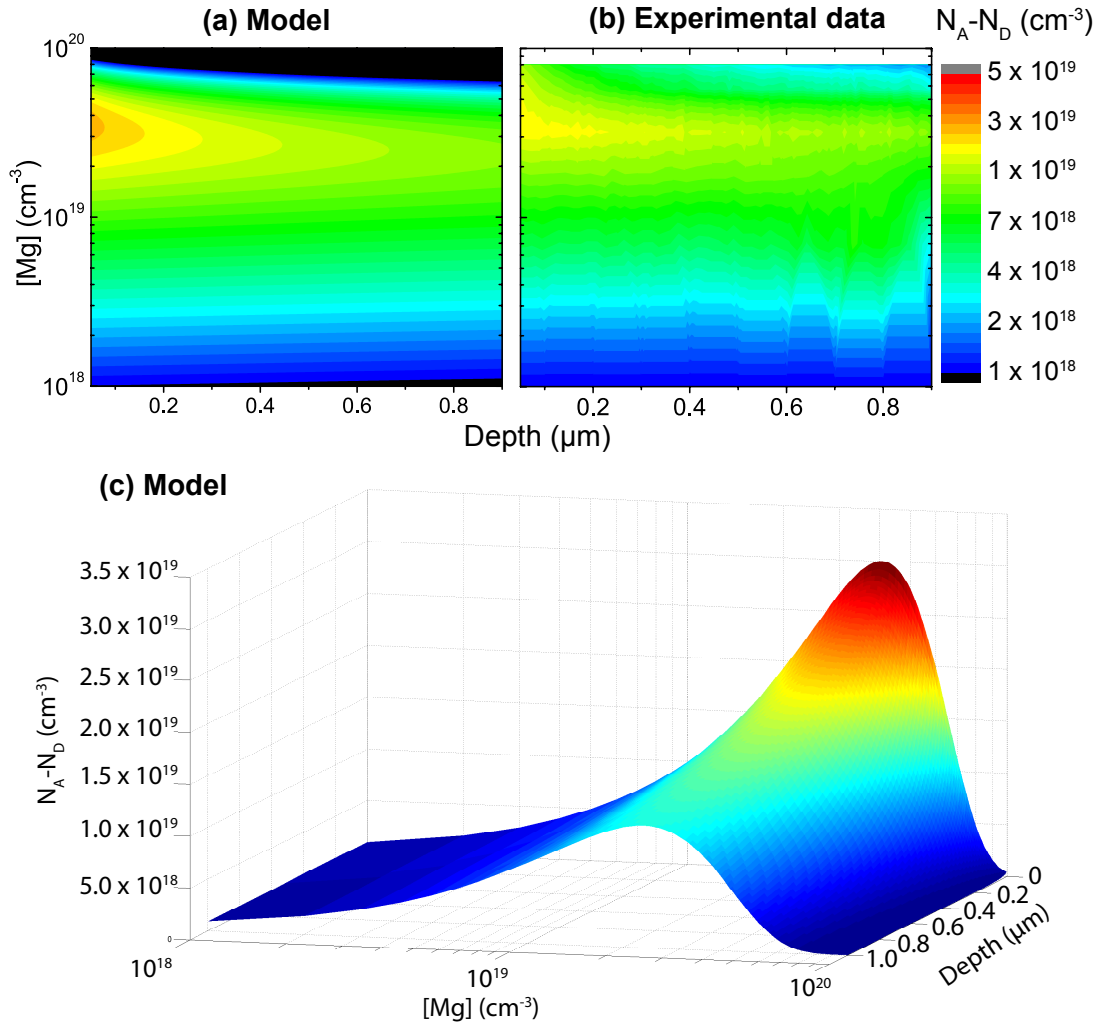


Figure 2.32: Comparison between (a) the model and (b) the experimental data. In (a) and (b) the first 50 nm are not shown as they cannot be modeled with the same approach. (c) 3D map of the modeled acceptor compensation as a function of measurement depth and [Mg].

2.6 Summary

In this chapter the optimization of the *p*-type doping by NH₃-MBE was discussed. A set of growth parameters were identified. Low growth temperatures around 740°C, moderate V/III ratios, and high growth rates, lead to epilayers exhibiting excellent doping characteristics. The use of In as a surfactant was also studied. The optimization resulted in high $N_A - N_D$ levels, suitable for LDs and TJs as presented in the next chapters.

Thanks to ECV profiling, several intriguing aspects related to the *p*-type doping of GaN layers were highlighted. First, the evolution of the net acceptor concentration along the sample thickness for high [Mg] levels was shown for both MBE and MOVPE. Secondly a decrease in the $N_A - N_D$ values was observed when annealing NH₃-MBE grown *p*-doped epilayers in a HVPE

reactor already for moderate doping levels ($[Mg] < 1 \times 10^{19} \text{ cm}^{-3}$). MOVPE grown samples did not show the same trend, and the net acceptor profiles remained unchanged upon thermal treatment in this doping range. This was attributed to higher point defect concentrations in MBE grown p -doped samples, leading to compensation only when the sample temperature is sufficiently high, indicating a thermally activated process. In view of this result we consider that the low growth temperatures in the MBE reactor prevent the compensation process up to high $[Mg]$ values. For $[Mg] > 2 \times 10^{19} \text{ cm}^{-3}$, the thermal annealing treatment degraded the doping properties of MOVPE epilayers as well. The degradation was shown to depend both on the annealing gas and on the actual $N_A - N_D$ value along the layer. These results were explained by Fermi level arguments and by hydrogen passivation effects on the latter, again indicating that point defects play a role on dopant compensation.

Concerning hydrogen, its incorporation in NH_3 -MBE was largely discussed. It was shown that H does not passivate the Mg acceptor despite the use of ammonia. However Mg doping was shown to be accompanied by $[H]$ increase. The possibility to introduce H passivation in MBE was also investigated thanks to the use of a plasma formed from a mixture of H_2 and N_2 . For this sample, an activation step (RTA) was required to reach low compensation values, indicating H passivation. The reduction of the compensation by H passivation highlights once more the role of the Fermi level on the p -type doping.

The doping of AlGaIn alloys was also discussed. AlGaIn layers with compositions up to 20% could be grown exhibiting compensation values below 20%. For higher Al compositions, the layers exhibit higher point defect concentrations.

Finally an empirical model was developed and presented to account for both the $N_A - N_D$ dependence on $[Mg]$ and on the depth/time of growth. The model clearly shows that higher $N_A - N_D$ values can be obtained for short growth times. It also indicates the need for tailoring the doping profiles along the sample thickness to obtain the best average net acceptor values.

Further work should focus on the Fermi level control either by increasing the hydrogen passivation for high doping levels, or through above bandgap sample illumination during growth. The latter approach has been proposed by Hoffmann *et al.* [143].

3 Devices I: Hybrid laser diodes

In this chapter the realization of hybrid LDs on *c*-plane substrates, combining MOVPE and NH₃-MBE growth techniques is discussed. First, a brief overview of the issues related to long wavelength LDs together with the theoretical working principle are presented. Secondly, the electrical characteristic of NH₃-MBE *p*-doped layers are presented. The results obtained on hybrid violet LDs are then shown in combination with the challenges related to the hybrid scheme. Finally a large section related to the properties of the hybrid green LDs realized during this thesis will conclude this chapter.

3.1 Lasing in semiconductor LDs

The term laser stands for light amplification by stimulated emission of radiation. In the following pages, the working principles of QW-based LDs are described. In a 2D quantum system, *i.e.* in a QW, the allowed energy levels are quantized, giving rise to subbands separated from the conduction or valence band by a confinement energy e_i and hh_j , for electrons and holes, respectively. The confinement energies are inversely proportional to L^2 (simple case of an infinite potential well), the QW thickness squared, and the indices i and j are integers corresponding to the subband confined level number for the two carriers respectively. The dispersion relation for the two subbands when considering the first confined level in the parabolic band approximation writes:

$$e(hh)_1(k_{\parallel}) = e(hh)_1 + \frac{\hbar^2 k_{\parallel}^2}{2m_{e(hh)}} , \quad (3.1)$$

where k_{\parallel} is the wavevector and $m_{e(hh)}$ is the effective mass of the electron (hole). Thus the photon energy for a transition between conduction subband n and valence subband m is given by:

$$\hbar w = E_g + e_i + hh_j + \frac{\hbar^2 k_{\parallel}^2}{2m_r} , \quad (3.2)$$

where E_g is the semiconductor bandgap and $m_r = \left(\frac{1}{m_e} + \frac{1}{m_{hh}}\right)^{-1}$ is the reduced effective mass. The density of states for a 2D system (ρ_{2D}) as a function of energy $\hbar\omega$ writes:

$$\rho_{2D,e(hh)}(\hbar\omega) = \frac{m_{e(hh)}}{\pi\hbar^2} \sum_{i(j)=1}^{\infty} \theta(\hbar\omega - e(hh)_{n(m)}), \quad (3.3)$$

where θ is the Heaviside function which is used to reproduce the step-like density of states of such system. The absorption coefficient (α) when only the first subbands $i = j = 1$ are considered is given by:

$$\alpha(\hbar\omega) = -g_m(\hbar\omega) = \alpha_{2D} [f_v^1(\hbar\omega) - f_c^1(\hbar\omega)] \theta(\hbar\omega - E_g - e_1 - hh_1), \quad (3.4)$$

where α_{2D} is the carrier-free absorption coefficient of the QW, f_c^1 and f_v^1 are the Fermi-Dirac distributions for the first conduction and valence band, respectively, and g_m is the material gain. α_{2D} is given by [31]:

$$\alpha_{2D} = \frac{2\pi q^2 x_{vc}^2 m_r}{\lambda_0 n_{sc} \epsilon_0 \hbar^2 d}, \quad (3.5)$$

where $x_{vc}^2 = \frac{1}{3} \frac{\hbar^2 E_p}{E_g^2 m_0}$ is the dipolar matrix element with E_p the Kane energy, λ_0 the emission wavelength in vacuum, d the QW thickness, and n_{sc} the refractive index of the material forming the QW. The Fermi level distributions in the first subband are given by:

$$f_c^1(\hbar\omega) = \frac{1}{1 + \exp(\beta(E_c^1 - E_{Fc}))}, \quad (3.6a)$$

$$E_c^1(\hbar\omega) = E_g + e_1 + \frac{m_r}{m_e}(\hbar\omega - E_g - e_1 - hh_1), \quad (3.6b)$$

$$f_v^1(\hbar\omega) = \frac{1}{1 + \exp(\beta(E_v^1 - E_{Fv}))}, \quad (3.6c)$$

$$E_v^1(\hbar\omega) = -hh_1 + \frac{m_r}{m_{hh}}(\hbar\omega - E_g - e_1 - hh_1), \quad (3.6d)$$

where $\beta = 1/k_B T$. From Eqn. (3.4) the relationship between absorption and gain is evident. Negative absorption values correspond to photon amplification, *i.e.* gain and positive g_m . When $f_v^1(\hbar\omega) - f_c^1(\hbar\omega) = 0$, hence $E_{Fc} - E_{Fv} = E_g + e_1 + hh_1$ the QW absorption is zero and the transparency condition reached. If the difference between the quasi-Fermi levels is further increased, the photons in the QW will be amplified by stimulated emission and the Bernard-Duraffourg condition is fulfilled, which writes:

$$E_{Fc} - E_{Fv} \geq \hbar\omega \geq E_g + e_1 + hh_1. \quad (3.7)$$

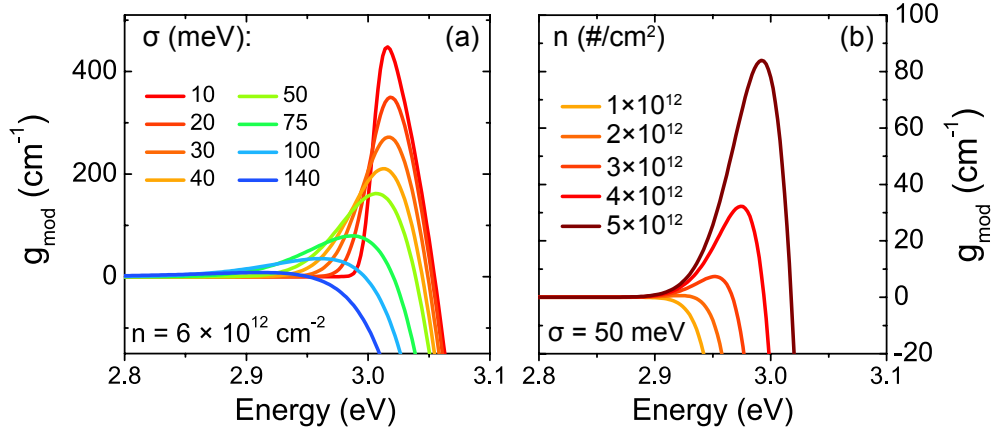


Figure 3.1: Evolution of the modal gain (g_{mod}) as a function of (a) the inhomogeneous broadening (σ) and (b) the electrically injected carrier density (n) for an InGaN/GaN QW. See text for details.

The quasi-Fermi levels (E_{Fc} and E_{Fv}) can be easily calculated when considering a constant 2D density of states for the transition between the first levels using:

$$E_{Fc} = E_g + e_1 + k_B T \ln \left[\exp \left(\frac{n}{n_c} \right) - 1 \right], \quad (3.8a)$$

$$E_{Fv} = -hh_1 - k_B T \ln \left[\exp \left(\frac{n}{n_v} \right) - 1 \right], \quad (3.8b)$$

where n is the carrier density and n_c and n_v are the 2D critical carrier densities for the conduction and valence band, respectively, given by the product of the electron/hole density of states times $k_B T$. To account for the inhomogeneous broadening, when the QWs exhibit alloy fluctuations and interface disorder, the density of states can no longer be considered constant but instead writes [144, 145]:

$$\rho_{2D,e}(\hbar\omega) = \frac{m_e}{\pi\hbar^2} \left[\frac{1}{2} + \frac{1}{2} \operatorname{erf} \left(\frac{\hbar\omega - E_g - e_1}{\sqrt{2}\sigma} \right) \right], \quad (3.9a)$$

$$\rho_{2D,hh}(\hbar\omega) = \frac{m_{hh}}{\pi\hbar^2} \left[\frac{1}{2} + \frac{1}{2} \operatorname{erf} \left(\frac{\hbar\omega - hh_1}{\sqrt{2}\sigma} \right) \right], \quad (3.9b)$$

where σ corresponds to the inhomogeneous broadening. In fact, in Eqs. (3.9(a) and 3.9(b)) the Heaviside function is replaced by an error function which corresponds to the convolution of Gaussian and Heaviside functions. In this context the quasi-Fermi levels need to be calculated, to evaluate gain/absorption, from the expressions:

$$n = \int_{-\infty}^{+\infty} \rho_{2D,e} f_c^1(E) dE, \quad (3.10a)$$

$$n = \int_{-\infty}^{+\infty} \rho_{2D,hh} (1 - f_v^1(E)) dE, \quad (3.10b)$$

were n is the electrically injected carrier density. The introduction of inhomogeneous broadening leads to gain dilution, especially for high σ values, as shown in Fig. 3.1(a) for constant carrier densities. This is detrimental for device operation since it leads to increased threshold currents as discussed in the following paragraphs. It also redshifts the gain maximum, because of the introduction of tail states in the bandgap.

In a LD structure, the optical mode section overlapping with the gain region (the QWs) experiences gain, and is defined by the optical confinement factor (Γ):

$$\Gamma = \frac{\int_{-d/2}^{+d/2} |E(z)|^2 dz}{\int_{-\infty}^{+\infty} |E(z)|^2 dz}, \quad (3.11)$$

where $E(z)$ is the field distribution along the growth direction, and d is the active region thickness. Indeed, only a fraction of the photons experiences gain. Thus the modal gain (g_{mod}) parameter is introduced to account for the effective gain in the cavity. It writes:

$$g_{mod} = \Gamma g_m, \quad (3.12)$$

Whenever g_{mod} is positive, amplification in the cavity takes place. In order to get lasing, both the internal (α_i), and the mirror losses (α_m) need to be overcome. The lasing condition thus writes:

$$\Gamma g_{m,th} = g_{mod,th} = \alpha_i + \frac{1}{2L} \ln \left(\frac{1}{R_1 R_2} \right), \quad (3.13)$$

where the index $_{th}$ stands for threshold, L is the cavity length, and R_1 and R_2 are the mirror reflectivities for the front and rear facet, respectively. The last term in Eq. 3.13 corresponds to α_m . The internal losses can be due to deep level absorption, scattering losses introduced by the ridge-waveguide geometry and from free carrier absorption, especially in the case of p -type material [146]. The overlap of the optical mode with the lossy regions needs to be taken into account for α_i determination as well [147]. In the logarithmic approximation of the gain evolution as a function of carrier density, g_m can be expressed as:

$$g_m(n) = g_0 \ln \left(\frac{n}{n_{tr}} \right) \quad \text{and Eqn. 3.13 is rewritten as:} \quad \Gamma g_0 \ln \left(\frac{n_{th}}{n_{tr}} \right) = \alpha_i + \alpha_m, \quad (3.14)$$

where n_{tr} is the carrier density at transparency ($\alpha = g_m = 0$) and g_0 is the gain coefficient. Finally, the laser threshold current density can be written as [148]:

$$J_{th} = \frac{n_{tr} q d}{\eta_i \tau} \exp \left(\frac{\alpha_i + \alpha_m}{\Gamma g_0} \right), \quad (3.15)$$

where d is the active region thickness, η_i the internal quantum efficiency (IQE), and τ is the carrier lifetime. In Eqn. (3.15) the η_i and τ values used are the ones corresponding to the transparency condition. In fact, the prefactor before the exponential term corresponds to the transparency current density (J_{tr}). On the other hand, the differential efficiency η_d is given by:

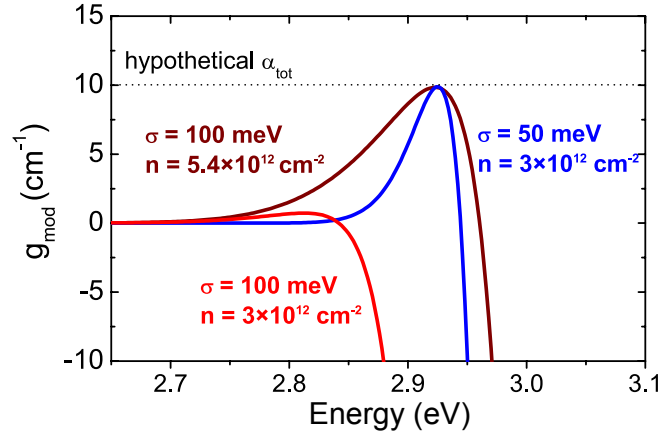


Figure 3.2: Comparison of the gain curves for σ values of 50 meV (blue curve), and 100 meV (red and brown curves).

$$\eta_d = \frac{\eta_i \eta_{inj} \alpha_{out}}{\alpha_m + \alpha_i} \quad \text{with} \quad \eta_d = \frac{q}{\hbar \omega} \eta_s, \quad (3.16)$$

where η_{inj} is the injection efficiency, α_{out} is the loss associated to the outcoupling mirror, and η_s is the slope efficiency. Depending on the application, α_{out} can be varied. For example, in high power LDs it is preferable to coat the front facet with an anti-reflective coating, to maximize the output power. In other cases, when the threshold current needs to be reduced, high reflectivity coatings are used, lowering both J_{th} and η_s .

The effect of varying σ on the gain curves is also shown in Fig. 3.2. When σ is increased, at the same carrier density the gain value is redshifted but also considerably lowered (blue vs red curve). In order to reach the same maximum g_{mod} for lasing, the carrier density must be strongly increased for high σ values (brown curve). This blueshifts the gain maximum and no substantial difference is obtained in terms of lasing wavelength. In terms of threshold current, the higher σ values lead to higher threshold currents. Therefore it is clear that the redshift arising from the increased density of tail-states is not a viable solution to increase the lasing wavelength of green LDs.

The modal gain in Figs. 3.1 and 3.2, is calculated for a 3×4.5 nm thick InGaN/GaN multiple-QW (MQW) structure using a confinement factor of 5% and a bandgap energy of 2.94 eV. The MQW is considered to be under flat band conditions. In these calculations, performed on active regions with doped barriers and for large carrier densities, the polarization fields are assumed to be screened and the transition matrix element constant [145]. A more rigorous treatment should consider a Schrödinger-Poisson solver to calculate the potential profile of the QW(s) under optical injection and to evaluate both the transition energy and the matrix element as a function of the carrier number. Much more pronounced blue-shift is expected.

3.2 Green laser diodes: a challenging spectral region

In 2009, the lasing wavelength of III-nitride based devices overcame the 500 nm limit [149, 150]. During the last five years, a remarkable effort was put into the development of long-wavelength AlInGaN-based LDs with the primary objective to realize efficient direct green LDs that could be used in compact RGB laser projection systems. The achievement of lasing in the 515–536 nm spectral range was demonstrated by several groups on polar [9, 151] or semipolar [8, 152–155] crystal orientations with a continuous improvement in the device performance. However the only commercially available devices are on *c*-plane orientation. All these devices were grown by MOVPE, in line with the InGaN based LED industry. Lasing in the green spectral range was achieved thanks to drastic improvement in the material gain of In-rich QWs, which nowadays matches well the values measured in QWs designed for blue emission [148]. The problems to solve are the followings: to emit beyond 500 nm, the InGaN QW must possess an In composition higher than 25% [151]. Because of the high lattice mismatch with respect to GaN, defect-free material is difficult to obtain and the QW thickness is limited [156]. The incorporation of such high molar fractions also requires the reduction of the growth temperature which promotes the formation of non-radiative recombination channels such as point defects. Furthermore, when increasing the In composition, the compositional broadening of the alloy is expected to increase because of random composition fluctuations. Phase separation may also add up to this effect, eventually leading to gain dilution. In addition, given the large lattice mismatch, the magnitude of the polarization fields is much higher in these structures when compared to blue, or violet LDs [157], thus decreasing the wavefunction overlap. Finally, given the reduced QW thickness, the carriers are more sensitive to the disorder at the QW interfaces, which further increases the inhomogeneous broadening and leads to reduced gain values.

3.2.1 Thermal budget reduction

While the majority of the above-mentioned challenges can be overcome by optimizing the active region structure and growth conditions, the thermal instability of the InGaN alloy expressed by phase separation, or more in general by regions exhibiting increased non-radiative recombinations, requires specific cares. In fact, while initially of excellent quality, high indium ($x_{In} > 25\%$) content QWs were shown to degrade when subjected to an annealing temperature above 900°C [158–160]. For this reason the growth temperature of the subsequent waveguiding and cladding layers must be low enough to avoid QW degradation, which results in a dramatic decrease in the internal quantum efficiency and in an increased non uniformity of the emission pattern. This effect can be clearly revealed in fluorescence images, where a high density of dark spots indicates the presence of degraded QW regions [161] as shown in Fig. 3.3. In short wavelength devices the *p*-type GaN is generally grown at a temperature over 1000°C by MOVPE to guarantee excellent electro-optical performance. Since all the reports on long wavelength ($\lambda > 500$ nm) AlInGaN based LDs employed MOVPE growth technology, even if scarcely discussed, it is reasonable to believe that the growth temperature of the *p*-doped

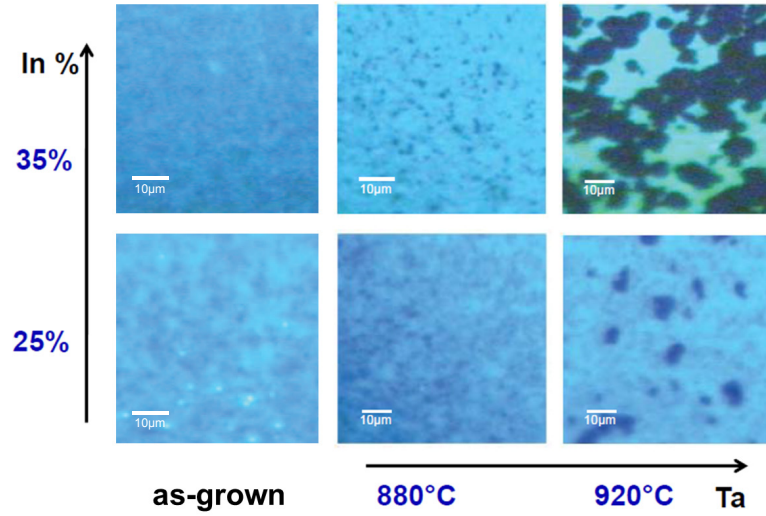


Figure 3.3: Fluorescence images under high excitation showing the degradation of InGaN double QWs as a function of In content and annealing temperature (T_a) after a 2 hour long annealing step in HVPE. Courtesy of N. A. K. Kaufmann (EPFL).

layers has been efficiently reduced below 900°C to reach wavelengths beyond 500 nm. One report has shown the possibility to decrease this temperature down to 840°C while using MOVPE [159]. At present, the impacts of such a low growth temperature on the electrical (conductivity), optical (internal losses), and morphological characteristics of these layers are still unclear and the I - V characteristics obtained from green LDs always exhibit higher series resistance with respect to standard 405 nm LDs. Other approaches were also investigated to mitigate the thermal impact on the active region. Above all, researchers from Nichia proposed the use of indium tin oxide (ITO) to complete the top cladding layer, benefiting from its low refractive index, high conductivity, and low deposition temperature [162]. This approach has been attempted as well at the University of California at Santa Barbara (UCSB) [163].

The effort put in the thermal budget reduction indicates that the growth temperature of the p -type layers might still be one of the limiting parameters to extend the lasing wavelength even beyond the green spectral range. Indeed, further decreasing this temperature might be challenging by MOVPE because of reduced Mg incorporation [85], reduced precursor cracking, and increased carbon and oxygen incorporation [164]. The thermal-degradation problem could be effectively tackled by exploiting the intrinsic low growth temperature of MBE for which high quality p -type doping can be achieved below 750°C , as shown in the previous chapter. At the same time we will demonstrate that state-of-the-art electrical characteristics and low carbon and oxygen contamination can also be obtained. The growth temperature window is 100°C lower than the lowest reported MOVPE value, and 300°C lower if compared with the optimal MOVPE doping temperature [160]. Moreover, NH_3 -MBE benefits from stable nitrogen rich conditions which relieve the growth complexity of PAMBE.

3.2.2 Optical confinement

Another issue arising in long wavelength InGaN based LDs is the decrease in the refractive index contrast between the waveguide and the cladding layers for energies much lower than the (Al)GaN bandgap [165]. Because of the low critical thickness and reduced material gain values exhibited by green QWs (especially in academic laboratories), high vertical confinement factors are required to increase the modal gain. This is in conflict with the reduced refractive index contrast, meaning that special designs need to be considered. Increasing the Al content of the cladding layers only is not viable as it would further increase the tensile strain in the structure eventually leading to crack formation for the case of *c*-plane devices. Thus the strain management becomes critical when using Al containing cladding layers. To mitigate the tensile strain, the use of quaternary alloys has been shown by researchers from Sumitomo Electric Industries [166]. The composition control in such layers is however extremely complicated. AlInN lattice matched to GaN could also be employed, but the difficulties related to the *p*-type doping are still preventing its use [167]. Another option is to adopt InGaN waveguides, a solution used in all the published works related to green LDs. In this case as well, the amount of In is limited by the compressive strain generated and relaxation must be avoided.

A strong optical confinement is not only needed to increase the modal gain of the device, but also to reduce losses generating from the *p*-doped layers and from absorption in the *p*-metal contact. Furthermore the bottom cladding on the *n*-side of a LD must be designed in a way to prevent photon leakage to the substrate, leading to substrate modes and additional losses [168].

Researchers at UCSB have demonstrated AlGaIn-cladding free green LDs thanks to relatively high In mole fractions in the InGaIn waveguide [169, 170]. With respect to Al-containing layers, the *p*-GaIn cladding can be grown at a much higher growth rate in MOVPE, resulting in a shorter high temperature exposure of the active region, but at the expense of the optical confinement factor. By PAMBE as well, AlGaIn-cladding free LDs have been demonstrated [171], lasing up to 482 nm in CW operation [172]. Notice that a detailed discussion about the waveguide and cladding layer design can be found in Refs. [168, 173].

3.3 Growth approach

In this work, the combination of active regions exhibiting high IQE grown by MOVPE, with *p*-doped layers grown at low temperature by NH₃-MBE, was attempted for the realization of LDs. This approach is referred to as hybrid, and the so-formed devices are called hybrid LDs. The exact location where the MOVPE growth was stopped varied along this thesis. The first devices fabricated featured an electron blocking layer (EBL) grown by MOVPE. However, the best characteristics were successively obtained on devices where the totality of the *p*-doped regions, namely electron blocking, waveguide, cladding and contact layers, were grown by NH₃-MBE.

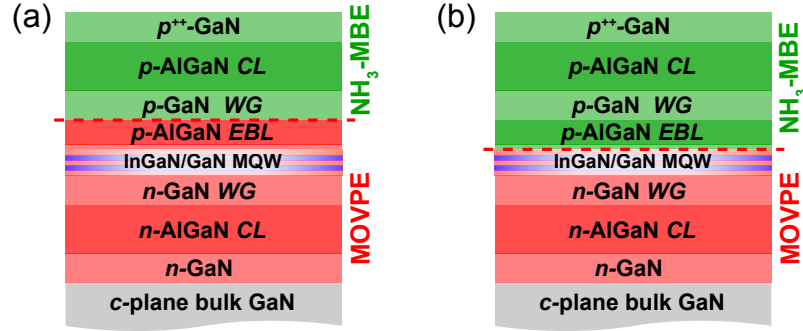


Figure 3.4: Hybrid sample structure for the samples (a) featuring the EBL grown by MOVPE, (b) where the whole p -doped layers are grown by MBE. *CL* and *WG* stand for cladding and waveguide layers, respectively. The red dashed line indicates the regrowth interface.

3.4 Transfer method

In order to heat the samples in the MBE reactor, the wafers are generally coated on the backside with molybdenum (Mo) or titanium (Ti), which absorb the radiation generated by the heater. In our case, 1 μm thick Mo layers are generally sputtered using either a Pfeiffer SPIDER 600 cluster system or a Balzer BAS 450 single chamber system.

However, this step was considered an important source of contamination when attempting the realization of hybrid LDs. We therefore developed an alternative approach during this thesis. In fact, the strong intentional impurity concentration in the FS GaN substrates used for the LD growth, provides absorption by free-carriers of the infrared heater radiation. Therefore, when using these substrates, it is possible to avoid the coating on the backside.

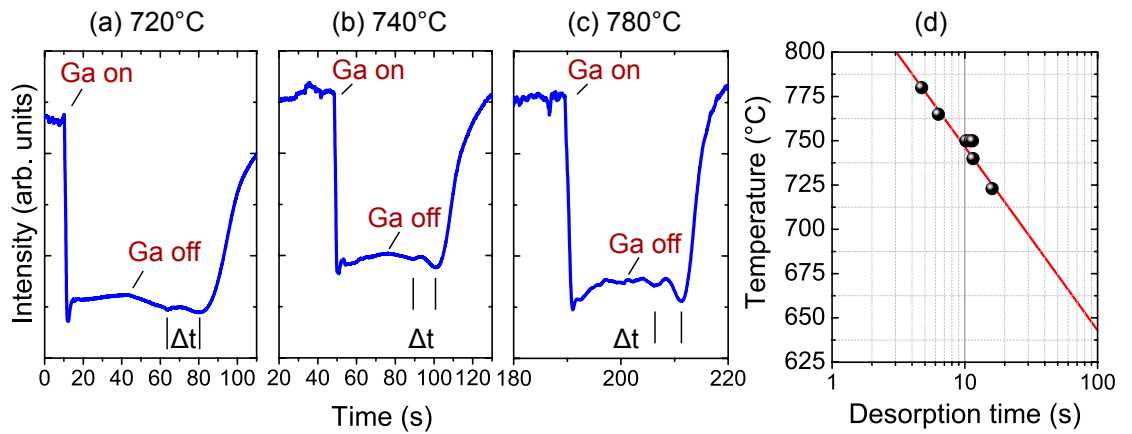


Figure 3.5: (a), (b), and (c) show the RHEED specular beam intensity as a function of time at temperatures of 720, 740, and 780 °C. (d) Evolution of the desorption time as a function of the growth temperature.

To calibrate the surface temperature to the heater power, Ga desorption time was investigated. When the backside of the wafer is coated with Mo, the growth temperature is measured by optical pyrometry calibrated on the emissivity of Mo. By supplying Ga in the absence of ammonia, the latter can accumulate on the surface, provided that the impinging flux is higher than the desorption rate. When the Ga supply is stopped, the accumulated atoms on the surface start to desorb, leading to RHEED oscillations when the last two monolayers leave the surface. The desorption time (Δt) can thus be measured and related to the temperature measured by optical pyrometry. When the FS GaN wafer is placed in the reactor, the temperature can be determined by measuring the desorption time at fixed heater power. In Fig. 3.5 the specular beam intensity is plotted as a function of time for three temperatures. The desorption time of one monolayer corresponds to two successive minima indicated in the graph by Δt . In this way, a Δt value of 12 s was associated to the growth temperature of 740 °C.

The calibration allowed the direct transfer of the LD structures on Mo free substrates from the MOVPE to the MBE reactor, limiting the exposure to unwanted impurities possibly contaminating the sample. In this way, the samples were exposed to the atmosphere only during the loading in the MBE.

3.5 Electrical characteristics of p - n junctions

Here we report on the electrical characteristics obtained on NH_3 -MBE grown homojunctions and hybrid LEDs. This represented the first test bed for the p -type layers grown by NH_3 -MBE. Standard Pd/Au and Ti/Al/Ti/Au contacts were used for the top p -type electrode and bottom n -type electrode, respectively. Mesas were formed by optical lithography to contact n -type material, without particular attention in optimizing the current spreading, as discussed in the next chapter.

For the three homojunctions shown in Fig. 3.6, the thickness of the p -doped GaN layers was 500 nm, which compares well with the thickness of blue-violet LD top claddings. The doping in the bulk region was kept in the vicinity of $1 \times 10^{19} \text{ cm}^{-3}$, while during the deposition of the last 50 nm, the Mg cell temperature was augmented to increase the [Mg] level near the contact layer. The effect of increasing the doping in the contact layer on the I - V characteristics is striking: the series resistance (R_s) decreases, allowing reduced forward voltages as shown in Fig. 3.6. The depletion width reduction in the contact layer (discussed in Sec. 1.4.2) allows for increased carrier tunneling between the metal and the semiconductor, thus lowers the contact resistance. Interestingly, similarly to MOVPE, the $N_A - N_D$ value in the contact layer exceeds the net acceptor levels achievable for bulk layers. In fact, the growth conditions employed for growing the homojunctions do not allow reaching $N_A - N_D$ levels higher than $2 \times 10^{19} \text{ cm}^{-3}$ (Fig. 2.18) in thick samples, suggesting reduced compensation in the surface layer.

The electrical quality of the homojunctions indicated the possibility to obtain state-of-the-art I - V characteristics by NH_3 -MBE, provided the the doping profile is accurately controlled, as the results compared well with MOVPE grown p - n junctions measured under the same

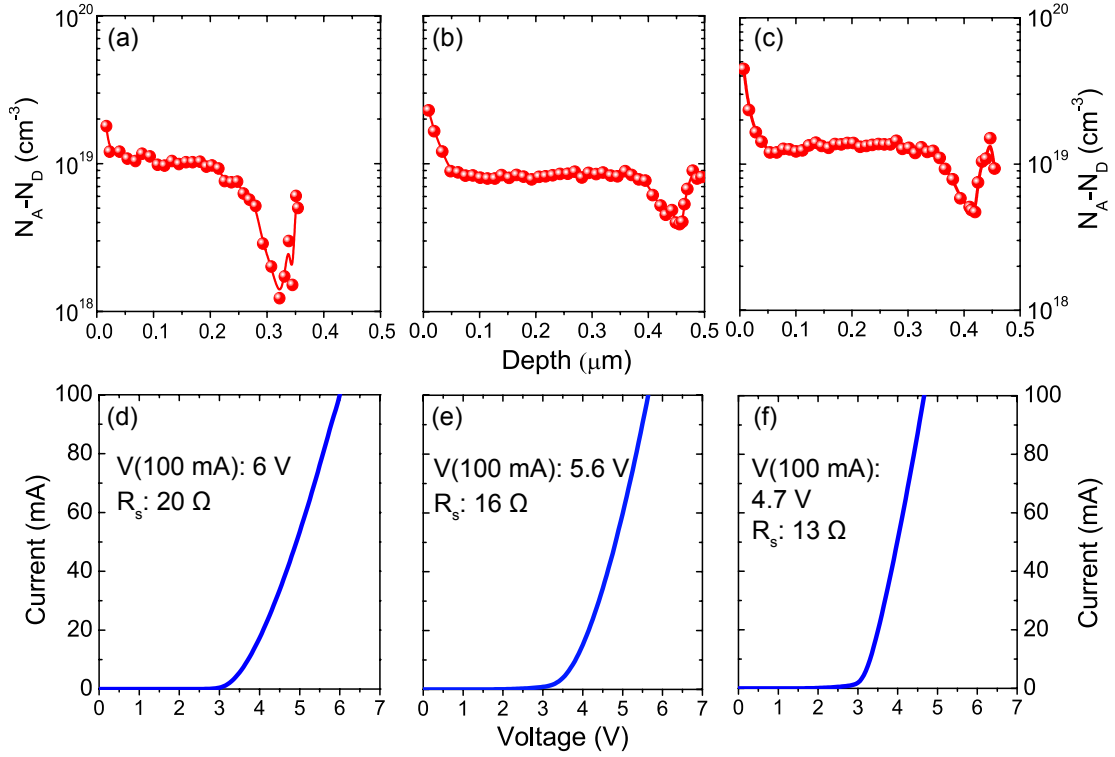


Figure 3.6: (a), (b), and (c) $N_A - N_D$ profiles and corresponding I - V characteristics for three NH_3 -MBE grown homojunctions. The I - V characteristics have been measured on $150 \mu\text{m}$ wide circular devices.

geometry. Several hybrid LEDs were also fabricated, to inquire the possibility to combine the low temperature MBE growth to MOVPE grown active regions. In these structures, fabricated prior to the investigation of the doping of AlGaIn layers, the MOVPE growth included the EBL deposition.

The I - V characteristics of a hybrid device featuring an In-rich active region are shown in Fig. 3.7(a). Low forward voltages are obtained, despite the growth interruption and the transfer step prior to the growth of the MBE p -doped layers. Indeed, no evidence could be found of an effect of the hybrid scheme on the electrical characteristics. Note that the thickness of the MBE p -doped region is 350 nm for this sample. The red line shown in Fig. 3.7(a) is measured on $400 \mu\text{m}$ circular devices fabricated on the same wafer for comparison. For this device size, the forward voltage is 3.3 V at 20 mA . Nevertheless, by improving the device geometry, the forward biases could still be lowered, as the current does not scale with the contact area due to current crowding effects. In fact the I - V characteristics scale with the device perimeter.

Moreover, the resistivity of $(\text{Al})\text{GaIn:Mg}$ was measured by TLM. The results are shown in Fig. 3.8(a). The resistivity (ρ) decreases considerably as the doping is increased in the 10^{19} cm^{-3} range. For higher $[\text{Mg}]$ and $N_A - N_D$ values, the resistivity saturates around $0.4 \Omega\cdot\text{cm}$. This is due to the decrease in the carrier mobility, because of ionized impurity scattering. Our

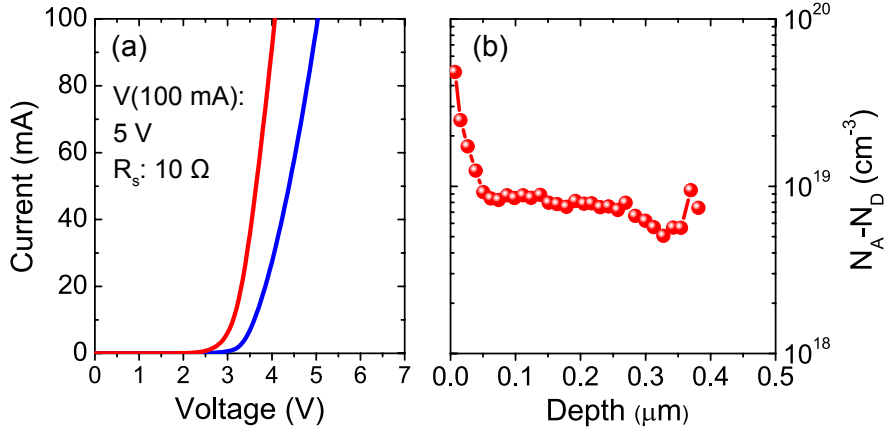


Figure 3.7: (a) I - V characteristics of a hybrid LED for 150 μm wide (blue), and 400 μm wide (red) circular devices. (b) Net acceptor profile.

experimental observations indicate that $\text{Al}_{0.06}\text{Ga}_{0.94}\text{N}:\text{Mg}$ layers exhibit characteristics in line with $\text{GaN}:\text{Mg}$. For MOVPE grown samples, Nakamura and coworkers reported resistivities as low as 0.2 $\Omega\cdot\text{cm}$ [174]. In MBE, values of 0.3 $\Omega\cdot\text{cm}$ were also obtained [175].

With the objective of growing LDs, one can clearly notice in Fig. 3.8(a) that for doping concentrations above $2 \times 10^{19} \text{ cm}^{-3}$, the effect on the I - V characteristics will be negligible. In addition, the increase in free carrier absorption as a function of the doping level needs to be taken into account. Huang *et al.* proposed a linear increase in the internal losses (α_i) of 25 cm^{-1} for each $1 \times 10^{19} \text{ cm}^{-3}$ increase in $[\text{Mg}]$ (more precisely $N_A - N_D$) [173]. Given the general trend of reduced absorption for lower emission energies (for the case of green LDs), here we consider

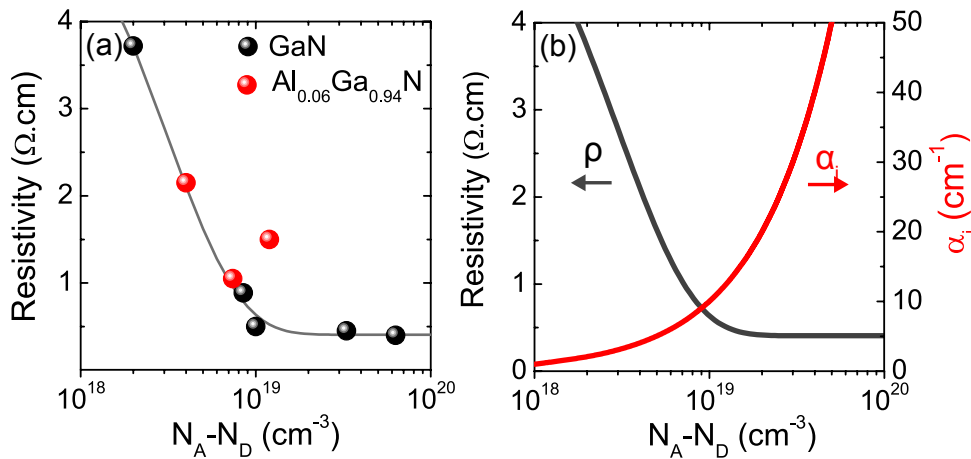


Figure 3.8: (a) Resistivity as a function of $N_A - N_D$ for NH_3 -MBE epilayers. (b) Resistivity (ρ , grey) and internal losses induced by free carrier absorption (α_i , red) as a function of $N_A - N_D$.

only 10 cm^{-1} :

$$\alpha_i = \frac{N_A - N_D}{1 \times 10^{19}} \cdot 10 \text{ cm}^{-1}, \quad (3.17)$$

as depicted by the red line shown in Fig. 3.8(b). In a LD, a compromise between low resistivity and low optical absorption losses need to be found. When the doping is too low, the electrical characteristics are degraded, leading to higher forward voltages, reduced wall plug efficiency, and potentially preventing CW operation by Joule heating. On the other hand, for high doping levels, high α_i values lead to the increase in the threshold currents frustrating laser action in extreme cases. Thus, a doping compromise must be found to lower the resistivity layers without introducing too large optical losses. We see in Fig. 3.8 that for $N_A - N_D \approx 1 \times 10^{19} \text{ cm}^{-3}$ both α_i and the layer resistivity values are low. For extremely low [Mg] values, the layer resistivity becomes an issue. However, in the special case of green LDs, the low gain values obtained during this thesis required that a particular attention should be paid to the α_i reduction, at the expenses of the I - V characteristics. This will be illustrated in the following sections.

In conclusion NH_3 -MBE p -doped layers exhibit good I - V characteristics, even when combined in a hybrid scheme to MOVPE active regions. Resistivity values down to $0.4 \Omega \cdot \text{cm}$ have been obtained. When considering the growth of LDs, extremely high doping levels are detrimental to device operation. A compromise for the p -cladding layer doping lies around $1 \times 10^{19} \text{ cm}^{-3}$.

3.6 Index-guided LDs at EPFL

Mainly index-guided LDs were investigated during this work. In these structures single mode operation is obtained by the lateral confinement of the optical mode when narrow ridges are used. The ridge is defined by post-growth photolithographic steps: to this aim, the p -cladding regions where current is not injected are etched. Dielectric layers such as SiO_2 or ZrO_2 are then deposited on the etched regions and on the ridge sidewalls. The index-contrast with the ridge provides the lateral optical confinement. In addition, the dielectric layers allow to deposit a large area top electrode as they provide electrical isolation where current injection must be avoided. A self-aligned fabrication process was used during this thesis, for which the ridge formation and the p -contact electrode deposition were performed during the same step. A schematic representation of the index-guided LD geometry is shown in Fig. 3.9(a).

All the fabrication processes were performed at EPFL. The state-of-the-art for LDs designed for lasing at 405 nm at LASPE is shown in Fig. 3.9(b) for MOVPE grown devices. Threshold currents of 3 kA cm^{-2} are obtained on uncoated $600 \times 2 \mu\text{m}^2$ devices. The threshold voltage is 4.5 V and the slope efficiency is 0.8 W/A. The injection efficiency is 90% as measured by the variable facet coating method, which will be described later on in this chapter.

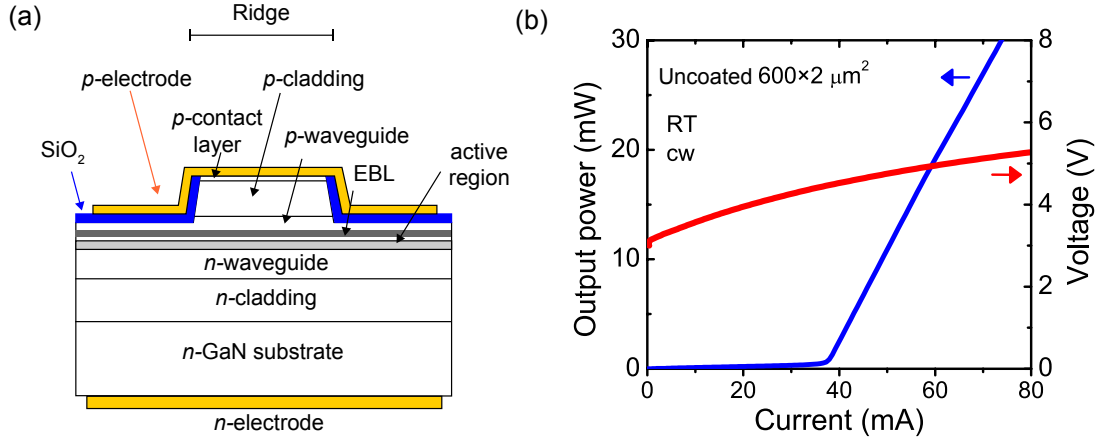


Figure 3.9: (a) Schematic cross-section of an index guided LD. (b) L - I - V characteristics of a 405 nm LD grown by MOVPE at EPFL with uncoated facets.

3.7 First generation violet LDs

The Mg-doped (Al)GaN epilayers grown by NH₃-MBE were implemented into a LD structure emitting at 430 nm. The structure is schematically represented in Fig. 3.4(a). Thus, the bottom part of the laser was grown by MOVPE and consists of a 1 μm thick AlGaIn:Si cladding layer deposited on top of a commercially available 2 in. *c*-plane freestanding GaN substrate (with a dislocation density of $\approx 10^6 \text{ cm}^{-2}$), followed by a GaN waveguide, an InGaIn/GaN MQW active region, and a *p*-doped AlGaIn EBL. During the transfer process the sample was activated by standard RTA and the backside of the wafer was coated with molybdenum. It was then introduced into the MBE reactor for the regrowth of the *p*-doped upper waveguide, cladding, and contact layers. Once loaded in the reactor, the sample was outgassed for 1 h at 450°C under high vacuum. Before the regrowth, a 10 min long cleaning step under NH₃ at 850°C was performed before setting the growth temperature to 740°C.

The Al composition of the 480 nm thick cladding is 6 % as measured by XRD. The top of the structure features a 50 nm-thick p^{++} -GaN contact layer with a $[\text{Mg}] \approx 2 \times 10^{19} \text{ cm}^{-3}$ while in the cladding layer it is $\approx 1 \times 10^{19} \text{ cm}^{-3}$. The epiwafer was then processed into index-guided LDs with an $800 \times 2 \text{ μm}^2$ ridge dimension. Standard Pd/Au and Ti/Al/Ti/Au contacts were used for the top *p*-type electrode and bottom (backside of the freestanding GaN wafer) *n*-type electrode, respectively. No mirror coatings were deposited on the facets.

Lasing at 430 nm was obtained in pulsed operation with a duty cycle of 1%. This device represented, in 2012, the first InGaIn based LD grown by combining MBE and MOVPE. Nevertheless, poor light-current (L - I) characteristics with low slope efficiencies of only 0.1 W/A were obtained. Despite a high turn on voltage ($\approx 4.5 \text{ V}$), the I - V characteristics were encouraging, with a forward bias of 6 V at 100 mA. On the other hand, the threshold current density was as high as 33 kA cm^{-2} , 10 times higher than the state-of-the-art at EPFL. The external quantum efficiency (EQE) was measured from the backside of the wafer using a calibrated

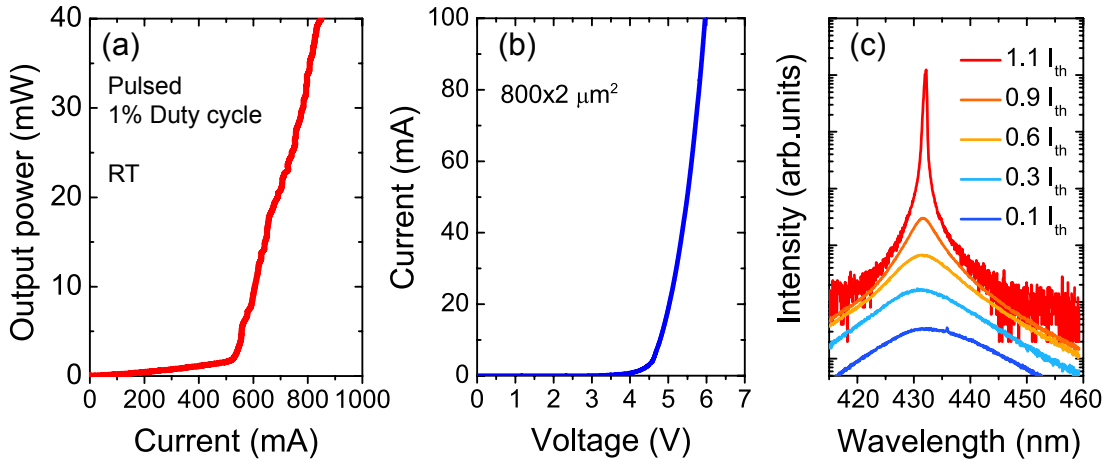


Figure 3.10: (a), (b), and (c) show the L - I characteristics, I - V characteristics, and electroluminescence spectra of the hybrid laser diode, respectively.

silicon photodiode on $100 \times 100 \mu\text{m}^2$ LEDs present on the same wafer. This value generally peaks at current densities of few hundreds of A cm^{-2} and reaches values around 12% for the best MOVPE grown devices measured in this configuration. For this hybrid LD, the EQE was seen to peak at current densities 10 times higher at $2\text{--}3 \text{ kA cm}^{-2}$ with a peak value of 2–3 % which is 5 times lower.

The low slope efficiency values and the EQE measurements indicated limited carrier injection in the QWs. This issue was certainly arising from the hybrid approach for which the exposure to atmospheric and process (Mo) contaminants could affect the p -doping properties of the regrowth interface, therefore the injection. At this step, improvements in the transfer method process and of the doping in the vicinity of regrowth interface were considered to be crucial.

3.8 Interface contamination

The contamination of the regrowth interface was investigated by ECV. GaN:nid templates grown by MOVPE were introduced in the MBE reactor and three different cleaning procedures were performed prior to the growth of 500 nm of GaN:nid at 750°C . For one sample, no cleaning was performed and the growth directly started (Fig. 3.11, brown line). Another one was kept at 850°C during 10 min under 200 sccm of ammonia (red line). The third sample underwent the same cleaning procedure as the previous one but in addition, the surface was exposed to a Ga flux in the absence of ammonia during 10 s. During this time interval Ga would accumulate on the sample surface. The Ga supply was then stopped for 30s leaving the excess gallium to evaporate and the process repeated three times before the growth (orange line). Finally, one last sample was kept under a 60 W ozone lamp for 25 min. Successively, the sample was introduced in the MBE where it was kept 5 min at 750°C under 100 sccm of NH_3 , followed by 5 min under the same conditions but with In supplied to the surface.

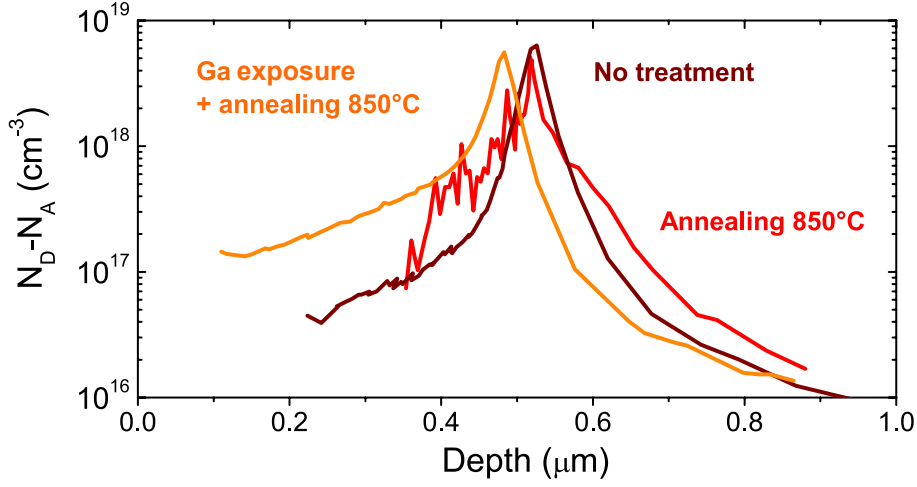


Figure 3.11: Net donor profile of the samples used to investigate the interface cleaning procedure. Net donors could not be measured in the sample treated with the ozone lamp and with In supplied at 750°C.

All samples except for the last one exhibited a peak in net donor concentration ($N_D - N_A$) centered around the regrowth interface and reaching levels up to $6 \times 10^{18} \text{ cm}^{-3}$. Interestingly, the sample treated with the ozone lamp and cleaned under In exhibited an extremely wide depletion region ($> 1 \mu\text{m}$), and no peak could be observed. Therefore, a high temperature cleaning step is not required prior to the regrowth, allowing the whole process to be performed at low temperature.

3.9 Second generation violet LDs

Thanks to the calibration of the growth temperature on FS GaN substrates, a quick transfer process (limited to a few minutes of exposure to the atmosphere) was possible, avoiding Mo sputtering. In this case, the MOVPE growth was stopped 10 nm before the EBL without introducing any p -type doping. The totality of the p -doped layers were indeed deposited by NH_3 -MBE, including an $\text{Al}_{0.15}\text{Ga}_{0.85}\text{N}$ EBL, and the cleaning was performed at 740°C under simultaneous supply of In and NH_3 to the surface during 10 minutes. The LD structure is the same as the one described in Sec. 3.7, except from the active region which has a lower In composition, with a targeted emission close to 400 nm. The p -type doping was increased both in the cladding ($[\text{Mg}] = 1.3 \times 10^{19} \text{ cm}^{-3}$) and in the p -contact layer ($[\text{Mg}] \approx 8 - 10 \times 10^{19} \text{ cm}^{-3}$). The $N_A - N_D$ profile is shown in Fig. 3.12(a).

The so-formed LD, processed into index-guided structures by standard lithographic steps, with ridge dimensions of $800 \times 2 \mu\text{m}^2$, was coated with a high reflectivity (98%) distributed Bragg reflector (DBR) mirror on the rear facet. State-of-the-art I - V characteristics were obtained, with a voltage as low as 4.7 V at a current density of 10 kA cm^{-2} (Fig. 3.12(b)). The series resistance obtained was as low as 6Ω , confirming excellent electrical properties.

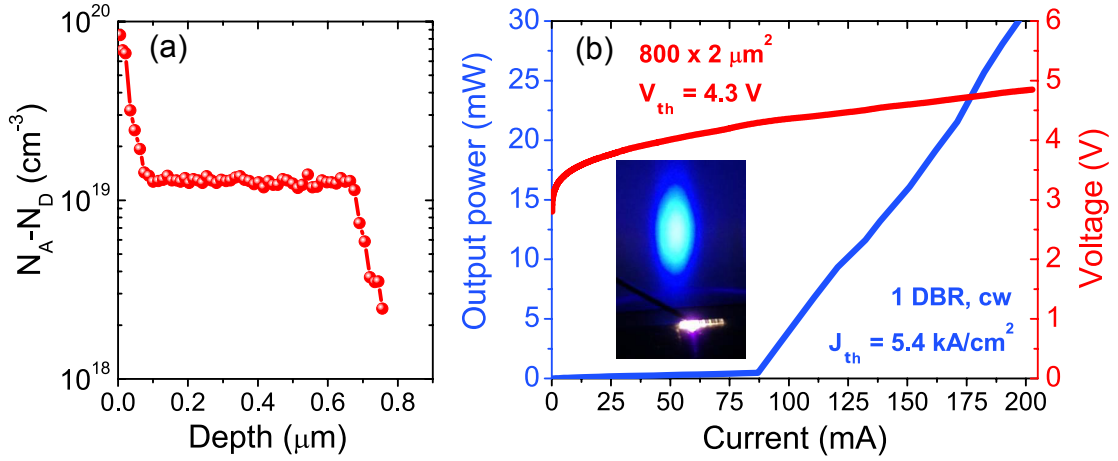


Figure 3.12: (a) Net acceptor profile of the hybrid LD. (b) L - I - V characteristics of the hybrid LD and its far-field pattern (inset) in cw operation. V_{th} and J_{th} stand for threshold voltage and threshold current density, respectively.

TLM measurements indicated a resistivity and a specific contact resistance for this sample of $1.5 \Omega \text{ cm}$ and $5 \times 10^{-4} \Omega \text{ cm}^2$, respectively. The L - I - V curves and far-field pattern are shown in Fig. 3.12(b) for continuous wave (cw) operation. The threshold current is 87 mA, which corresponds to a current density of 5.4 kA cm^{-2} for a lasing wavelength of 400 nm. The threshold voltage was as low as 4.3 V matching that of the best devices reported in the literature.

When the performance of this hybrid LD is compared to LDs fully grown by MOVPE in our laboratory [176], a reduction in the slope efficiency (0.27 W/A) together with a slight increase in the threshold current is observed. This is ascribed to a lower injection efficiency in the hybrid device, which could be related to the regrowth interface. The injection efficiency issue is reinforced by the behavior of the L - I characteristics as a function of the duty cycle measured on a device without DBR back mirror and shown in Figs. 3.13(a) and 3.13(b). By increasing the duty cycle, the slope efficiency increased and the threshold current decreased. However, the output power at threshold was the same in all conditions, indicating similar losses. In addition, the change of duty cycle did not affect the I - V characteristics, which remained unchanged. We suspect that a barrier is formed at the regrowth interface which limits the carrier injection. By increasing the duty cycle, the devices heats up and the carriers (holes) have additional energy to overcome the barrier and inject the QWs, instead of recombining non-radiatively in the upper cladding or waveguide layers.

The sample was also characterized by SIMS, looking for carbon (C), oxygen (O), and silicon (Si). The [C] and [O] levels are below 10^{17} cm^{-3} in the whole structure, with a slightly higher [O] at the MOVPE/MBE interface. On the other hand, a strong peak related to Si is observed. This peak could also be ascribed to carbon monoxide (CO) because of the analogous total atomic mass. Such a contamination could originate from metalorganic by-product adsorption

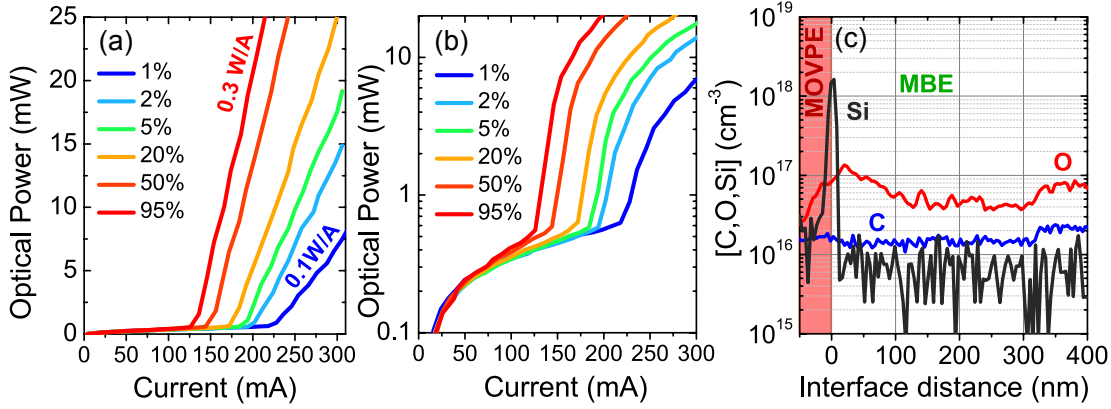


Figure 3.13: (a) and (b) show the L - I characteristics of devices free of DBR mirrors as a function of the duty cycle in linear and semi-logarithmic scale, respectively. (c) [O], [C], and [Si] SIMS profiles measured across a hybrid MOVPE/MBE LD structure.

occurring during the cool-down of the sample in the MOVPE reactor.

Interestingly, a radial symmetry in the EQE performances is observed in the as-grown half wafer, centered at the original full wafer center. While being typical of our MOVPE reactor (for which the EQE at the wafer edge is 2 times lower than the one at the center) and therefore not related to MBE, in this case the EQE is 10 times lower than the center value. One can speculate that, due to the large wafer bowing, during the cool down in the MOVPE reactor the wafer edges cool at a faster rate than the center and the condensation of some residual metalorganic by-products in these regions is increased. Unfortunately, to limit the exposure time to the atmosphere, the ozone cleaning was not performed on this device.

In conclusion cw lasing operation was achieved with state-of-the-art I - V characteristics in a hybrid LD sample. The threshold current density compares well with results obtained by PAMBE on violet-blue LDs [177–180] but it is still higher than for LDs fully grown by MOVPE [181]. On the other hand the I - V characteristics match the best results obtained by MOVPE.

3.10 Optical pumping

Optical pumping in the variable stripe length configuration was performed on a variety of unprocessed LD structures, from violet to green. This experimental technique allows to quickly access the gain properties of the devices, and to evaluate the inhomogeneous broadening. To measure the latter parameters, the sample is pumped in the 800 μm wide region starting from the output facet. Further away from the facet the unpumped region strongly absorbs the photons, thus preventing lasing. In such a way, the emitted photons experience only single-pass amplification. The set up can also be used to pump laser bars, and observe lasing. In this configuration 800-1000 μm long laser bars are homogeneously pumped, and the cavity feedback enables lasing. The same pumping scheme is described in Ref. [60].

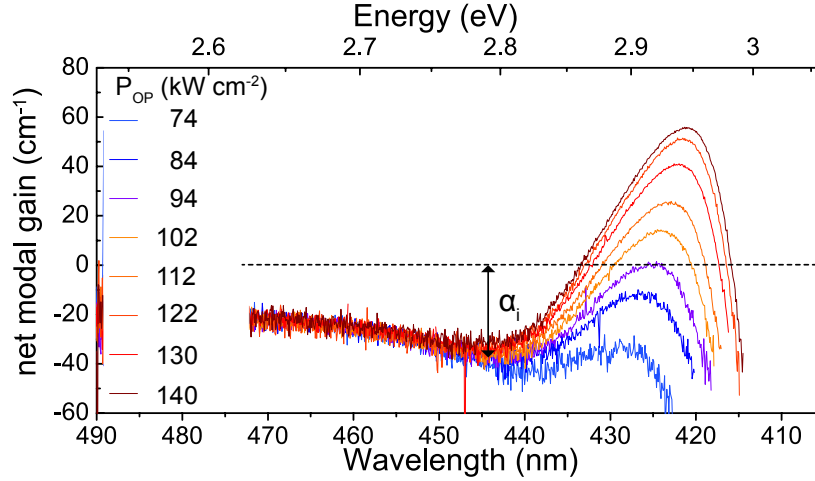


Figure 3.14: Net modal gain spectra of a blue-violet MOVPE LD under increasing pumping powers.

In this work, full laser structures, including doped waveguides and cladding layers, were investigated after RTA activation, to include the effects of free carrier absorption on the internal losses. This technique was adopted to optimize the active region of long wavelength laser diodes and provided valuable information to achieve lasing above 500 nm.

The quantity measured by the VSL method is the net modal gain value, *i.e.* $g_{mod} - \alpha_i$. The internal losses (α_i) can be evaluated from the separation between the plateau on the low energy side of the gain spectrum to the x -axis ($y = 0$) as indicated in Fig. 3.14. In the low energy region of the gain spectra a constant value is expected as $g_{mod} = 0$. This is however hardly seen experimentally making the determination of α_i difficult. In Fig. 3.14 the results obtained on a MOVPE grown LD are plotted for several pumping powers showing the net modal gain evolution. In this case all spectra overlap in the low energy side where the modal gain is expected to be zero and indicate a precise α_i value independently of the pumping power. An α_i value of $35 \pm 10 \text{ cm}^{-1}$ can be extracted.

When moving towards the green spectral range the determination of both α_i and g_{mod} becomes more difficult: when both quantities are reduced the experimental sources of error can strongly affect the measurements. To overcome this issue, a vertical offset can be introduced for each measurement in order to make the spectra overlapping on the low energy side region at $g_{mod} = 0$. However, this is not always possible and to determine the exact value for the offset, an iterative procedure between the experimental and theoretical g_{mod} value was introduced. The latter approach is routinely used in the literature. When this procedure is performed, only g_{mod} can be extracted. In fact, the vertical offset is introduced to remove the effect of α_i on the gain spectra. On the other hand, the fitting of the modal gain curve allows the determination of the inhomogeneous broadening (σ).

This is shown in Fig. 3.15 for two MOVPE LD structures lasing under electrical pumping (not

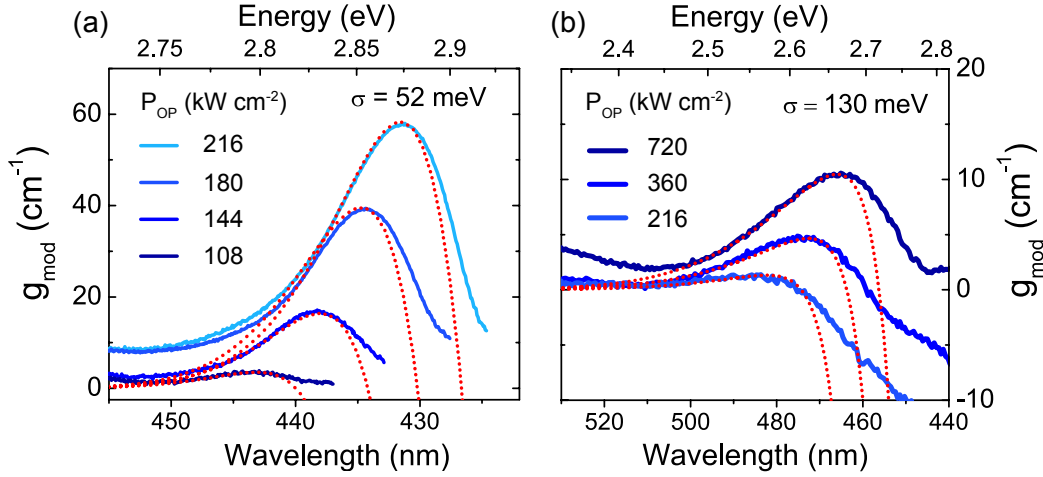


Figure 3.15: Modal gain spectra of (a) blue and (b) aquamarine MOVPE LDs under optical pumping. The dotted lines in (a) and (b) are generated using inhomogeneously broadened density of states as expressed by Eqs. (3.9) with σ values of 52 meV and 130 meV, respectively.

shown) at 445 nm (a) and 490-495 nm (b). Under optical pumping, lasing is observed for the two structures 10 nm below at 435 nm and 480 nm. The difference is ascribed to the applied bias tilting the band structure during electrical injection. The inhomogeneous broadening values of 50 and 130 meV are found for the two devices, respectively, indicating the difficulty of growing high In content InGa_N QWs. The approach employed is the one described in Ref. [144] using $\Gamma_{445} = 3\%$ and $\Gamma_{480} = 1.5\%$ for simulating the gain curves. The sample lasing at 445 nm features two 3.5 nm thick InGa_N/Ga_N QWs, while the one lasing at 480 nm has three 2 nm thick InGa_N/Ga_N QWs. Note that the model employed to simulate the gain curves does not take into account the homogeneous broadening, the longitudinal-optical (LO) phonon interaction [182], the built-in field in the QW, and the gain contribution of higher confined levels. On the high energy side of the spectrum a deviation between the model and the experimental data is observed, especially for the high In content structure. This can be related to the simplicity of the model used and/or to the possible presence of non-identical QWs in the structure. A slight overestimation of σ is thus likely.

The inhomogeneous broadening of the active regions grown in our laboratory is much larger than the state-of-the-art. At 490 nm and 512 nm, σ of only 70 meV [182] and 95 meV [183] have been reported by OSRAM and Nichia, respectively. Our results are actually in line with the values published by Nichia in 2007 [145], as shown in Fig. 3.16.

The inhomogeneous broadening parameter alone does not fully govern the gain properties. Radiative and non radiative recombinations must also be taken into account. Two identical QWs (In composition, thickness, σ) grown under different growth conditions can exhibit different gain properties due to different material quality. To evaluate the differences, the gain values were measured under identical optical pumping conditions for different active regions. This was performed together with internal quantum efficiency measurements under

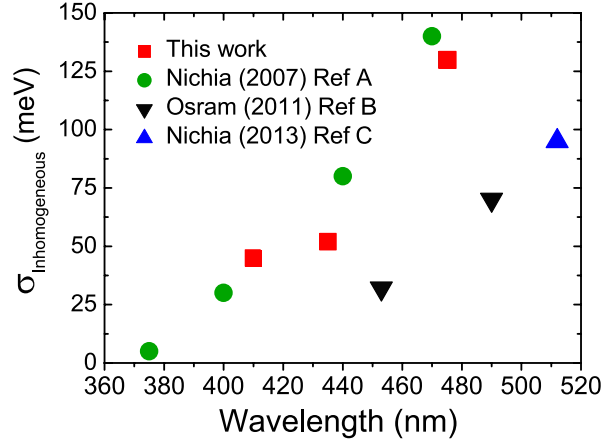


Figure 3.16: Evolution of the inhomogeneous broadening compared to Refs. A [145], B [182], C [183].

electrical pumping. The tuning of the MOVPE growth parameters allowed to increase the maximum g_{mod} of $\text{In}_{0.25}\text{Ga}_{0.75}\text{N}$ QWs by a factor of 6 during this work. In fact, we have been able to increase the maximum g_{mod} at a pumping power of 700 kW cm^{-2} from around $1\text{-}2 \text{ cm}^{-1}$ to $\approx 10 \text{ cm}^{-1}$.

In order to estimate the internal losses in long wavelength devices, unprocessed laser bars of 1 mm length were employed for optical pumping experiments. The uncoated laser bars were only partially pumped by stripes measuring 400 and $800 \mu\text{m}$ in length. The emission spectra were collected from the laser bar facet and compared for the two pumping lengths using the VSL method to measure g_{mod} . High reflectivity mirror coatings were successively placed on both facets, reducing α_m below 1 cm^{-1} . The laser bars were then optically pumped along their whole length (1 mm) at different pumping powers, while recording the output spectra to determine the threshold pumping power (P_{th}). From the fact that at threshold $\alpha_i + \alpha_m = g_{mod}$, α_i could be determined. This is shown for a hybrid laser diode in Fig. 3.17, lasing at 495 nm. For this structure, which will be further discussed in the following sections, $\alpha_i \approx 4 \text{ cm}^{-1}$. In this case, InGaN-GaN waveguides and $3 \times \text{InGaN/GaN}$ QWs with an In composition of 25% compose the waveguide and the active region. The internal losses value compares well with similar long wavelength devices fully grown by MOVPE at EPFL for which, using the same method, $\alpha_i \approx 6 \text{ cm}^{-1}$. Note that by optically pumping unprocessed devices, the scattering loss introduced with the ridge-waveguide geometry and the possible absorption at the p -contact metal/semiconductor interface are not taken into account resulting in an underestimation of α_i .

In conclusion, thanks to the variable stripe length method we were able to evaluate the inhomogeneous broadening of the $\text{In}_{0.25}\text{Ga}_{0.75}\text{N}$ QWs. Furthermore, by investigating the samples under constant pumping conditions, the growth conditions of the QWs were optimized, increasing the gain in high In content active regions by a factor of 6. By optically pumping long wavelength devices, low modal gain values were measured, indicating the need of lowering

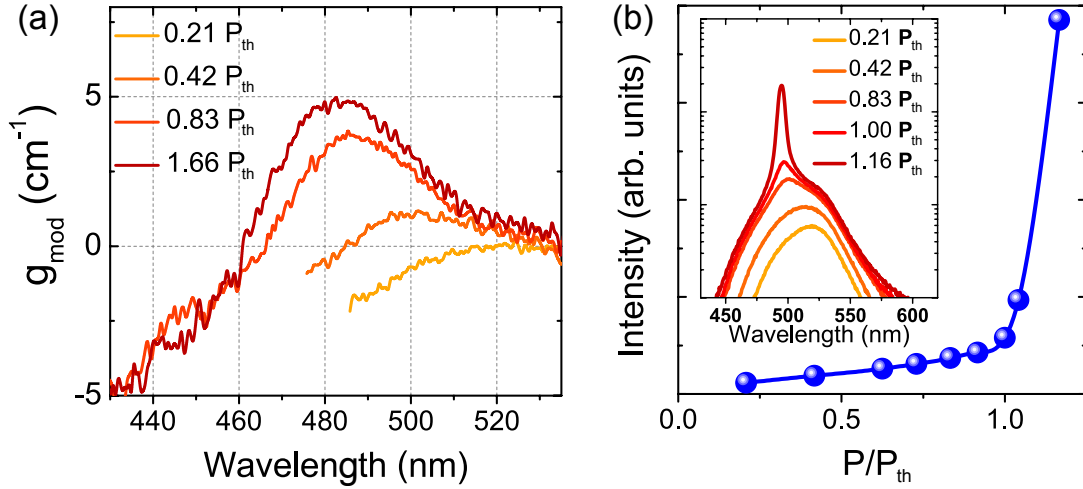


Figure 3.17: (a) Evolution of the gain spectra with increasing pump power for the uncoated laser bars. (b) Integrated laser output intensity under optical pumping of unprocessed LD structure with high reflectivity mirror coatings as a function of the optical power normalized to the threshold power (P_{th}). The spectral characteristics with increasing pump power are shown in the inset. $P_{\text{th}} = 380 \text{ kW cm}^{-2}$.

as much as possible the internal and mirror losses in order to achieve lasing. Our results show a big room for improvement for the the active region growth (σ reduction) to match the state-of-the-art characteristics.

3.11 Long wavelength hybrid laser diodes

Hybrid long wavelength LDs were realized during this thesis. The MBE regrowth was performed on top of MOVPE structures comprising thick $\text{Al}_{0.08}\text{Ga}_{0.92}\text{N}$ bottom cladding, $\text{GaN-In}_{0.06}\text{Ga}_{0.94}\text{N}$ waveguide, three $\text{In}_{0.25}\text{Ga}_{0.75}\text{N}/\text{GaN}$ 2 nm thick QWs, and 80 nm thick $\text{In}_{0.04}\text{Ga}_{0.96}\text{N}$ top waveguide. The MOVPE growth was finished with 10 nm of GaN:nid . The same transfer and cleaning procedure as the one described in Sec. 3.9 was performed for these structures. The so-formed wafer was cleaved in half and two successive regrowth were performed by MBE, one without EBL (Sample A) and the other including 15 nm thick $\text{Al}_{0.15}\text{Ga}_{0.85}\text{N:Mg}$ EBL (Sample B). Apart from the EBL, the MBE growth consisted of a 600 nm thick $p\text{-AlGaIn}$ cladding with an average Al composition of 6% and a 50 nm thick $p^{++}\text{-GaN}$ contact layer. The average doping in the cladding layers is 5 and $7 \times 10^{18} \text{ cm}^{-3}$ for samples A and B, respectively. In fact, especially in the vicinity of the active region, the doping was intentionally kept low to reduce free carrier absorption losses and was successively increased towards the contact layer by increasing the Mg cell valve opening. The $N_A - N_D$ profiles are shown in Fig. 3.18 for both samples. The nominal thickness of the entire p -doped region is 660 nm for sample A and 675 nm for sample B. One can notice that the ECV depth measurement is slightly underestimated for sample A and overestimated for sample B, probably because of the

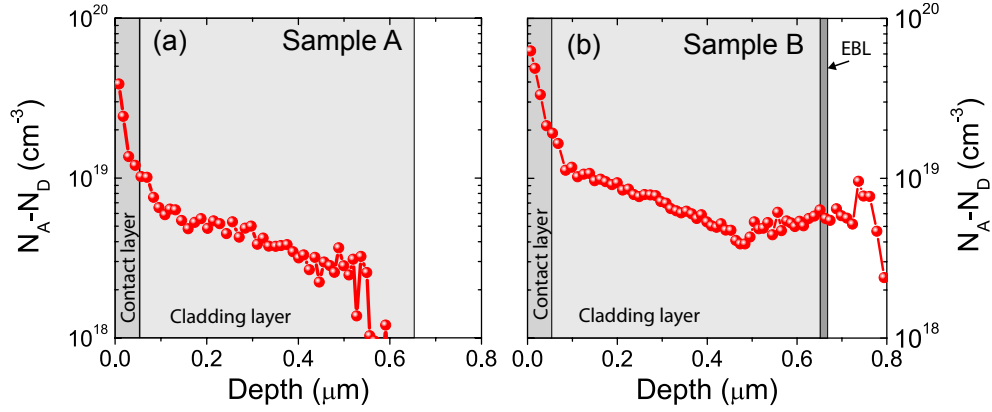


Figure 3.18: Net acceptor profile for the two hybrid long wavelength LDs, (a) sample A and (b) sample B. The grey areas indicate the nominal layer thicknesses for the two samples.

etching difficulty when the doping is low.

After growth, the luminescence mapping at low excitation power densities (for which nonradiative recombination centers, if any, govern the luminescence efficiency) of the two samples was recorded (Fig. 3.19). The third harmonic ($\lambda = 355$ nm) of a Q-switched Nd:YAG laser was used to excite the sample at room temperature. On the same image the luminescence map of a LD wafer with the same active region but fully grown by MOVPE is displayed for comparison (Fig. 3.19(c)). For this specific sample, the growth temperature and the growth duration of the p -type layers were 950°C and 20 min, respectively, and resulted in a severe degradation of the active region, highlighted by the appearance of black spots exhibiting limited radiative recombination. While the green luminescence from the QWs is extremely homogeneous for sample A, indicating that the MBE overgrowth does not induce noticeable damage, sample B exhibits reduced radiative recombinations with small darker regions appearing in the photoluminescence map, indicating the presence of defects probably generated during the EBL

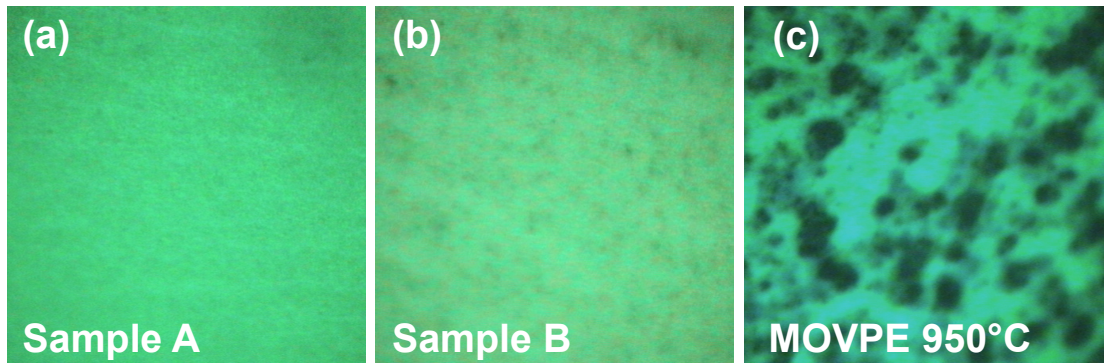


Figure 3.19: (a) and (b) show the $60 \times 60 \mu\text{m}^2$ photoluminescence maps of the hybrid MBE LDs active regions for sample A and B, respectively. In (c) the photoluminescence map for the same dimension is presented for a sample fully grown by MOVPE.

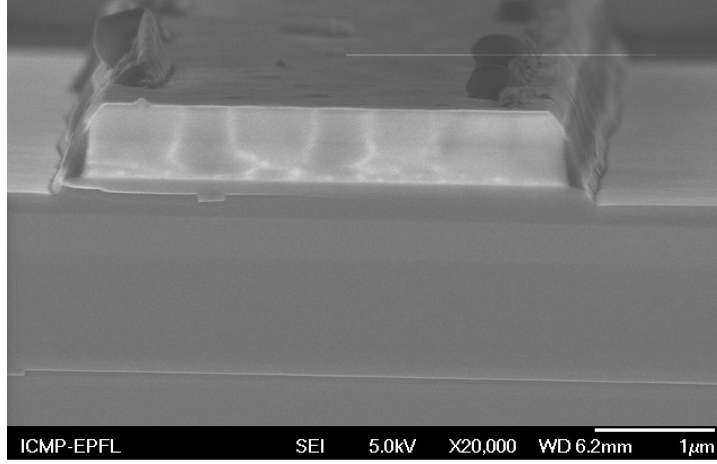


Figure 3.20: (a) Cross-sectional SEM image of the output facet of a hybrid long wavelength LD from sample A.

growth. Furthermore microcracks are present on sample B, originating from the excessive tensile strain introduced by the EBL. The latter resulted in difficulties in the cleavage of sample B, for which LDs exhibiting better performance with respect to sample A could not be obtained. the following discussion is therefore restricted to sample A.

The optical pumping of sample A was shown in Fig. 3.17 leading to lasing at 495 nm and to the estimation of $\alpha_i = 4 \text{ cm}^{-1}$ for an unprocessed laser bar. Lasing under electrical injection was first achieved on gain guided structures characterised by $750 \times 10 \text{ } \mu\text{m}^2$ wide stripe contacts. The facets were coated with dielectric DBRs with reflectivities of 92% and 80%. Lasing at 497 nm was obtained under pulsed operation with a duty cycle of 1% and a repetition rate of 10 kHz. The threshold current density was 11 kA cm^{-2} . Full devices were then fabricated in the form of index-guided LDs with $800 \times 4 \text{ } \mu\text{m}^2$ ridge dimensions. Standard Pd/Au and Ti/Al/Ti/Au metallizations were used for the top *p*-type electrode and bottom (back side of the freestanding GaN wafer) *n*-type electrode, respectively. Large metallic pads for the evaluation of the *p*-contact resistance ρ_c by TLM were also applied over the top wafer surface. To confirm the ridge dimension, the front facet of an uncoated long wavelength hybrid LD was investigated by scanning electron microscopy (SEM) (Fig. 3.20). The image shows the abruptness of the doping interface, with a clear delimitation between the undoped upper waveguide layer, and the *p*-doped region grown by NH_3 -MBE (lighter region).

Typical current–voltage (*I*–*V*) characteristics of a LD of Sample A are shown in Fig. 3.21(a). The operating voltage at a driving current of 100 mA is lower than 5 V and increases to 5.6 V at 450 mA in cw operation. These voltages are low when compared with those of the current state-of-the-art green narrow ridge-waveguide LDs grown by standard MOVPE techniques [149, 151, 184], indicating the excellent electrical properties of the low-temperature *p*-doped epilayers grown by NH_3 -MBE. This is also confirmed by TLM measurements revealing a low contact resistance of $\rho_c \approx 8 \times 10^4 \text{ } \Omega\text{cm}^2$. This value does not change if calculated versus the

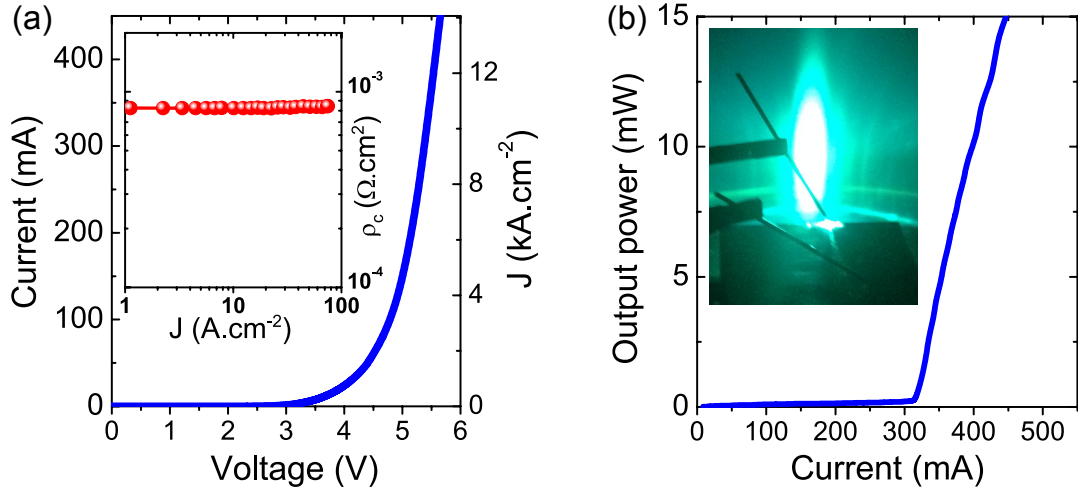


Figure 3.21: (a) *I-V* characteristics of an $800 \times 4 \mu\text{m}^2$ hybrid laser diode measured in cw operation with the corresponding current density (J) values. The inset shows the evolution of the contact resistance as a function of J extracted from TLM measurements. (b) *L-I* characteristics and far-field emission pattern (inset) of the hybrid LD under pulsed operation.

density of current flowing through the TLM pads [185], indicating an excellent ohmicity of the *p*-contact (inset of Fig. 3.21(a)). The current density in the inset is calculated from $J = I/wl_t$ where I is the current, w is the width of the TLM contact, and l_t is the transfer length corresponding to the lateral dimension of the contact which is really flown through by the current as defined in Sec. 1.5.5. Lasing and gain characteristics were investigated on laser bars formed by standard cleaving techniques. The back facet was coated with five dielectric pairs ($\text{SiO}_2/\text{TiO}_2$) to obtain a reflectivity of 94%. The impact of the mirror loss on the device output characteristics was investigated by implementing $\text{SiO}_2/\text{TiO}_2$ DBRs with different reflectivities on the output facet. The DBR reflectivities were 46, 75, and 89% for one, two, and three pairs, respectively.

The *L-I* characteristics obtained in pulsed operation (1% duty cycle and $1 \mu\text{s}$ pulses) of a device with a two-dielectric-pair DBR on the front facet are shown in Fig. 3.21(b). The threshold current is 310 mA (9.7 kA cm^{-2}) at 5.4 V and the slope efficiency is 0.1 W/A . The light output power reaches 15 mW at 450 mA for a lasing wavelength of 501 nm. A far-field emission picture is also presented in the inset of Fig. 3.21(b) and shows a typical single-mode pattern. The lasing spectrum is shown in Fig 3.22(a). Lasing is obtained more than 20 nm away from the spontaneous emission maximum measured at low injection currents due to the combined screening of the polarization fields and the blue-shift of the gain maximum (which is proportional to σ) as the carrier density is increased. By increasing both the duty cycle and the injected current, the lasing wavelength can be increased up to 506 nm as shown in Fig. 3.22(b), but this is done at the expense of the single mode emission. Unfortunately, despite the state-of-the-art electrical characteristics of the devices, lasing action on unmounted bars (without heat sinking) could not be obtained under cw operation because of the relatively

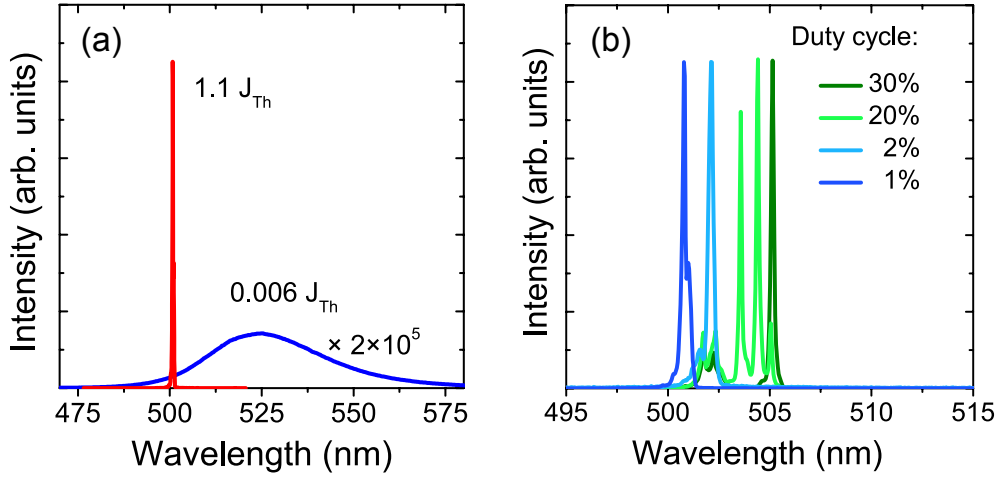


Figure 3.22: (a) Electroluminescence spectra acquired below and above the lasing threshold. (b) Normalized lasing wavelength under increasing duty cycles and injection currents.

high threshold current.

When changing the front facet DBR coating from one to three pairs, the threshold current density (J_{th}) decreases from 14.2 to 8.1 kA cm⁻². As expected, increasing the output facet reflectivity strongly affects the slope efficiency of the LD as well, with a maximum value of almost 0.2 W/A achieved for a single-dielectric-pair DBR (Fig. 3.23). Threshold currents and slope efficiencies are shown in Fig. 3.23 as a function of the outcoupling mirror loss, which is inversely proportional to the front facet reflectivity.

By the variable facet coating method (VFC), which is described hereafter, crucial device parameters such as α_i , η_{inj} , J_{tr} and g_0 can be extracted. For example, the threshold evolution as a function of the outcoupling mirror losses can be fitted using Eq. (3.15(a)), allowing to extrapolate both J_{tr} and g_0 . On the other hand, the slope efficiency values allow the determination of α_i and η_{inj} using Eq. (3.16). In addition g_0 can also be determined independently of J_{tr} using the relationship $\alpha_m^1 - \alpha_m^2 = \Gamma g_0 \ln(I_{th}^1 / I_{th}^2)$ [148]. Indeed, from the slope of the experimental data when $\alpha_m^1 - \alpha_m^2$ is plotted against $\ln(I_{th}^1 / I_{th}^2)$, g_0 is determined provided that Γ is known. To this aim, the total mirror loss (α_m) and the outcoupling mirror loss (α_{out}) were calculated in each case using the measured DBR reflectivities, and the internal efficiency (η_i) above the lasing threshold was assumed to be $\eta_i = 1$ (the clamping of the spontaneous emission above threshold was confirmed experimentally for these LDs). The confinement factor was estimated to be 1.5% using a commercial full vectorial Maxwell solver.

In this way from Fig. 3.23(a), $\alpha_i = 6$ cm⁻¹, $\eta_{inj} = 17.5\%$, and $g_0 = 490$ cm⁻¹ were determined. The methodology proposed in Ref. [148] leads to the same g_0 value of 490 cm⁻¹ (Fig. 3.23(b)). The internal optical loss is in agreement with that obtained by VSL under optical pumping. The slightly higher values measured under electrical pumping are consistent with increased scattering loss introduced with the ridge-waveguide geometry and possible absorption at

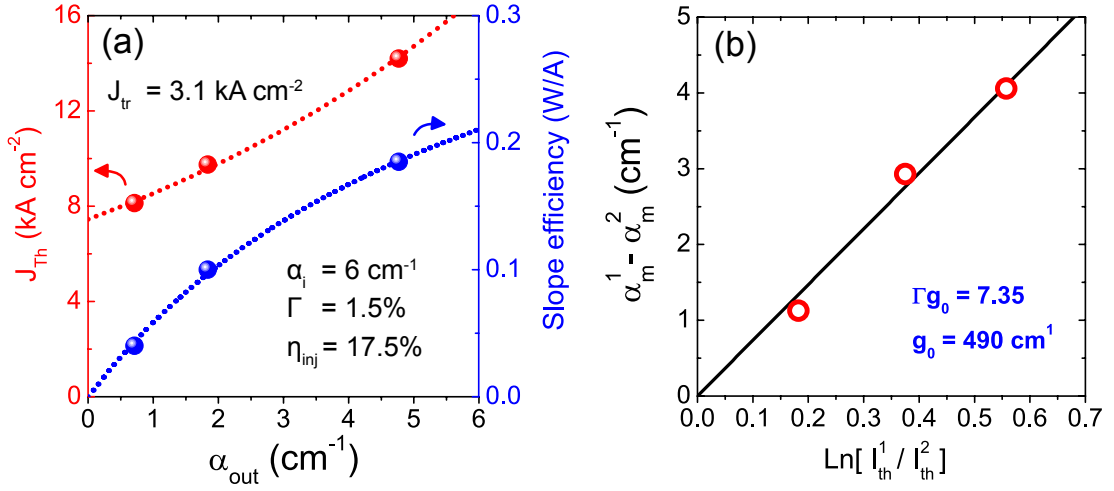


Figure 3.23: (a) Threshold current (red) and slope efficiency evolution as a function of the outcoupling mirror losses. The fitting of the experimental results is shown by the two dotted lines. (b) Extrapolation of the gain coefficient using the method described in Ref. [148].

the p -contact metal/semiconductor interface. This value is low when compared to the ones reported in the literature which are around $8\text{--}15 \text{ cm}^{-1}$ [146, 148, 183]. However, the thick (80 nm) InGaIn upper waveguide combined to the low doping level of the p -cladding close to the active region, can easily explain the result. The same argument can be used for the low injection efficiency value. Furthermore, given the reduced thickness of the QWs composing the active region, possible hole overflow was proposed, further reducing η_{inj} [186, 187]. Nevertheless, our value is 4 times lower than the state-of-the-art for green LDs which is set at 71% [188]. The poor electrical injection efficiency adds up to the reduced gain coefficient, which is less than half of the best reported values, clearly limiting the device performance. Finally, Γ values as high as 6% have been obtained on green LDs [183], compared to $\Gamma = 1.5\%$ for this structure. The low internal loss value proves that by NH_3 -MBE p -doped layers with high optical quality can be achieved and that the quality of the doping is not only restricted to high net acceptor concentrations and good I - V characteristics. It is clear that hybrid LDs can be further improved. For example, by doubling the injection efficiency the slope efficiency can be doubled and the threshold reduced by a factor of 2, possibly leading to longer lasing wavelengths.

The comparison with samples fully grown by MOVPE, featuring nominally identical active regions and with the p -claddings grown at 860°C , indicated higher slope efficiency, longer lasing wavelengths, and similar threshold currents for the hybrid devices. The maximum lasing wavelength at threshold was 496 nm for the MOVPE samples. For a 75% outcoupling mirror reflectivity the slope efficiency for the latter samples is only 0.05–0.065 W/A. This is ascribed to a lower injection efficiency, as low as 10% (measured by VFC). Similar gain coefficient values were extracted, slightly higher for the full MOVPE sample. Hakki-Paoli measurements were unsuccessfully attempted. Because the devices could not be operated in CW, the steady state

lasing condition could not be obtained, and the evaluation of the gain properties proved impossible with this method.

3.12 Summary

In conclusion, the possibility to achieve state-of-the-art electrical characteristics for NH_3 -MBE grown p -doped layers was demonstrated. These layers have been successfully implemented on hybrid LDs. cw lasing operation was achieved on a structure emitting at 400 nm combining an n -type AlGaIn cladding and an InGaIn active region grown by MOVPE, with the optimized p -doped waveguide and cladding layers grown by NH_3 -MBE. A threshold voltage as low as 4.3 V was demonstrated, matching the best results obtained by MOVPE. This was achieved thanks to the mastering of the doping profile, especially in the contact layer region, enabling a specific contact resistance as low as $5 \times 10^{-4} \Omega \text{ cm}^2$. A slight degradation in the slope efficiency compared to similar MOVPE samples was ascribed to parasitic contamination at the regrowth interface reducing the injection efficiency. The interface cleaning technique was discussed as well.

On the other hand, by optically pumping unprocessed hybrid and full MOVPE LD structures, the modal gain characteristics and the inhomogeneous broadening have been measured for different active regions pointing out the reduced modal gain and increased inhomogeneous broadening as the In content in the QWs is increased. The internal losses were also evaluated for a long wavelength hybrid LD structure by comparing the gain measurements to the threshold pumping powers.

The valuable information provided by the VSL measurements allowed for the realization of electrically injected hybrid LDs lasing beyond 500 nm. The processed devices exhibited again state-of-the-art I - V characteristics. Nevertheless, by using the variable facet coating method, low injection efficiencies and gain coefficient values were found. The improvement of these parameters would strongly affect the lasing characteristics, and allowing lasing at longer wavelengths. Finally, extremely low α_i values were measured on these devices, partially explained by the undoped upper waveguide, but still confirming the device-quality of AlGaIn:Mg layers grown by NH_3 -MBE.

4 Devices II: Tunnel junctions

In this chapter the realization of GaN tunnel junctions (TJs) grown by NH₃-MBE is reported. First, a brief overview of the motivations that led to this study together with the TJ theoretical background are discussed. Secondly, the electrical characteristics of the devices are presented. Different approaches are proposed for the fabrication of efficient TJ, including the realization of buried TJs (BTJs) to be used as current apertures to control the current injection in optoelectronic devices. A discussion on the TJ potential for future III-nitride based devices is also included at the end of this chapter.

4.1 Theory

In the particular case of a heavily doped p - n junction, the shrinkage of the depletion region can allow interband tunneling of carriers directly from the conduction band to the valence band or vice versa. The so-formed device is called a tunnel junction and exhibits specific characteristics for both the forward and reverse biases. In 1957 Esaki realized the first TJs devices using germanium [189], which were further implemented in other semiconducting materials.

In quantum mechanics, it is well known that the carrier tunneling probability (T_t) depends on the height and width of the potential barrier, determined by the bandgap (E_g) and the depletion width (W), respectively, and on the effective mass of the tunneling particle. In the Wentzel-Kramers-Brillouin (WKB) approximation, T_t is given by [31]:

$$T_t = \exp \left[-2 \int_{-x_p}^{x_n} |k(x)| dx \right], \quad (4.1)$$

where $k(x)$ is the wave vector of the carrier and x_p , x_n are the extent of the space charge region in the p -type and n -type side of the junction, respectively, with $x_p + x_n = W$. The potential profile in the junction region can be approximated to a triangular barrier, thus $k(x)$ can be

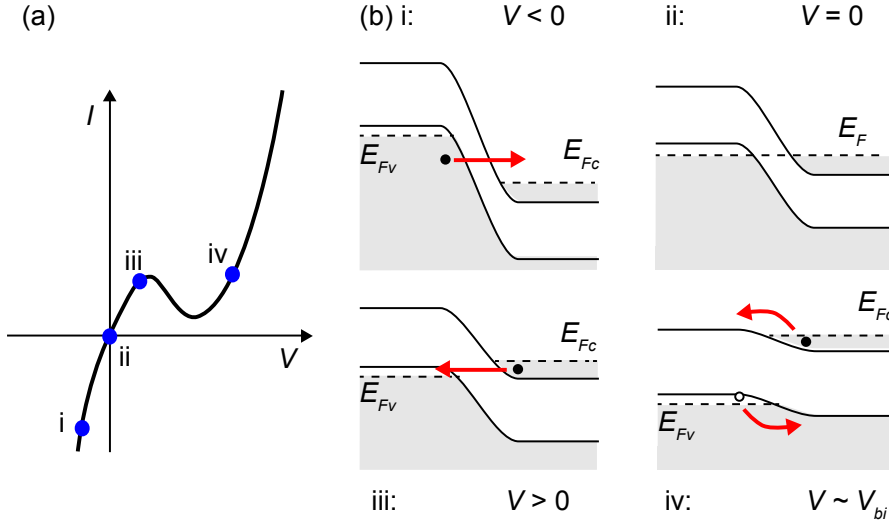


Figure 4.1: (a) I - V characteristics of a tunnel diode. (b) Schematic energy-band diagrams at (i): reverse bias, (ii): thermal equilibrium, (iii): low forward bias, and (iv): forward bias approaching V_{bi} .

written as:

$$k(x) = \sqrt{\frac{2m^*}{\hbar^2} \left(\frac{E_g}{2} - qFx \right)}, \quad (4.2)$$

where F is the electric field. When a bias is applied to the junction, the tunneling current flowing through the device is given by [189]:

$$I = A \int_{E_{Fv}}^{E_{Fc}} [f_c(E) - f_v(E)] T_t \rho_j(E) dE, \quad (4.3)$$

where ρ_j is the joint density of states, E_{Fc} and E_{Fv} the quasi-Fermi levels in the n - and p -type region, respectively, and $f_c(E)$ and $f_v(E)$ the Fermi-Dirac distribution functions for the conduction and valence bands, respectively.

Interestingly, when degenerately doped p and n -type semiconductors are used, at thermal equilibrium the energy states occupied by the electrons in the n -type material lie at an energy below the energy of the unoccupied energy levels (filled by holes) on the p -side, as shown in Fig. 4.1(b). In this configuration, a small positive bias allow for the interband tunneling of the electrons from the conduction to the valence band, as the two become aligned (Fig. 4.1(b)iii). When the applied bias is increased, and the built-in potential reduced, the occupied conduction band states on one side are not aligned anymore with the unoccupied levels on the other side, resulting in a decrease of the the tunneling current as the voltage is increased and known as negative differential resistance ($R = \frac{dI}{dV} < 0$). By further increasing the applied bias, the typical diode characteristics are obtained as the built-in electrostatic potential is strongly reduced.

Under reverse bias, the tunneling proceeds in the opposite direction, *i.e.* electrons tunnel from the filled valence band states on the p -side band to the empty conduction band states on the n -side, leaving behind holes (Fig. 4.1(b)(i)). In this regime, the current increases approximately exponentially with the applied bias and can be written in the form [31]:

$$I = B_1 \exp(+ |V| / B_2) , \quad (4.4)$$

where B_1 and B_2 are positive quantities slowly varying with respect to the applied bias. One of the reasons of their voltage dependence is the change in the depletion width as a function of V . When operated under reverse biases, heavily doped p - n junctions allowing for current flows are often referred as to "backward diodes" or Zener diodes. If at least one side is not degenerately doped, for small positive biases the tunneling cannot occur, thus the negative differential resistance when the bias is increased cannot be observed. However, in reverse bias, the tunneling is allowed for this configuration as well, and the backward diode behavior can be obtained.

4.2 III-nitride based TJs

In wide bandgap semiconductors such as III-nitrides, the tunneling barrier is high. Furthermore, degenerate doping is difficult to obtain, especially for p -type material because of the more pronounced dopant compensation together with the large activation energy of the Mg impurity. Moderate p -doping levels imply wide depletion widths, frustrating the interband tunneling process. Thus the scientific community is facing challenges for the realization of TJs in this material system.

TJs formed by an heavily doped p^{++}/n^{++} GaN junction in series with a p - n junction (n - p - n architecture) exhibiting good I - V characteristics have only been reported once [190]. However, the device featured a blue emitting InGaN based active region and no light could be observed up to current densities of 2 kA cm^{-2} , suggesting strong leakage paths. These devices were grown by MOVPE. During the same time period at Agilent Technologies Laboratories, GaN-based tunnel junctions featuring an InGaN interlayer at the junction interface were demonstrated with moderate tunneling currents [191], together with a vertical cavity light emitting diode [192]. The use of a 15 nm thick InGaN interlayer was motivated by higher acceptor and hole concentrations in this materials system.

The working principle of this TJs design was elucidated in 2007 by Grundmann *et al.* [193]: when a dissimilar material is placed at the junction interface, a polarization induced dipole is formed at the interfaces with the surrounding material because of the giant built-in polarization fields of III-nitrides. The potential drop induced by the dipole can assist the carrier tunneling thanks to the reduction of the depletion region, when the field is oriented in the same direction of the p^{++} - n^{++} junction one [194]. If the band bending resulting from the introduction of the interface layer is even stronger than the one induced by the p^{++} - n^{++} junction, accumulation regions (2DEG and 2DHG) are formed at the interfaces and the depletion width

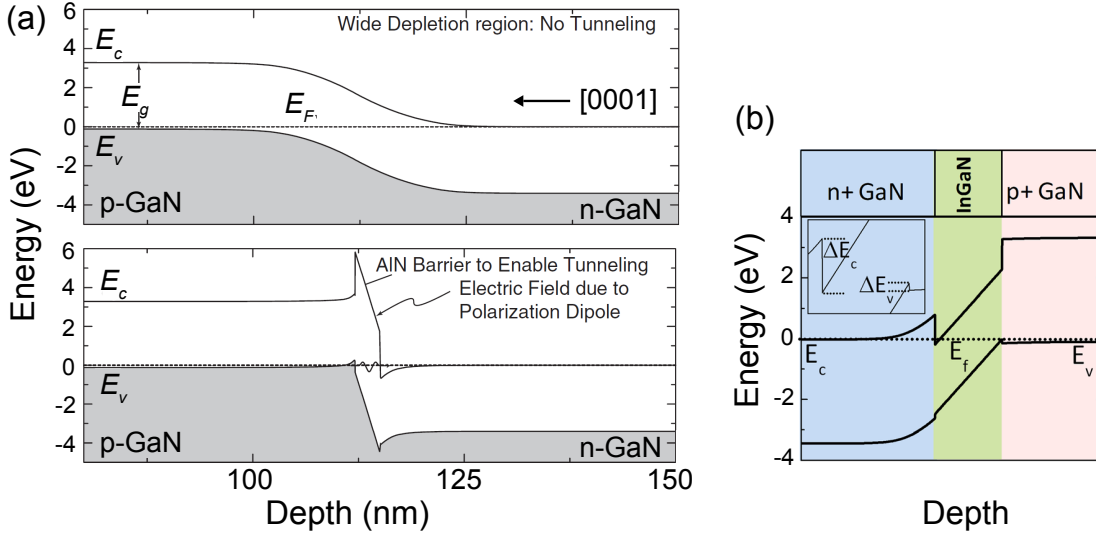


Figure 4.2: (a) Energy band diagram of a p - n junction doped with $N_A \approx N_D \approx 1 \times 10^{19} \text{ cm}^{-3}$, and (bottom) the same structure with a 3 nm thick AlN interlayer where the polarization field reduces the depletion region width. (b) Energy band diagram of a GaN/InGaN/GaN tunnel junction. (a) and (b) have been taken from Refs. [10, 195], respectively.

can be even lower than the thickness of the interlayer. For example, at the AlN/GaN interfaces, a polarization sheet charge density of $6 \times 10^{13} \text{ cm}^{-2}$ is present, resulting in an electric field of 12 MV cm^{-1} when no other charges are considered [195]. Simon *et al.* have shown that it is possible to reduce the depletion width down to the interlayer thickness [195] by inserting a 2.8 nm thick AlN interlayer between n -GaN and p -GaN following the growth direction (Fig. 4.2(a)).

The reduction of W can also be achieved using InGaN interlayers, but the device structure must be reversed given the direction of the polarization fields. Therefore, the n -type region of the tunnel junction must be grown after the p -type region when growing along the [0001] crystal direction (Fig. 4.2). The lowest TJ specific resistance have been obtained, down to $1.2 \times 10^{-4} \Omega \text{ cm}^2$ [10], by employing a 4 nm thick $\text{In}_{0.25}\text{Ga}_{0.75}\text{N}$ interlayer and performing the growth by PAMBE. This configuration is advantageous with respect to AlN for two reasons: first, the lower bandgap of the interlayer material reduces the tunneling barrier, and secondly, the TJ is placed at the end of the p -type growth where the doping control is easier. Because of surface segregation effects and/or doping delays, the Mg level when starting the growth is difficult to control. Furthermore, when considering the time/depth dependent Mg compensation process, it is preferable to grow the highly doped p -doped region forming the TJ as late as possible. The drawback, however, is the light absorption of the interlayer with a high In composition, limiting its application in VCSELs for instance.

To overcome the InGaN absorption losses, the introduction of midgap states at the junction interface was proposed. To this aim, gadolinium nitride nanoislands (GdN), with a theoretical indirect bandgap of 0.7 - 0.85 eV [196], were inserted in the TJ. The midgap states reduce

the tunneling width and thus increase the tunneling currents. With this approach a specific resistance of $1.3 \times 10^{-3} \Omega \text{ cm}^2$ was obtained [196].

Given the high $N_A - N_D$ concentrations mastered by NH_3 -MBE, the growth of GaN TJ was attempted during this thesis, without the use of either polarization engineered layers nor midgap states. The potential advantages are: high transparency (low optical losses), relatively simple process, and the absence of potential contaminating species (Gd) in the MBE reactor. In this configuration, the doping in the TJ region is required to be as high as possible, while keeping a high structural quality.

4.3 Interest in III-nitride tunnel junctions

Apart from a mere scientific interest, TJs in this material system could enhance device performance and enable novel designs. For several III-nitride based devices, the low conductivity of the p -doped layers limits the device performance. For example in LEDs, the p -contact electrode must entirely cover the electrically injected active region because of the reduced lateral carrier spreading in p -type GaN. Often this p -electrode is an Ag-based layer which on top of its electrical role is used as reflector, the light being emitted from the bottom n -side of the device in a flip-chip design where the substrate can be removed [197]. However, one of the most efficient designs for increasing the light extraction employs patterned sapphire substrates, which scatter the light coming from the active region back to the top surface, limiting total internal reflection (TIR) issues [198]. The light is thus extracted from the top p -doped surface, setting the requirement for a transparent contact. Currently, transparent conducting oxides (TCOs), principally ITO are used. However they could be replaced by a TJ used to inject holes in p -type material in combination with a n^+ top layer, allowing low resistivity n -type contacts.

Issues related to the poor conductivity of p -type Al containing III-nitride cladding layers in LDs could also be relaxed. The TJ could be used between the upper waveguide and cladding layers, decreasing the total device resistivity, especially in UV LDs. Furthermore, given the above-mentioned spreading capabilities of the TJ, the top contact above the ridge could be moved to the side and air used as top cladding, increasing thereby the confinement factor.

TJs could also be employed to overcome the efficiency droop: while the peak IQE is high for standard LEDs used for general lighting, this value quickly decreases as the injected current density increases. Therefore the output power per device area is limited. Indeed, nano- or micro-column LEDs are currently investigated to increase the active region volume per unit area which would translate into higher output powers at similar current densities. Another approach is to cascade several active regions interconnected by TJs, making use of tunneling-based carrier regeneration [199]. In this way as well, the increase in the injected QW number should result in higher output powers at constant current densities.

Another application TJs may find is the current aperture definition in VCSELs. One solution is

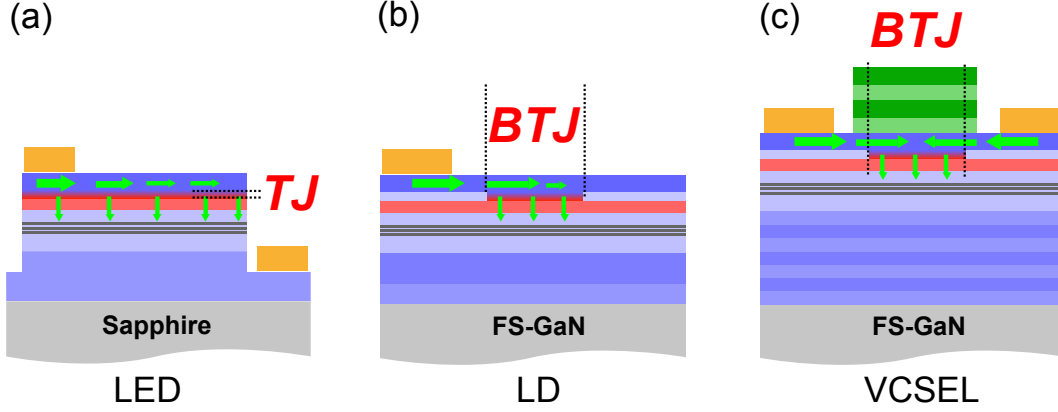


Figure 4.3: Schematic representation of three device designs featuring a TJ: (a) LED, (b) edge emitting LD where the ridge is formed by a buried tunnel junction, and (c) a VCSEL. Blue is used for n -type and n^{++} layers, red for the p -type ones. The VCSEL features a bottom epitaxial DBR, and a top dielectric DBR. The n -type metal contacts for the LD and the VCSEL are not shown for the sake of simplicity.

to use an ITO layer that spreads the current below the top DBR, where a current aperture is placed. The current aperture is generally formed by opening a window in a SiO_2 or SiN layer [200–202], or by plasma damage on the p -surface prior to ITO deposition [202] where reactive ion etching is used to strongly degrade the electrical properties of p -GaN except from the region where current needs to be injected. However, especially at short wavelengths, the ITO layer in the cavity introduces absorption losses. If a buried TJ (BJT) is used instead for defining the current aperture, the top n^+ layer can be employed to spread the current below the DBR, and the ITO layer can be removed, thus reducing the internal losses. It is worth noticing that the majority of arsenide and phosphide based VCSELs feature BTJs [203–205].

Finally, in a similar configuration, a buried TJ could also be implemented in photonic crystals (PhC) to inject the current in the active region while placing the contacts far away from the PhC structure.

In conclusion, TJ could be used in a variety of configurations to improve the performance of III-nitride based devices.

4.4 Technical challenges for achieving efficient TJs

The problem of Mg segregation and incorporation delays was introduced in Sec. 4.2. TJs having the overdoped p -type region above the n -type one, require an extremely sharp Mg doping profile at the interface. Therefore incorporation delays or segregation of Mg towards the surface must be limited.

On the other hand, in the p -type-down configuration, the latter effects do not play a major role

on the TJ doping profile. However, the sharpness of the transition from p - to n -type materials determines the actual net acceptor and net donor concentrations in the junction region, thus the depletion width and eventually the tunneling rates. This could be an issue when attempting the growth by MOVPE, where Mg memory effects make this fast transition challenging. Besides, strong Mg memory effects have not been reported so far in MBE. Hydrogen passivation of the Mg acceptor must also be taken into account when designing a tunnel junction. In III-nitrides, when p -type material is buried under n -type one, the low permeability to hydrogen of (Al)GaN:Si layers, makes the removal of hydrogen in the buried layer difficult [206]. In general it was suggested that hydrogen migrates in p -type material but not in the n -type one [207, 208]. A channel to extract H passivating Mg can be formed by etching material surrounding the device, with hydrogen diffusing along the p -layers towards the etched mesa sidewalls [206]. The absence of hydrogen passivation under standard growth conditions combined to the reduced memory effects makes MBE growth advantageous with respect to MOVPE for growing p -type-down TJs.

Several n - p - n structures were grown by NH_3 -MBE during this thesis in the p -down configuration, given the absence of hydrogen passivation in NH_3 -MBE.

4.5 n^+ -type doping of GaN in NH_3 -MBE

To achieve efficient tunnel junctions net donor concentrations above $1 \times 10^{20} \text{ cm}^{-3}$ have to be mastered. n -type doping of GaN was investigated in the framework of a project between EPFL and ETHZ for the realization of regrown ohmic contacts for high electron mobility transistors (HEMTs) [209, 210]. Given the reduced growth temperatures of MBE, this growth technique was identified as the technology of choice for making highly doped regrown contacts while reducing the impact on the 2DEG properties. The n -type doping was thus optimized at 700°C in our Riber Compact 21 MBE reactor. Given the low growth temperature, low growth rates were employed to minimize kinetics roughening effects. To keep a smooth 2D morphology the layers were grown at 80 nm/h . High ammonia fluxes were seen to limit the Si incorporation. Thus the NH_3 flow employed during growth was 50 sccm , ensuring stable nitrogen rich conditions. Silicon was provided from a standard single-filament effusion cell with temperatures ranging from 1240 to 1285°C .

The typical sample structure corresponds to 80 - 100 nm of n^{++} -GaN grown by NH_3 -MBE on top of semi-insulating buffer layers grown by MOVPE on sapphire substrates. Hall effect measurements were used to determine the electron carrier density and mobility in the so-formed layers. C - V profiling could not be performed on these layers, as the high electron concentration made the creation of the holes necessary for the electrochemical etching extremely difficult. For carrier densities varying between $5 \times 10^{19} \text{ cm}^{-3}$ and $2 \times 10^{20} \text{ cm}^{-3}$ electron mobility values ranging from 112 to $69 \text{ cm}^2\text{V}^{-1}\text{s}^{-1}$ were measured, respectively. Those values are inversely proportional to the [Si] as shown in Fig. 4.4(b). The resistivity decreases as well as [Si] is increased, reaching a record value of $3.5 \times 10^{-4} \Omega \text{ cm}$ for a doping level of $1.8 \times 10^{20} \text{ cm}^{-3}$

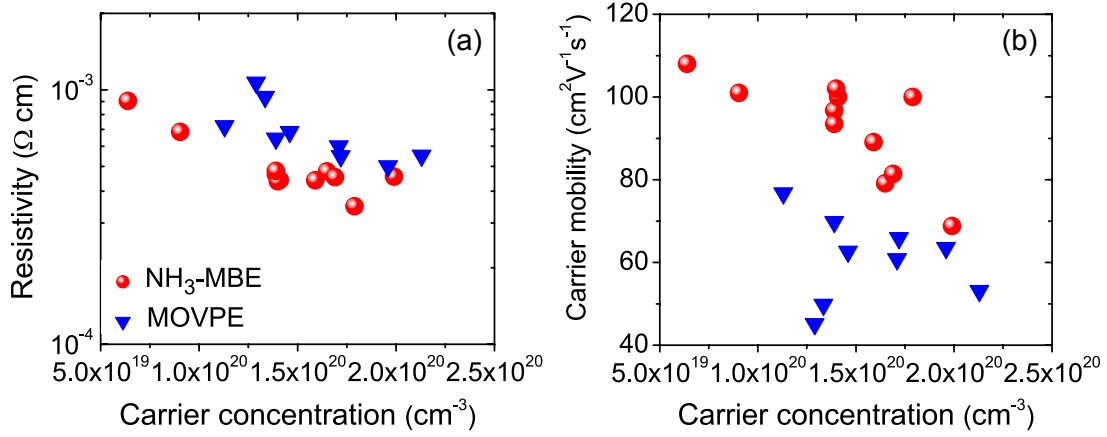


Figure 4.4: (a) Resistivity and (b) mobility as a function of the carrier concentration measured by Hall effect measurements on highly doped n -GaN layers at RT.

(Fig. 4.4(a)). The resistivity is seen to saturate around this value when the doping is increased likely due to impurity scattering limiting the carrier mobility. Those results are in line with the published data reported on highly Si-doped GaN by PAMBE [211] and NH₃-MBE grown GaN [212].

The layer exhibiting the lowest resistivity was further investigated by SIMS for [O], [C], and [Si], to access the Si impurity level and potential sources of contamination (Fig. 4.5(a)). The Si profile of this layer is flat at a level of $[\text{Si}] = 1.7 \times 10^{20} \text{ cm}^{-3}$, which is consistent with the level determined by Hall effect. The [O] slightly increases in the n -type region to $\approx 2 \times 10^{18} \text{ cm}^{-3}$ while [C] remains unchanged at a value of $\approx 3 \times 10^{16} \text{ cm}^{-3}$ close to the detection limit. The reported values correspond to the 50-90 nm depth range of the SIMS measurements. Note that artifacts are present at surface. In fact, a special cleaning procedure was also performed

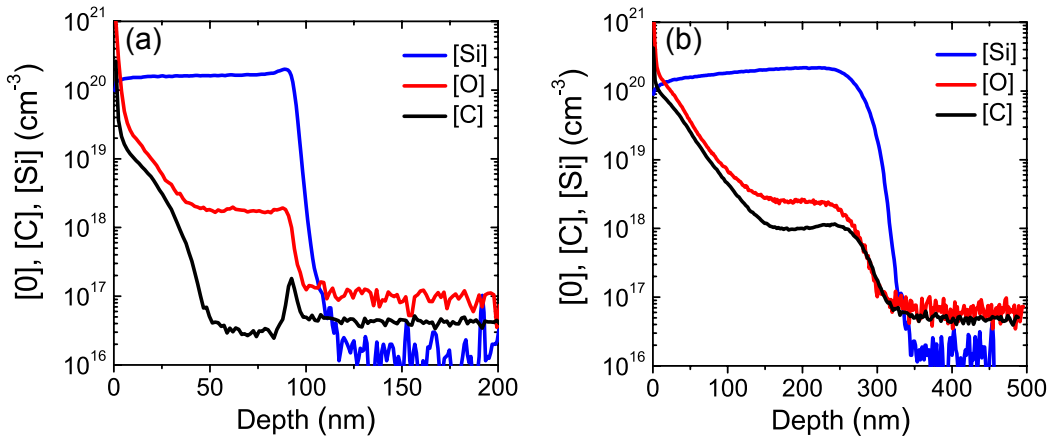


Figure 4.5: SIMS profiles for [Si], [O], and [C], of GaN:Si epilayers grown by (a) NH₃-MBE, and (b) MOVPE.

prior to SIMS analysis to minimize those unwanted effects.

An MOVPE grown layer with similar carrier concentration was also investigated by SIMS for comparison (Fig. 4.5(b)). For this 300 nm thick layer, the special cleaning procedure was not performed. The [Si] and [O] levels are similar for the two samples. However, the [C] level in the sample grown by MOVPE is two orders of magnitude higher. In Fig. 4.4(b) the lower mobility exhibited by MOVPE samples is evident. The reason could be attributed to the higher [C] level, which is often reported to limit the carrier mobility in GaN [213].

In conclusion high $N_D - N_A$ concentrations can be achieved by MBE, while keeping a high mobility. Indeed, the so-formed layers exhibit state-of-the-art resistivity values, saturating for doping levels above $1.5 \times 10^{20} \text{ cm}^{-3}$. Thanks to the reduced growth temperature (700°C), and the absence of H passivation in the MBE environment, these epilayers are compatible with the growth of III-nitride TJs.

4.6 *n-p-n* structures featuring TJs

The doping levels demonstrated by NH_3 -MBE, together with expected sharp interfaces and the lack of hydrogen passivation, are key assets for achieving TJs. In the following we focused on the *n-p-n* configuration, where *n*- contacts can be used for efficient current spreading.

4.6.1 Hybrid LEDs with TJs

As a proof of concept, the first test structures are LEDs featuring a TJ in the upper portion of the structure, as shown in Fig. 4.3(a). The bottom part of the structure, up to the *p*-AlGaIn EBL was deposited by MOVPE. The sample was then transferred to the MBE reactor for the growth of 150 nm of GaN:Mg, followed by the TJ composed of 50 nm of p^{++} -GaIn and 15 nm of n^{++} -GaIn, and 60 nm of *n*-GaIn serving as a current spreading layer with a gradual decrease in [Si] when moving away from the TJ down to $4 \times 10^{18} \text{ cm}^{-3}$ at the surface. A growth interruption was performed at the TJ interface to adjust the growth conditions for the *n*-type growth.

The sample was then processed by standard lithographic steps. 500 nm high circular mesas of varying diameters (from 500 down to 150 μm) were realized by ICP etching. Standard Ti/Al/Ti/Au contact electrodes were used to contact the top and bottom *n*-GaIn layers. The top electrode consisted of an annular contact in order to access the spreading characteristics, as shown in the inset of Fig. 4.6(b). Decent forward currents were obtained, with current densities of 20 A cm^{-2} at a forward bias (TJ in reverse bias) of 4.9 V, at least 1.5 V higher with respect to standard LEDs. However, light was seen to be homogeneously generated across the whole device, despite the annular contact, confirming the spreading characteristics of the TJ. The low forward current density for which light is observed ($1 \text{ mA} \approx 0.5 \text{ A cm}^{-2}$) on 500 μm devices demonstrates the presence of low leakage paths. This is confirmed by the *J-V* currents below the detection limit in the 0-2 V range. However, both the turn on voltage and

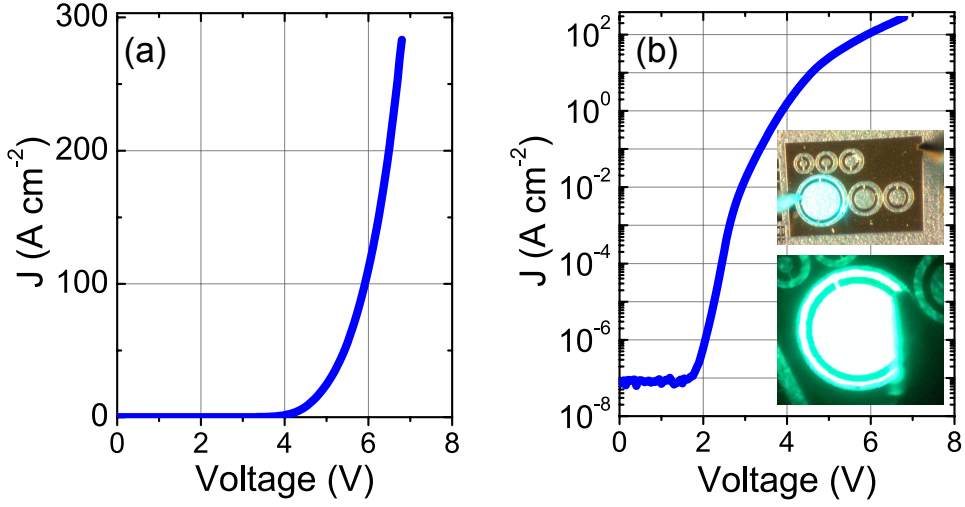


Figure 4.6: J - V characteristics of the n - p - n structure measured on a $150\ \mu\text{m}$ wide circular mesa. (a) linear and (b) semi-logarithmic plot. The insets in (b) show the homogeneous light emission of a $500\ \mu\text{m}$ wide device driven under $1\ \text{mA}$ of current.

the specific resistivity of the device when measured on $150\ \mu\text{m}$ wide circular mesas are high, above $4\ \text{V}$ and in the mid $10^{-3}\ \Omega\ \text{cm}^2$, respectively. Those values are much higher than the state-of-the-art [10]. We suspect that, given the geometry of the two contacts shown in the inset of Fig. 4.6(b), current crowding occurs in the vicinity of the mesa borders, where the path to reach the bottom n -contact is shorter, limiting the device performance.

We investigated the doping profile by SIMS due to the difficulty of measuring ECV profiles on highly n -type doped layers (Fig. 4.7). The n - and p -type doped regions reach doping levels of $1.6 \times 10^{20}\ \text{cm}^{-3}$ and $7.2 \times 10^{19}\ \text{cm}^{-3}$, respectively. The potential carbon and oxygen contamination is low, below $4 \times 10^{17}\ \text{cm}^{-3}$, along the TJ despite the growth interruption. On

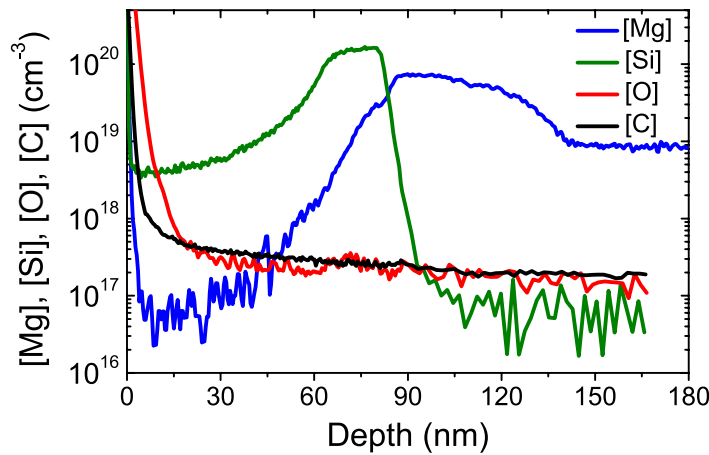


Figure 4.7: SIMS profiles for Mg, Si, O, and C around the NH_3 -MBE grown TJ.

the other hand, at the tunnel junction interface, a dip is observed in the doping profile: 6 nm separate the Si peak from the Mg one in the TJ region. This results in larger depletion widths, strongly affecting the carrier tunneling. In the absence of doping delay, the width of the depletion region for these doping concentrations would be around 8 nm, calculated from Eq. (1.8), for zero applied bias. It is therefore of primary interest to improve the sharpness of the doping transition. Furthermore, [Mg] is seen to decrease slowly after the closing of the shutter cell, at a rate of one decade/15 nm. During the growth of this sample, the Mg valve was not closed together with the cell shutter at the end of the *p*-type region, and possibly unwanted Mg was supplied in the chamber while completing the structure, explaining the slowly decreasing Mg tail in Fig. 4.7.

In conclusion, TJ were grown by NH_3 -MBE on top of MOVPE grown active regions exhibiting moderate *I-V* characteristics. SIMS measurements indicated a non-optimal doping profile in the vicinity of the junction interface, leading to reduced tunneling currents.

4.6.2 TJs on FS-GaN substrates

The entire growth by NH_3 -MBE of the *n-p-n* structure was also attempted in order to limit issues arising from the hybrid approach. In addition, a FS GaN substrate was used, enabling to take the bottom *n*-type contact on the substrate backside. The sample structure is similar to the previous one. A Ga-polar *c*-plane FS GaN substrate with a dislocation density in the low 10^6 cm^{-2} was used. After 600 nm of GaN:Si, *p*-doped GaN layers were successively grown without growth interruption. The sequence consisted of 140 nm of GaN:Mg with [Mg] of $1 \times 10^{19} \text{ cm}^{-3}$, 50 nm with [Mg] of $3 \times 10^{19} \text{ cm}^{-3}$, and a 25 nm thick cap having a Mg level doping of $1 \times 10^{20} \text{ cm}^{-3}$. A growth interruption of 10 min was then performed to adapt the growth conditions

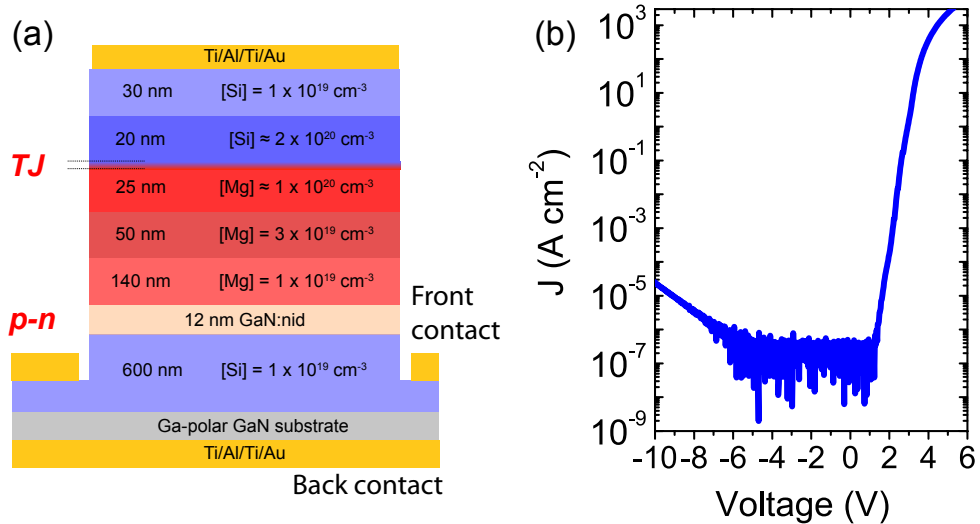


Figure 4.8: (a) Schematic diagram of the sample structure. (b) Semi-logarithmic plot of *J-V* characteristics measured on $50 \times 50 \mu\text{m}^2$ devices.

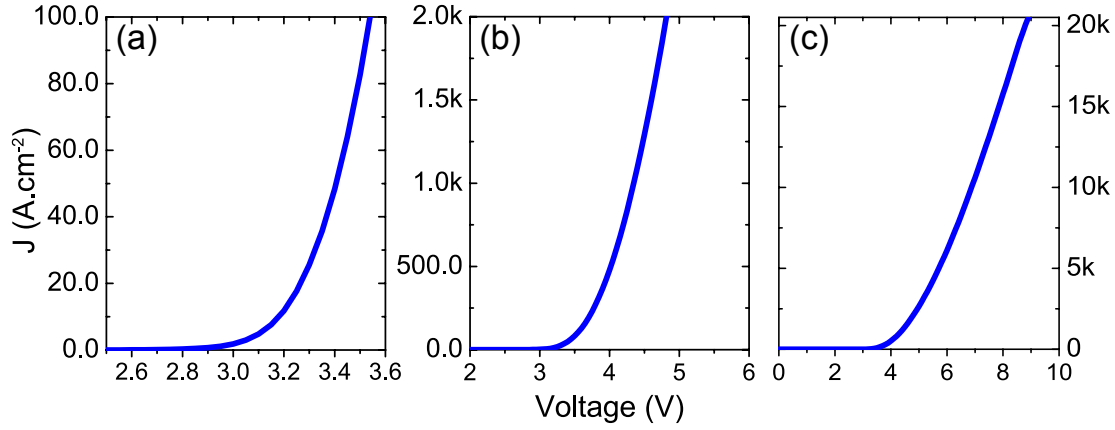


Figure 4.9: (a),(b), and (c), show the J - V characteristics of the full NH_3 -MBE TJ using different J and V scales measured on $50 \times 50 \mu\text{m}^2$ devices.

for the deposition of the GaN:Si^{++} layer at 700°C . The structure was terminated by 20 nm of GaN:Si with $[\text{Si}]$ of about $2 \times 10^{20} \text{ cm}^{-3}$ and 30 nm with a Si level of $1 \times 10^{19} \text{ cm}^{-3}$. A schematic representation of the sample structure is shown in Fig. 4.8.

The epiwafer was then processed into devices ranging from 300×300 to $30 \times 30 \mu\text{m}^2$ square devices. The bottom n -contact was first placed on the surface of the lower n -type layer (front contact). The top contact covered the whole mesa structure. The so-formed devices exhibited remarkable electrical characteristics as shown in Fig. 4.8(b): at a reverse bias of 10 V, the current density is as low as $4 \times 10^{-5} \text{ A cm}^{-2}$, indicating low leakage currents in the whole processed structure. In forward bias (TJ in reverse bias, Fig. 4.9), the voltage is as low as 3.3 V and 4.8 V for current densities of 20 and 2000 A cm^{-2} , respectively. In addition, the stability and low resistance of the TJ enable reaching current densities above 20 kA cm^{-2} in cw operation. From the J - V characteristics one can calculate the total specific resistance (ρ_{tot}) which account for the metal-semiconductor contact, series, and TJ resistance. A value $\rho_{tot} = 3.7 \times 10^{-4} \Omega \text{ cm}^2$ was measured at 5 V (Fig. 4.10). This value is close to the best reported one using polarization engineered TJs for which $\rho_{tot} = 4.7 \times 10^{-4} \Omega \text{ cm}^2$ [10]. When subtracting the contact resistance contribution measured by TLM, the authors evaluated a ρ_{TJ} of $1.2 \times 10^{-4} \Omega \text{ cm}^2$ [10]. In our case, a precise value for the contact resistance of the bottom n -type layer over which the current flows from one TLM pad to another. For the top electrode, a value of $6 \times 10^{-6} \Omega \text{ cm}^2$ is found by TLM.

On 1/6 of the wafer a bottom n -type contact was placed on the backside of the FS GaN substrate (back contact). This was done to reduce the contact resistance of the bottom contact and to reduce potential current spreading limitations. The devices were then measured on both configurations (Fig. 4.10)(b). A lower resistance was found for the backside contact configuration, with an average forward bias reduction of 0.17 V at a current density of 1

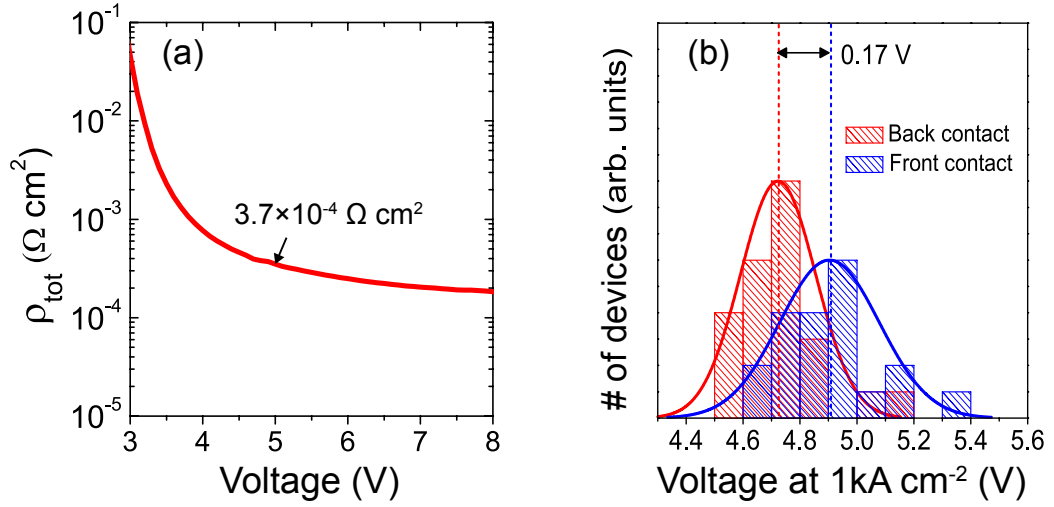


Figure 4.10: (a) Total specific resistance as a function of applied bias. (b) Comparison of the electrical characteristics when using a top contact electrode or one on the backside of the GaN substrate.

kA cm^{-2} when measured on $50 \times 50 \mu\text{m}^2$ devices. Unfortunately, the devices on this wafer region exhibited slightly higher resistance values than the best ones found previously. It is however clear that the J - V characteristics measured with the frontside contact could be further improved using the bottomside contact configuration.

In conclusion, structures featuring TJs in series with a p - n junction were grown by NH_3 -MBE. They exhibit state-of-the-art electrical characteristics, while avoiding the use of polarization engineered layer which could introduce optical losses when combined with optoelectronic devices. Total specific resistivity values for the entire n - p - n structure are as low as $3.7 \times 10^{-4} \Omega \text{ cm}^2$.

4.6.3 Hybrid TJs

At present, efficient tunnel junctions cannot be grown by MOVPE at EPFL. The difficulty of removing the hydrogen-induced passivation when the p -doped layers are buried below the n -type ones, combined with the MOVPE characteristics memory effects, still prevent their realization. Thus, to benefit from the high quality of InGaN based active regions grown by MOVPE, a hybrid TJ structure was designed. To this aim a standard LED wafer was fully grown by MOVPE, featuring a highly doped p -type contact layer. After the growth, the structure was activated under normal RTA annealing conditions. The wafer was then cleaved in half, and one part was processed with Pd/Au and Ti/Al/Ti/Au metal contacts for the p - and n -type contact electrodes, respectively. The remaining half wafer was inserted in the MBE reactor, where 25 nm of highly doped GaN:Si were deposited at 700°C to form a TJ, thus a n - p - n structure. During the whole MBE growth the RHEED remained streaky, indicating a 2D surface morphology. This wafer was processed as well by photolithographic steps using the same

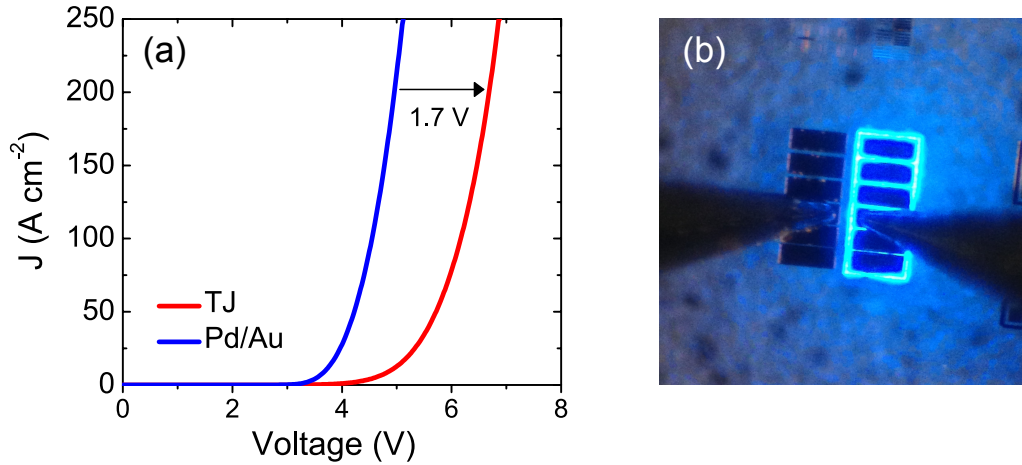


Figure 4.11: (a) Comparison between the J - V characteristics of a normal LED (blue line), and a hybrid $n-p-n$ structure fabricated from the same wafer (red line). (b) Electroluminescence of the $n-p-n$ structure under forward bias (TJ in reverse bias). The TLM structures are 200 μ m wide.

masks and process as the previous one, but with top and bottom n -type Ti/Al/Ti/Au contact electrodes.

The electrical characteristics were then measured on 200 \times 200 μ m² devices. Tunnel injection of holes in the p -doped layer was confirmed by the luminescence of the device featuring the tunnel junction. This occurs already for low forward currents (0.2 mA) as shown in Fig. 4.11(b). The luminescence is shown from the TLM mesa of the top electrode. The current spreading characteristic of the $n-p-n$ structure can be noticed on this picture where light is seen to arise from the whole mesa without being confined to a single TLM pad.

The comparison of the J - V characteristics is displayed in Fig. 4.11(a). For comparable current densities (200 A cm⁻²) the TJ junction structure requires forward biases 1.7 V higher than the standard LED one. The difference is large, but the result is obtained without performing any optimization of the p -doping profile in the MOVPE grown contact layer which has a maximum $N_A - N_D$ level of $\approx 4 \times 10^{19}$ cm⁻³ at the surface. Therefore, the tunneling characteristics could still be improved. More importantly, the problems limiting the realization of efficient TJs in our reactor were identified allowing efficient tunnel injection of the carriers.

4.6.4 Buried tunnel junctions

Buried TJs are another interesting use of $n-p-n$ structures for which the current spreading is combined to the current confinement. Such structures are of especial interest for VCSELs. These are realized by selectively etching through the TJ down to the p^- -layer in the region where the current injection wants to be suppressed. By successively overgrowing a thick n -layer, starting with low [Si], the etched interface becomes a $p-n$ junction in reverse bias

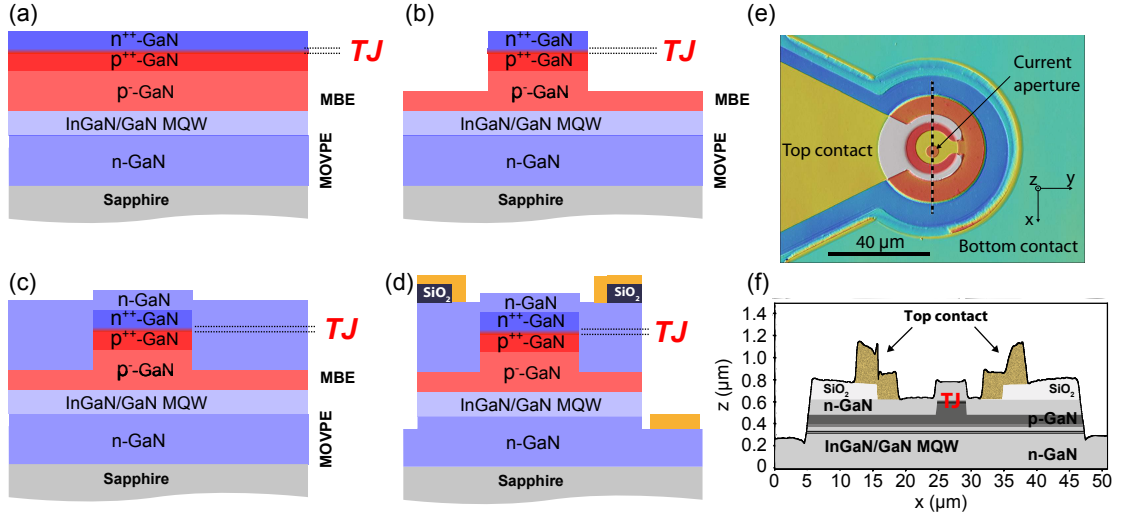


Figure 4.12: (a),(b), (c), and (d), schematic representation of the process flow. (a) *p*-type doping and TJ growth by MBE on top of a MOVPE active region. (b) Aperture definition via ICP etching, (c) MBE *n*-GaN regrowth, (d) Device isolation and contact deposition. (e) Confocal microscopy image of the processed device. (f) Confocal microscopy profile of the device (black line) with a schematic representation of the layer structure measured along the dotted line in (e).

where the low *n*- and *p*-type doping give rise to large depletion widths and therefore negligible tunneling currents. In such a scheme the current will flow only in the region where the TJ is not etched and therefore current confinement can be achieved. With this method one could for example obtain current injection only in the region below DBRs without the use of transparent conductive oxides in III-nitride based VCSELs.

A device was fabricated to assess the properties of GaN based BTJs. First, *p*-type doping was performed by MBE on top of an active region grown by MOVPE to form an LED. A TJ was deposited on top following the procedure described in Sec. 4.6.1. The wafer was then taken out from the MBE reactor and processed in order to define the current aperture. To this aim circular mesas ranging from 4 to 16 μm in diameter, and 150 nm in depth, were fabricated by ICP. A second regrowth step was then performed by NH₃-MBE to bury the TJ with 200 nm thick GaN:Si layer. The *n*-type doping in this case was graded and increased along the growth direction, from $3 \times 10^{18} \text{ cm}^{-3}$ up to close to $1 \times 10^{20} \text{ cm}^{-3}$. In order to electrically inject the devices, the wafer was once more processed by standard lithographic steps. Mesas measuring 100, 80, 60, and 40 μm in diameter and 600 nm in height, aligned on the previously formed ones, were made by ICP-RIE to expose the bottom *n*-type GaN layer and isolate the devices. A second step involved the deposition of a SiO₂ layer to prevent short-circuits during the deposition of the top contact. Windows in the SiO₂ were realized for the two contact electrodes by lift-off. Finally, Ti/Al/Ti/Au metal contacts were evaporated and the devices characterized. The process flow is schematically described in Figs. 4.12(a)-(d). Figure 4.12(e) shows the confocal microscopy image of a 4 μm current aperture on a 40 μm circular mesa.

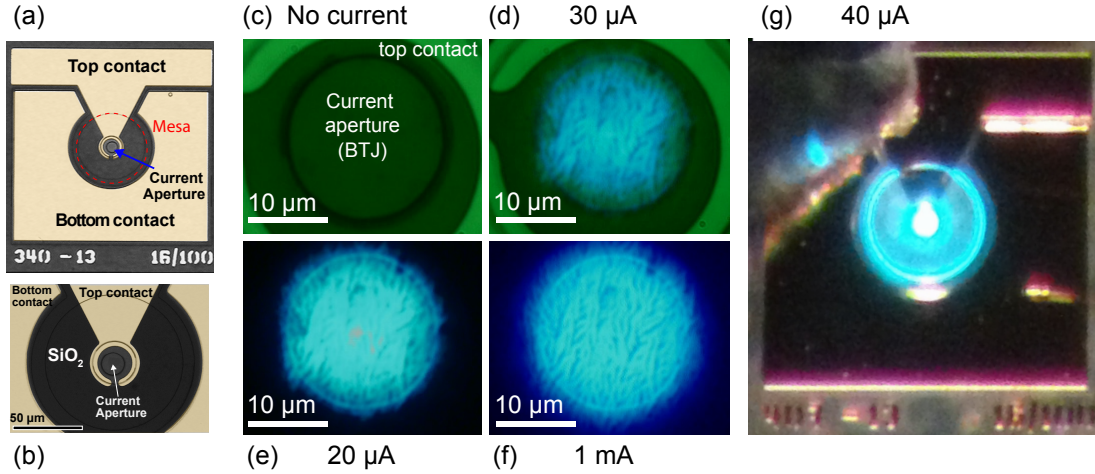


Figure 4.13: Optical micrographs of the current aperture defined by the BTJ. (a) and (b) show the contact geometry. In (d), (e), (f) and (g) the device is electrically injected. (c) and (d) are taken under external illumination. The current densities in (b) and (c) are ≈ 10 and 500 A cm^{-2} , respectively.

The depth profile for this structure is shown in Fig. 4.12(f).

The final processed device contact configuration is reported in Figs. 4.13(a) and (b). The top metal electrode is not in direct contact with the current aperture defined by the BTJ. It lies on the regrown *n*-GaN layer, aside from the BTJ as can be seen in Fig. 4.13(f) as well. The current must hence flow through the *n*-type layer before reaching the TJ. By means of a micro-PL objective, the emission from a $16 \mu\text{m}$ wide circular aperture was investigated under electrical injection. When a forward bias is applied, the light emission is confined to the region defined by the BTJ, even for high injection currents (Figs. 4.13(d), (e), and (f)). Already for low current densities the electroluminescence signal is detected in the BTJ region, an indication of low leakage currents. Light is uniformly generated below the circular current aperture suggesting negligible current crowding effects. The slight modulation of the EL intensity is associated to morphological features of the InGaN QWs arising from growth meandering [214].

The sample was also investigated by high-angle annular dark-field scanning transmission electron microscopy (HAADF-STEM). The TJ position is deduced from the nominal layer thicknesses using the InGaN/GaN QWs as a reference. Compositional variations in the BTJ region are not observed (no contrast with the GaN layers), confirming the presence of a GaN homojunction. Despite the high doping level in the p^{++} GaN layer, no pyramidal defects could be seen. In addition, lighter or darker regions are not observed at the interface between MOVPE and MBE growth, indicating the absence of extended contamination.

The *J-V* characteristics of these micro-LEDs are shown in Fig. 4.14. For the lowest aperture size ($4 \mu\text{m}$), the applied bias to reach a current density of 1 kA cm^{-2} is close to 5.5 V , a value potentially low enough for cw VCSEL operation. Despite the reduction of the BTJ to metal

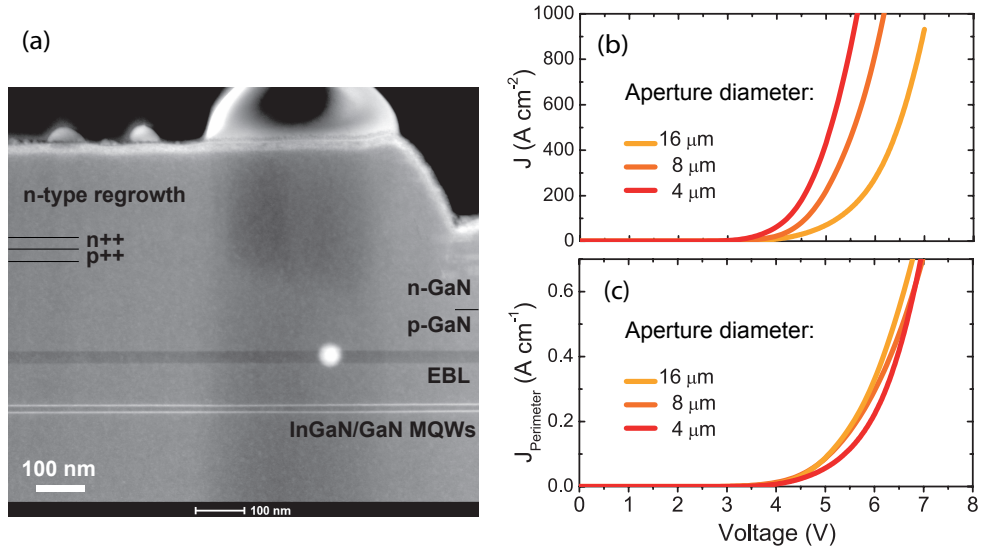


Figure 4.14: (a) High-angle annular dark-field scanning transmission electron microscopy image of the edge of the current aperture. (b) J - V characteristics for three current aperture dimensions. (c) I - V characteristics scaled with the device perimeter ($J_{\text{Perimeter}} = I / \pi D$, where D is the aperture diameter).

contact separation when the current aperture dimension is increased, the J - V characteristics degrade for larger aperture dimensions. We can postulate that the access resistance to the current aperture is affected by the small thickness of the regrown n -GaN layer (200 nm), which is of the order of the TJ etching depth (150 nm), and by a reduced doping at the regrowth interface. The scaling of the electrical characteristics with the device perimeter, as shown in Fig. 4.14, strongly supports this assumption. Further improvement of the J - V characteristics is thus expected providing a reduction of the access resistance through thicker n -GaN layer and reduced etching depth.

4.7 Towards LDs featuring BTJs

In Sec. 4.3, the use of BTJs in edge emitting LDs and VCSELs was briefly introduced. For the former devices, the advantage of such an approach resides in the possibility of avoiding the growth of thick highly resistive p -AlGaIn cladding layers. In addition, transparent n^+ -type GaN contacts allow using air as top cladding which could potentially increase the confinement factor. Alternatively, while employing standard AlGaIn cladding layers, the device could be buried below thick n -type layers in order to increase the heat dissipation limiting the device performance especially in high power LDs.

In order to test these design, and to develop a scheme to process these devices, the realization of gain-guided edge emitting LDs featuring BTJs was attempted. A hybrid approach was used for these samples as well, with the bottom cladding and active region grown by MOVPE on

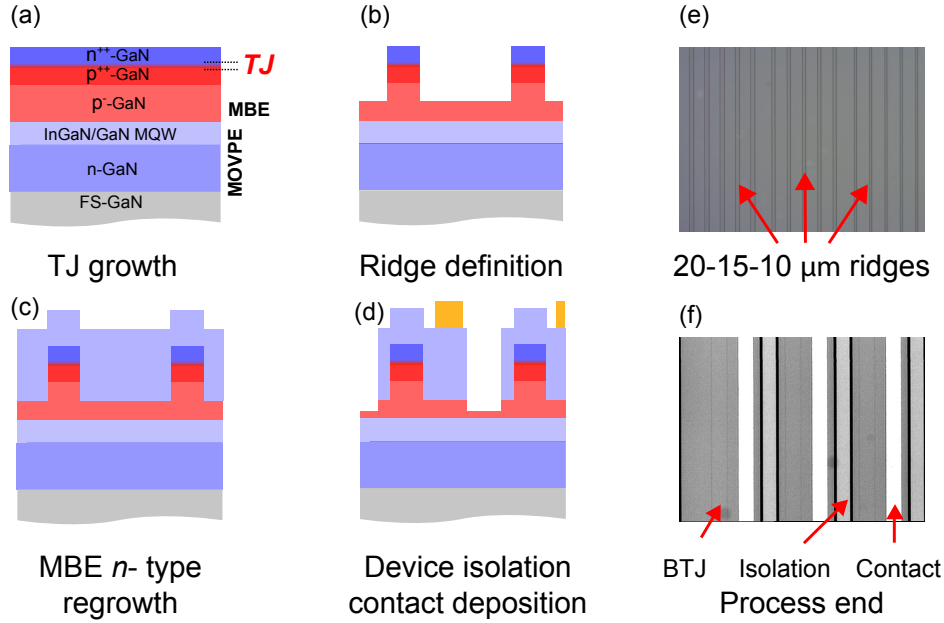


Figure 4.15: (a), (b), (c), and (d), schematic representation of the process flow. (e) and (f) are Nomarski micrographs of the sample surface after the ridge definition step, and at the end of the process, respectively.

top of a FS GaN substrate. The samples were then transferred to the MBE for the growth of the p -doped layers and TJ. The processing employed was similar to the one described in Sec. 4.6.4, but ridge-like current apertures were formed by the BTJ in contrast to the circular ones. A 400 nm thick n -GaN MBE regrowth was used to bury the TJ, to ensure a good current spreading and low access resistance. The processing was then concluded with the contact deposition and device isolation and is schematically shown in Fig. 4.15. Unfortunately, several issues have been encountered during the realization of these devices: first, the RHEED pattern of the MOVPE surface, prior to the MBE growth was not streaky but strongly blurred, an indication of a degraded surface. However during the MBE growth a streaky RHEED pattern was recovered. Secondly, the tensile strain introduced by the strong n -type doping led to crack formation, especially during the thick n -GaN regrowth step. The same process was attempted twice, and during the second regrowth the surface morphology even turned 3D. Several cleaning procedures were unsuccessful to avoid the surface becoming 3D, including HF, HCl and piranha. Therefore the processing was finished only on one sample for which the Nomarski microscopy images of the processed wafer surface can be seen in Fig. 4.15(f).

On the sample turning 3D, the surface quality after the ridge definition step (Figs. 4.15 (b) and (e)), was investigated by SEM (Fig. 4.16). An abundant contamination of the sample surface was observed together with pits in the ridge region, arising during the MBE growth. This can be noticed in Fig. 4.16. A large number of small white spheres are found away from the ridge, possibly arising from photoresist burned during the ICP etch. Black hairy-like defects

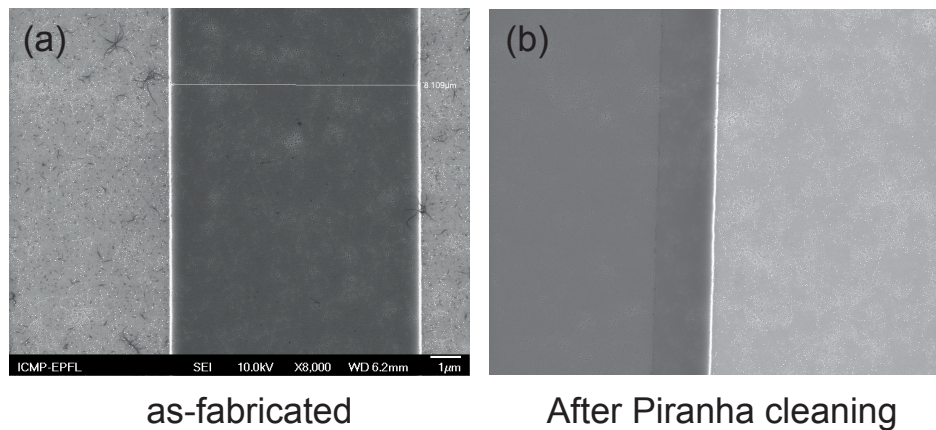


Figure 4.16: SEM micrograph of nominally 10 μm wide current apertures (a) before and (b) after piranha cleaning showing surface contamination.

are also seen in Fig. 4.15(a) but were removed during piranha cleaning. The origin of this contamination is still not well understood.

Despite the successful processing of one sample, the L - I - V characteristics were not optimal, with high turn on voltages ($> 8\text{ V}$), together with low and inhomogeneous light emission. However, the current confinement below the BTJ and light emission from the ridge like region was obtained (Fig. 4.17).

Additional attempts must thus be performed in order to achieve lasing from these structures.

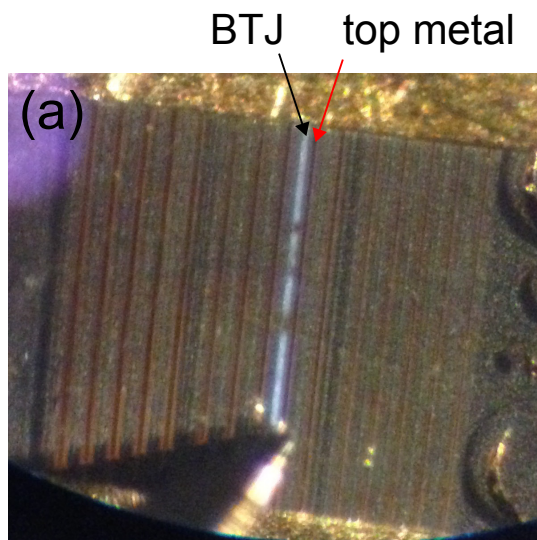


Figure 4.17: (a) optical micrograph of the structure showing the electroluminescence signal arising on the side of the metal contact where the BTJ is located. The investigated laser bar is 1 mm long.

Improvements in the MOVPE sample, in the n -type layers strain management, and on the contamination control (arising either from the processing or from the epitaxial layers) should allow reaching the objective. Unfortunately, during this thesis time did not permit any further work.

4.8 Summary

In this chapter we have demonstrated the possibility to grow TJs by NH_3 -MBE thanks to the absence of hydrogen passivation, reduced memory effects with respect to MOVPE and high net acceptor concentration.

This allowed for the demonstration of GaN tunnel homojunctions implemented in n - p - n structures exhibiting state-of-the-art electrical characteristics, matching the best values reported using either polarization engineered layers [10] or mid gap states [196]. A total specific resistance value as low as $3.7 \times 10^{-4} \Omega \text{ cm}^2$ was measured on a full MBE grown n - p - n structure. The comparison is shown in Fig. 4.18.

Several designs of optoelectronic devices were discussed making use of the TJ characteristics. In particular, the successful realization of micro-LEDs featuring a BTJ used to define a current aperture was presented. These BTJs exhibited excellent current confinement characteristics, with low leakage currents and good electrical characteristics. Such BTJs could be used in blue VCSELs or in lasers/LEDs with the aim of replacing the current TCO technology by transparent n^+ -type GaN layers. LD structures featuring buried TJs were also attempted but lasing action could not be achieved due to the combination of several technical issues.

In conclusion, the possibility to realize efficient TJs paves the way to new device architectures

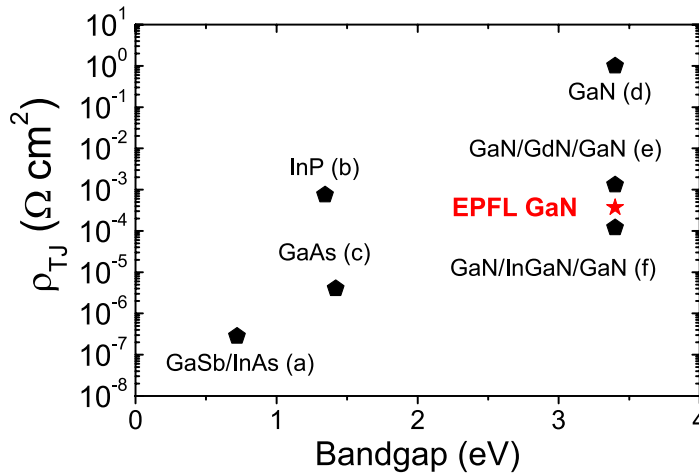


Figure 4.18: Tunnel junction specific resistance values found in the literature for different material systems. (a), (b), (c), (d), (e), and (f) have been taken from Refs. [10, 195, 196, 215–217], respectively.

which could possibly further increase the already remarkable performance of III-nitride based optoelectronic devices.

Conclusion and Perspectives

The objective of this PhD thesis was to develop a new growth approach for the realization of long wavelength III-nitride based LDs combining MOVPE and NH_3 -MBE growth technologies. The p -type doping growth by NH_3 -MBE was successfully optimized. The ultimate goal was to achieve p -type (Al)GaN epilayers exhibiting good electrical characteristics and low optical losses when introduced in hybrid LD devices. This growth technique allows to obtain extremely high net acceptor concentrations while keeping low dopant compensation. The device quality of the so-formed layers was confirmed by the demonstration of hybrid LDs operating beyond 500 nm, with state-of-the-art I - V characteristics. The unprecedented doping characteristics also enabled the growth of TJs exhibiting specific resistance matching the best values reported in the literature, while avoiding the use of polarization engineered layers which pose a threat for their integration in optoelectronic devices, especially in VCSELs.

In Chapter 1 the fundamental properties of III-nitrides were introduced together with some of the experimental techniques used in this work. The p -type doping of III-nitrides, more precisely of the (Al)GaN compound, was presented in Chapter 2 with particular attention paid to the compensation processes. The growth conditions in terms of growth temperature, V/III ratio, and growth rate were finely tuned while keeping an eye on the morphological properties of the layers. A discussion related to the reproducibility of the doping with respect to the Mg cell type was included. p -type 1 μm thick epilayers exhibiting low compensation (below 5%) along the whole epilayer thickness up to $[\text{Mg}] \approx 7 \times 10^{19} \text{ cm}^{-3}$ were obtained. The extensive use of ECV profiling has partially elucidated the p -type compensation process for samples grown by MBE and MOVPE. For both growth techniques, the onset of strong compensation corresponded to ECV profiles showing decreasing $N_A - N_D$ values when probing away from the surface, indicating a time dependent process compatible with the clustering of nitrogen vacancies with Mg. This indicates that the hole concentration cannot be considered uniformly distributed in highly doped layers. In addition, the offset between the $N_A - N_D$ and the $[\text{Mg}]$ values at the layer surface highlighted the importance of surface effects on the doping characteristics. The role of hydrogen passivation on the compensation process was experimentally confirmed by the means of thermal annealings under N_2 and NH_3 atmospheres. The absence of H passivation for MBE growth was discussed and related to the low pressure environment. Finally, an empirical model was presented to account for the compensation dependence versus time and $[\text{Mg}]$.

In Chapter 3, the incorporation of the *p*-type layers in hybrid LD structures was treated. The design considerations and challenges when attempting to grow long wavelength devices were first presented. In particular, the required thermal budget reduction on the active region was exemplified. By investigating the electrical characteristics of the *p*-doped layers, the contact layer was shown to strongly impact the *I-V* characteristics. The precise tailoring of the doping profile along the cladding layer growth aiming at the reduction of the absorption losses was also discussed. This allowed the demonstration of hybrid LDs lasing in the violet and aquamarine/green spectral regions. Thus, the thermal budget reduction on the active region proved to be effective and fulfilled the objective of this thesis. Special care was given to the transfer and cleaning of the MOVPE grown half LD structures. Moreover, the above-mentioned LD devices exhibited state-of-the-art *I-V* characteristics, confirming the doping potential of NH₃-MBE. Using the variable facet coating method, the optical quality of NH₃-MBE grown (Al)GaN layers was confirmed by the determination of internal optical losses around 6 cm⁻¹. Along Chapter 3, the detrimental effect of the inhomogeneous broadening occurring in high indium content InGaN active regions, which leads to gain dilution, was also treated both theoretically and experimentally using the variable stripe length method.

The last chapter presented the realization of GaN-only TJs grown by NH₃-MBE. First, the working principle of the TJs and the theoretical background were addressed. In the context of III-nitrides, such TJs were shown to be of major interest, but some materials limitations linked in particular to the *p*-type doping were brought to the attention. Several TJ designs were discussed, including the ones employing polarization engineered layers. The growth and characterization of highly *n*-doped layers was also included in this chapter. The introduction of a tunnel junction in series with a *p-n* junction was first demonstrated in a LED configuration to spread the current across the device. In a second attempt, by employing a similar configuration, high tunneling currents were obtained and a low specific resistance value was measured for the entire structure. The possibility to use TJs to define a current aperture was demonstrated. To this aim, a buried tunnel junction design was used, exhibiting excellent current confinement characteristics and low leakage. This latter result is particularly encouraging for the realization of VCSELs avoiding the use of indium-tin-oxide as current spreading layers.

In conclusion we demonstrated that NH₃-MBE has a great potential for *p*-type doping, and that Mg doped epilayers can be grown with excellent electrical and optical characteristics.

Outlook and perspectives

The p -type doping in III-nitrides is still far from being fully understood. A variety of experiments are still to be performed. For example, the incorporation mechanism of Mg in the GaN lattice is not well documented. The influence of the growth parameters on the surface segregation of Mg are not clear. In addition, the role of surface segregation on the compensation must be further investigated. Also, the time dependent compensation process, defined in this work as dynamical compensation, must be elucidated. To this aim, layers with high [Mg] levels could be buried below layers having reduced [Mg] levels. A difference in the dynamical compensation between the two layers could be used to understand the underlying mechanisms. On the other hand, the achievement of H passivation by MBE opens new prospects for the doping of III-nitrides with this growth technology and must be pursued. Also the surfactant effect of In, and its influence on the p -type doping needs further investigation. The potential to smooth the surface morphologies in NH_3 -MBE is technologically relevant. Above bandgap illumination of the sample during growth could also be attempted in order to decrease point defect concentration in the layers, through the Fermi level control. Finally, the doping of AlGaIn alloy can be considerably improved, as the growth conditions have not been investigated in detail during this work.

Concerning hybrid devices, the surface cleaning should be fully investigated to reduce the interface contamination. The effort should be dedicated to the optimization of the MOVPE cooling down in order to avoid C contamination from unwanted species. It could be obtained with the deposition of an In or InN protective layer in the MOVPE reactor that could then be easily removed in the MBE system before regrowth. X-ray photoelectron spectroscopy (XPS) could be employed for studying the interface contamination. Moreover, the exact location of the regrowth interface can still be improved. Together with the optimization of the doping profile in the first tens of nanometers of regrowth, it should lead to higher injection efficiency values, thus higher slope efficiencies and lower threshold values.

Further work needs to be performed on the TJs. The optical losses introduced by the TJ configuration are still unknown and could be studied. Also, doping delays at the interface between n -type and p -type GaN should be further optimized. In addition, TJs in AlGaIn alloys with moderate Al compositions should be attempted for UV LEDs and LDs applications. The processing steps to bury the TJ require further validation. To this aim, processing contamination must be kept low. Moreover, the tunneling mechanism needs to be investigated in detail: it is unclear if the high tunneling currents could be explained or improved by a high concentration of point defects at the junction interface. This could generate midgap states which reduce the tunneling width.

In conclusion, the work to fully understand the experimental results on TJs and hybrid devices has just started. Many interesting devices could be developed in the future, from deep UV LEDs to blue VCSELs.

A Appendix

A.1 Resistivity vs net acceptor concentration

Along this thesis the doping characteristics were extensively discussed in terms of $N_A - N_D$ values. Here, the relationship between the sheet resistance and the net acceptor concentration is discussed. Both values are measured on 1 μm thick MOVPE grown samples and TLM measurements are used to extract R_s . Figure A.1(a) shows the evolution of both values as a function of $[\text{Mg}]$ (the net acceptor value is taken in the middle of the layer). It is clear that the $N_A - N_D$ maximum correspond to a minimum in R_s . When the doping is further increased, the decrease in net acceptor is accompanied by an increase in R_s . When plotting R_s as a function of $N_A - N_D$ the relationship becomes evident (Fig. A.1(b)): the sheet resistance strictly depends on the net acceptor value and does not depend on $[\text{Mg}]$. When similar $N_A - N_D$ values are

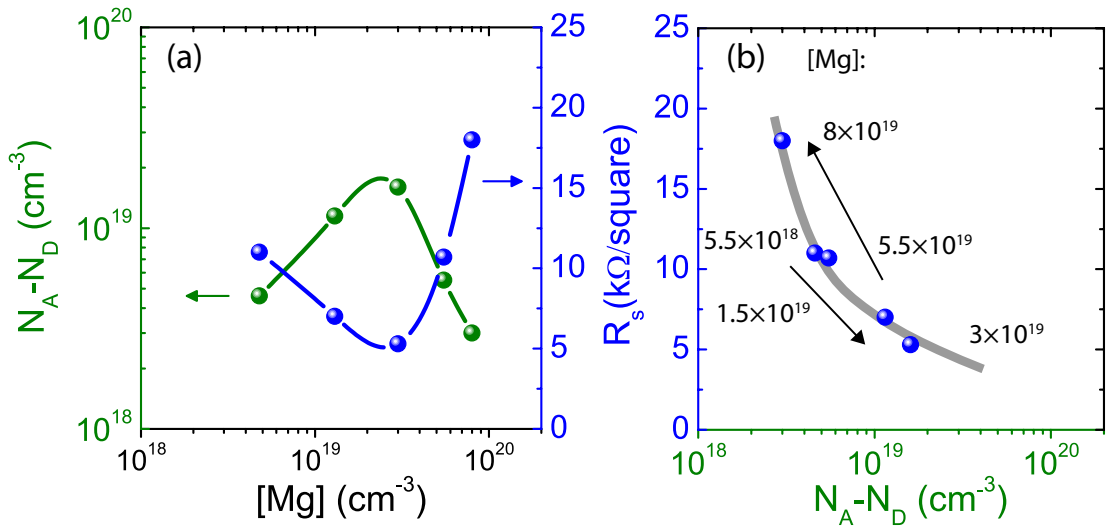


Figure A.1: (a) Evolution of $N_A - N_D$ and R_s as a function of $[\text{Mg}]$. (b) R_s as a function of $N_A - N_D$, the corresponding $[\text{Mg}]$ is indicated close to the experimental points. Courtesy of A. Castiglia.

considered, the same R_s value is obtained from two samples having an order of magnitude difference in $[Mg]$ ($N_A - N_D \approx 6 \times 10^{18} \text{ cm}^{-3}$ in Fig. A.1(b)). In conclusion high $N_A - N_D$ values directly translate to low resistivity values. For the experimental range considered, the saturation of the sheet resistance due to increased impurity scattering is not observed yet.

A.2 MOVPE net acceptor profiles

We have extensively discussed the $N_A - N_D$ profiles for MBE grown layers together with the depth dependence for highly doped samples. Figure A.2 presents the corresponding profiles for MOVPE grown layers. We have seen that up to $[Mg] \approx 1.8 \times 10^{19} \text{ cm}^{-3}$, the profiles are flat. For $[Mg] = 2.8\text{--}3.2 \times 10^{19} \text{ cm}^{-3}$ an evolution along the epilayer thickness is already observed, but both $N_A - N_D$ in the middle of the layer (depth = 500 nm), and the average net acceptor value, reach the maximum level for this set of growth conditions. For higher doping levels (Fig. A.2(b)) the $N_A - N_D$ level decreases when moving away from the surface. The average and mid-layer values are both lower than the previous one despite higher $[Mg]$.

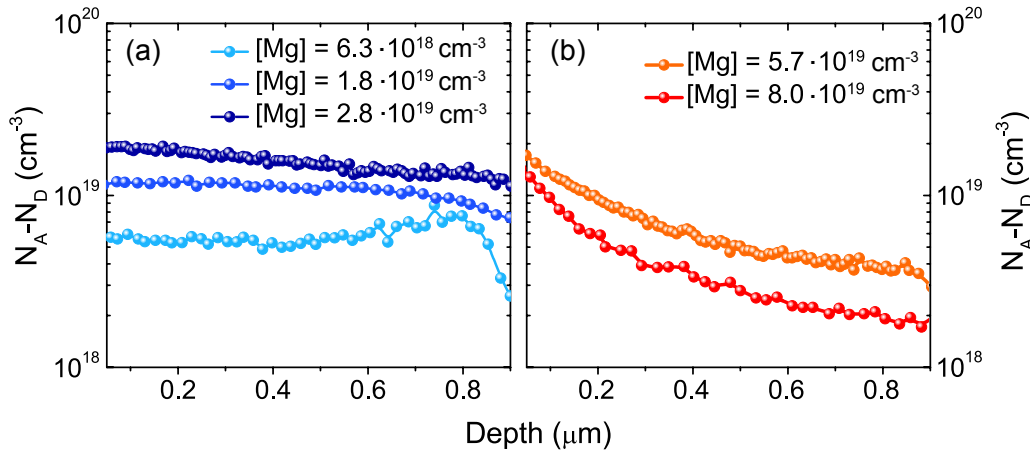


Figure A.2: (a) and (b) show the net acceptor ECV profiles for samples exhibiting (a) $< 10\%$, $\approx 30\%$, and 45% compensation values, and (b) 90% , and $> 95\%$ [80].

Bibliography

- [1] H. P. Maruska and J. Tietjen, "The preparation and properties of Vapor-Deposited single-crystal-line GaN," *Appl. Phys. Lett.* **15**, 327 (1969).
- [2] H. Amano, M. Kito, K. Hiramatsu, and I. Akasaki, "P-type conduction in Mg-doped GaN treated with low-energy electron beam irradiation (LEEBI)," *Jpn. J. Appl. Phys.* **28**, L2112 (1989).
- [3] S. Nakamura, T. Mukai, M. Senoh, and N. Iwasa, "Thermal annealing effects on *p*-type Mg-doped GaN films," *Jpn. J. Appl. Phys.* **31**, L139 (1992).
- [4] S. Nakamura, T. Mukai, and M. Senoh, "Candela-class high-brightness InGaN/AlGaIn double-heterostructure blue-light-emitting diodes," *Appl. Phys. Lett.* **64**, 1687 (1994).
- [5] S. Nakamura, M. Senoh, S.-i. Nagahama, N. Iwasa, T. Yamada, T. Matsushita, Y. Sugimoto, and H. Kiyoku, "Room-temperature continuous-wave operation of InGaIn multi-quantum-well structure laser diodes," *Appl. Phys. Lett.* **69**, 4056 (1996).
- [6] M. Kneissl, T. Kolbe, C. Chua, V. Kueller, N. Lobo, J. Stellmach, A. Knauer, H. Rodriguez, S. Einfeldt, Z. Yang, *et al.*, "Advances in group III-nitride-based deep UV light-emitting diode technology," *Semicond. Sci. Technol.* **26**, 014036 (2011).
- [7] J.-i. Kasai, R. Akimoto, T. Hasama, H. Ishikawa, S. Fujisaki, S. Tanaka, and S. Tsuji, "Green-to-yellow continuous-wave operation of BeZnCdSe quantum-well laser diodes at room temperature," *Appl. Phys. Express* **4**, 082102 (2011).
- [8] S. Takagi, Y. Enya, T. Kyono, M. Adachi, Y. Yoshizumi, T. Sumitomo, Y. Yamanaka, T. Kumanano, S. Tokuyama, K. Sumiyoshi, *et al.*, "High-power (over 100 mW) green laser diodes on semipolar 2021 GaN substrates operating at wavelengths beyond 530 nm," *Appl. Phys. Express* **5**, 082102 (2012).
- [9] S. Masui, T. Miyoshi, T. Yanamoto, and S.-I. Nagahama, "1 W AlInGaIn based green laser diodes," in *Conference on Lasers and Electro-Optics/Pacific Rim* (Optical Society of America, 2013) p. WH3_1.
- [10] S. Krishnamoorthy, F. Akyol, P. S. Park, and S. Rajan, "Low resistance GaN/InGaIn/GaN tunnel junctions," *Appl. Phys. Lett.* **102**, 113503 (2013).

Bibliography

- [11] D. Minamikawa, M. Ino, S. Kawai, T. Takeuchi, S. Kamiyama, M. Iwaya, and I. Akasaki, "GaInN-based tunnel junctions with high InN mole fractions grown by MOVPE," *Phys. Status Solidi A* (2015).
- [12] S. Limpijumnong and W. R. Lambrecht, "Homogeneous strain deformation path for the wurtzite to rocksalt high-pressure phase transition in GaN," *Phys. Rev. Lett.* **86**, 91 (2001).
- [13] S. Limpijumnong and W. R. Lambrecht, "Theoretical study of the relative stability of wurtzite and rocksalt phases in MgO and GaN," *Phys. Rev. B* **63**, 104103 (2001).
- [14] T. Hanada, "Basic Properties of ZnO, GaN, and Related Materials," in *Oxide and Nitride Semiconductors* (Springer, 2009) p. 1.
- [15] I. Vurgaftman and J. Meyer, "Band parameters for nitrogen-containing semiconductors," *J. Appl. Phys.* **94**, 3675 (2003).
- [16] O. Ambacher, J. Majewski, C. Miskys, A. Link, M. Hermann, M. Eickhoff, M. Stutzmann, F. Bernardini, V. Fiorentini, V. Tilak, *et al.*, "Pyroelectric properties of Al (In) GaN/GaN hetero- and quantum well structures," *J. Phys. Condens. Matter* **14**, 3399 (2002).
- [17] S.-H. Park, "Crystal orientation effects on electronic properties of wurtzite InGa_N/GaN quantum wells," *J. Appl. Phys.* **91**, 9904 (2002).
- [18] M. Leroux, N. Grandjean, M. Laügt, J. Massies, B. Gil, P. Lefebvre, and P. Bigenwald, "Quantum confined Stark effect due to built-in internal polarization fields in (Al, Ga) N/GaN quantum wells," *Phys. Rev. B* **58**, R13371 (1998).
- [19] A. Hangleiter, F. Hitzel, S. Lahmann, and U. Rossow, "Composition dependence of polarization fields in GaInN/GaN quantum wells," *Appl. Phys. Lett.* **83**, 1169 (2003).
- [20] Y. Jho, J. Yahng, E. Oh, and D. Kim, "Field-dependent carrier decay dynamics in strained In_xGa_{1-x}N/GaN quantum wells," *Phys. Rev. B* **66**, 035334 (2002).
- [21] C. Wood and D. Jena, *Polarization Effects in Semiconductors* (Springer, New York, 2007).
- [22] R. Butte and N. Grandjean, "Effects of polarization in optoelectronic quantum structures," in *Polarization Effects in Semiconductors* (Springer, New York, 2007) p. 467.
- [23] C. Choi, Y. Kwon, B. Little, G. Gainer, J. Song, Y. Chang, S. Keller, U. Mishra, and S. Den-Baars, "Time-resolved photoluminescence of In_xGa_{1-x}N/GaN multiple quantum well structures: Effect of Si doping in the barriers," *Phys. Rev. B* **64**, 245339 (2001).
- [24] M.-Y. Ryu, P. W. Yu, E.-j. Shin, J. I. Lee, S. K. Yu, E. Oh, O. H. Nam, C. S. Sone, and Y. J. Park, "Effects of Si-doping in the barriers on the recombination dynamics in In_{0.15}Ga_{0.85}N/In_{0.015}Ga_{0.985}N quantum wells," *J. Appl. Phys.* **89**, 634 (2001).

-
- [25] A. Reale, G. Massari, A. Di Carlo, P. Lugli, A. Vinattieri, D. Alderighi, M. Colocci, F. Se-
mond, N. Grandjean, and J. Massies, "Comprehensive description of the dynamical
screening of the internal electric fields of AlGaIn/GaN quantum wells in time-resolved
photoluminescence experiments," *J. Appl. Phys.* **93**, 400 (2003).
- [26] J.-F. Carlin and M. Ilegems, "High-quality AlInN for high index contrast Bragg mirrors
lattice matched to GaN," *Appl. Phys. Lett.* **83**, 668 (2003).
- [27] K. Lorenz, N. Franco, E. Alves, I. Watson, R. Martin, and K. O'donnell, "Anomalous ion
channeling in AlInN/GaN bilayers: determination of the strain state," *Phys. Rev. Lett.*
97, 085501 (2006).
- [28] J. Wu, W. Walukiewicz, K. Yu, J. Ager, S. Li, E. Haller, H. Lu, and W. J. Schaff, "Universal
bandgap bowing in group-III nitride alloys," *Solid State Commun.* **127**, 411 (2003).
- [29] R. Dingle, D. Sell, S. Stokowski, and M. Ilegems, "Absorption, reflectance, and lumines-
cence of GaN epitaxial layers," *Phys. Rev. B* **4**, 1211 (1971).
- [30] D. Sizov, R. Bhat, and C.-E. Zah, "Gallium indium nitride-based green lasers," *J. Light-
wave Technol* **30**, 679 (2012).
- [31] S. M. Sze and K. K. Ng, *Physics of semiconductor devices* (John Wiley & Sons, 2006).
- [32] Y. Yoshizumi, S. Hashimoto, T. Tanabe, and M. Kiyama, "High-breakdown-voltage
pn-junction diodes on GaN substrates," *J. Cryst. Growth* **298**, 875 (2007).
- [33] K. Baik, Y. Irokawa, F. Ren, S. Pearton, S. Park, and Y. Park, "Temperature dependence
of forward current characteristics of GaN junction and Schottky rectifiers," *Solid-State
Electron.* **47**, 1533 (2003).
- [34] C. A. Hurni, O. Bierwagen, J. R. Lang, B. M. McSkimming, C. S. Gallinat, E. C. Young, D. A.
Browne, U. K. Mishra, and J. S. Speck, "*pn* junctions on Ga-face GaN grown by NH₃
molecular beam epitaxy with low ideality factors and low reverse currents," *Appl. Phys.
Lett.* **97**, 222113 (2010).
- [35] J. M. Shah, Y.-L. Li, T. Gessmann, and E. Schubert, "Experimental analysis and theo-
retical model for anomalously high ideality factors ($n > 2.0$) in AlGaIn/GaN pn junction
diodes," *J. Appl. Phys.* **94**, 2627 (2003).
- [36] C. Wu, A. Kahn, N. Taskar, D. Dorman, and D. Gallagher, "GaN (0001)-(1 × 1) surfaces:
Composition and electronic properties," *J. Appl. Phys.* **83**, 4249 (1998).
- [37] K. Motoki, "Development of gallium nitride substrates," *SEI Tech. Rev* **70**, 28 (2010).
- [38] R. Dwiliński, J. Baranowski, M. Kamińska, R. Doradziński, J. Garczyński, and
L. Sierzputowski, "On GaN crystallization by ammonothermal method," *Acta. Phys.
Pol. A* **90**, 763 (1996).

Bibliography

- [39] W. Jiang, D. Ehrentraut, J. Cook, D. S. Kamber, R. T. Pakalapati, and M. P. D'Evelyn, "Transparent, conductive bulk GaN by high temperature ammonothermal growth," *Phys. Status Solidi B* (2015).
- [40] I. C. Kizilyalli, A. P. Edwards, H. Nie, D. Disney, and D. Bour, "High voltage vertical GaN $p-n$ diodes with avalanche capability," *IEEE Trans. Electron Dev.* **60**, 3067 (2013).
- [41] SEI, "Sumitomo Electric announces the World's First 6-inch GaN Substrates for White LED Applications," Sumitomo Electric Industries website, press release (2010).
- [42] J. Arthur Jr, "Interaction of Ga and As₂ molecular beams with GaAs surfaces," *J. Appl. Phys.* **39**, 4032 (1968).
- [43] A. Cho, "Morphology of epitaxial growth of GaAs by a molecular beam method: the observation of surface structures," *J. Appl. Phys.* **41**, 2780 (1970).
- [44] A. Cho and J. Arthur, "Molecular beam epitaxy," *Prog. Solid State Ch.* **10**, 157 (1975).
- [45] L. Chang, L. Esaki, and R. Tsu, "Resonant tunneling in semiconductor double barriers," *Appl. Phys. Lett.* **24**, 593 (1974).
- [46] C. Tarde, "RIBER Compact 21: the World Best Seller Molecular Beam Epitaxy System," *Acta. Phys. Pol. A* **116**, 176 (2009).
- [47] M. Mesrine, *Épitaxie par jets chimiques: application à la croissance de structures mixtes arséniures-phosphures et de nitrures d'éléments III*, Ph.D. thesis, Université de Sophia Antipolis, France (1999).
- [48] G. Koblmüller, J. Brown, R. Averbek, H. Riechert, P. Pongratz, and J. S. Speck, "Ga adlayer governed surface defect evolution of (0001) GaN films grown by plasma-assisted molecular beam epitaxy," *Jpn. J. Appl. Phys.* **44**, L906 (2005).
- [49] J. Neave, B. Joyce, P. Dobson, and N. Norton, "Dynamics of film growth of GaAs by MBE from RHEED observations," *Appl. Phys. A* **31**, 1 (1983).
- [50] T. Ambridge and M. Faktor, "An automatic carrier concentration profile plotter using an electrochemical technique," *J. Appl. Electrochem.* **5**, 319 (1975).
- [51] P. Blood, "Capacitance-voltage profiling and the characterisation of III-V semiconductors using electrolyte barriers," *Semicond. Sci. Technol.* **1**, 7 (1986).
- [52] T. Wolff, M. Rapp, and T. Rotter, "Electrochemical Etching and CV-Profiling of GaN," *Phys. Status Solidi A* **201**, 2067 (2004).
- [53] H. Berger, "Models for contacts to planar devices," *Solid-State Electron.* **15**, 145 (1972).
- [54] H. Berger, "Contact resistance and contact resistivity," *J. Electrochem. Soc.* **119**, 507 (1972).

-
- [55] H. Murrmann and D. Widmann, "Current crowding on metal contacts to planar devices," *IEEE Trans. Electron Dev.* **16**, 1022 (1969).
- [56] D. C. Look, "Electrical characterization of GaAs materials and devices," (John Wiley & Sons, Danvers, 1989).
- [57] K. Shaklee and R. Leheny, "Direct determination of optical gain in semiconductor crystals," *Appl. Phys. Lett.* **18**, 475 (1971).
- [58] C. Lange, M. Schwalm, S. Chatterjee, W. Rühle, N. Gerhardt, S. Johnson, J.-B. Wang, and Y.-H. Zhang, "The variable stripe-length method revisited: Improved analysis," *Appl. Phys. Lett.* **91**, 191107 (2007).
- [59] M. Vehse, J. Meinertz, O. Lange, P. Michler, J. Gutowski, S. Bader, A. Lell, and V. Härle, "Analysis of gain saturation behavior in GaN based quantum well lasers," *Phys. Status Solidi C*, 43 (2003).
- [60] D. S. Sizov, R. Bhat, J. Napierala, J. Xi, D. E. Allen, C. S. Gallinat, and C.-E. Zah, "Lasing and optical gain around 500 nm from optically pumped lasers grown on c -plane GaN substrates," *Opt. Lett.* **34**, 328 (2009).
- [61] B. Pödör, "Acceptor ionization energies in gallium nitride: chemical trends and electronegativities," *Semicond. Sci. Technol.* **11**, L827 (1996).
- [62] H. Morkoç, *Handbook of Nitride Semiconductors and Devices, Materials Properties, Physics and Growth*, Vol. 1 (John Wiley & Sons, Danvers, 2009).
- [63] P. Bogusl, E. Briggs, J. Bernholc, *et al.*, "Amphoteric properties of substitutional carbon impurity in GaN and AlN," *Appl. Phys. Lett.* **69**, 233 (1996).
- [64] F. Bernardini, V. Fiorentini, and A. Bosin, "Theoretical evidence for efficient p-type doping of GaN using beryllium," *Appl. Phys. Lett.* **70**, 2990 (1997).
- [65] C. G. Van de Walle, S. Limpijumnong, and J. Neugebauer, "First-principles studies of beryllium doping of GaN," *Phys. Rev. B* **63**, 245205 (2001).
- [66] A. Ptak, L. Wang, N. Giles, T. Myers, L. Romano, C. Tian, R. Hockett, S. Mitha, and P. Van Lierde, "Incorporation-related structural issues for beryllium doping during growth of GaN by rf-plasma molecular-beam epitaxy," *Appl. Phys. Lett.* **79**, 4524 (2001).
- [67] B. Šantić, "Statistics of the Mg acceptor in GaN in the band model," *Semicond. Sci. Technol.* **21**, 1484 (2006).
- [68] W. Götz, R. Kern, C. Chen, H. Liu, D. Steigerwald, and R. Fletcher, "Hall-effect characterization of III/V nitride semiconductors for high efficiency light emitting diodes," *Mater. Sci. Eng. B* **59**, 211 (1999).

- [69] S. Brochen, J. Brault, S. Chenot, A. Dussaigne, M. Leroux, and B. Damilano, "Dependence of the Mg-related acceptor ionization energy with the acceptor concentration in p -type GaN layers grown by molecular beam epitaxy," *Appl. Phys. Lett.* **103**, 032102 (2013).
- [70] J. S. Blakemore, *Semiconductor statistics* (Dover Publications, Mineola, 2002).
- [71] G. L. Pearson and J. Bardeen, "Electrical properties of pure silicon and silicon alloys containing boron and phosphorus," *Phys. Rev.* **75**, 865 (1949).
- [72] Y. Taniyasu, M. Kasu, and T. Makimoto, "An aluminium nitride light-emitting diode with a wavelength of 210 nanometres," *Nature* **441**, 325 (2006).
- [73] K. Nam, M. Nakarmi, J. Li, J. Lin, and H. Jiang, "Mg acceptor level in AlN probed by deep ultraviolet photoluminescence," *Appl. Phys. Lett.* **83**, 878 (2003).
- [74] M. Nakarmi, K. Kim, M. Khizar, Z. Fan, J. Lin, and H. Jiang, "Electrical and optical properties of Mg-doped $\text{Al}_{0.7}\text{Ga}_{0.3}\text{N}$ alloys," *Appl. Phys. Lett.* **86**, 092108 (2005).
- [75] J. Li, T. Oder, M. Nakarmi, J. Lin, and H. Jiang, "Optical and electrical properties of Mg-doped p -type $\text{Al}_x\text{Ga}_{1-x}\text{N}$," *Appl. Phys. Lett.* **80**, 1210 (2002).
- [76] M. Suzuki, J. Nishio, M. Onomura, and C. Hongo, "Doping characteristics and electrical properties of Mg-doped AlGaIn grown by atmospheric-pressure MOCVD," *J. Cryst. Growth* **189**, 511 (1998).
- [77] M. Suzuki, T. Uenoyama, and A. Yanase, "First-principles calculations of effective-mass parameters of AlN and GaN," *Phys. Rev. B* **52**, 8132 (1995).
- [78] P. Drude, "Zur elektronentheorie der metalle," *Annalen der Physik* **306**, 566 (1900).
- [79] U. Kaufmann, P. Schlotter, H. Obloh, K. Köhler, and M. Maier, "Hole conductivity and compensation in epitaxial GaN: Mg layers," *Phys. Rev. B* **62**, 10867 (2000).
- [80] A. Castiglia, J.-F. Carlin, and N. Grandjean, "Role of stable and metastable Mg-H complexes in p -type GaN for cw blue laser diodes," *Appl. Phys. Lett.* **98**, 213505 (2011).
- [81] D. Iida, K. Tamura, M. Iwaya, S. Kamiyama, H. Amano, and I. Akasaki, "Compensation effect of Mg-doped a - and c -plane GaN films grown by metalorganic vapor phase epitaxy," *J. Cryst. Growth* **312**, 3131 (2010).
- [82] H. Obloh, K. Bachem, U. Kaufmann, M. Kunzer, M. Maier, A. Ramakrishnan, and P. Schlotter, "Self-compensation in Mg doped p -type GaN grown by MOCVD," *J. Cryst. Growth* **195**, 270 (1998).
- [83] H. Alves, M. Böhm, A. Hofstaetter, H. Amano, S. Einfeldt, D. Hommel, D. Hofmann, and B. Meyer, "Compensation mechanism in MOCVD and MBE grown GaN: Mg," *Physica B: Condensed Matter* **308**, 38 (2001).

-
- [84] J. S. Kwak, O.-H. Nam, and Y. Park, "Abnormal dependence of contact resistivity on hole concentration in nonalloyed ohmic contacts to p -GaN," *Appl. Phys. Lett.* **80**, 3554 (2002).
- [85] J. Neugebauer and C. G. Van de Walle, "Role of hydrogen in doping of GaN," *Appl. Phys. Lett.* **68**, 1829 (1996).
- [86] V. Ramachandran, R. Feenstra, W. Sarney, L. Salamanca-Riba, J. Northrup, L. Romano, and D. Greve, "Inversion of wurtzite GaN (0001) by exposure to magnesium," *Appl. Phys. Lett.* **75**, 808 (1999).
- [87] N. Grandjean, A. Dussaigne, S. Pezzagna, and P. Vennéguès, "Control of the polarity of GaN films using an Mg adsorption layer," *J. Cryst. Growth* **251**, 460 (2003).
- [88] S. Pezzagna, P. Vennéguès, N. Grandjean, and J. Massies, "Polarity inversion of GaN (0001) by a high Mg doping," *J. Cryst. Growth* **269**, 249 (2004).
- [89] S. Tomiya, T. Hino, T. Miyajima, O. Goto, and M. Ikeda, "Defects and degradation of nitride-based laser diodes," in *Integrated Optoelectronic Devices 2006* (International Society for Optics and Photonics, 2006) p. 613308.
- [90] M. Leroux, P. Vennéguès, S. Dalmaso, P. de Mierry, P. Lorenzini, B. Damilano, B. Beaumont, P. Gibart, and J. Massies, "Pyramidal defects in highly Mg-doped GaN: atomic structure and influence on optoelectronic properties," *Eur. Phys. J.* **27**, 259 (2004).
- [91] P. Vennegues, M. Benaissa, B. Beaumont, E. Feltin, P. De Mierry, S. Dalmaso, M. Leroux, and P. Gibart, "Pyramidal defects in metalorganic vapor phase epitaxial Mg doped GaN," *Appl. Phys. Lett.* **77**, 880 (2000).
- [92] P. Vennéguès, M. Leroux, S. Dalmaso, M. Benaissa, P. De Mierry, P. Lorenzini, B. Damilano, B. Beaumont, J. Massies, and P. Gibart, "Atomic structure of pyramidal defects in Mg-doped GaN," *Phys. Rev. B* **68**, 235214 (2003).
- [93] M. Hansen, L. Chen, S. Lim, S. DenBaars, and J. Speck, "Mg-rich precipitates in the p -type doping of InGaN-based laser diodes," *Appl. Phys. Lett.* **80**, 2469 (2002).
- [94] T. Remmele, M. Albrecht, K. Irmscher, R. Fornari, and M. Strassburg, "Pyramidal inversion domain boundaries revisited," *Appl. Phys. Lett.* **99**, 141913 (2011).
- [95] B. Lange, C. Freysoldt, and J. Neugebauer, "Native and hydrogen-containing point defects in Mg₃N₂: A density functional theory study," *Phys. Rev. B* **81**, 224109 (2010).
- [96] C. G. Van de Walle, "Interactions of hydrogen with native defects in GaN," *Phys. Rev. B* **56**, R10020 (1997).
- [97] M. Ganchenkova and R. Nieminen, "Nitrogen vacancies as major point defects in gallium nitride," *Phys. Rev. Lett.* **96**, 196402 (2006).

Bibliography

- [98] C. G. Van de Walle and J. Neugebauer, "First-principles calculations for defects and impurities: Applications to III-nitrides," *J. Appl. Phys.* **95**, 3851 (2004).
- [99] J. Neugebauer and C. G. Van de Walle, "Chemical trends for acceptor impurities in GaN," *J. Appl. Phys.* **85**, 3003 (1999).
- [100] A. Uedono, S. Ishibashi, K. Tenjinbayashi, T. Tsutsui, K. Nakahara, D. Takamizu, and S. Chichibu, "Defect characterization in Mg-doped GaN studied using a monoenergetic positron beam," *J. Appl. Phys.* **111**, 014508 (2012).
- [101] D. Blavette, A. Bostel, J. Sarrau, B. Deconihout, and A. Menand, "An atom probe for three-dimensional tomography," (1993).
- [102] J. R. Riley, S. Padalkar, Q. Li, P. Lu, D. D. Koleske, J. J. Wierer, G. T. Wang, and L. J. Lauhon, "Three-dimensional mapping of quantum wells in a GaN/InGaN core-shell nanowire light-emitting diode array," *Nano Lett.* **13**, 4317 (2013).
- [103] S. Khromov, D. Gregorius, R. Schiller, J. Lösch, M. Wahl, M. Kopnarski, H. Amano, B. Monemar, L. Hultman, and G. Pozina, "Atom probe tomography study of Mg-doped GaN layers," *Nanotechnology* **25**, 275701 (2014).
- [104] S. Bennett, P. Clifton, R. Ulfing, M. Kappers, J. Barnard, C. Humphreys, and R. Oliver, "Mg dopant distribution in an AlGaIn/GaN p-type superlattice assessed using atom probe tomography, TEM and SIMS," in *JPCS*, Vol. 209 (IOP Publishing, 2010) p. 012014.
- [105] D. Larson, T. Prosa, D. Olson, W. Lefebvre, D. Lawrence, P. Clifton, and T. Kelly, "Atom probe tomography of a commercial light emitting diode," in *JPCS*, Vol. 471 (IOP Publishing, 2013) p. 012030.
- [106] S. E. Bennett, P. H. Clifton, R. M. Ulfing, M. J. Kappers, J. S. Barnard, C. J. Humphreys, and R. A. Oliver, "Atom probe extended to AlGaIn: three-dimensional imaging of a Mg-doped AlGaIn/GaN superlattice," *Phys. Status Solidi C* **7**, 1781 (2010).
- [107] S. Nakamura, N. Iwasa, M. Senoh, and T. Mukai, "Hole compensation mechanism of p-type GaN films," *Jpn. J. Appl. Phys.* , 1258 (1992).
- [108] W. Götz, N. Johnson, J. Walker, D. Bour, H. Amano, and I. Akasaki, "Hydrogen passivation of Mg acceptors in GaN grown by metalorganic chemical vapor deposition," *Appl. Phys. Lett.* **67**, 2666 (1995).
- [109] J. Neugebauer and C. G. Van de Walle, "Hydrogen in GaN: novel aspects of a common impurity," *Phys. Rev. Lett.* **75**, 4452 (1995).
- [110] T. Moustakas and R. Molnar, "Growth and Doping of GaN Films by ECR-Assisted MBE," in *MRS Proceedings*, Vol. 281 (Cambridge Univ Press, 1992) p. 753.

-
- [111] A. Dussaigne, B. Damilano, J. Brault, J. Massies, E. Feltin, and N. Grandjean, "High doping level in Mg-doped GaN layers grown at low temperature," *J. Appl. Phys.* **103**, 013110 (2008).
- [112] K. Ploog, "Delta-doping in MBE-grown GaAs: Concept and device application," *J. Cryst. Growth* **81**, 304 (1987).
- [113] E. Schubert, W. Grieshaber, and I. Goepfert, "Enhancement of deep acceptor activation in semiconductors by superlattice doping," *Appl. Phys. Lett.* **69**, 3737 (1996).
- [114] P. Kozodoy, Y. P. Smorchkova, M. Hansen, H. Xing, S. P. DenBaars, U. K. Mishra, A. Saxler, R. Perrin, and W. Mitchel, "Polarization-enhanced Mg doping of AlGa_N/Ga_N superlattices," *Appl. Phys. Lett.* **75**, 2444 (1999).
- [115] S. Nakamura, M. Senoh, S.-i. Nagahama, N. Iwasa, T. Yamada, T. Matsushita, H. Kiyoku, Y. Sugimoto, T. Kozaki, H. Umemoto, *et al.*, "InGa_N/Ga_N/AlGa_N-based laser diodes with modulation-doped strained-layer superlattices," *Jpn. J. Appl. Phys.* **36**, L1568 (1997).
- [116] J. Simon, V. Protasenko, C. Lian, H. Xing, and D. Jena, "Polarization-induced hole doping in wide-band-gap uniaxial semiconductor heterostructures," *Science* **327**, 60 (2010).
- [117] H. Reiss, C. Fuller, and F. Morin, "Chemical interactions among defects in germanium and silicon," *Bell Syst. Tech. J.* **35**, 535 (1956).
- [118] H. Katayama-Yoshida, R. Kato, and T. Yamamoto, "New valence control and spin control method in Ga_N and Al_N by codoping and transition atom doping," *J. Cryst. Growth* **231**, 428 (2001).
- [119] R. Korotkov, J. Gregie, and B. Wessels, "Codoping of wide gap epitaxial III-Nitride semiconductors," *Opto-electron. Rev.* , 243 (2002).
- [120] K. Johnson, V. Bousquet, S. Hooper, M. Kauer, C. Zellweger, and J. Heffernan, "High-power InGa_N light emitting diodes grown by molecular beam epitaxy," *Electron. Lett.* **40**, 1299 (2004).
- [121] I. Smorchkova, E. Haus, B. Heying, P. Kozodoy, P. Fini, J. Ibbetson, S. Keller, S. DenBaars, J. Speck, and U. Mishra, "Mg doping of Ga_N layers grown by plasma-assisted molecular-beam epitaxy," *Appl. Phys. Lett.* **76**, 718 (2000).
- [122] F. Naranjo, E. Calleja, Z. Bougrioua, A. Trampert, X. Kong, and K. Ploog, "Efficiency optimization of *p*-type doping in Ga_N: Mg layers grown by molecular-beam epitaxy," *J. Cryst. Growth* **270**, 542 (2004).
- [123] M. McLaurin, T. Mates, and J. Speck, "Molecular-beam epitaxy of *p*-type *m*-plane Ga_N," *Appl. Phys. Lett.* **86**, 262104 (2005).

Bibliography

- [124] M. Kauer, V. Bousquet, S. Hooper, J. Barnes, J. Windle, W. Tan, and J. Heffernan, "Nitrides optoelectronic devices grown by molecular beam epitaxy," *Phys. Status Solidi A* **204**, 221 (2007).
- [125] W. P. Gilbreath, *The vapor pressure of magnesium between 223 and 385 C*, Tech. Rep. (Ames Research Center, National Aeronautics and Space Administration, Moffett Field, Calif., 1965).
- [126] C. A. Hurni, J. R. Lang, P. G. Burke, and J. S. Speck, "Effects of growth temperature on Mg-doped GaN grown by ammonia molecular beam epitaxy," *Appl. Phys. Lett.* **101**, 102106 (2012).
- [127] C. Rauch, Ö. Tuna, C. Giesen, M. Heuken, and F. Tuomisto, "Point defect evolution in low-temperature MOCVD growth of InN," *Phys. Status Solidi A* **209**, 87 (2012).
- [128] I. Grzegory, "High pressure growth of bulk GaN from solutions in gallium," *J. Phys. Condens. Matter* **13**, 6875 (2001).
- [129] S. Vézian, F. Natali, F. Semond, and J. Massies, "From spiral growth to kinetic roughening in molecular-beam epitaxy of GaN (0001)," *Phys. Rev. B* **69**, 125329 (2004).
- [130] C. Adelmann, J. Brault, D. Jalabert, P. Gentile, H. Mariette, G. Mula, and B. Daudin, "Dynamically stable gallium surface coverages during plasma-assisted molecular-beam epitaxy of (0001) GaN," *J. Appl. Phys.* **91**, 9638 (2002).
- [131] G. Ehrlich and F. Hudda, "Atomic view of surface self-diffusion: Tungsten on tungsten," *J. Chem. Phys.* **44**, 1039 (1966).
- [132] R. L. Schwoebel and E. J. Shipsey, "Step motion on crystal surfaces," *J. Appl. Phys.* **37**, 3682 (1966).
- [133] N. A. K. Kaufmann, *Investigation of indium-rich InGaN alloys and kinetic growth regime of GaN*, Ph.D. thesis, ÉCOLE POLYTECHNIQUE FÉDÉRALE DE LAUSANNE (2013).
- [134] M. Copel, M. Reuter, E. Kaxiras, and R. Tromp, "Surfactants in epitaxial growth," *Phys. Rev. Lett.* **63**, 632 (1989).
- [135] J. Massies and N. Grandjean, "Surfactant effect on the surface diffusion length in epitaxial growth," *Phys. Rev. B* **48**, 8502 (1993).
- [136] S. D. Burnham, G. Namkoong, W. Henderson, and W. A. Doolittle, "Mg doped GaN using a valved, thermally energetic source: enhanced incorporation, and control," *J. Cryst. Growth* **279**, 26 (2005).
- [137] N. Grandjean, J. Massies, F. Semond, S. Y. Karpov, and R. Talalaev, "GaN evaporation in molecular-beam epitaxy environment," *Appl. Phys. Lett.* **74**, 1854 (1999).

- [138] L. Romano, M. Kneissl, J. Northrup, C. Van de Walle, and D. Treat, "Influence of microstructure on the carrier concentration of Mg-doped GaN films," *Appl. Phys. Lett.* **79**, 2734 (2001).
- [139] B. Mitchell, D. Lee, Y. Fujiwara, and V. Dierolf, "Vibrationally induced center reconfiguration in co-doped GaN: Eu, Mg epitaxial layers: Local hydrogen migration vs. activation of non-radiative channels," *Appl. Phys. Lett.* **103**, 242105 (2013).
- [140] A. Wright and T. Mattsson, "N vacancy diffusion and trapping in Mg-doped wurtzite GaN," *J. Appl. Phys.* **96**, 205501 (2004).
- [141] Z. Liliental-Weber, T. Tomaszewicz, D. Zakharov, M. O'Keefe, S. Hautakangas, K. Saari-nen, J. Freitas, and R. Henry, "Atomic structure of pyramidal defects in GaN: Mg: Influence of annealing," *Phys. Status Solidi A* **203**, 1636 (2006).
- [142] C. Stampfl and C. G. Van de Walle, "Doping of $\text{Al}_x\text{Ga}_{1-x}\text{N}$," *Appl. Phys. Lett.* **72**, 459 (1998).
- [143] M. P. Hoffmann, J. Tweedie, R. Kirste, Z. Bryan, I. Bryan, M. Gerhold, Z. Sitar, and R. Collazo, "Point defect management in GaN by Fermi-level control during growth," in *SPIE OPTO* (International Society for Optics and Photonics, 2014) p. 89860T.
- [144] A. Yamaguchi, M. Kuramoto, M. Nido, and M. Mizuta, "An alloy semiconductor system with a tailorable band-tail and its application to high-performance laser operation: I. A band-states model for an alloy-fluctuated InGa N -material system designed for quantum well laser operation," *Semicond. Sci. Technol.* **16**, 763 (2001).
- [145] U. T. Schwarz, H. Braun, K. Kojima, M. Funato, Y. Kawakami, S. Nagahama, and T. Mukai, "Investigation and comparison of optical gain spectra of (Al, In) GaN laser diodes emitting in the 375 nm to 470 nm spectral range," in *Proc. SPIE*, Vol. 6485 (2007) p. 648506.
- [146] D. S. Sizov, R. Bhat, A. Heberle, K. Song, and C.-E. Zah, "Internal optical waveguide loss and p -type absorption in blue and green InGa N quantum well laser diodes," *Appl. Phys. Express* **3**, 122104 (2010).
- [147] J. Son, S. Lee, H. Paek, T. Sakong, H. Kim, Y. Park, H. Ryu, O. Nam, J. Hwang, and Y. Cho, "Measurement of optical loss variation on thickness of InGa N optical confinement layers of blue-violet-emitting laser diodes," *J. Appl. Phys.* **103**, 103101 (2008).
- [148] J. Müller, U. Strauß, T. Lerner, G. Brüderl, C. Eichler, A. Avramescu, and S. Lutgen, "Investigation of long wavelength green InGa N lasers on c -plane GaN up to 529 nm continuous wave operation," *Phys. Status Solidi A* **208**, 1590 (2011).
- [149] T. Miyoshi, S. Masui, T. Okada, T. Yanamoto, T. Kozaki, S.-i. Nagahama, and T. Mukai, "510–515 nm InGa N -based green laser diodes on c -plane GaN substrate," *Appl. Phys. Express* **2**, 062201 (2009).

Bibliography

- [150] A. Avramescu, T. Lermer, J. Muller, S. Tautz, D. Queren, S. Lutgen, and U. Strauß, "InGaN laser diodes with 50 mW output power emitting at 515 nm," *Appl. Phys. Lett.* **95**, 071103 (2009).
- [151] A. Avramescu, T. Lermer, J. Müller, C. Eichler, G. Brüederl, M. Sabathil, S. Lutgen, and U. Strauss, "True green laser diodes at 524 nm with 50 mW continuous wave output power on *c*-plane GaN," *Appl. Phys. Express* **3**, 061003 (2010).
- [152] M. Adachi, Y. Yoshizumi, Y. Enya, T. Kyono, T. Sumitomo, S. Tokuyama, S. Takagi, K. Sumiyoshi, N. Saga, T. Ikegami, *et al.*, "Low threshold current density InGaN based 520–530 nm green laser diodes on semi-polar {2021} free-standing GaN substrates," *Appl. Phys. Express* **3**, 121001 (2010).
- [153] Y.-D. Lin, S. Yamamoto, C.-Y. Huang, C.-L. Hsiung, F. Wu, K. Fujito, H. Ohta, J. S. Speck, S. P. DenBaars, and S. Nakamura, "High quality InGaN/AlGaIn multiple quantum wells for semipolar InGaIn green laser diodes," *Appl. Phys. Express* **3**, 082001 (2010).
- [154] D. Sizov, R. Bhat, K. Song, D. Allen, B. Paddock, S. Coleman, L. C. Hughes, and C.-E. Zah, "60 mW Pulsed and Continuous Wave Operation of GaN-Based Semipolar Green Laser with Characteristic Temperature of 190 K," *Appl. Phys. Express* **4**, 102103 (2011).
- [155] M. C. Schmidt, C. Poblenz, Y.-C. Chang, B. Li, M. J. Mondry, J. Iveland, M. R. Krames, R. Craig, J. W. Raring, J. S. Speck, *et al.*, "High-performance blue and green laser diodes based on nonpolar/semipolar GaN substrates," in *SPIE Defense, Security, and Sensing* (International Society for Optics and Photonics, 2011) p. 80390D.
- [156] D. Holec, Y. Zhang, D. S. Rao, M. J. Kappers, C. McAleese, and C. J. Humphreys, "Equilibrium critical thickness for misfit dislocations in III-nitrides," *J. Appl. Phys.* **104**, 123514 (2008).
- [157] D. Queren, A. Avramescu, G. Brüderl, A. Breidenassel, M. Schillgalies, S. Lutgen, and U. Strauß, "500 nm electrically driven InGaIn based laser diodes," *Appl. Phys. Lett.* **94**, 081119 (2009).
- [158] W. Lee, J. Limb, J.-H. Ryou, D. Yoo, T. Chung, and R. D. Dupuis, "Effect of thermal annealing induced by p-type layer growth on blue and green LED performance," *J. Cryst. Growth* **287**, 577 (2006).
- [159] M. T. Hardy, F. Wu, C.-Y. Huang, Y. Zhao, D. F. Feezell, S. Nakamura, J. S. Speck, and S. P. DenBaars, "Impact of *p*-GaN Thermal Damage and Barrier Composition on Semipolar Green Laser Diodes," *IEEE Photon. Technol. Lett.* **26**, 43 (2014).
- [160] "Improvement of green LED by growing *p*-GaN on In_{0.25}Ga_{0.75}N/gaN mqw's at low temperature," .
- [161] D. Queren, M. Schillgalies, A. Avramescu, G. Brüderl, A. Laubsch, S. Lutgen, and U. Strauß, "Quality and thermal stability of thin InGaIn films," *J. Cryst. Growth* **311**, 2933 (2009).

-
- [162] T. Miyoshi, "Nitride semiconductor laser diode," (2010), uS Patent App. 13/387,855.
 - [163] M. T. Hardy, C. O. Holder, D. F. Feezell, S. Nakamura, J. S. Speck, D. A. Cohen, and S. P. DenBaars, "Indium-tin-oxide clad blue and true green semipolar InGaN/GaN laser diodes," *Appl. Phys. Lett.* **103**, 081103 (2013).
 - [164] D. Koleske, A. Wickenden, R. Henry, and M. Twigg, "Influence of MOVPE growth conditions on carbon and silicon concentrations in GaN," *J. Cryst. Growth* **242**, 55 (2002).
 - [165] G. Laws, E. Larkins, I. Harrison, C. Molloy, and D. Somerford, "Improved refractive index formulas for the $\text{Al}_x\text{Ga}_{1-x}\text{N}$ and $\text{In}_y\text{Ga}_{1-y}\text{N}$ alloys," *J. Appl. Phys.* **89**, 1108 (2001).
 - [166] Y. Yoshizumi, M. Adachi, Y. Enya, T. Kyono, S. Tokuyama, T. Sumitomo, K. Akita, T. Ikegami, M. Ueno, K. Katayama, *et al.*, "Continuous-wave operation of 520 nm green ingan-based laser diodes on semi-polar {2021} gan substrates," *Appl. Phys. Express* **2**, 092101 (2009).
 - [167] Y. Taniyasu, J.-F. Carlin, A. Castiglia, R. Butté, and N. Grandjean, "Mg doping for p-type AlInN lattice-matched to GaN," *Appl. Phys. Lett.* **101**, 082113 (2012).
 - [168] T. Lermer, M. Schillgalies, A. Breidenassel, D. Queren, C. Eichler, A. Avramescu, J. Müller, W. Scheibenzuber, U. Schwarz, S. Lutgen, *et al.*, "Waveguide design of green InGaN laser diodes," *Phys. Status Solidi A* **207**, 1328 (2010).
 - [169] A. Tyagi, R. M. Farrell, K. M. Kelchner, C.-Y. Huang, P. S. Hsu, D. A. Haeger, M. T. Hardy, C. Holder, K. Fujito, D. A. Cohen, *et al.*, "AlGaIn-cladding free green semipolar GaN based laser diode with a lasing wavelength of 506.4 nm," *Appl. Phys. Express* **3**, 011002 (2010).
 - [170] J. Dorsaz, A. Castiglia, G. Cosendey, E. Feltin, M. Rossetti, M. Duell, C. Velez, J.-F. Carlin, and N. Grandjean, "AlGaIn-free blue III-nitride laser diodes grown on c-plane GaN substrates," *Appl. Phys. Express* **3**, 092102 (2010).
 - [171] C. Skierbiszewski, M. Siekacz, H. Turski, G. Muzioł, M. Sawicka, A. Feduniewicz-Żmuda, G. Cywiński, C. Cheze, S. Grzanka, P. Perlin, *et al.*, "AlGaIn-free laser diodes by plasma-assisted molecular beam epitaxy," *Appl. Phys. Express* **5**, 022104 (2012).
 - [172] C. Skierbiszewski, H. Turski, G. Muziol, P. Wolny, G. Cywiński, S. Grzanka, J. Smalc-Koziorowska, M. Sawicka, P. Perlin, Z. R. Wasilewski, *et al.*, "AlGaIn cladding-free 482 nm continuous wave nitride laser diodes grown by plasma-assisted molecular beam epitaxy," *Journal of Vacuum Science & Technology B* **32**, 02C112 (2014).
 - [173] C.-Y. Huang, Y.-D. Lin, A. Tyagi, A. Chakraborty, H. Ohta, J. S. Speck, S. P. DenBaars, and S. Nakamura, "Optical waveguide simulations for the optimization of InGaIn-based green laser diodes," *J. Appl. Phys.* **107**, 023101 (2010).
 - [174] S. Nakamura, M. Senoh, and T. Mukai, "Highly *p*-typed Mg-doped GaN films grown with GaN buffer layers," *Jpn. J. Appl. Phys.* **30**, L1708 (1991).

Bibliography

- [175] A. Bhattacharyya, W. Li, J. Cabalu, T. Moustakas, D. J. Smith, and R. Hervig, “Efficient p -type doping of GaN films by plasma-assisted molecular beam epitaxy,” *Appl. Phys. Lett.* **85**, 4956 (2004).
- [176] E. Feltin, A. Castiglia, G. Cosendey, L. Sulmoni, J.-F. Carlin, N. Grandjean, M. Rossetti, J. Dorsaz, V. Laino, M. Duelk, *et al.*, “Broadband blue superluminescent light-emitting diodes based on GaN,” *Appl. Phys. Lett.* **95**, 081107 (2009).
- [177] C. Skierbiszewski, Z. Wasilewski, I. Grzegory, and S. Porowski, “Nitride-based laser diodes by plasma-assisted MBE—From violet to green emission,” *J. Cryst. Growth* **311**, 1632 (2009).
- [178] G. Muziol, M. Siekacz, H. Turski, P. Wolny, S. Grzanka, E. Grzanka, A. Feduniewicz-Żmuda, J. Borysiuk, K. Sobczak, J. Domagała, *et al.*, “High power nitride laser diodes grown by plasma assisted molecular beam epitaxy,” *J. Cryst. Growth* (2015).
- [179] G. Muziol, H. Turski, M. Siekacz, P. Wolny, M. Sawicka, S. Grzanka, P. Perlin, T. Suski, Z. Wasilewski, I. Grzegory, *et al.*, “True-blue laser diodes grown by plasma-assisted MBE on bulk GaN substrates,” *Phys. Status Solidi C* **11**, 666 (2014).
- [180] C. Skierbiszewski, M. Siekacz, H. Turski, G. Muziol, M. Sawicka, P. Perlin, Z. Wasilewski, and S. Porowski, “MBE fabrication of III-N-based laser diodes and its development to industrial system,” *J. Cryst. Growth* **378**, 278 (2013).
- [181] S. Nagahama, M. Sano, T. Yanamoto, D. Morita, O. Miki, K. Sakamoto, M. Yamamoto, Y. Matsuyama, Y. Kawata, T. Murayama, *et al.*, “GaN-based laser diodes emitting from ultraviolet to blue-green,” in *Integrated Optoelectronics Devices* (International Society for Optics and Photonics, 2003) p. 108.
- [182] T. Lermer, A. Gomez-Iglesias, M. Sabathil, J. Müller, S. Lutgen, U. Strauss, B. Pasenow, J. Hader, J. Moloney, S. Koch, *et al.*, “Gain of blue and cyan InGaN laser diodes,” *Appl. Phys. Lett.* **98**, 021115 (2011).
- [183] M. Funato, Y. S. Kim, Y. Ochi, A. Kaneta, Y. Kawakami, T. Miyoshi, and S.-I. Nagahama, “Optical Gain Spectra of a (0001) InGaN Green Laser Diode,” *Appl. Phys. Express* **6**, 122704 (2013).
- [184] J. W. Raring, M. C. Schmidt, C. Poblentz, B. Li, Y.-C. Chang, M. J. Mondry, Y.-D. Lin, M. R. Krames, R. Craig, J. S. Speck, *et al.*, “High-performance blue and green laser diodes based on nonpolar/semipolar bulk GaN substrates,” in *SPIE OPTO* (International Society for Optics and Photonics, 2011) p. 79390Y.
- [185] A. Weimar, A. Lell, G. Brüderl, S. Bader, and V. Härle, “Investigation of low-resistance metal contacts on p -type GaN using the linear and circular transmission line method,” *Phys. Status Solidi A* **183**, 169 (2001).

-
- [186] T. Hager, M. Binder, G. Bröderl, C. Eichler, A. Avramescu, T. Wurm, A. Gomez-Iglesias, B. Stojetz, S. Tautz, B. Galler, *et al.*, “Carrier transport in green AlInGaN based structures on c-plane substrates,” *Appl. Phys. Lett.* **102**, 231102 (2013).
 - [187] D. Sizov, R. Bhat, J. Wang, and C.-E. Zah, “Reliability and degradation of InAlGaN semipolar plane green lasers with relaxed InGaN waveguide core,” *Appl. Phys. Express* **7**, 112701 (2014).
 - [188] U. Strauss, T. Hager, G. Bröderl, T. Wurm, A. Somers, C. Eichler, C. Vierheilig, A. Löffler, J. Ristic, and A. Avramescu, “Recent advances in c-plane GaN visible lasers,” in *SPIE OPTO* (International Society for Optics and Photonics, 2014) p. 89861L.
 - [189] L. Esaki, “New phenomenon in narrow germanium $p - n$ junctions,” *Phys. Rev.* **109**, 603 (1958).
 - [190] S.-R. Jeon, C. S. Oh, J.-W. Yang, G. M. Yang, and B.-S. Yoo, “GaN tunnel junction as a current aperture in a blue surface-emitting light-emitting diode,” *Appl. Phys. Lett.* **80**, 1933 (2002).
 - [191] T. Takeuchi, G. Hasnain, S. Corzine, M. Hueschen, R. P. Schneider Jr, C. Kocot, M. Blomqvist, Y.-l. Chang, D. Lefforge, M. R. Krames, *et al.*, “GaN-based light emitting diodes with tunnel junctions,” *Jpn. J. Appl. Phys.* **40**, L861 (2001).
 - [192] M. Diagne, Y. He, H. Zhou, E. Makarona, A. Nurmikko, J. Han, K. Waldrip, J. Figiel, T. Takeuchi, and M. Krames, “Vertical cavity violet light emitting diode incorporating an aluminum gallium nitride distributed Bragg mirror and a tunnel junction,” *Appl. Phys. Lett.* **79**, 3720 (2001).
 - [193] M. J. Grundmann and U. K. Mishra, “Multi-color light emitting diode using polarization-induced tunnel junctions,” *Phys. Status Solidi C* **4**, 2830 (2007).
 - [194] D. Jena, J. Simon, A. K. Wang, Y. Cao, K. Goodman, J. Verma, S. Ganguly, G. Li, K. Karda, V. Protasenko, *et al.*, “Polarization-engineering in group III-nitride heterostructures: New opportunities for device design,” *Phys. Status Solidi A* **208**, 1511 (2011).
 - [195] J. Simon, Z. Zhang, K. Goodman, H. Xing, T. Kosel, P. Fay, and D. Jena, “Polarization-induced Zener tunnel junctions in wide-band-gap heterostructures,” *Phys. Rev. Lett.* **103**, 026801 (2009).
 - [196] S. Krishnamoorthy, T. F. Kent, J. Yang, P. S. Park, R. C. Myers, and S. Rajan, “GdN Nanoisland-Based GaN Tunnel Junctions,” *Nano Lett.* **13**, 2570 (2013).
 - [197] S. Nakamura and M. R. Krames, “History of gallium–nitride-based light-emitting diodes for illumination,” *Proc. IEEE* **101**, 2211 (2013).
 - [198] Y. Narukawa, M. Ichikawa, D. Sanga, M. Sano, and T. Mukai, “White light emitting diodes with super-high luminous efficacy,” *J. Phys. D: Appl. Phys.* **43**, 354002 (2010).

Bibliography

- [199] F. Akyol, S. Krishnamoorthy, and S. Rajan, "Tunneling-based carrier regeneration in cascaded GaN light emitting diodes to overcome efficiency droop," *Appl. Phys. Lett.* **103**, 081107 (2013).
- [200] D. Kasahara, D. Morita, T. Kosugi, K. Nakagawa, J. Kawamata, Y. Higuchi, H. Matsumura, and T. Mukai, "Demonstration of blue and green GaN-based vertical-cavity surface-emitting lasers by current injection at room temperature," *Appl. Phys. Express* **4**, 072103 (2011).
- [201] C. Holder, J. S. Speck, S. P. DenBaars, S. Nakamura, and D. Feezell, "Demonstration of nonpolar GaN-based vertical-cavity surface-emitting lasers," *Appl. Phys. Express* **5**, 092104 (2012).
- [202] G. Cosendey, A. Castiglia, G. Rossbach, J.-F. Carlin, and N. Grandjean, "Blue monolithic AlInN-based vertical cavity surface emitting laser diode on free-standing GaN substrate," *Appl. Phys. Lett.* **101**, 151113 (2012).
- [203] E. Kapon and A. Sirbu, "Long-wavelength VCSELs: power-efficient answer," *Nature Photon.* **3**, 27 (2009).
- [204] J. Boucart, C. Starck, F. Gaborit, A. Plais, N. Bouche, E. Derouin, J. Remy, J. Bonnet-Gamard, L. Goldstein, C. Fortin, *et al.*, "Metamorphic DBR and tunnel-junction injection. A CW RT monolithic long-wavelength VCSEL," *Selected Topics in Quantum Electronics, IEEE Journal of* **5**, 520 (1999).
- [205] W. Hofmann, M. Müller, P. Wolf, A. Mutig, T. Gründl, G. Böhm, D. Bimberg, and M.-C. Amann, "40 Gbit/s modulation of 1550 nm VCSEL," *Electron. Lett.* **47**, 270 (2011).
- [206] Y. Kuwano, M. Kaga, T. Morita, K. Yamashita, K. Yagi, M. Iwaya, T. Takeuchi, S. Kamiyama, and I. Akasaki, "Lateral hydrogen diffusion at p-GaN Layers in nitride-based light emitting diodes with tunnel junctions," *Jpn. J. Appl. Phys.* **52**, 08JK12 (2013).
- [207] J. Pankove, C. Magee, and R. Wance, "Hole-mediated chemisorption of atomic hydrogen in silicon," *Appl. Phys. Lett.* **47**, 748 (1985).
- [208] G. Antell, A. Briggs, B. Butler, S. Kitching, J. Stagg, A. Chew, and D. Sykes, "Passivation of zinc acceptors in InP by atomic hydrogen coming from arsine during metalorganic vapor phase epitaxy," *Appl. Phys. Lett.* **53**, 758 (1988).
- [209] L. Lugani, M. Malinverni, S. Tirelli, D. Marti, E. Giraud, J.-F. Carlin, C. Bolognesi, and N. Grandjean, " n^+ -GaN grown by ammonia molecular beam epitaxy: Application to regrown contacts," *Appl. Phys. Lett.* **105**, 202113 (2014).
- [210] D. Marti, S. Tirelli, V. Teppati, L. Lugani, J.-F. Carlin, M. Malinverni, N. Grandjean, and C. Bolognesi, "94 GHz large-signal operation of AlInN/GaN high-electron-mobility transistors on silicon with regrown ohmic contacts," *IEEE Electron Device Lett.* **36**, 17 (2015).

-
- [211] F. A. Faria, J. Guo, P. Zhao, G. Li, P. K. Kandaswamy, M. Wistey, H. G. Xing, and D. Jena, "Ultra-low resistance ohmic contacts to GaN with high Si doping concentrations grown by molecular beam epitaxy," *Appl. Phys. Lett.* **101**, 032109 (2012).
- [212] E. C. Kyle, S. W. Kaun, P. G. Burke, F. Wu, Y.-R. Wu, and J. S. Speck, "High-electron-mobility GaN grown on free-standing GaN templates by ammonia-based molecular beam epitaxy," *J. Appl. Phys.* **115**, 193702 (2014).
- [213] W. Goetz, F. Ahmed, J. Bhat, L. Cook, N. Gardner, E. Johnson, M. Misra, R. Kern, A. Kim, J. Kim, *et al.*, "Power III-Nitride LEDs," in *International Conf. Nitride Semiconductors* (2001).
- [214] S. Sonderegger, E. Feltin, M. Merano, A. Crottini, J.-F. Carlin, R. Sachot, B. Deveaud, N. Grandjean, and J. D. Ganiere, "High spatial resolution picosecond cathodoluminescence of InGaN quantum wells," *Appl. Phys. Lett.* **89**, 232109 (2006).
- [215] K. Vizbaras, M. Törpe, S. Arafin, and M.-C. Amann, "Ultra-low resistive GaSb/InAs tunnel junctions," *Semicond. Sci. Technol.* **26**, 075021 (2011).
- [216] M. P. Lumb, M. K. Yakes, M. González, I. Vurgaftman, C. G. Bailey, R. Hoheisel, and R. J. Walters, "Double quantum-well tunnel junctions with high peak tunnel currents and low absorption for InP multi-junction solar cells," *Appl. Phys. Lett.* **100**, 213907 (2012).
- [217] N. Suzuki, T. Anan, H. Hatakeyama, and M. Tsuji, "Low resistance tunnel junctions with type-II heterostructures," *Appl. Phys. Lett.* **88**, 231103 (2006).

MARCO MALINVERNI

(+41)786540946, (+39)3338809775
mm.malinverni@gmail.com



HOME ADDRESS :

Chemin de Belle Vue 14,
1020 Renens, Switzerland

PERSONAL INFORMATION:

Male, Italian, 27 years old.
Driving license. Permit B.

PROFESSIONAL EXPERIENCES

Ph.D. Thesis at EPFL

Development of III-nitride based devices:

- GaN tunnel junctions.
- Thermal budget reduction for long wavelength laser diodes.
- Regrown contacts for high electron mobility transistors (HEMTs) in collaboration with ETHZ.

Master project at EPFL

- Characterization of GaN grown on various substrates including diamond.
- Realization of HEMT devices on single-crystal diamond (111).

Internship project at the Italian Interbanking Deposit Guarantee Fund (FITD, www.fitd.it/en/)

- Financial data analysis.
- Interaction with top level banking representatives.

EDUCATION

2010-present **Ph.D. in Photonics** at *Ecole Polytechnique Fédérale de Lausanne -EPFL- (Switzerland)*

2006-2010 **M.Sc. in Physics** at Imperial College London (*England*).
Final mark: First class.

1994-2006 **European Baccalaureate** at European school of Bruxelles (*Belgium*) and Varese (*Italy*).

SKILLS

Technical skills Molecular beam epitaxy (MBE), spectroscopy (variable stripe length, photoluminescence, reflectivity), general cleanroom processing (photolithography, deposition, etching), scanning electron microscopy (SEM), electrical characterization techniques (capacitance-voltage profiling, Hall effect).

Computer skills LaTeX, Matlab, Origin, Adobe Illustrator.

LANGUAGES

Italian Mother tongue | **English** Proficient user (C1) | **French** Fluent (C2) | **Spanish** Basic (A2)

MISCELLANEOUS WORK EXPERIENCE

Sailing instructor for Les Glénans: volunteer skipper of 30/40 feet boats, responsible of the sailing activities and teaching for adults.

Project supervisor of master students at EPFL.

Teaching assistant at EPFL: managed bachelor and master courses specialized in general physics and electronic and optical semiconductor devices.

Students' representative of the European School of Varese (2006) and **CoSup member** (Conseil Supérieur des Elèves, en.wikipedia.org/wiki/European_School).

EXTRA ACTIVITIES

Venture challenge course: team leader for the development of a technology based start-up fabricating power amplifiers in the E-band (proposal selected over 30 presented projects).

PUBLICATIONS

Publications list: <http://infoscience.epfl.ch/search?ln=en&p=Malinverni%2C+M&f=author>

1. **M. Malinverni**, D. Martin, and N. Grandjean. *InGaN based micro light emitting diode featuring buried GaN tunnel junction*, submitted to Appl. Phys. Lett. (2015).
2. **M. Malinverni**, J.-M. Lamy, D. Martin, L. Lahourcade, E. Feltin, J. Dorsaz, A. Castiglia, M. Rossetti, M. Duelk, C. Vélez, and N. Grandjean. *InGaN laser diodes emitting at 500 nm with p-layers grown by molecular beam epitaxy*, Appl. Phys. Express **8**, 022105 (2015).
3. D. Marti, S. Tirelli, V. Teppati, L. Lugani, J.-F. Carlin, **M. Malinverni**, N. Grandjean, and C.R. Bolognesi. *94-GHz Large-Signal Operation of AlInN/GaN High-Electron-Mobility Transistors on Silicon With Regrown Ohmic Contacts*, IEEE Electron Device Lett. **36**, 17 (2015).
4. **M. Malinverni**, J. M. Lamy, D. Martin, E. Feltin, J. Dorsaz, A. Castiglia, M. Rossetti, M. Duelk, C. Vélez, and N. Grandjean. *Low temperature p-type doping of (Al)GaN layers using ammonia molecular beam epitaxy for InGaN laser diodes*, Appl. Phys. Lett. **105** (2014).
5. L. Lugani, **M. Malinverni**, S. Tirelli, D. Marti, and E. Giraud, J.-F. Carlin, C.R. Bolognesi and N. Grandjean. *n⁺-Ga_{0.5}N grown by ammonia molecular beam epitaxy: Application to regrown contacts*, Appl. Phys. Lett. **105**, 202113 (2014).
6. A. Dussaigne, M. Gonschorek, **M. Malinverni**, M. A. Py, D. Martin, A. Mouti, P. Stadelmann, and N. Grandjean. *High-Mobility AlGa_{0.5}N/GaN Two-Dimensional Electron Gas Heterostructure Grown on (111) Single Crystal Diamond Substrate*, Jpn. J. Appl. Phys. **49**, 061001 (2010).
7. A. Dussaigne, **M. Malinverni**, D. Martin, A. Castiglia, and N. Grandjean. *GaN grown on (111) single crystal diamond substrate by molecular beam epitaxy*, J. Cryst. Growth **311**, 4539-4542 (2009).

ORAL PRESENTATIONS

1. Buried tunnel junction for micro-LED and VCSELs, *invited talk at SPIE Photonic West 2015*, San Francisco (USA), February 11th 2015.
2. Advantages of the low temperature doping by MBE, *invited talk at the experimental nanophysics and photonics group seminar (TUB)*, Heimback (Germany), September 11th 2014.
3. Low temperature p-(Al)Ga_{0.5}N for long wavelength hybrid LDs, *International Workshop on Nitride Semiconductors*, Wroclaw (Poland), August 24th-29th 2014.
4. P-type doping of (Al,Ga)N by NH₃-MBE, *17th European Molecular Beam Epitaxy Workshop*, Levi (Finland), March 10th-13th 2013.
5. Low temperature p-type GaN:Mg grown by NH₃-MBE for green lasers, *17th International Conference on Molecular Beam Epitaxy*, Nara (Japan), September 28th 2012.
6. Comparison between MBE and MOVPE grown p-doped layers, *Wocsdice Workshop on Compound Semiconductor Devices and Integrated Circuits Europe*, Porquerolles (France), May 31st 2012.